



UNIVERSITY OF  
BIRMINGHAM

PERFORMANCE OF COBALT-BASED EGGSHELL CATALYST IN  
LOW-TEMPERATURE FISCHER-TROPSCH SYNTHESIS PROCESS  
TO PRODUCE LONG-CHAIN HYDROCARBONS FROM SYNTHESIS  
GAS UTILIZING FIXED-BED REACTOR TECHNOLOGY

*by*

**HAMID MAHMOUDI**

*A thesis submitted to the University of Birmingham for the degree of*

**DOCTOR OF PHILOSOPHY**

School of Mechanical Engineering  
College of Engineering and Physical Sciences  
University of Birmingham  
Submitted on: February 2015

UNIVERSITY OF  
BIRMINGHAM

**University of Birmingham Research Archive**

**e-theses repository**

This unpublished thesis/dissertation is copyright of the author and/or third parties. The intellectual property rights of the author or third parties in respect of this work are as defined by The Copyright Designs and Patents Act 1988 or as modified by any successor legislation.

Any use made of information contained in this thesis/dissertation must be in accordance with that legislation and must be properly acknowledged. Further distribution or reproduction in any format is prohibited without the permission of the copyright holder.

# با نام پروردگار بختشاپند لا و مهر بان

با احترام تقدیم به

پدرم، اول آموزگارم، که همواره چتر محبتش بر سرم است  
بزرگواری که القبای زندگانی را از او آموختم

مادرم، بلند تکیه گاهم، که دامن پر مهرش یگانه پناهم است  
مهربانی که عشق ورزیدن را از او آموختم

و برادران عزیزم، به پاس محبت های بی دریغشان که هرگز فروکش نمی کند  
و به پاس عاطفه سرشار و گرمای امید بخش وجودشان که در این روزگاران بهترین پشتیبان من هستند

حمید

شهریور ۱۳۹۳

*This thesis is dedicated to my supervisor,*

*Professor Mirosław Ł Wyszynski*

*for his endless support, guidance and encouragement*

## **Acknowledgments**

I would not be able to write this doctoral thesis without the kind help and immense support of dozens of people around me. To only some of whom it is possible to give a particular mention here.

Above all, I would like to express my special thanks and appreciation to my second supervisor, Dr Athanasios Tsolakis, for his patient guidance and advice, as well as his support throughout my research programme at the University of Birmingham.

In addition, I would like to express my sincere gratitude to Professor Joe Wood for his tremendous support of my study and research. He welcomed me to his highly-equipped laboratory to design and develop the catalyst. The good advice and friendly support from him, as well as from his research group: Dr Martin Khzouz, Dr Abdullah Almarshed, Dr Ju Zhu, Dr James Courtney and Dr Abarasi Hart were invaluable at both a personal and academic level; I am extremely thankful to all of them.

My sincere thanks also go to Mr Peter Thornton, Mr Carl Hingley, Mr David Boylin, Mr Jack Garrod and Mr Lee Gauntlett for their technical support. Moreover, I would like to greatly acknowledge Mr John Wedderburn, Dr Jackie Deans, Mr Jeff Sutton, Mrs Theresa Morris and Mr Paul Stanley who aided me during my research programme with their technical and scientific support. I am most grateful to Mr Tony Rogers; it was particularly kind of him to provide me with his support.

I would like to express my deepest gratitude to Dr Mohammad Hossein Zoualfaghari and Dr Saeed Hajimirzaee for their unwavering efforts, guidance and encouragement during my research programme. The scientific support of Dr Majid Sadeqzadeh and Mr Arash Izadpanah

is greatly acknowledged, particularly for providing the extremely useful guidance and encouragement. I also take this opportunity to record my sincere thanks to Dr Shahrouz Norouzi, Dr Aydin Sabouri and Mr Nima Moazami for their expert and valuable guidance and cooperation during my research programme.

Amongst my fellow postgraduate and undergraduate students in the School of Mechanical Engineering, the effort made by Miss Nazanin Akbari in developing the bio-fuel generator and formulating the highly-effective catalyst for synthesis of liquid fuel is highly acknowledged. In addition, I would like to appreciate the effort of Mr Jia Lu in simulating the Low-Temperature Fischer-Tropsch synthesis process by utilizing Aspen Plus software. Finally, I would like to deeply thank Mr Hessam Jahangiri and Mr Omid Doustdar not only for their scientific support, but also for providing me a welcoming social and academic environment, as well as their encouragement throughout my research programme.

This thesis was proofread for conventions of language, spelling and grammar by “Janet’s Proofreading Service”.

The support of Fuji Silysia ® Chemical Ltd (Head Office: 2-1846 Kozoji-cho, Kasugai, Aichi, 487-0013 Japan) is highly appreciated and acknowledged by the author for providing distinguished catalyst support materials.

## **Abstract**

Preliminary studies of the Fischer-Tropsch synthesis (FTS) process were begun in 2010 at the University of Birmingham. A mini-scale F-T plant was designed and built at the School of Mechanical Engineering to study the production of long-chain hydrocarbons over a cobalt-based FTS process. For this purpose, a series of eggshell cobalt catalysts supported with silica powder with a dissimilar porous structure were investigated to examine the effect of support variables on the catalysts' performance. The prepared catalysts were characterized with nitrogen adsorption/desorption, X-Ray Diffraction (XRD), Temperature-Programmed Reduction (TPR), Scanning-Electron Microscopy (SEM) and Energy-Dispersive X-ray Spectroscopy (EDS) experiments to ensure the qualification of the catalysts for the F-T plant. A highly metal-dispersed catalyst was achieved by controlling three key parameters: (i) cobalt content, (ii) impregnation solution and (iii) meso-porous silica of average pore diameter during catalyst preparation. The catalysts were relatively activated at high temperature because of the formation of small particles. The concentration of the active site was maximized in order to enlarge the hydrogenation activity of the cobalt-based eggshell catalyst to produce middle distillates products.

The optimisation study of the F-T process at low-temperature and low/medium pressure was performed to acquire the maximum production of liquid diesel fuel in a single-pass F-T process. The orthogonal arrays' approach was employed to design a set of experiments. The investigations were successful to maximise the conversion in reactants (up to 98%) and lower the activity of the co-reactions at the same time. The change in reactant consumption and hydrocarbons' selectivity was monitored over the time on stream and the responsible mechanisms for short-term deactivation within the first reaction cycle were studied, to achieve the optimum reaction conditions in terms of later deactivation of the catalyst.

## Table of contents

<b>List of illustration</b>	<b>V</b>
<b>List of tables</b>	<b>IX</b>
<b>List of symbols</b>	<b>X</b>
<b>List of abbreviation</b>	<b>XI</b>
<b>1 Introduction</b>	<b>1</b>
1.1 Fischer Tropsch Synthesis (FTS) technology	2
1.2 Aims, objectives and approaches	7
1.3 Thesis outlines	9
<b>2 Literature review on Fischer-Tropsch Synthesis process</b>	<b>13</b>
2.1 Fischer-Tropsch Synthesis (FTS) process overview	14
2.1.1 Introduction	14
2.1.2 History of F-T Synthesis	14
2.1.3 Significance of bio-energy	16
2.2 Characteristics of biomass	19
2.3 Fischer-Tropsch Synthesis mechanisms	23
2.4 Amorphous silica surface chemistry	30
2.4.1 Introduction of silica materials and general forms	30
2.4.2 Silica surface structure (physisorbed water, silanol groups and siloxane bridges)	31
2.4.3 De-hydroxylation and re-hydroxylation of the silica surface	36
2.5 Catalyst formulation and reaction engineering in the F-T process	42
2.5.1 F-T catalyst formulation	42
2.5.2 Catalyst carrier materials	44
2.5.3 F-T reactor technology	47
2.5.4 Overview of previous works regarding the Fischer-Tropsch synthesis process	48
<b>3 Catalyst preparation and development of experimental set-up</b>	<b>55</b>
3.1 Catalyst preparation and characterization experiments	56
3.1.1 Impregnation technique to deposit active metal over the support	56
3.1.2 Characterization of catalysts	64
3.1.2.1 X-Ray Fluorescence (XRF) spectrometry	64
3.1.2.2 Nitrogen adsorption/desorption	67
3.1.2.3 X-Ray powder Diffraction (XRD)	72
3.1.2.4 Scanning Electron Microscopy – Energy Dispersive X-Ray Spectroscopy	76
3.1.2.5 Temperature-Programmed Reduction (TPR) analysis	80
3.2 Fischer-Tropsch synthesis measurements	82

3.2.1	<i>Development of experimental set-up (bio-diesel generator)</i>	82
3.2.2	<i>Measurement of hydrogenation activity</i>	91
3.2.2.1	<i>Loading of the reactor</i>	91
3.2.2.2	<i>Start-up procedures of F-T experiments</i>	92
3.2.2.3	<i>Liquid and gas products analyses</i>	93
3.2.2.4	<i>Reactor performance characterization</i>	96
3.2.3	<i>Design of Experiments (DOE), the Taguchi method</i>	98
<b>4</b>	<b>Effect of support variables on catalytic performance</b>	<b>105</b>
4.1	<i>X-ray Fluorescence (XRF) analysis of Si and Co in derived catalysts</i>	106
4.2	<i>Nitrogen physisorption measurements</i>	109
4.3	<i>X-Ray Diffraction (XRD) analysis</i>	111
4.4	<i>Micro-structural and morphological structure of the catalysts</i>	114
4.5	<i>Catalyst activity and selectivity in the FTS process</i>	118
4.6	<i>Deactivation of a cobalt-based catalyst during FT synthesis</i>	122
4.7	<i>Conclusion</i>	127
<b>5</b>	<b>Process optimization at low-pressure reaction condition</b>	<b>129</b>
5.1	<i>Experimental results</i>	130
5.2	<i>Effect of the process conditions on the catalyst activity and products' selectivity</i>	131
5.3	<i>Cobalt-based F-T deactivation mechanisms</i>	138
5.4	<i>Signal to Noise (SN) ratio, Analysis of Variance (ANOVA)</i>	142
5.5	<i>Conclusion</i>	145
<b>6</b>	<b>Process optimization at high-pressure reaction condition</b>	<b>147</b>
6.1	<i>Experimental results</i>	148
6.1.1	<i>The rate of reaction</i>	151
6.2	<i>Effect of reaction conditions on F-T synthesis process</i>	152
6.2.1	<i>Effect of temperature</i>	152
6.2.2	<i>Effect of pressure</i>	158
6.2.3	<i>Effect of WHSV</i>	159
6.3	<i>Effect of increase in conversion</i>	161
6.4	<i>The Taguchi design of experiment</i>	165
6.5	<i>Conclusion</i>	169
<b>7</b>	<b>Optimization of metal loading</b>	<b>172</b>
7.1	<i>X-ray Fluorescence (XRF) elemental analysis of derived catalysts</i>	173
7.2	<i>Nitrogen adsorption/desorption analysis</i>	177
7.3	<i>Temperature-Programmed Reduction (TPR) analysis</i>	180
7.4	<i>X-ray Diffraction (XRD) analysis</i>	183

7.5	<i>Microstructural and morphological structure of the catalysts</i>	186
7.6	<i>Catalyst activity and selectivity in the FTS process</i>	190
7.7	<i>Conclusion</i>	194
<b>8</b>	<b>Conclusion</b>	<b>196</b>
<b>Appendix A</b>		<b>204</b>
<b>Appendix B</b>		<b>206</b>
<b>Appendix C</b>		<b>207</b>
<b>Appendix D</b>		<b>214</b>
<b>Appendix E</b>		<b>216</b>
<b>Appendix F</b>		<b>218</b>
<b>Reference</b>		<b>220</b>

## List of illustrations

- Figure 1.1:** Overview of indirect liquefaction process for Gas-To-Liquid (GTL) and Biomass-To-Liquid (BTL) conversion via methanol synthesis and Fischer-Tropsch synthesis respectively 3
- Figure 1.2:** Different type of gasification technologies 4
- Figure 2.1:** Professor Franz Fischer (left) and Doctor Hans Tropsch (middle), inventors of Fischer-Tropsch Synthesis process and Professor Friedrich Bergius (right) coal liquefaction process inventor 16
- Figure 2.2:** Molecular structure of biomass' cellulose constituent 20
- Figure 2.3:** Hemicellulose (xylan) molecular structure 21
- Figure 2.4:** Structural units of lignin, 4-propenyl phenol (left), 4-propenyl-2-methoxy phenol (middle) and 4-propenyl-2.5-dimethoxyl phenol (right) 21
- Figure 2.5:** Initiation step in carbide mechanism during Fischer-Tropsch synthesis reaction 25
- Figure 2.6:** Chain propagation of monomer units in carbide mechanism during FTS process 26
- Figure 2.7:** Schematic drawing of the most likely paths in termination step in carbide mechanism for formation of alkanes and alkenes 27
- Figure 2.8:** General chain growth pattern in CO insertion mechanism, R represents H or alkyl group 27
- Figure 2.9:** Mechanism scheme of hydroxycarbene intermediates' formation and chain growth pattern during F-T synthesis 28
- Figure 2.10:** Condensation-polymerization (a) and re-hydroxylation of de-hydroxylated silica (b) processes to form hydroxyl groups on the surface of SiO<sub>2</sub> 32
- Figure 2.11:** Representation of different silanol groups (isolated, silanediol and Silanetriol silanols), H-bonded silanols (single and silanediol) alongside siloxanes bridges on the surface of colloidal silica 34
- Figure 2.12:** Multi-layer physically adsorbed water de-hydration process, transition from stage 1 to 2 36
- Figure 2.13:** Complete removal of physisorbed water to achieve a dry silica surface (transition from stage 2 to 3, 180 °C ≤ T ≤ 200 °C) 37
- Figure 2.14:** Condensation process of silica surface by heat treatment, transition from stage 3 to 4 (stage 4a: 450 °C ≤ T ≤ 500 °C, stage 4b: 800 °C ≤ T ≤ 900 °C) 39
- Figure 2.15:** H-bonded silanols on the silica surface, acidic and no acidic hydrogens 40
- Figure 2.16:** Fully de-hydroxylated surface of silica, transition from stage 4 to 5 (1200 °C ≤ T) 40
- Figure 3.1:** Laboratory set-up for impregnation of silica supports to wetness solution of cobalt precursor and filtration process of solid phase from waste liquid phase 60
- Figure 3.2:** Separation of precipitated solid phase from filter paper and catalyst heat treatment (drying and calcination) to generate the active phase over the silica surface 61
- Figure 3.3:** Silica support (left) and derived supported cobalt catalyst (right) 62
- Figure 3.4:** Configuration of electrons within different energy shells in cobalt and silicon (electron shell 027 cobalt 014 silicon) along with the X-ray fluorescence generations due to X-ray bombardment 64
- Figure 3.5:** Bruker<sup>®</sup> S8 Tiger Wavelength Dispersive X-Ray Fluorescence (WDXRF) spectrometer using for elemental analysis of the samples 66
- Figure 3.6:** Micromeritics<sup>®</sup> ASAP 2010 instrument to analyse the surface area and pore size distribution 67
- Figure 3.7:** Multipoint BET plot 69
- Figure 3.8:** Different existing zones of a pore 70
- Figure 3.9:** Representation of Bragg's law, diffraction condition (constructive interference) as the reflection of X-rays from lattice (atomic) planes (h k l) 74

- Figure 3.10:** X-Ray diffractometer with motorization free curved detector (Inel<sup>®</sup> EQUINOX 3000) 75
- Figure 3.11:** Basic image formation in a Scanning Electron Microscope (SEM) 76
- Figure 3.12:** Sputter coating of Au before imaging in Scanning Electron Microscopy (SEM) 77
- Figure 3.13:** JEOL 6060 instrument 78
- Figure 3.14:** Micromeritics<sup>®</sup> AutoChem II 2920 chemisorption analyser to characterize the heterogeneous catalysts by the TPR analysis 80
- Figure 3.15:** Schematic diagram of small scale bio-diesel generator via Fischer-Tropsch Synthesis (FTS) process and utilized equipment along with Process Path Flow (PPF) to implement conversion of synthesis gas into the liquid heavy hydrocarbons (shown with thicker line) 83
- Figure 3.16:** Different components of mini bio-diesel generator in Fisher-Tropsch Synthesis process 85
- Figure 3.17:** Different components of mini bio-diesel generator in Fisher-Tropsch Synthesis process 86
- Figure 3.18:** GC chromatogram of standard gas (image directly taken from HP<sup>®</sup> 5890 software), the time taken for lighter hydrocarbons to travel through the column to the detector are shorter 94
- Figure 4.1:** X-ray Fluorescent spectra of CAT-Q-3 in the vicinity of Co K<sub>α</sub>, Co K<sub>β</sub>, Co L<sub>β</sub>, Si K<sub>α</sub> and Si K<sub>β</sub> 107
- Figure 4.2:** X-ray Fluorescent spectra of CAT-Q-6 in the vicinity of Co K<sub>α</sub>, Co K<sub>β</sub>, Co L<sub>β</sub>, Si K<sub>α</sub> and Si K<sub>β</sub> 107
- Figure 4.3:** X-ray Fluorescent spectra of CAT-Q-10 in the vicinity of Co K<sub>α</sub>, Co K<sub>β</sub>, Co L<sub>β</sub>, Si K<sub>α</sub> and Si K<sub>β</sub> 108
- Figure 4.4:** X-ray Fluorescent spectra of CAT-Q-30 in the vicinity of Co K<sub>α</sub>, Co K<sub>β</sub>, Co L<sub>β</sub>, Si K<sub>α</sub> and Si K<sub>β</sub> 108
- Figure 4.5:** X-Ray diffraction spectrogram of different calcined and unreduced supported catalysts 112
- Figure 4.6:** SEM micrographs (Figures 4.6.a and 4.6.b) and EDX micro-analysis (Figure 4.6.c) of sample CAT-Q-3 116
- Figure 4.7:** SEM micrographs (Figures 4.7.a and 4.7.b) and EDX micro-analysis (Figure 4.7.c) of sample CAT-Q-6 116
- Figure 4.8:** SEM micrographs (Figures 4.8.a and 4.8.b) and EDX micro-analysis (Figure 4.8.c) of sample CAT-Q-10 117
- Figure 4.9:** SEM micrographs (Figures 4.9.a and 4.9.b) and EDX micro-analysis (Figure 4.9.c) of sample CAT-Q-3 117
- Figure 4.10:** Effect of average pore diameter of catalyst on CO conversion, CO<sub>2</sub>, CH<sub>4</sub> and C<sub>5+</sub> selectivity. Reaction conditions; P: 20 bar, T: 510 K, WHSV: 3.0 NL/h.gcat 121
- Figure 4.11:** Performance of sample CAT-Q-3 in F-T synthesis regime, trend of CO conversion, CO<sub>2</sub>, CH<sub>4</sub> and C<sub>5+</sub> selectivity as a function of time on stream over cobalt catalyst supported silica 123
- Figure 4.12:** Performance of sample CAT-Q-6 in F-T synthesis regime, trend of CO conversion, CO<sub>2</sub>, CH<sub>4</sub> and C<sub>5+</sub> selectivity as a function of time on stream over cobalt catalyst supported silica 123
- Figure 4.13:** Performance of sample CAT-Q-10 in F-T synthesis regime, trend of CO conversion, CO<sub>2</sub>, CH<sub>4</sub> and C<sub>5+</sub> selectivity as a function of time on stream over cobalt catalyst supported silica 124
- Figure 4.14:** Performance of sample CAT-Q-30 in F-T synthesis regime, trend of CO conversion, CO<sub>2</sub>, CH<sub>4</sub> and C<sub>5+</sub> selectivity as a function of time on stream over cobalt catalyst supported silica 124
- Figure 5.1:** Effect of synthesis reaction conditions (Temperature, Pressure and space velocity) on CO conversion 132
- Figure 5.2:** Effect of synthesis reaction conditions (Temperature, Pressure and space velocity) on CO<sub>2</sub> selectivity 132

- Figure 5.3:** Effect of synthesis reaction conditions (Temperature, Pressure and space velocity) on CH<sub>4</sub> selectivity 133
- Figure 5.4:** Effect of synthesis reaction conditions (Temperature, Pressure and space velocity) on C<sub>5+</sub> hydrocarbons selectivity 133
- Figure 5.5:** Effect of synthesis reaction conditions on liquid production 137
- Figure 5.6:** Performance of single channel fixed-bed reactor for 9 experiments runs based on Taguchi L<sub>9</sub>, trends of CO conversion, CO<sub>2</sub>, CH<sub>4</sub> and C<sub>5+</sub> selectivity as a function of time on stream over a cobalt catalyst supported by silica 140
- Figure 5.7:** Main effect plots of Signal to Noise (SN) ratio for three control parameters (temperature, pressure and space velocity) and impact of that on responses (CO conversion, CO<sub>2</sub>, CH<sub>4</sub> and C<sub>5+</sub> selectivity as well as Liquid Produced (LP) along with R-squared (R-Sq) values 143
- Figure 6.1:** A comparison in conversion of carbon monoxide (X<sub>CO</sub>), selectivity of carbon dioxide (S<sub>CO<sub>2</sub></sub>), methane (S<sub>CH<sub>4</sub></sub>) and heavy hydrocarbon (S<sub>C<sub>5+</sub></sub>) for 16 experiments run based on Taguchi L<sub>16</sub> 150
- Figure 6.2:** A comparison in composition of different hydrocarbons cuts (C<sub>7</sub>-C<sub>11</sub>, C<sub>12</sub>-C<sub>22</sub>, C<sub>23+</sub>) in liquid products analysed qualitatively by GC-MS for 16 experiments run based on Taguchi L<sub>16</sub> DOE 150
- Figure 6.3:** Effect of synthesis reaction conditions on CO conversion. Reaction conditions; P: 10 - 25 bar, T: 503 - 543 K, WHSV: 1.8 - 3.6 NL/h.g<sub>cat</sub> 154
- Figure 6.4:** Effect of synthesis reaction conditions on CO<sub>2</sub> selectivity. Reaction conditions; P: 10 - 25 bar, T: 503 - 543 K, WHSV: 1.8 - 3.6 NL/h.g<sub>cat</sub> 154
- Figure 6.5:** Effect of synthesis reaction conditions on methane selectivity. Reaction conditions; P: 10 - 25 bar, T: 503 - 543 K, WHSV: 1.8 - 3.6 NL/h.g<sub>cat</sub> 155
- Figure 6.6:** Effect of synthesis reaction conditions on C<sub>5+</sub> hydrocarbons selectivity. Reaction conditions; P: 10 - 25 bar, T: 503 - 543 K, WHSV: 1.8 - 3.6 NL/h.g<sub>cat</sub> 155
- Figure 6.7:** Effect of synthesis reaction conditions on C<sub>7</sub>-C<sub>11</sub> HC cut. Reaction conditions; P: 10 - 25 bar, T: 503 - 543 K, WHSV: 1.8 - 3.6 NL/h.g<sub>cat</sub> 156
- Figure 6.8:** Effect of synthesis reaction conditions on C<sub>12</sub>-C<sub>22</sub> HC cut. Reaction conditions; P: 10 - 25 bar, T: 503 - 543 K, WHSV: 1.8 - 3.6 NL/h.g<sub>cat</sub> 156
- Figure 6.9:** Performance of fixed bed reactor for 16 experiment runs, variation of CO conversion, CO<sub>2</sub>, CH<sub>4</sub> and C<sub>5+</sub> selectivity as a function of time on stream over cobalt catalyst supported silica 162
- Figure 6.10:** Main effect plots of SN ratio for three control parameters and impact on responses along with percentage of contribution of parameters in responses (R-Sq value) 166
- Figure 7.1:** X-ray Fluorescent spectra of CAT-Q-15 in the vicinity of Co K $\alpha$ , Co K $\beta$ , Co L $\beta$ , Si K $\alpha$  and Si K $\beta$  174
- Figure 7.2:** X-ray Fluorescent spectra of CAT-Q-22 in the vicinity of Co K $\alpha$ , Co K $\beta$ , Co L $\beta$ , Si K $\alpha$  and Si K $\beta$  174
- Figure 7.3:** X-ray Fluorescent spectra of CAT-Q-29 in the vicinity of Co K $\alpha$ , Co K $\beta$ , Co L $\beta$ , Si K $\alpha$  and Si K $\beta$  175
- Figure 7.4:** X-ray Fluorescent spectra of CAT-Q-36 in the vicinity of Co K $\alpha$ , Co K $\beta$ , Co L $\beta$ , Si K $\alpha$  and Si K $\beta$  175
- Figure 7.5:** Comparative elemental analysis of catalysts in the vicinity of Co (K $\alpha$ , K $\beta$ , and L $\beta$ ) and Si (K $\alpha$ , K $\beta$ ) 176
- Figure 7.6:** Comparative elemental analysis of four derived catalysts in the vicinity of Co K $\alpha$  and Co K $\beta$  176
- Figure 7.7:** Nitrogen adsorption (filled circle) and desorption (empty circle) type IV isotherms for different catalysts obtained at 77 K 179

- Figure 7.8:** Temperature-Programmed Reduction (TPR) profiles of calcined catalysts with different concentrations of active sites (metal oxides) obtained from a chemisorption analyser 181
- Figure 7.9:** XRD diffraction spectrogram of different calcined and un-reduced supported catalysts 184
- Figure 7.10:** SEM micrographs (Figures 7.10.a and 7.10.b) and EDX micro-analysis (Figure 7.10.c) of sample CAT-Q-15 187
- Figure 7.11:** SEM micrographs (Figures 7.11.a and 7.11.b) and EDX micro-analysis (Figure 7.11.c) of sample CAT-Q-22 187
- Figure 7.12:** SEM micrographs (Figures 7.12.a and 7.12.b) and EDX micro-analysis (Figure 7.12.c) of sample CAT-Q-29 188
- Figure 7.13:** SEM micrographs (Figures 7.13.a and 7.13.b) and EDX micro-analysis (Figure 7.13.c) of sample CAT-Q-36 188
- Figure 7.14:** Effect of active metal concentration over support material surface on the catalytic performance of Co/SiO<sub>2</sub> catalyst in F-T synthesis of heavy hydrocarbons, reaction conditions: P=20 bar, T=510 K and WHSV=3.0 NI/h.<sub>g<sub>cat</sub></sub> 191
- Figure A.1:** X-ray Fluorescent (XRF) spectra of CAT-Q-3, CAT-Q-6, CAT-Q-10 and CAT-Q-30 in the vicinity of Co K $\alpha$ , Co K $\beta$ , Co L $\beta$ , Si K $\alpha$  and Si K $\beta$  204
- Figure A.2:** X-ray Fluorescent (XRF) spectra of CAT-Q-15, CAT-Q-22, CAT-Q-29 and CAT-Q-36 in the vicinity of Co K $\alpha$ , Co K $\beta$ , Co L $\beta$ , Si K $\alpha$  and Si K $\beta$  205
- Figure D.1:** Energy-Dispersive Spectroscopy (EDS) spectra of calcined and unreduced catalysts (CAT-Q-3, CAT-Q-6, CAT-Q-10 and CAT-Q-30) for elemental analysis of cobalt and silica 214
- Figure D.2:** Energy-Dispersive Spectroscopy (EDS) spectra of calcined and unreduced catalysts (CAT-Q-15, CAT-Q-22, CAT-Q-29 and CAT-Q-36) for elemental analysis of cobalt and silica 215
- Figure E.1:** Gas-Chromatography Mass-Spectroscopy spectra of liquid sample (reaction operating conditions: P: 20 bar, T: 510 K, WHSV: 3.0 NI/h.<sub>g<sub>cat</sub></sub> (picture directly taken from PerkinElmer software) 216
- Figure F.1:** Gas-Chromatography Flame-Ionization Detector (GC-FID) spectra of gaseous sample (reaction operating conditions: P: 20 bar, T: 510 K, WHSV: 3.0 NI/h.<sub>g<sub>cat</sub></sub> (picture directly taken from HP @ 5890 software) 218

## List of Tables

<b>Table 3.1:</b> Certificate of analysis provided by Fuji Silysia Chemical Ltd. for different silica supports	57
<b>Table 3.2:</b> Characteristics of wetness impregnation solutions and impregnation processes for the catalysts prepared to perform the catalyst-characterization experiments	59
<b>Table 3.3:</b> Characteristics of wetness impregnation solutions and impregnation processes for the catalysts prepared to perform the metal-loading optimization experiments	63
<b>Table 3.4:</b> Characteristics' wavelength of energy for cobalt and silicon along with their specifications	65
<b>Table 3.5:</b> List of different components in experimental rig, specifications and products' suppliers	88
<b>Table 3.6:</b> Different constituent of standard gas bottle for quantitative analysis of gaseous products	95
<b>Table 3.7:</b> Control factors and levels for different optimisation studies at different pressure conditions	99
<b>Table 3.8:</b> Factor settings for Taguchi $L_9$ design (left) for optimisation study at low pressure F-T reaction conditions and Taguchi $L_{16}$ design (right) for optimization study at high pressure F-T reaction conditions	99
<b>Table 3.9:</b> Analysis of Variance (ANOVA) table	103
<b>Table 4.1:</b> Analytical results for Co and Si acquired by XRF in prepared supported cobalt catalysts	106
<b>Table 4.2:</b> Variables derived from nitrogen physisorption to measure the total surface area	110
<b>Table 4.3:</b> Textural characteristics of meso-macro porous silica supports and cobalt supported catalysts measured by nitrogen physisorption technique	111
<b>Table 4.4:</b> Average $\text{Co}_3\text{O}_4$ crystallite size, estimated $\text{Co}^0$ particle diameter and estimated cobalt dispersion for different supported catalysts	113
<b>Table 4.5:</b> Elemental analysis of catalysts' surface by SEM-EDX to characterize metal content	115
<b>Table 4.6:</b> Catalytic performance of the different catalysts in FT synthesis: CO conversion ( $X_{\text{CO}}$ ), hydrocarbon selectivity ( $S_{\text{CO}_2}$ , $S_{\text{CH}_4}$ , $S_{\text{C}_2\text{-C}_4}$ , $S_{\text{C}_5+}$ ) and mass fraction of liquid phase's products	119
<b>Table 5.1:</b> Experimental data: changes in CO conversion ( $X_{\text{CO}}$ ), hydrocarbon selectivity ( $S_{\text{CO}_2}$ , $S_{\text{CH}_4}$ , $S_{\text{C}_2\text{-C}_4}$ , $S_{\text{C}_5+}$ ) for 9 experiments run	130
<b>Table 5.2:</b> Significance of control factors on responses utilizing Signal-to-Noise ratio	142
<b>Table 6.1:</b> Experimental data, changes in CO concentration ( $X_{\text{CO}}$ ), carbon dioxide selectivity ( $S_{\text{CO}_2}$ ), methane selectivity ( $S_{\text{CH}_4}$ ) as well as hydrocarbon selectivity, liquid phase mass fraction ( $W_i$ ), rate of reaction and Liquid Produced (LP) for 16 experiments run based on Taguchi $L_{16}$	149
<b>Table 6.2:</b> Significance of control factors (T, P and W) on responses ( $X_{\text{CO}}$ ), $S_{\text{CO}_2}$ , $S_{\text{CH}_4}$ , $S_{\text{C}_5+}$ , $W_{\text{C}_7\text{-C}_{11}}$ , $W_{\text{C}_{12}\text{-C}_{22}}$ , $W_{\text{C}_{23+}}$ ) and LP) utilizing Signal-to-Noise ratio	166
<b>Table 7.1:</b> XRF elemental analysis to determine the Co and Si concentrations in the derived catalysts	173
<b>Table 7.2:</b> Textural characteristics of meso-macro porous silica supports and cobalt supported catalysts measured by nitrogen physisorption technique	177
<b>Table 7.3:</b> Variables derived from nitrogen physisorption to measure the total surface area	178
<b>Table 7.4:</b> Average $\text{Co}_3\text{O}_4$ crystallite size, estimated $\text{Co}^0$ particle diameter and estimated cobalt dispersion for different supported catalysts	183
<b>Table 7.5:</b> Elemental analysis of catalysts' surface by SEM-EDX to characterize metal content	186
<b>Table 7.6:</b> Catalytic performances of the different catalysts in F-T synthesis: CO conversion ( $X_{\text{CO}}$ ), products selectivity ( $S_{\text{CO}_2}$ , $S_{\text{CH}_4}$ , $S_{\text{C}_2\text{-C}_4}$ , $S_{\text{C}_5+}$ ), reaction conditions: 510 K, 20 bar and 3.0 $\text{NL}/\text{min.g}_{\text{cat}}$	190
<b>Table B.1:</b> Variables derived from nitrogen physisorption to measure the total surface area different support materials including SUP-Q-3, SUP-Q-6, SUP-Q-10, and SUP-Q-30,	206
<b>Table C.1:</b> Tables of Analysis of Variance (ANOVA) for low/medium pressures optimisation studies	207

## List of Symbols

$a$	Mass of adsorption	g
$A_{cs}$	Cross-sectional area of adsorbate	nm <sup>2</sup>
$B$	Full-Width Half-Maximum	-
$C_{BET}$	BET constant	-
$d$	Distance of lattice plane	nm
$d$	Average metal particle size	nm
$d$	Mean crystalline diameter	nm
$D$	Metal dispersion	%
$\Delta H$	Reaction enthalpy	kJ.mol <sup>-1</sup>
$E_1$	Heat of adsorption	kJ.mol <sup>-1</sup>
$E_L$	Heat of liquefaction	kJ.mol <sup>-1</sup>
$f_A$	Reactant A conversion	-
$i$	y-intercept	g/cm <sup>3</sup> STP
$k$	Dimensionless shape factor	-
$K$	Reaction rate constant	-
$n$	Integer number	-
$N$	Avogadro's number	6.02214129(27)×10 <sup>23</sup> mol <sup>-1</sup>
$p$	Partial pressure	mmHg
$P$	Pressure	Atm, bar
$P$	Equilibrium vapor pressure	mmHg
$P_0$	Saturation vapor pressure	mmHg
$r_c$	Radius of curvature	nm
$R$	Universal gas constant	J.K <sup>-1</sup> .mol <sup>-1</sup>
$R$	Rate of reaction	Mol.min <sup>-1</sup> .g <sub>catalyst</sub> <sup>-1</sup>
$S$	Product selectivity	Mol %
$S$	slope	g/cm <sup>3</sup> STP
$S$	BET surface area	m <sup>2</sup> .g <sup>-1</sup>
$t$	Time	s, min, h
$T$	Temperature	K, C
$V_{ads}$	Adsorbed volume of gas	cm <sup>3</sup> /g STP
$V_L$	Molar volume of liquid	cm <sup>3</sup> /g STP
$V_{ml}$	Adsorbate mono-layer volume	cm <sup>3</sup> /g STP
$W_i$	Mass fraction of component $i$	-
$WHSV$	Weight-Hourly Space velocity	Nl.h <sup>-1</sup> .g <sub>catalyst</sub> <sup>-1</sup>
$X$	Reactant conversion	Mol %
$\alpha$	Chain growth probability	-
$\lambda$	Radiation wavelength	Å
$\theta$	Bragg angle	degree
$\sigma$	Product selectivity	Mol %
$\gamma$	Surface tension	N.m-1

## List of abbreviations

$\text{Al}_2\text{O}_3$	Aluminium oxide
ANOVA	Analysis of Variance
Au	Gold
BET	Brunauer-Emmett-Teller
BJH	Barrett, Joyner, and Halenda
BTL	Biomass-To-Liquid
C	Celsius
C	Carbon atom
$\text{C}_{(x)}$	Atomic carbon (carbon number)
CHOH	hydroxycarbene
$\text{CH}_2$	Methylene group
$\text{CH}_2\text{O}$	formaldehyde
$\text{CH}_3$	Methyl group
$\text{CH}_3\text{OH}$	Methanol
$\text{CH}_4$	Methane
$\text{C}_2\text{H}_4$	Ethylene
$\text{C}_2\text{H}_6$	Ethane
$\text{C}_3\text{H}_6$	Propene
$\text{C}_3\text{H}_8$	propane
$\text{C}_4\text{H}_6$	butadiene
$\text{C}_4\text{H}_{10}$	Isobutane
$\text{C}_4\text{H}_{10}$	1 - butane
$\text{C}_4\text{H}_{10}$	n-butane
$\text{C}_5\text{H}_8$	3-Methyl 1-butene
$\text{C}_5\text{H}_{12}$	Iso-pentane
$\text{C}_5\text{H}_{12}$	n-pentane
$\text{C}_5\text{H}_8\text{O}_4$	Hemi-cellulose
$\text{C}_6\text{H}_6$	benzene
$\text{C}_6\text{H}_{14}$	n-hexane
$\text{C}_6\text{H}_{10}\text{O}_5$	Glucose
$\text{C}_6\text{H}_{12}\text{O}_6$	Waste
$\text{C}_7\text{H}_8$	Toluene
$\text{C}_7\text{H}_{16}$	n-heptane
$\text{C}_7\text{H}_{16}$	Heptane
$\text{C}_8\text{H}_{18}$	Octane
$\text{C}_9\text{H}_{20}$	Nonane
$\text{C}_{10}\text{H}_{22}$	Decane
$\text{C}_{11}\text{H}_{24}$	Undecane
$\text{C}_{12}\text{H}_{26}$	Dodecane
$\text{C}_{13}\text{H}_{28}$	Tridecane
$\text{C}_{14}\text{H}_{30}$	Tetradecane
$\text{C}_{15}\text{H}_{32}$	Pentadecane

$C_{16}H_{34}$	Hexadecane
$C_{17}H_{36}$	Heptadecane
$C_{18}H_{38}$	Octadecane
$C_{19}H_{40}$	Nonadecane
$C_{20}H_{42}$	Eicosane
$C_{21}H_{44}$	Heneicosane
$C_{22}H_{46}$	Docosane
$C_{23}H_{48}$	Tricosane
$C_{24}H_{50}$	Tetracosane
$CH_mO_n$	Glucose
$C_nH_{2n}$	Alkene also known as Olefin
$C_nH_{2n+1}$	Alky; group
$C_nH_{2n}O$	Carbonyl
$C_nH_{2n+2}$	Alkane also known as paraffin
$C_nH_{2n+1}OH$	Alcohol
Co	Cobalt
CoO	Cobalt (II) oxide (Cobalt monoxide)
Co <sub>3</sub> O <sub>4</sub>	Cobalt (II, III) oxide (Tri-cobalt tetra-oxide)
CO	Carbon monoxide
CO <sub>2</sub>	Carbon dioxide
COS	organic sulphur
CTL	Coal-To-Liquid
Cu	Copper
DOE	Design of Experiment
EDS	Energy-Dispersive Spectroscopy
EIA	Energy Information Administration
EJ	Exa-Joule
EXP	Experiment
$f$	Degree of Freedom
$F$	variance ratio also known as F statistics
FID	Flame Ionisation Detector
FTS	Fischer Tropsch Synthesis
F-T	Fischer-Tropsch
FWHM	Full-Width Half-Maximum
GC	Gas-Chronogram
GHG	Greenhouse Gases
GTL	Gas-To-Liquid
H <sub>2</sub>	Hydrogen
H:C	Hydrogen-to-carbon monoxide ratio
HCs	Hydrocarbons
HCN	hydrogen cyanide
H <sub>2</sub> O	Water
H <sub>2</sub> S	hydrogen sulphide
$i$	Experiment number
in	Inch
ICDD	international Centre for Diffraction Data
K	Kelvin

K	Electron shell
$K_{\alpha}$	K-alpha emission line (electron transition from L to K shell)
$K_{\beta}$	K-beta emission line (electron transition from M to K shell)
KCps	Kilo Counts per second
KeV	Kilo electron Volts
KWI	Kaiser Wilhelm Institute
L	Electron shell
$L_{\beta}$	L-beta emission line (electron transition from M to L shell)
LTFT	Low-Temperature Fischer-Tropsch
LPG	Liquefied Petroleum Gas
mm	Millimetre
M	Metal surface
M	Electron shell
MFC	Mass Flow Controller
MODT	Million Oven Dried Tonnes
MS	mass spectrometry
MS	Mean Squares
MSW	Municipal Solid Waste
MTH	Methanol-To-Hydrocarbon
$N_2$	Nitrogen
$N_i$	Number of trial for experiment
$NH_3$	ammonia
NIST	National Institute of Standards and Technology
$NO_x$	nitrogen oxide
O	Oxygen atom
$O_2$	Oxygen
O:C	Oxygen-to-carbon monoxide ratio
PVD	Physical Vapor Deposition
R-CO	Acyl group
RDF	Refuse-Derived Fuel
Rh	Rhodium
R-OH	Hydroxyl group
R-Sq	R-squared
RTFO	Renewable Transport Fuels Obligation
PDF	Powder Diffraction File
PHE	Public Health England
PID	Proportional-Integral-Derivative
PM	Particulate Matter
ppm	Parts-per notation
S	variance
SED	Secondary Electron Detector
SEI	Secondary Electron Imaging
SEM	Scanning Electron Microscopy
SN	Signal-to-Noise
Si	Silicon atom
$SiO_2$	Silicon dioxide also known as Silica

SO <sub>2</sub>	Sulphur dioxide
SS	Sum of Squared
≡Si-OH	Single (isolated) silanol
=Si-(OH) <sub>2</sub>	geminal (silanediol) silanol
-Si-(OH) <sub>3</sub>	Silanetriol silanol
≡Si-O-Si≡	Siloxane
Si(OH) <sub>4</sub>	Silicic acid
TCD	Thermal Conductivity Detector
TiO <sub>2</sub>	Titanium dioxide
TPR	Temperature-Programmed Reduction
u	Trial number
UK	United Kingdom (of Great Britain)
US	United States (of America)
V	Variance
WDXRF	Wavelength Dispersive X-ray Fluorescence
WGS	Water-Gas-Shift
WHSV	Weight-Hourly Space Velocity
WTL	Waste-To-Liquid
WWII	World War II
$\bar{X}$	Grand mean
$X_j$	deviation of the means of groups
XRD	X-ray Diffraction
XRF	X-ray Fluorescence
$y_i$	mean value (value of performance characteristics)



---

# Chapter 1

---

## INTRODUCTION

Chapter 1 covers the indirect liquefaction processes in the conversion of carbonaceous materials to long-chain liquid transportable fuels via Fischer-Tropsch synthesis and methanol synthesis. The thermo-chemical gasification process in which the carbon-based feedstock is converted into the gaseous product is explained in this chapter as well. A brief description of the project is presented and the primary aims and objectives to achieve a cost-effective bio-fuel generator via Fischer-Tropsch synthesis are outlined. The approaches to obtain the proposed objectives of the project are presented as well. The chapter expresses an overview of what this investigation should accomplish (project outlines) regarding the second generation of bio-fuels via Fischer-Tropsch synthesis. The preliminary studies on the conversion of bio-syngas to bio-diesel could accelerate the scale-up progress as well as lead to an efficient design of a pilot-plant bio-diesel generator in the scaling up process.

### ***1.1 Fischer Tropsch Synthesis (FTS) technology***

For more than half a century, Fischer-Tropsch synthesis of liquid hydrocarbons was a technology of great potential for the indirect liquefaction of solid or gaseous carbon-based energy sources (Coal-To-Liquid (CTL) and Gas-To-Liquid (GTL)) into liquid transportable fuels. During the past decades, natural gas and coal were used as feedstock for the chemical industry as well as in the market of transportation fuels. With regard to the high energy content of petroleum in comparison to coal and wood, petroleum became required more and more for the economies of industrialized countries in the early 19<sup>th</sup> century. By the 1920s, with the advent of the mass-market car, the introduction of aircraft as well as liquid fuel-powered ships, the industries were forced to respond to the fuel demand. Hence, the commercialization process of F-T technology was started. The first commercial F-T plant to produce liquid fuel was built in the late 1930s. The name of this commercial-sized F-T generator was the Steinkohlen-Bergwerk Rheinpreussen plant which was located in Homberg, Germany to carry out the CTL process [1]. During and after World War II, a great number of investigations were carried out by Japanese technology to make an aircraft lubricating oil from F-T derived liquids. The first polymerization plant of lubricating oil was constructed by the Mike Synthetic Oil Company in Japan [2].

In contrast with the past, nowadays transport fuels are mainly produced from crude oil and there is not considerable diversity in their variety. Due to some limitations in the first generation bio-fuels, the second generation biofuels' technology was developed to perform the Biomass-To-Liquid (BTL) process. The BTL is a well-known multi-step process to convert the carbonaceous feedstock (biomass) into liquid fuels via Fischer-Tropsch synthesis technology. The BTL process was developed due to limitations in the first generation bio-

fuels' manufacturing. Figure 1.1 indicates the alternative process routes to convert carbonaceous materials into transport fuels within an indirect liquefaction process. Two principal processes are followed within indirect liquefaction to convert synthesis gas into oil; the first step is to convert the feedstock into a gaseous product which is a mixture of carbon monoxide, carbon dioxide, hydrogen, nitrogen (when air is the gasification medium) and water. Prior to the second step, the produced gas is purified to produce syngas. The synthesis gas is then converted into synthesis liquid fuel. The properties of the oil are not dependent on the raw material, rather it is the production process of synthesis fuel which reflects the properties of the produced oil [3].

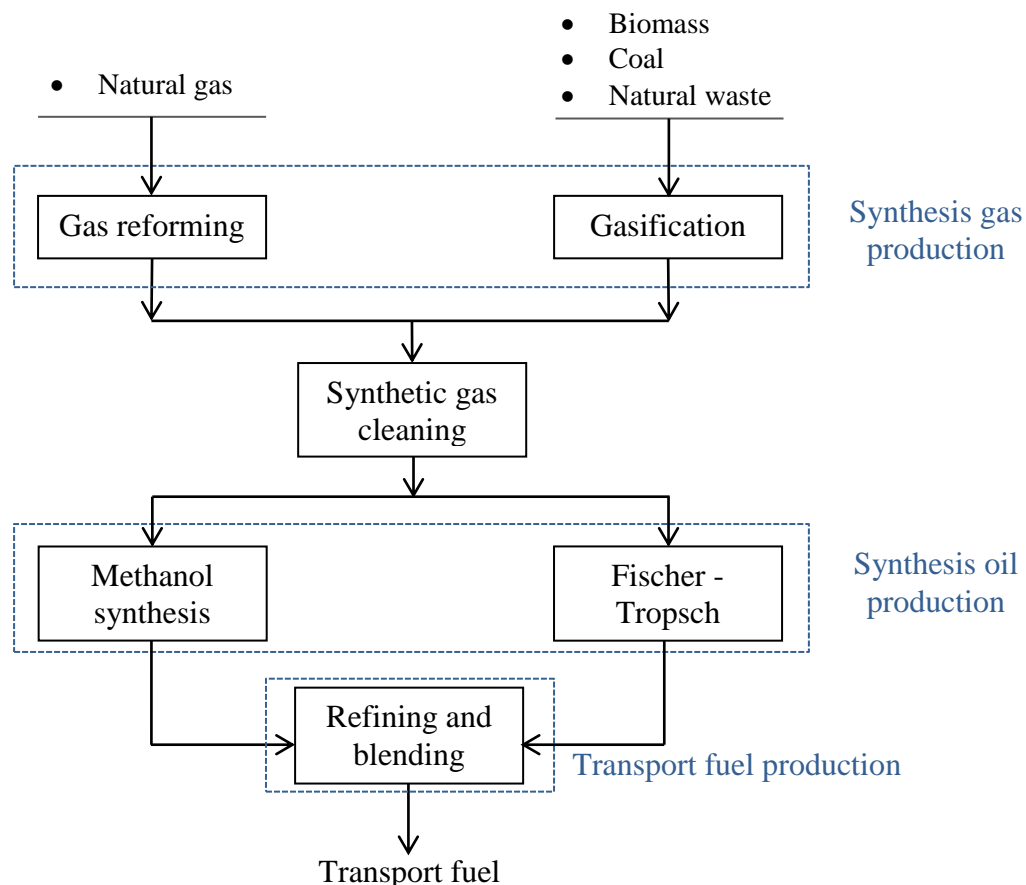


**Figure 1.1:** Overview of indirect liquefaction process for Gas-To-Liquid (GTL) and Biomass-To-Liquid (BTL) conversion via methanol synthesis and Fischer-Tropsch synthesis respectively

Gasification is a thermo-chemical process in which the solid feedstock (carbon-based feed associated with mineral matter) is converted into gaseous fuel or chemical feedstock. During the gasification process, the energy is packed into the chemical bonds in the produced gas. Hence, the product of the gasification process can be utilized to produce energy or can be used to produce value-added chemicals. The solid carbon and heavier hydrocarbons are converted into low-molecular-weight gases (carbon monoxide and hydrogen) by reacting them with gasifying mediums (oxygen, steam and air). The nature as well as amount of gasifying agent which is used during the gasification process strongly determines the heating value of the produced gas composition [4]. The melting behaviour is a specification of feed which is determined by the mineral matter composition. Eventually, the mineral matters are recovered from the gasifier as molten slag or ash. The synthesis gas outlet as well as gasifier

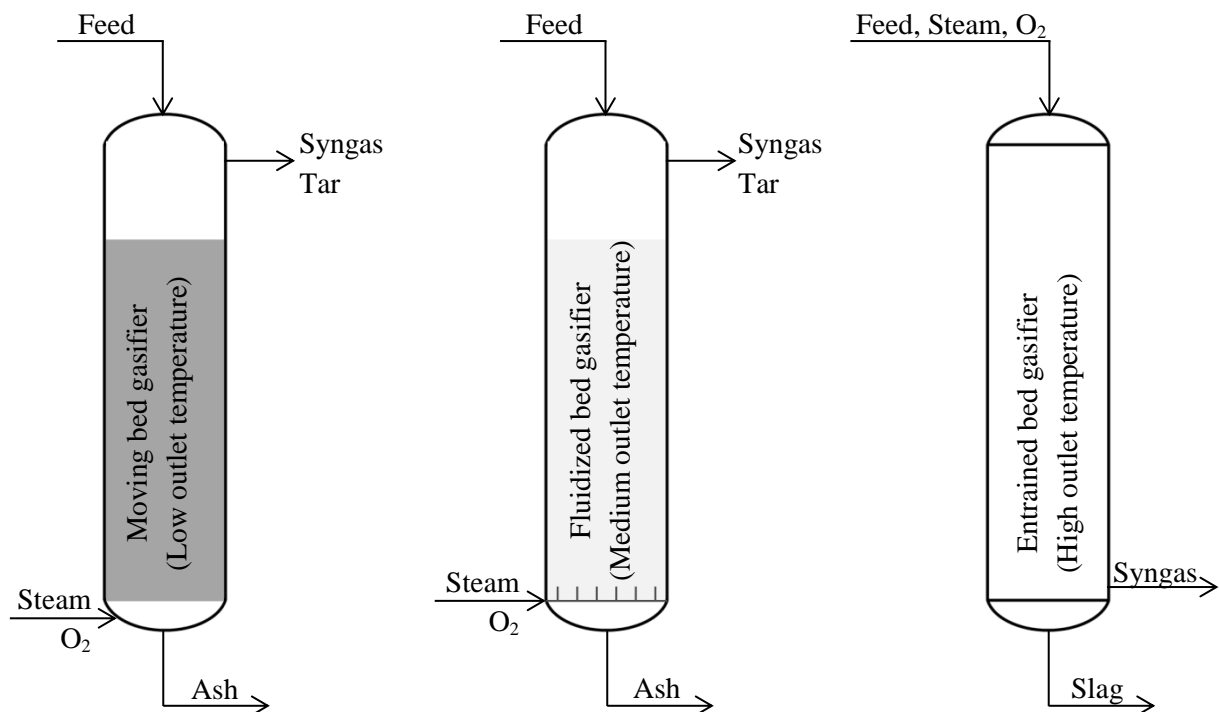
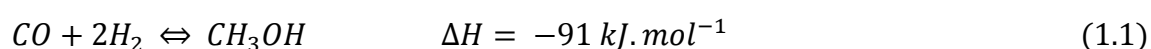


**Figure 1.2:** Different type of gasification technologies

reactor type are two parameters which specify the type of gasifier. According to this definition, the gasifiers are classified into three categories, (i) entrained bed (ii) fluidised bed and (iii) moving bed gasifiers. It should be mentioned that a generally higher ratio of hydrogen to carbon monoxide as well as more tar content are produced through the lower gasifier outlet temperature. Hereupon, the outlet temperature of synthesis gas in the gasifier is very important. The condensation of condensable vapor produced during this process forms tar as liquid product from the pyrolysis of the feed materials [3]. Figure 1.2 indicates the configuration of different types of gasifiers.

Fischer-Tropsch synthesis constitutes one of the routes within the indirect liquefaction process. As a result of hydrogenation of carbon monoxide and consequently polymerization of carbide metal, a wide range of products (hydrocarbons, oxygenates and water) are produced with a vast distribution in carbon number. The product of the second route which is known as methanol synthesis is not really an oil, but methanol, which is the result of a partial carbon monoxide hydrogenation reaction. The carbon monoxide is not polymerized during the methanol synthesis [3]. Equation 1.1 represents the general form of CO hydrogenation in methanol synthesis.



Higher selectivity of final product (methanol) along with minor amounts of co-products is a key advantage of this process. The process design in methanol synthesis is analogous to that of F-T indirect liquefaction. Copper-based catalysts are employed in most new technologies to conduct methanol synthesis at 473-573 K and 35-100 bar reaction conditions. Since the Water-Gas-Shift (WGS) reaction is activated over Cu-based catalysts, hence the methanol synthesis could be performed by using carbon dioxide, particularly when the hydrogen to

carbon monoxide ratio is higher than two in the synthesis gas product. The ease of recovering methanol from unconverted syngas leads to less involvement of product recovery as well as the recycling system, compared to F-T synthesis. Because methanol is a single product as well as this product is liquid at ambient conditions. The key disadvantage of using methanol on its own is that it has low energy density compared to that of standard transport fuel. For example, in comparison to gasoline fuel derived from petroleum, 41% more methanol is required to be consumed for the same travel range [3]. Therefore, methanol is converted into mainly olefinic hydrocarbon products [5, 6] utilizing a ZSM5 catalyst [7-9]. The main reaction of methanol synthesis is represented by Equation 1.2, producing oxygenated- free predominantly branched and cyclic olefin hydrocarbons. Paraffin and aromatics are produced through a Methanol-To-Hydrocarbons (MTH) process as well [3].



At the moment, approximately 90 million barrels of crude oil are demanded per day from which about 85 percent is required to produce liquid transport fuels. The contribution of the production of liquid transport fuels via alternative processes such as BTL, GTL and Waste-To-Liquid (WTL) is still less than five percent. Crude oil is not a sustainable source of energy. In addition, it is estimated that within the next half century, countries will face a shortfall in production of crude oil in comparison to the demand of transporting energy. This is one of the consequences of global economy growth which makes the investigation regarding the alternative sustainable energies very essential. Hence, a huge amount of research is in progress to convert part of agricultural products (ligno-cellulose bio-mass) which do not include products suitable for the human food chain into a required liquid fuel. This idea could not solve the country's energy needs but could reduce dependency on crude oil.

## ***1.2 Aims, objectives and approaches***

The aim of the proposed investigation was to design, build and commission a bio-diesel generator via a Fischer-Tropsch synthesis (FTS) process to convert simulated nitrogen-rich syngas (33% hydrogen, 17% carbon monoxide and 50% nitrogen (volume %)) to consumable bio-fuel. Hence, the main objectives of the proposed work were to:

1. Design, develop and build a cobalt-based Low-Temperature Fischer-Tropsch synthesis (LTFT) generator utilizing a fixed-bed reactor with maximizing the synthesis driving force as well as liquid fuel production.
2. Design and develop suitable eggshell cobalt catalyst supported silica powder for F-T synthesis and improving the catalytic performance by controlling the support characteristics to govern metal dispersion, strength of metal-support interaction, mechanical strength and especially its porosity.
3. Carry out an optimisation study of Low-Temperature Fischer-Tropsch (LTFT) synthesis at low-pressure reaction conditions ( $2 \leq P \leq 10$  bar), in order to find the most advantageous reaction conditions for maximum production of long chain hydrocarbons combined with the highest conversion of carbon monoxide in a single pass F-T process.
4. Carry out an optimisation study of Low-Temperature Fischer-Tropsch (LTFT) synthesis at medium range pressure reaction conditions ( $10 \leq P \leq 30$  bar), in order to find the most advantageous reaction conditions for maximum production of long-chain hydrocarbons combined with the highest conversion of carbon monoxide in a single pass F-T process.

5. Optimize the active sites' content with maximizing the metal loading over the support surface, in order to reach the maximum conversion of the reactant in a single pass F-T process.

The first phase of the project was devoted to the design and development of the mini scale F-T liquid fuel generator as well as to building the parts (second year). The research methodology required the design and preparation of the in-house developed F-T catalyst in the first phase of the project (parallel work in the second year). The second stage (third year) was the optimization investigation to achieve the most advantageous condition and combination of eggshell catalyst with a fixed-bed reactor. The final stage (parallel work in the third stage) was devoted to investigate the deactivation mechanism of the catalysts.

A mini-scale Fischer-Tropsch synthesis was designed and built in a laboratory of the School Mechanical Engineering, the University of Birmingham, to find the best combination of in-house developed Co/SiO<sub>2</sub> catalyst, fixed-bed reactor and operating conditions to attain the particular objective of the investigation; which was to achieve the optimal F-T technology with a combination of operating regime and catalyst formulation. The designing of an appropriate, effective and inexpensive catalyst for a low temperature / low pressure FTS process is a complex task for researchers working in this area. This investigation made an effort to design, develop and prepare the cobalt-based catalyst considering all three aspects of FTS catalytic design (chemical, mechanical and cost); which could help to promote the F-T catalyst technology. Hence, the investigation advanced the research towards designing an inexpensive and efficient cobalt-based F-T catalyst. The deactivation mechanism of different catalysts over the reaction time depends on their type and use. To reduce the influence of the relatively high price of the cobalt precursor, effort was made to increase the performance and

life time of this catalyst by delaying its deactivation. The utilization of an eggshell catalyst in a mini scale bio-diesel generator is an innovative intention which could overcome the mass transfer limitation in a fixed-bed reactor system. The proposed study advanced the research towards integrated catalyzed liquid fuel production using micro-sized catalyst pellets' distribution. The primary pathway to impact was the utilization of a fixed-bed reactor combined with an eggshell catalyst which could easily be scaled up and commercialized to produce highly-selective heavy hydrocarbons. Thermodynamic study of the FTS process in laboratory-scale will result in the best and most effective use of a cobalt catalyst, taking into consideration the high cost of the cobalt precursor. The optimization study gives an understanding of the effect of reaction thermodynamics in terms of selectivity of product with respect to carbon number, using nitrogen-rich synthesis gas. In addition, maximizing of active sites' concentration over the support surface could result in higher conversion of reactants and subsequently higher production of proposed fuel per unit of time; which makes the process cost-effective.

### ***1.3 Thesis outlines***

An introduction to the conversion of carbonaceous materials to synthetic fuel via Fischer-Tropsch synthesis and methanol synthesis were represented in Chapter 1. The continuation of this thesis is categorized within 6 more chapters which are as follows:

**Chapter 2** presents a comprehensive literature review on the Fischer-Tropsch synthesis (FTS) process including a history of production of liquid hydrocarbons through F-T technology; the importance of second generation bio-fuels in future transporting energy and its advantages as well as the characteristics, of organic materials which are exploited as

feedstock in the F-T process to be converted to long-chain hydrocarbons. In addition this chapter represents the surface polymerization mechanisms for the production of a wide-range of hydrocarbons in the Fischer-Tropsch process. The silanol functional groups are represented in this chapter as well as the attempt to achieve a comprehension in de-hydration, de-hydroxylation as well as re-hydroxylation mechanisms of the silica surface. Catalyst formulation and reaction engineering in Fischer-Tropsch synthesis are reviewed in Chapter 2 as well.

**Chapter 3** outlines the catalyst preparation procedures to derive a silica supported cobalt catalyst. The most common characterization experiments in the study of supported solid catalyst, along with the methods utilized to carry out the characterization experiments, are described in this chapter as well, including a Wavelength-Dispersive X-Ray Fluorescence (WDXRF) spectrometer, nitrogen adsorption/desorption, X-ray powder Diffraction (XRD) analysis, Scanning Electron Microscope (SEM) with Energy Dispersive X-Ray Spectroscopy (SEM-EDS) and Temperature-Programmed-Reduction (TPR). The experimental work to develop the miniaturised version (laboratory scale) of an F-T bio-fuel generator is described in this chapter comprehensively. The experimental procedures including reactor loading, F-T experiment start-up, as well as the analysing of liquid/gas products, are widely explained in this chapter. In addition, this chapter presents the analytical section to measure the performance of the reactor in F-T synthesis. The techniques used to design a set of experiments to examine the influence of individual parameters in the F-T process are explained as well.

**Chapter 4** presents the kinetic experiments of carbon monoxide hydrogenation over the series of cobalt catalysts supported with dissimilar silica powders. The effect of support

variables on physico-chemical characteristics of cobalt catalysts is represented in this chapter as well. Furthermore, this chapter discusses the short-term deactivation of a cobalt catalyst in the Low-Temperature F-T process (LTFT) over the reaction time.

**Chapter 5** describes the optimisation study of cobalt-based Fischer-Tropsch synthesis to acquire the maximum production of heavy hydrocarbons in a low pressure/temperature F-T process. The investigation of this chapter is based on an orthogonal array approach derived in Chapter 3. The impact of control levels on response variables are considered in this chapter by using the Signal-to-Noise ratio (SN). The significant control factors are determined in Chapter 5 by employing the Analysis-of-Variance (ANOVA).

**Chapter 6** represents the kinetic study of a cobalt-based F-T catalyst in order to optimise the reaction conditions for the production of liquid hydrocarbons at medium-range pressure. The quality characteristics are optimised in this chapter by using Signal-to-Noise ratio (SN). In addition, the analytical results for Analysis-of-Variance (ANOVA) are represented in Chapter 6 as well in order to find the significant process parameters and their influence on the entire process.

**Chapter 7** introduces the kinetic experiments in the optimization study of metal loading over the support surface. The active metal deposition (cobalt) is maximized and optimized in this chapter to enhance the performance of the supported cobalt catalyst. A series of four catalysts with different concentrations of active sites are characterized by using X-Ray Fluorescence (XRF), X-Ray Diffraction (XRD), Temperature-Programmed Reduction (TPR), Scanning-Electron Microscopy (SEM) and Energy-Dispersive X-ray Spectroscopy (EDS). The catalyst's activity in F-T synthesis was examined at an industrially relevant condition.



---

# Chapter 2

---

## LITERATURE REVIEW ON

## FISCHER-TROPSCH SYNTHESIS PROCESS

Chapter 2 presents a brief history of Fischer-Tropsch synthesis technology used to convert coal into liquid hydrocarbons; as well as its industrialization during and after World War II (WWII). The significance of bio-energy and second generation bio-fuels is discussed in this chapter. Chapter 2 covers the characteristics of biomass which is used as feedstock in the Biomass-to-Liquid (BTL) process. Different mechanisms in the Fischer-Tropsch synthesis process to describe carbon monoxide hydrogenation as well as surface polymerization reaction are discussed widely in this chapter. The discussed mechanisms consist of carbide, CO-insertion and the hydroxycarbene mechanism. The surface chemistry of silica support is discussed in section 2.6. Silanol functional groups in silicon chemistry are explained extensively. In section 2.7, the catalyst formulation in the F-T process as well as F-T reaction engineering are discussed. In addition, the most common catalysts are introduced and the current reactor technologies in the F-T indirect liquefaction process are considered.

## ***2.1 Fischer-Tropsch Synthesis (FTS) process overview***

### ***2.1.1 Introduction***

The over-reliance of the world's nations on conventional fossil fuels puts our planet in peril. The continuity of the current situation will result in the rise of a combined average temperature over global land and ocean surfaces by 5 °C in 2100, bringing a rise in sea levels, food and water shortages and an increase in extreme weather events. The global warming, caused by humans, is one of the biggest threats to our future well-being [10]. In addition, oil reserves are limited and these reserves are decreasing dramatically. This reduction alongside the other relevant economic factors affects the world's oil prices. The need to run engines with the new generation of liquid fuels is inevitable. The investigations by the US Energy Information Administration (EIA) published in 2013 expressed a 56 percent increase in the world's energy consumption by the year 2040. Total world energy demand will have risen to 865 EJ (exajoule) by this year. The total world energy consumption was reported as 553 EJ in 2010. The outlook indicates that renewable energy is one of the fastest-growing energy sources in the world; where its usage increases 2.5 percent per year. Despite increasing success in the renewable energies, it is predicted that the fossil fuels will supply almost 80 percent of the world's energy demand through to 2040 [11].

### ***2.1.2 History of F-T Synthesis***

Fischer-Tropsch synthesis (FTS) has drawn a great deal of interest in the recent decades from researchers, since it has been believed that liquid hydrocarbons' production through this promising clean technology is a potential alternative method which could solve the shortage

of liquid transport fuels [12]. Second generation bio-fuels can be made from cellulosic biomass by thermal production of syngas followed by Fischer-Tropsch synthesis. This process is known as the Biomass-To-Liquid (BTL) process for producing liquid fuels. F-T synthesis is a technology that has an extensive history of production of gasoline and diesel from coal and natural gas. Recently great interest has been generated in applying this relatively well-known technology to cellulosic biomass and agricultural waste, to convert them to linear- and branched-chain synthetic hydrocarbon (HCs).

The Bergius coal liquefaction and Fischer-Tropsch synthesis of liquid hydrocarbons were invented and subsequently developed between the years 1910 to 1926. The first step to overcome the lack of petroleum by synthesising Germany's abundant coal supplies was taken by Friedrich Bergius (1884-1949), who invented high-pressure coal hydrogenation in Rheinau-Mannheim during the first and second decades of the 20<sup>th</sup> century. Bergius prepared a coal-oil paste by crushing and dissolving the coals containing less than 85 percent carbon in heavy oil; afterwards he reacted the prepared paste with hydrogen gas at 200 atm and 673 K; the resulting products were petroleum-like liquids [1].

In 1926, a decade after this success by German scientists, Franz Fischer and Hans Tropsch invented a process to convert coal into synthetic liquid hydrocarbons at the Kaiser Wilhelm Institute for Coal Research (KWI) in Mulheim Ruhr. First, Fischer and Tropsch hydrocracked the coal by reacting it with steam to produce synthesis gas (mixture of carbon monoxide and hydrogen) and then converted the gases to petroleum-like synthetic liquid at 1 to 10 atm and 453 to 473 K. The cobalt catalyst was first designed and developed by Fischer and his co-worker, Tropsch to achieve a successful process [1].

Among the industrialized nations, Germany was the first to synthesize petroleum from coal.

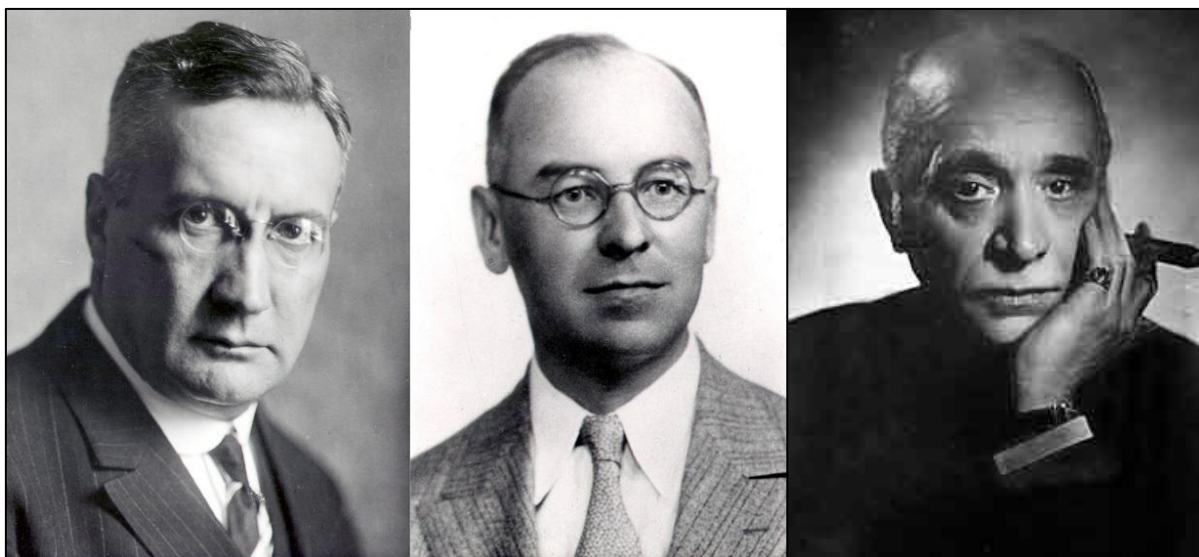


**Figure 2.1:** Professor Franz Fischer (left) and Doctor Hans Tropsch (middle), inventors of Fischer-Tropsch Synthesis process and Professor Friedrich Bergius (right) coal liquefaction process inventor

From the early 1930s to the end of the 20<sup>th</sup> century, Germany exported the technologically-successful F-T plant to the United States of America, Britain, Japan, France, South Africa and other nations. In Britain, the University of Birmingham was the pioneer in performing laboratory scale and pilot-plant sized Fischer-Tropsch synthesis investigations in 1920 [1]. Thenceforward, Germany and Britain were the most successful and pioneering in developing the generation of liquid synthetic hydrocarbons through F-T technology. The serious practical work on F-T synthesis in the US was began post-World War II; after that a rapid increase in petroleum consumption was observed leading to considerable concern from government [1].

### ***2.1.3 Significance of bio-energy***

Renewable energies such as bio diesel will play a significant role in the future for transporting energies, due to the abundant advantages of this fuel. Production of bio diesel from biomass

decreases the cost of the required fuel for farmers in comparison to oil/liquefied petroleum gas (LPG), because this fuel is produced by the farmer and there is no transporting cost and moreover, the feedstock is much cheaper than fossil fuels. In addition, bio-fuels are produced from plant waste that can be re-planted and re-grown by the interaction of carbon dioxide, water, air, soil and sunlight which guarantees the future transportation energies' sustainability. Bio-diesel made from biomass could easily replace fossil fuels due to its compatibility with the current engines' technology and their existing fuel system. Running the engines with bio-diesel produced from vegetable oils such as canola or rapeseeds, which are low in saturated fat, could prevent the formation of ice in frigid temperatures and subsequently prevent the vehicle's engine struggling with ice crystals. Bio-diesel increases the engine's lifetime as well. Production of bio fuels via sustainable energy crops could not solve the country's energy problem, but could reduce the dependency on foreign oil. The bitter experience of the industrialized countries in 1973, caused by the oil-producing countries of the Middle East, whereby they stopped exporting oil, propelled the western countries to become independent of them for their oil supplies [13].

Biodiesel-powered vehicles get 30 percent better fuel economy compared to gasoline-powered engines. Also, bio-diesel refineries are much cleaner than those of crude oil during the conversion of biomass into usable liquid products. The conventional fuel refineries release millions of pounds (lbs) of cancer-causing chemicals such as benzene ( $C_6H_6$ ), butadiene ( $C_4H_6$ ) and formaldehyde ( $CH_2O$ ) into the environment as well as nickel, sulphur dioxide ( $SO_2$ ), lead and some other pollutants which cause heart disease and asthma. It is therefore the case that bio-fuel refineries are much more environmentally friendly [13].

The amount of emissions of carbon dioxide by combustion of this fuel is the same as is absorbed by the organism of plants, which makes it carbon-neutral/greenhouse gases (GHG)

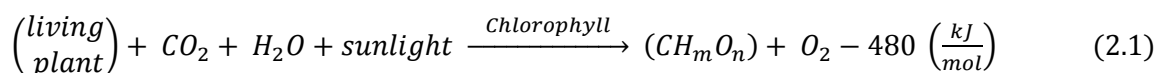
neutral fuel. Biodiesel produced via the Fischer-Tropsch synthesis (FTS) process seems to be a highly-promising alternative fuel due to such attractive specifications. Ultra-clean fuel, high cetane number of final liquid products, virtually zero emissions of sulphur compounds and aromatic hydrocarbons are some of the significant advantages of bio-fuel derived from F-T clean technology [14, 15]. Utilization of bio-diesel with compatible engines not only lowers the emissions of engines running on this fuel (nitrogen oxide (NO<sub>x</sub>), particulate matter (PM) and greenhouse gases (GHG)) also improve the catalytic after-treatment process [16]. The low emission of carbon monoxide, nitrogen monoxide, hydrocarbons and low sulphur and aromatic compounds make the synthetic fuels green and liquid clean fuels [17]. The absence of these compounds and the high cetane number of the generated products lead to high performance bio-diesel through F-T technology. The measurements of exhaust particle number concentration and size distribution in an engine fuelled with Gas-To-Liquid (GTL) are lower than those of an engine fuelled with conventional diesel [18].

The investigation of Public Health England (PHE) revealed that 5.3 percent of all the deaths in people aged over 25 correspond to air pollution. Under the Climate Change Act 2008, the UK Government is legally required to reduce the emission of GHG by 80% by the year 2050 [19]. The application of ultra-clean bio diesel by the farmers not only helps to reduce the emission of GHG but also lowers the emission of cancer-causing pollutants. This is one of the successful deliverables in the exploitation of renewable energies which benefits public health. The UK's Renewable Transport Fuels Obligation (RTFO) required the suppliers of fossil fuels to target 2.6% of road fuels to be made up of renewable fuels in 2011. This obligation first came into effect in 2008 and in that year, 84% from 1 million tonnes of bio-fuels in the UK market was made up of bio-diesel. The primary pathway of previous investigations in achieving an industrial impact is the significant advantage of a fixed-bed reactor which could

be easily scaled up for commercial plant. The success in commercialisation of bio-fuel generators could be effective in contributing to the achievement of a 13 percent substitution of bio-energy by volume in 2020 [20]. The exploitation of the bio-fuel generator in the agricultural industry could decrease the fuel demand by this sector. In addition, according to the report of the Biotechnology Industry Organization, the bio technology industry is expected to create 190,000 direct “green jobs” in the US. The commercialisation of bio-fuel generators in the UK will benefit society directly by creating new green job opportunities in United Kingdom [21].

## 2.2 Characteristics of biomass

In general, biomass is ascribed to the non-fossilized and biodegradable organic materials that have been derived from plants, animals and micro-organisms. The products of decomposition of non-fossilized organic materials are also referred to as biomass. The botanical (plant species) or biological (animal wastes and carcass) sources of biomass could be classified into agricultural, forest, municipal, energy and biological sources. The process of conversion of carbon dioxide into the botanical biomass (carbohydrate) in the presence of chlorophyll II and water is represented in Equation 2.1. Green plants break down the water in the presence of a particular wavelength of solar energy to obtain electrons and protons so that the carbon dioxide is converted into glucose ( $CH_mO_n$ ).



As represented in the above equation, for each mole of carbon dioxide absorbed, 1 mole of oxygen is released. Cellulose, hemicellulos and lignin are the three major constituents of non-

starch and fibrous ligno-cellulose biomass. This kind of biomass is not part of the human food chain as it is not easily digestible by humans. There is a great interest in the cultivation of ligno-cellulosic plants (willow, switch grass etc.) that are grown fast and yield a high amount of energy per unit of land. Unlike ligno-cellulose, carbohydrates are dissolved easily and could be converted into liquid fuels quickly. This is the reason that most of the commercial ethanol plants utilize crops [22].

The polymeric constituents of biomass widely vary in different biomasses. Cellulose is the most common organic compound on the earth which forms the cell walls of biomass' structural components. Cellulose ((C<sub>6</sub>H<sub>10</sub>O<sub>5</sub>)<sub>n</sub>) is a long chain polymer with a crystalline structure which is made up of many molecules of glucose. Figure 2.2 indicates the molecular structure of cellulose. Cellulose is made up of about 40 – 44 percent of dry wood weight which is not digestible by humans [22].

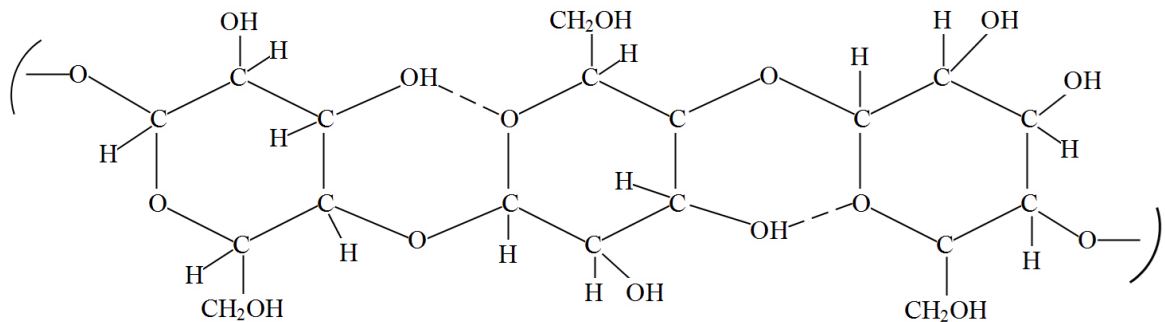


**Figure 2.2:** Molecular structure of biomass' cellulose constituent

Hemicellulose is an amorphous branched chain hydrocarbon structure of a cell wall's constituent. While cellulose has a high degree of polymerization (~10,000), hemicellulose has a lower degree of polymerization (~100-200). The generic formula of hemicellulose is

represented as  $(C_5H_8O_4)_n$ ; unlike cellulose resistant to hydrolysis, hemicellulose is hydrolyzed easily and solved in a solution of weak alkaline. Twenty to thirty percent of dry weight wood is made by hemicellulose. The hemicellulosic constituent of biomass cells yields less tar and more gases than the cellulosic constituent [22].

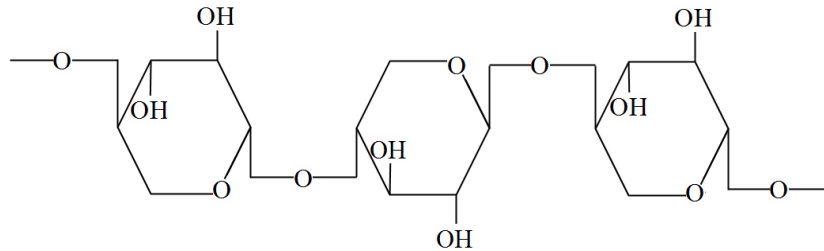


**Figure 2.3:** Hemicellulose (xylan) molecular structure

About 18 to 25 percent of a typical hardwood is made of a highly insoluble lignin constituent with a highly branched polymer of phenyl propane. These plentiful organic polymers in the earth make up the secondary cell walls of plants. Lignins act as cementing agents which hold the adjacent cells together [22].

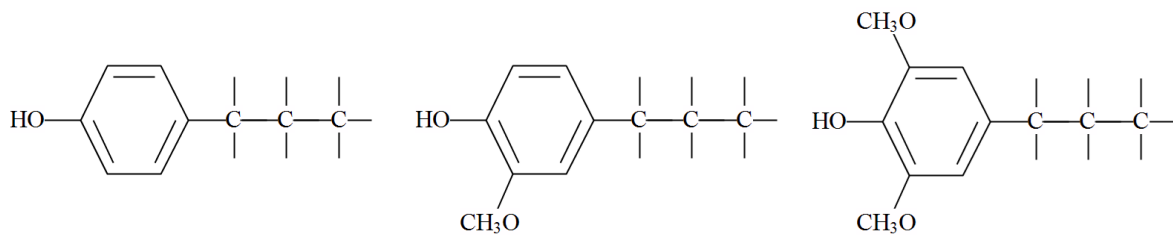


**Figure 2.4:** Structural units of lignin, 4-propenyl phenol (left), 4-propenyl-2-methoxy phenol (middle) and 4-propenyl-2,5-dimethoxy phenol (right)

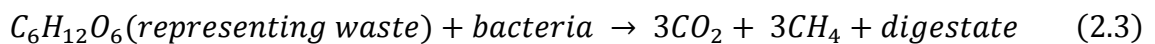
The higher hydrogen-to-carbon (H:C) ratio as well as high oxygen-to-carbon (O:C) ratio in fresh biomass, such as leaves, are correlated to the lower efficacious heating value of these

plants. A high amount of oxygen contents in biomass is not useful for the heating value of hydrocarbon fuel and makes the biomass liquefaction process more difficult. Moreover, the H:C ratio of biomass as well as its O:C ratio is much higher than that of fossil fuel. Equation 2.2 represents the linear function of these two ratios in a wide range of biomass:

$$(H:C) = 1.4125(O:C) + 0.5004 \quad (2.2)$$

The heating value of the biomass is related to its geological age meaning that the atomic ratio is increased in older fuels. Higher energy content results from biomass with a higher atomic ratio which increases with the increasing of the biomass' age. Moreover, the biomass with the same cellulose to lignin ratio and hemicellulose to lignin ratio, irrespective of their type, show similar behaviour in the transformation process [22].

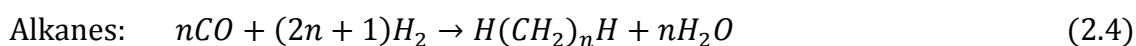
Municipal solid waste (MSW) is an important source of secondary waste that is derived from renewable (food scraps, paper etc) and non-renewable primary biomass (plastic, glass and metals). Refuse-derived fuel (RDF) is combustible part of MSW secondary waste. Sewage sludge is considered as an important biomass source. Aerobic and anaerobic digestions are two types of degradation process to reduce the amount of biodegradable waste. CO<sub>2</sub>, H<sub>2</sub>O and air are the products or microorganism's degradation process in aerobic digestion; while the second process produces methane. In anaerobic digestion, the leachate is collected from the landfill and pumped back in the absence of oxygen and the presence of methanogenic bacteria (thermophile, mesophile and psychophile) to the sealed land-filled solids. Equation 2.3 represents the exothermic biodegradation reaction which produces water and carbon dioxide. Methane is known as 21 times stronger than carbon dioxide among the greenhouse gases.

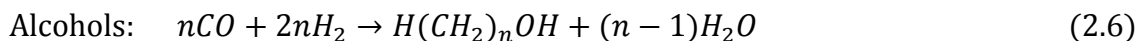
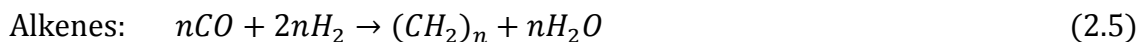


The United Kingdom Department of Energy and Climate Change estimated the availability of biomass as 6.1 to 15.3 Million Oven Dried Tonnes (MODT) in the year 2011; 8.1 to 15.5 MODT in 2015 and 10.4 to 16.3 MODT in 2020. Of these amounts, 3.2 to 5.0 MODT are estimated amounts of dry agricultural residue in 2015, with 3.7 to 5.0 MODT in 2020. On top of this, between 3.2 and 4.3 MODT are estimated amounts of waste wood which are expected in the years 2015 and 2020 respectively [23].

### 2.3 *Fischer-Tropsch Synthesis mechanisms*

Fischer-Tropsch synthesis is a surface polymerization reaction in which the reaction between the reagents, hydrogen and carbon monoxide, takes place on the surface of the catalyst in situ. First, reagents form monomer units. These building blocks are subsequently polymerized to yield a wide spectrum of the products (mainly paraffin) ranging from C<sub>1</sub> to C<sub>40</sub> HCs (heavy wax products) [24]. Several simultaneous chemical reactions occur in the F-T regime producing desired and undesired products. Equations 2.4 to 2.7 summarize the general forms of the reactions that take place in Fischer-Tropsch synthesis of hydrocarbons (paraffins, olefins and alcohols); whereby the term –CH<sub>2</sub>– represents a methylene group of normal paraffin. Polymerization of these blocks yields the products which depend on the thermodynamics and kinetics of the reactions [25]. Alkanes are the most preferred products in the F-T process. The produced alkanes from Equation 2.4 are mainly straight-chain hydrocarbons; while the alkene outputs of Equation 2.5 are mostly tertiary [26]. Equations 2.6 and 2.7 represent the general reaction forms which lead to formation of oxygenated products.





The portion of each of the above hydrocarbons in synthetic crude oil corresponds to the synthesis conditions and the catalytic bed in which the synthesis is conducted. Regardless of the reactions parameters, all of the F-T reaction mechanisms are based on the ability of the metallic elements of the catalyst to dissociatively chemisorb the carbon monoxide.

The mechanisms of the Fischer-Tropsch synthesis process have attracted many researchers in the past; such as B. H. Davis [27] and A. P. Anderson [28]. The definition of the complex reaction networks could describe the formation of carbon-carbon bonds, the hydrogenation of the carbon monoxide, as well as how subsequently the Fischer-Tropsch synthesis proceeds. These investigations lead to a comprehension of the F-T catalytic chemical surface reaction which could improve the design of F-T catalysts in the future. Different mechanisms based on different intermediates were proposed to govern the F-T syncrude composition. Carbide mechanism, CO insertion and hydroxycarbene mechanism are the main polymerization schemes that have been proposed within the three major steps (initiation, propagation and chain termination steps). The mechanisms differ with the nature of the formation of monomer units and the paths that the surface reactions govern which are to be converted to the proposed hydrocarbons.

In a carbide mechanism, adsorption of carbon monoxide on the catalyst surface initiates the F-T reaction. The initiation step results in the metal surface (M) being carbided by gaseous carbon monoxide. Carbon monoxide is chemisorbed initially in a bridge mode involving two surface sites of the catalyst and also is equilibrated in with a linear mode involving only one

site of the metal surface. The C–O bond is subsequently dissociated into the C and O surface species. Hydrogen as the second reactant is chemisorbed and dissociated on the metal surface site as well [26]. While it is the case that carbon monoxide is adsorbed more forcefully than the hydrogen on the catalytic surface sites [29]. C<sub>1</sub> intermediate species (M–CH<sub>x</sub>) are formed during the reaction of surface carbon with chemisorbed surface hydrogen atoms. The hydrogenation of surface C atoms of metal carbides to surface CH<sub>2</sub> (methylene species) removes the oxygen as water; which was the probable path in the original mechanism assumed by Professor Franz Fischer and Hans Tropsch in 1926 [30]. The reactions of the adsorbed oxygen with the adsorbed hydrogen lead to the elimination of the oxygen from the surface metals. Figure 2.5 illustrates the initiation step in a carbide mechanism with two different paths.

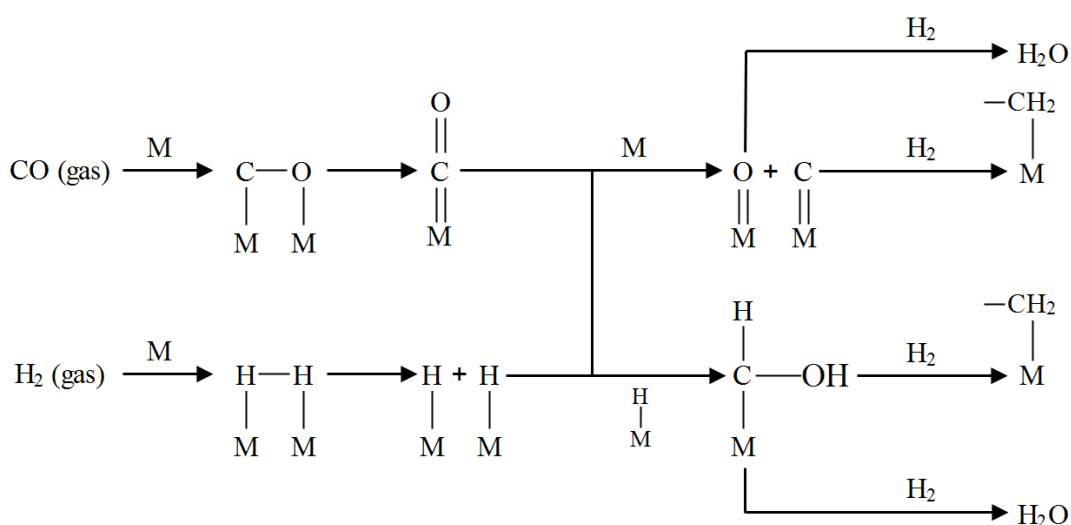


**Figure 2.5:** Initiation step in carbide mechanism during Fischer-Tropsch synthesis reaction

The second plausible path to form the monomer units is the formation of enol groups during the reaction of adsorbed CO with surface hydrogen. The hydrogenation of surface enol groups

result in the formation of methyl groups. The hydrogenation of surface enol eliminates the oxygen as water products (Figure 2.5). Once the initiation occurs, different routes could govern the propagation and chain termination in the synthesis process to produce hydrocarbon molecules. A high temperature F-T reaction condition favours the reaction to follow the first path and a lower F-T reaction temperature causes the oxygenation of the enol groups with a further reaction [26].

Afterwards the chain growth step takes place; when the surfaces  $M-CH_2$  are polymerized by reacting with another  $M-CH_2$  to form  $M-CH_2-CH_2-M$  intermediate. The insertion into the  $M-CH_2$  bonds and subsequently desorption and hydrogenation yields the cycloalkane and cycloalkanes respectively; which explains the formation of cyclic aliphatic hydrocarbons in F-T synthesis [29]. The insertion of  $CH_x$  groups into the metal-carbon bonds are the proposed the long chain hydrocarbons. The propagation of monomer units has been shown in Figure 2.6.

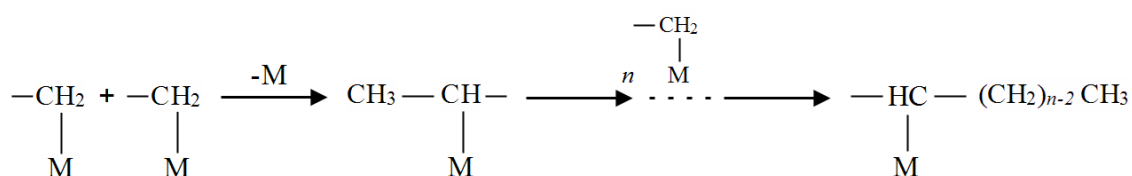


**Figure 2.6:** Chain propagation of monomer units in carbide mechanism during FTS process

The chain termination (Figure 2.7) occurs by hydrogenation of adsorbed surface alkyl groups ( $-HC-(CH_2)_{n-2}-CH_3$ ) to produce paraffins, or during the combination with adsorbed surface  $CH_3$ . Olefin products (alkenes) are formed through the  $\beta$ -elimination of the hydrogen from surface alkyl groups with an empty surface site [26].

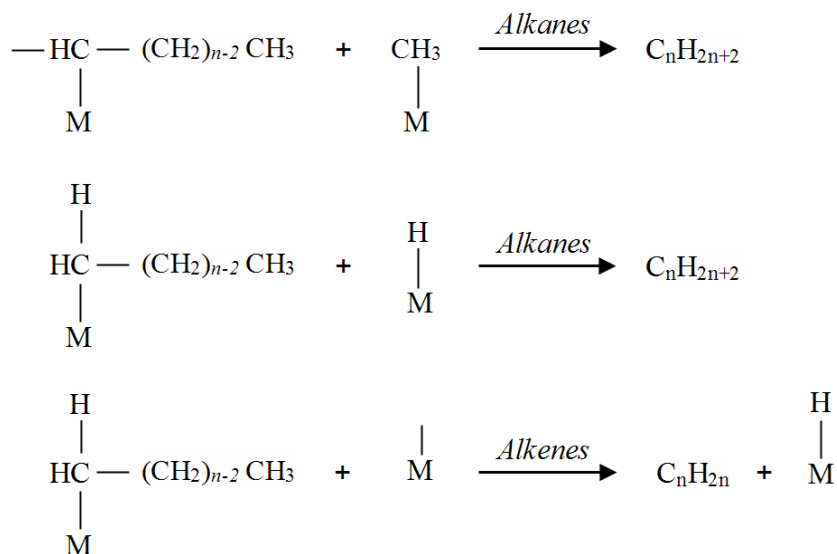


**Figure 2.7:** Schematic drawing of the most likely paths in termination step in carbene mechanism for formation of alkanes and alkenes

CO insertion into the metal-carbon bonds summarizes the general chain growth pattern of the CO insertion mechanism in the FTS process. The CO insertion into the M–H bond initiates the F-T reaction in this mechanism. The chains are grown by the insertion of carbon monoxide into the metal-alkyl bonds in homogeneous catalysis followed by reduction of the acyl group. The hydrogenation of the resulting acyl groups governs the termination of oxygenates or different hydrocarbons [31]. This mechanism is demonstrated in Figure 2.8.

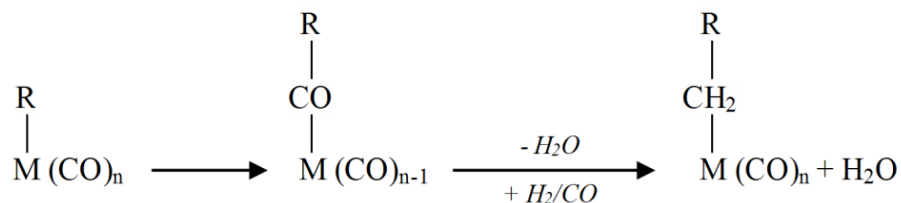


**Figure 2.8:** General chain growth pattern in CO insertion mechanism, R represents H or alkyl group

The third developed mechanism of F-T synthesis is known as the hydroxycarbene mechanism (Figure 2.9). This mechanism is based on the formation of hydroxycarbene (CHOH) intermediates. Hydrogenation of chemisorbed carbon monoxides on the metal surface by chemisorbed atomic hydrogen form hydroxycarbene. The water elimination through the condensation of two hydroxymethylene groups forms the C–C bonds. The chain is grown by the cooperation of oxygenated surface intermediates [31].

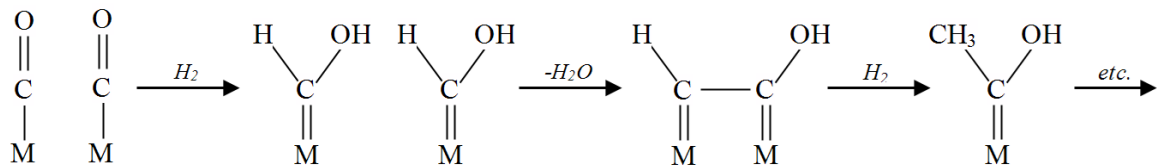
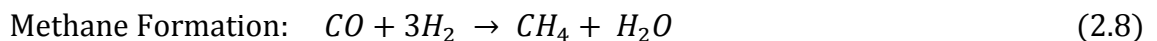


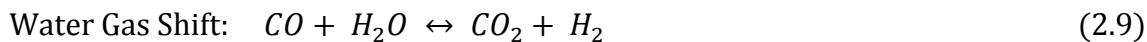
**Figure 2.9:** Mechanism scheme of hydroxycarbene intermediates' formation and chain growth pattern during F-T synthesis

The reaction for methane formation as an undesirable product in F-T synthesis can be summarized as follows. This reaction is considered as an irreversible and separate reaction. Methane formation increased with increasing of the temperature of the process, so controlling of the reactor temperature and exothermic reaction heat removal are significant considerations of F-T reactor design [32].



The other important reaction that occurs in the FTS process is Water Gas Shift (WGS) reaction that produces water as co-product; this reaction plays a significant, role especially in the reactors in which reactions take place over an iron-based catalyst and produce carbon

dioxide as an unwanted product. In general, a higher ratio of H<sub>2</sub>/CO forms more H<sub>2</sub>O, otherwise CO<sub>2</sub> is formed [33].



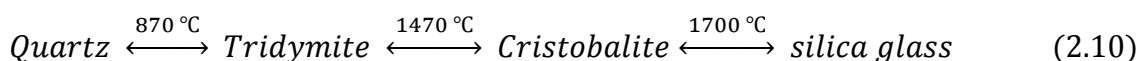
Sølvi Storsæter et al [34] developed a micro-kinetic model for formation of C<sub>1</sub> and C<sub>2</sub> species over supported cobalt catalysts in Fischer-Tropsch synthesis. The formation of methane, ethane and ethene were proposed within two sets of elementary reactions based on carbon monoxide hydrogenation and hydrogen assisted dissociation of carbon monoxide. These two sets of reaction patterns were combined and a micro-kinetic model was constructed. The activation energy, pre-exponential factors and rate constant were calculated for the elementary reactions involved in carbide and CO insertion mechanisms. The study concluded that the main part of carbon monoxides were converted and subsequently were propagated, yielding C<sub>2</sub> products through the CO insertion mechanism and insertion of carbon monoxide into the metal-methyl bonds, respectively. The mechanism of the Fischer-Tropsch synthesis' reaction as well as carbon monoxide activation and methane formation over a supported cobalt catalyst, were studied by Marton Kollar et al [35] and Jia Yang et al [36] respectively.

Rofer-DePoorter [37] performed a comprehensive investigation on Fischer-Tropsch synthesis reaction mechanisms, to bring forward the definition of the Fischer-Tropsch synthesis as the catalytic polymerization and hydrogenation of carbon monoxide to produce heavy hydrocarbons, as well oxygenated products. The elementary reactions within different mechanisms which take place in F-T synthesis have been described in this study. The study was focused on heterogeneous F-T catalytic mechanisms. The production of the side-products, carbon dioxide and water has been discussed. In addition, the paper provides the mechanism of the methanation reaction as a part of F-T synthesis.

## 2.4 Amorphous silica surface chemistry

### 2.4.1 Introduction of silica materials and general forms

The term silica refers to a large variety of naturally occurring abundant materials in minerals (quartz and flint). Moreover, silica is founded in plants such as rice and bamboo. The general formula for silica is  $\text{SiO}_2$  or  $\text{SiO}_2 \cdot x\text{H}_2\text{O}$ . Synthetic silica is mostly employed in the case of chemical application. The change in preparation conditions such as hydration degree, pressure and temperature could form different phases of silica. The increase of the temperature from  $870^\circ\text{C}$  to  $1470^\circ\text{C}$  at atmospheric pressure transforms the crystalline phase of quartz from its natural form to be classified in a cristobalite phase (high-temperature polymorph of  $\text{SiO}_2$ ). Amorphous vitreous silica glass is formed at  $1700^\circ\text{C}$  [38]. Equation 2.10 describes the transformation steps in which different phases of silicas are formed via heat treatment.



The outer surfaces of the crystalline particles participate in any physical or chemical interactions. Accordingly, the specific surface area of the active phase is similar to the geometric surface of silica in the crystalline form involving a high degree of ordering in a dense structure. The fabrication of amorphous silica forms sols, gels, fibres, sheets and powders based on their application. The specific characteristics of silica's texture (surface area, pore diameter and pore volume) are controlled during the preparation in which the physico-chemical behaviour of silica is governed. The amorphous form of silicas with a high degree of porosity could provide a large surface-to-mass ratio. This particular feature of silica makes it more and more attractive for chemical utilizations. The synthetic silicas are classified into the colloidal silica (silica sols) and silica gels (hydrogel, xerogel and aerogel) [38].

#### 2.4.2 *Silica surface structure (physisorbed water, silanol groups and siloxane bridges)*

Understanding of silanol functional groups in silicon chemistry could lead to a comprehension in de-hydration (removal of physically adsorbed water (physisorbed) and structurally bound water (chemisorbed)), de-hydroxylation (removal of the surface OH groups) and re-hydroxylation mechanisms of silica surface. The hydroxyl groups ( $\equiv\text{Si}-\text{OH}$ ) over the silica surface are made via valence bond between OH groups and both Si atoms on the surface and in some cases inside the silica's particles with the connectivity of Si-O-H [39]. Many of the chemical and catalytic characteristics of silica depend on the chemistry and geometry of its surface. Therefore, silica surface chemistry was the subject of a number of intensive investigations on molecular adsorption on silica's surface by using an infra-red spectroscopy experimental technique to determine the practical exploitation of this support [40]. Sheppard [41] proved the existence of hydroxyl groups on the  $\text{SiO}_2$  surface (porous glass) in various location types in his investigation about chemisorption system and physical adsorption. The presence of silanols on the surface of silica was proven for the first time in Yaroslavsky and Terenin's [39] investigation by employing the infra-red spectroscopy technique.

The course of silica synthesis and re-hydroxylation of de-hydroxylated silica are two principal processes to form the silanol groups on the amorphous silica surface (shown in Figure 2.10). The silanols' group within the first method are formed during the condensation-polymerization of  $\text{Si}(\text{OH})_4$ . Spherical colloidal particles which contain the hydroxyl groups are formed via the conversion of a super-saturated acid solution into its polymeric form. Finally, surface silanols are created by heat treatment of hydrogel which yields the xerogel. The water or aqueous treatments of de-hydroxylated silica form the surface silanols via the re-hydroxylation process. Within this method, the free valence of surface silicon atoms with

complete tetrahedral configuration becomes saturated with OH groups. The condensation of silanols under a specific condition form siloxanes bridges ( $\equiv\text{Si}-\text{O}-\text{Si}\equiv$ ). The formed silanols with hydrophilic features specify the surface properties of amorphous oxide adsorbent silica. The removal of surface hydroxyl groups which are considered as strong adsorption sites, gives the property of being more and more hydrophobic to the silica surface because of the existence of siloxanes [39].

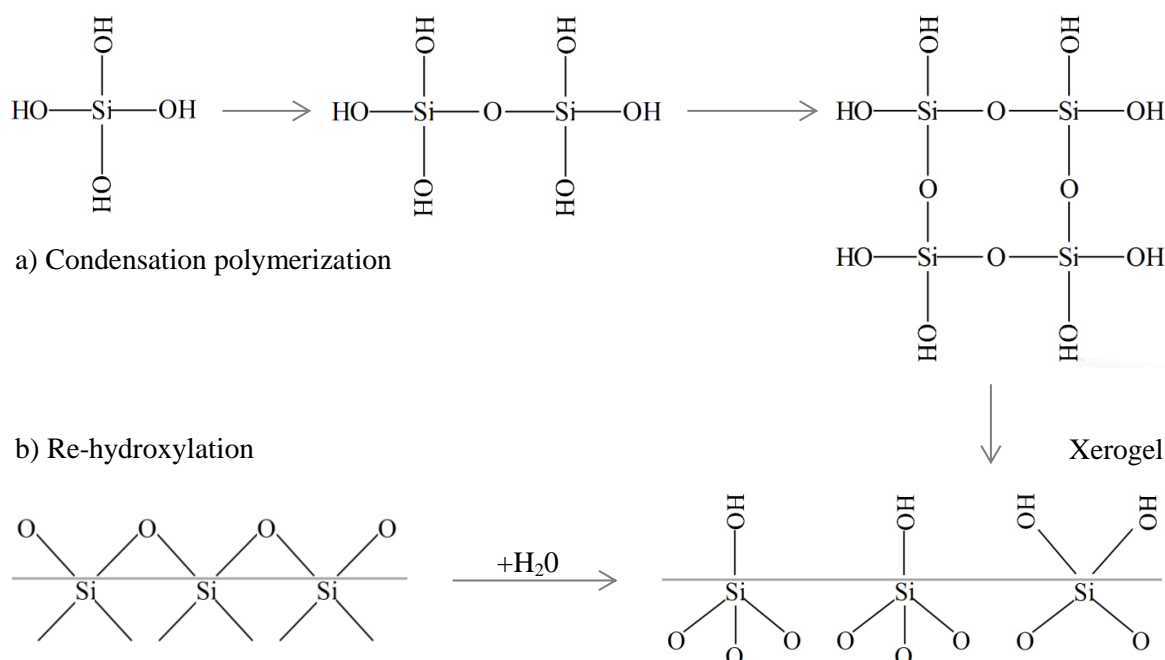


**Figure 2.10:** Condensation-polymerization (a) and re-hydroxylation of de-hydroxylated silica (b) processes to form hydroxyl groups on the surface of  $\text{SiO}_2$

Different kinds of silanols exist on the surface (external silanols) and even throughout the particle structure (internal silanols) of amorphous silica with a porous structure. The internal or intra-globular silanols are not accessible to water. Although there is no clear distinction between the silanols located on the surface with those internally located [38]. The study of Davydov [42] showed that the concentration of internal silanols in silica de-hydrated at  $200^\circ\text{C}$

was about 0.5 mmol/g. According to the same study no internal hydroxyl groups were reported for silica treated thermally at higher than 600 °C.

The existing silanol groups over silica's surface are classified based on their nature, association and multiplicity of sites. The numbers of bridging oxygens (Si-O-) bonded to the central silicon site in different categories are varied from 0 to 4. The single silanols with an OH group are the most preferred hydroxyls over the silica surface. This kind of silanols allocate an OH group per one surface Si atom and are the most probable compounds on a fully hydroxylated silica surface. This category of silanols is known as free or isolated silanols as well, which are located far from neighbouring hydroxyl groups. The isolated silanols are too far from the neighbouring hydroxyl groups, so the formation of hydrogen bonding is prevented. Three bridging oxygens from the bulk structure are bonded to the central silicon site in the free silanols [43]. Figure 2.11 illustrates schematically the different types of silanol groups and siloxane bridge presented on the surface of amorphous silica.

The silicon sites which are bonded to two bridging oxygens and consist of two hydroxyl groups (Si(OH)<sub>2</sub>) attached to the silicon atom are classified in geminal or silanediols silanol group. Peri [44] proposed the existence of geminal groups over the silica's surface for the first time. He concluded that de-hydrated surface structure of cristobalite at 400 °C includes about 95% geminal hydroxyl groups. In addition about 85% of de-hydrated silica surface at 600 °C was geminal hydroxyl groups. The geminals are close enough to hydrogen bond to each other [38]. It is now agreed that the relative contribution of the geminals on the silica's surface is relatively small to the total number of silanol groups. Morrow [45] observed that a small quantity of silicon atoms on the silica's surface (less than 5% of the total concentration of silanols) treated at 700 °C carried out geminal silanols; while most of the silicon atoms carried single hydroxyl groups being either free or vicinal silanols.

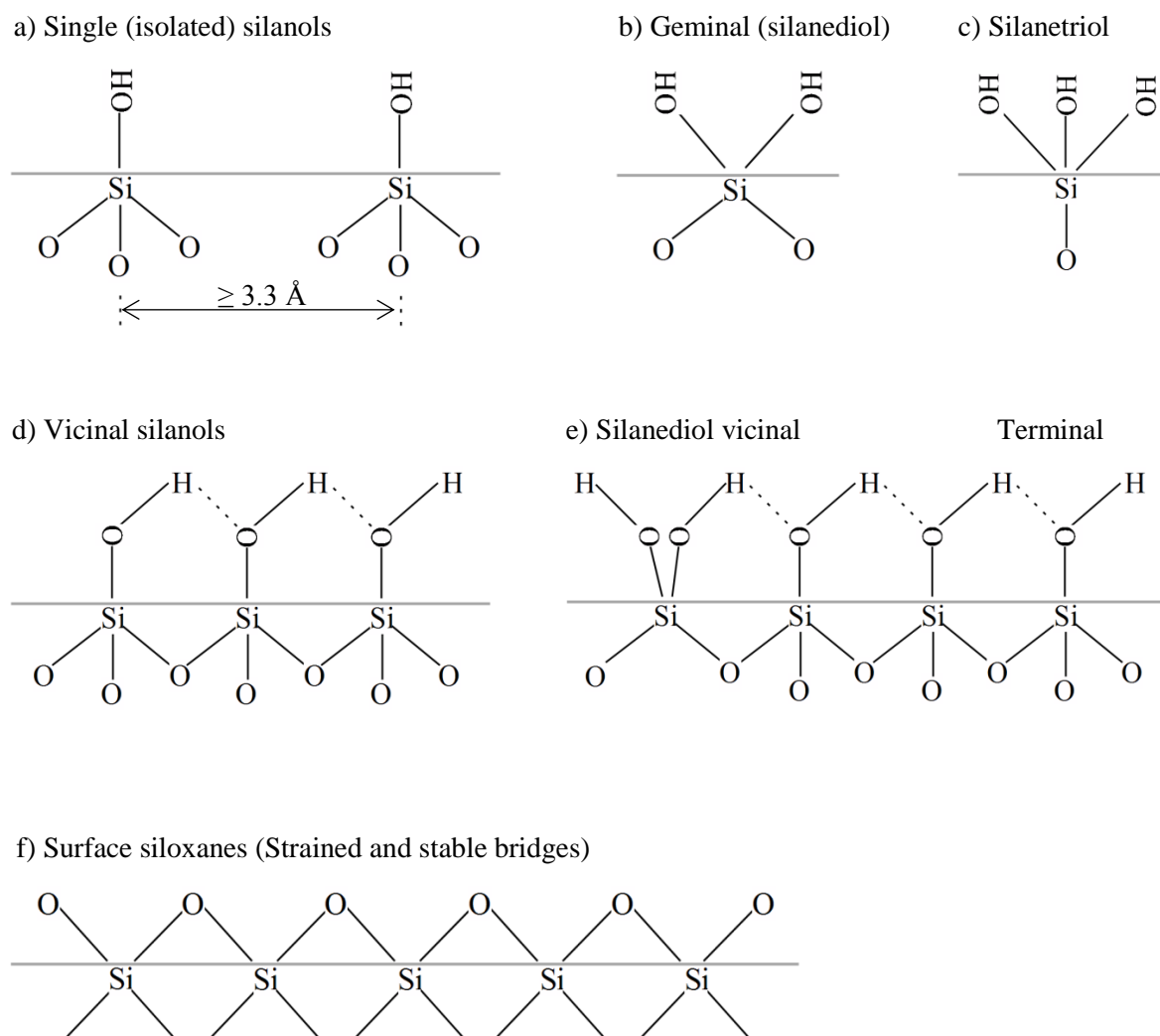
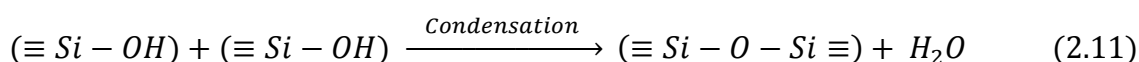


**Figure 2.11:** Representation of different silanol groups (isolated, silanediol and Silanetriol silanols), H-bonded silanols (single and silanediol) alongside siloxanes bridges on the surface of colloidal silica

When Si–OH groups are located a sufficient distance from neighbouring hydroxyl groups, the hydrogen bonding occurs between OH and O. These silanols are classified as vicinal or H-bonded silanols. The silanediols silanol are probably bonded to a neighbouring vicinal silanol through a single siloxanes bridge. The result of this bonding is a very weak H-bonded pair. The internal silanols, which in some cases are considered as structurally bonded water, form about 20 percent of the presented silanols in a hydrogel. These groups of silanols are within

the structure of the colloidal particles. The heat treatment between 600 – 800°C causes the condensation of internal silanols. At higher temperature the internal silanols' complete evolution occurs [43]. Siloxanes' bonds are formed through the condensation of internal and surface silanol groups. According to Equation 2.11, the de-hydroxylation (condensation) process is accompanied by the water formation. [38].



The thermally induced condensation of hydroxyl groups at about 500°C form the strained siloxane bridges. Stable siloxanes groups are the result of the conversion of strained siloxane groups at higher temperature. Both stable and strained siloxane groups are re-hydroxylated upon exposure to water. While it is the case that the re-hydroxylation rate of stable siloxanes are much slower than strained siloxanes. As an example, it takes about 5 years to completely re-hydroxylate the wide pore silica which is calcined at 900°C. Moreover, the strained siloxanes could completely be re-hydroxylated upon exposure to water [43].

Water molecules are adsorbed mainly to the OH groups of silica's surface. The hydrogen bond between hydrogen and highly electronegative oxygen is associated to any surface/internal silanols type. Due to the highly disordered surface structure of amorphous silica, a regular arrangement of silanol groups is not expected on the silica surface. Irrespective of what kind of hydroxyl groups exist on the surface, a fully hydroxylated surface can be achieved by complete surface coverage. When a porous silica surface is exposed to water at high partial pressure, the capillary condensation takes place on the adsorbed multi-layer of water by means of hydrogen bonding, which gradually fills the pore volume by liquid water. The increase in partial pressure of water results in adsorption of a multi-layer of water in a fully hydroxylated non-porous silica species as well [38].

### 2.4.3 De-hydroxylation and re-hydroxylation of the silica surface

Different treatments at different stages determine the concentration of hydroxyl groups on the silica surface. Physisorbed water de-hydration is an essential process to achieve a successful modified surface. Figures 2.12 to 2.16 indicate the silica surface physico-chemical model via heat treatments at different stages during the preparation process. Two types of molecularly adsorbed water have been established formerly (shown in Figure 2.12). Each of them is de-hydrated at various thermal sub-regions. The first de-hydration stage corresponds to poly-molecular adsorbed water; while the second relates to de-hydration of the monolayer of molecularly adsorbed water on the silica surface [46]. The desorption process of the first stage assigns much lower activation energy than that of the second stage; while the majority mass of the hydrogen-bonded waters are removed at the first stage. The sharp increase in activation energy of the desorption process from stage one to two corresponds to practically complete removal of the monolayer of waters which have been physically adsorbed. Both stages are greatly influenced by the size and morphology of the porous silica as well as its porosity [38].

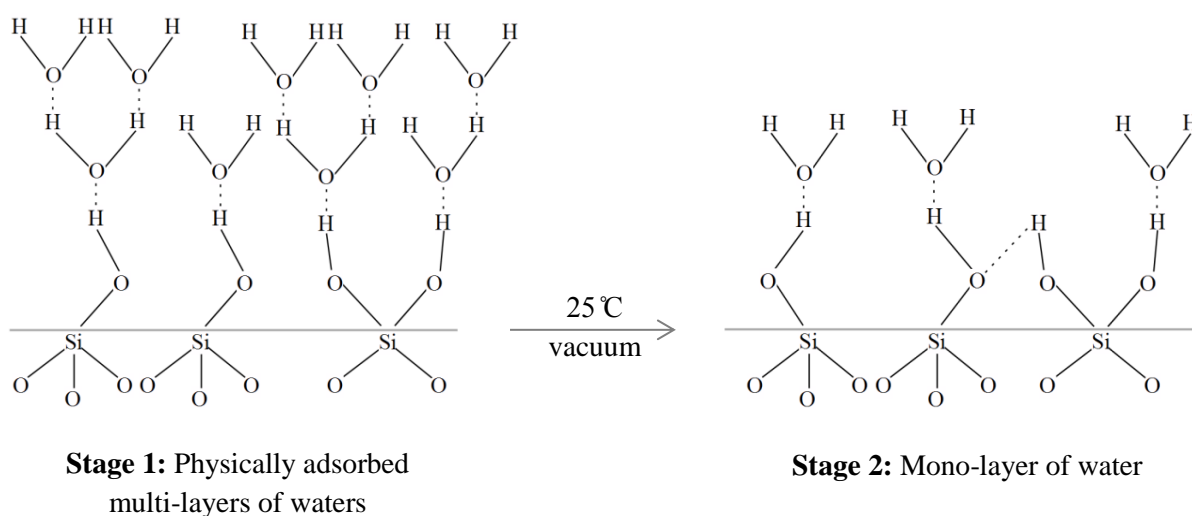


**Figure 2.12:** Multi-layer physically adsorbed water de-hydration process, transition from stage 1 to 2

As shown in Figure 2.12, at the initial stage, the silica surface is at its maximum state of hydroxylation. Multi-layers of water have been adsorbed physically which covers the silica surface containing different kinds of silanols (isolated, geminal and vicinal silanols). The H-bond networks alongside the water multi-layer cover the surface OH groups. At this stage, internal OH groups inside the silica skeleton exist. Transition to the second stage at 25°C removes the multi-layer of water. Thereupon, a single layer of physically adsorbed water is retained at this temperature. This stage is easily reversible to the first stage upon the exposure of water. Figure 2.12 (stage 2) indicates the mono layer or less of the physisorbed water on the silica surface, which is retained on the surface at temperatures less than 180°C [39].

Transition from stage two to three (Figure 2.13) results in complete removal of strongly physisorbed water. The threshold temperature for the complete de-hydration is estimated to be at  $190 \pm 10^\circ\text{C}$ . The re-hydroxylation stage is begun by completion of the de-hydration stage. Both of the stages, de-hydration and de-hydroxylation are very heterogeneous processes [47].

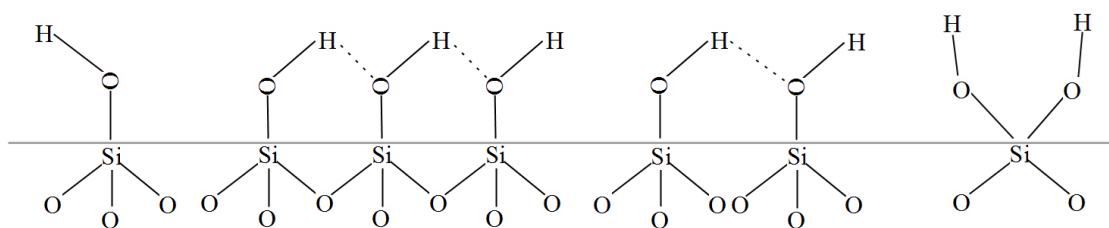


**Figure 2.13:** Complete removal of physisorbed water to achieve a dry silica surface (transition from stage 2 to 3,  $180^\circ\text{C} \leq T \leq 200^\circ\text{C}$ )

Zhuravlev [46] applied temperature-programmed desorption (TPD) experiments by employing the mass spectrometric thermal analysis method to investigate the de-hydration and de-hydroxylation of the silica surface. He concluded that more physisorbed water

coverage on the silica surface leads to a higher activation energy of water desorption process in the transition from stage one to two, as well as from the second stage to the third stage. The silica surface's behaviour at the introduction of water is the same as stage two.

The next stage is to condense the vicinal groups by further heat treating at about 450 to 500 °C. At this stage, the average distance between the neighbouring free hydroxyl groups are increased over the silica surface which causes a decrease in the de-hydroxylation process. The heat treatment of the silica surface at this stage releases water vapor. The resulting silanol groups of this stage consist of singles and geminals. The resulting surface coverage of silica at this stage has been shown in Figure 2.14, a). The numbers of isolated silanols are increased as a result of the transition from stage 3 to 4 by thermal treatment between 200 to 400 °C. The acid treatment of silica could result in a higher concentration of silanols over the silica surface as well [48]. On the other hand, the number of isolated silanols could be decreased by the re-hydroxylation process which increases the concentration of bonded silanols. With completion of the transition phase, further heat treatment at this stage decreases slightly the concentration of the silanols. The porous structure of the silica support could accelerate the de-hydroxylation process. For the silica with wide based pore structure, a decrease in the number of bridged silanols occurs at a higher temperature than for that with smaller pores [47]. As the temperature is relatively low, the siloxanes remain in a strained bridges state. In some cases, the complete re-hydroxylation occurs when the weakened strained siloxanes' bridges are split. The estimated ratio of isolated/geminal silanols is about 85/15 at this stage. The condensation of internal silanols occurred at about 600 – 800 °C; at this temperature the concentration of isolated and geminal silanols decrease respectively. At about 800 to 900 °C, the silica skeleton becomes free of internal OH groups as well as the geminal silanols disappearing completely from the silica's surface. Stable siloxane bridges are formed in considerable numbers while

isolated silanols remain on the silica surface (shown in Figure 2.14, b)). When the silica surface is covered by the stable siloxane, the OH groups' concentration is decreased, which leads to a sharp increase in activation energy of the de-hydroxylation process. The concentration ratio of OH group to siloxane bridges determines the hydrophilic or hydrophobic property of the silica surface. Re-hydroxylation at this stage hardly takes place at room temperature. The hydrophilic characteristic of the silica surface continues to decrease till the surface is covered entirely by Si–O–Si groups and Si atoms which make the surface fully hydrophobic.

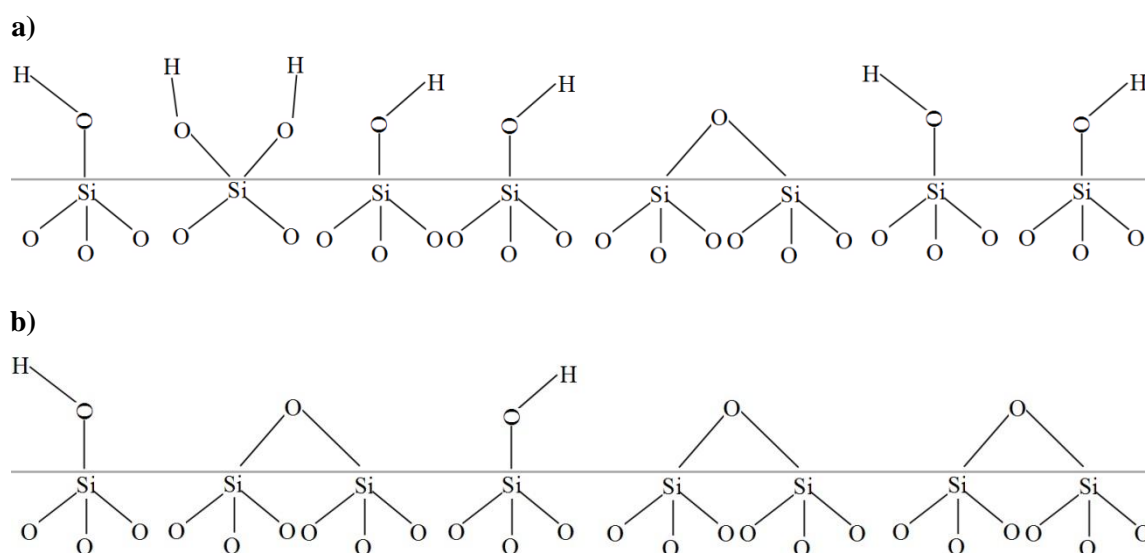


**Figure 2.14:** Condensation process of silica surface by heat treatment, transition from stage 3 to 4 (stage 4a:  $450\text{ }^{\circ}\text{C} \leq T \leq 500\text{ }^{\circ}\text{C}$ , stage 4b:  $8000\text{ }^{\circ}\text{C} \leq T \leq 900\text{ }^{\circ}\text{C}$ )

Different types of hydroxyl groups (bonded and isolated silanols) possess different activities of adsorption. The isolated silanols are considered to have more re-activity and adsorption activity than that of H-bonded silanols. The vicinal (H-bonded) silanols are formed in a linear or two-dimensional structure. In such a structure of hydroxyl groups, probably at least more

than two silanols are engaged. In that case, less re-active hydrogen, even in some cases no more re-active hydrogen, would be available due to the involving of the hydrogen in H-bonding in the vicinal groups' structure, which does not form pairs [47]. Figure 2.15 indicates the re-active hydrogen over the silica surface.

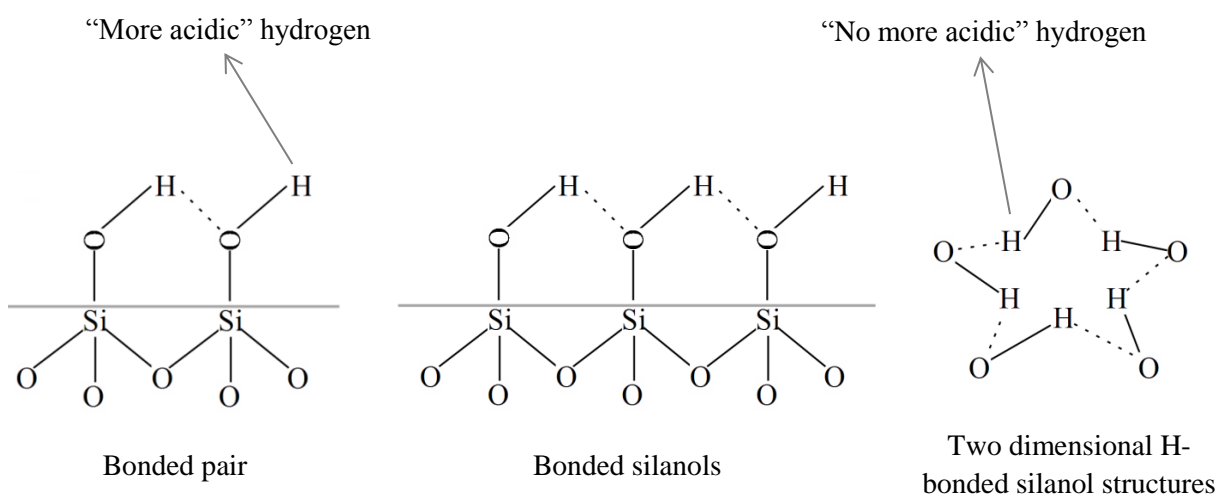


**Figure 2.15:** H-bonded silanols on the silica surface, acidic and no acidic hydrogens

Transition from stage four to five ( $T \geq 1200^\circ\text{C}$ ) results in complete removal of OH groups and full coverage of the silica surface with Si–O–Si groups. At this stage, the surface of  $\text{SiO}_2$  only consists of siloxane bridges [39, 43]. Figure 2.16 indicates the thermal removal of silanols as a result of siloxanes' formation.

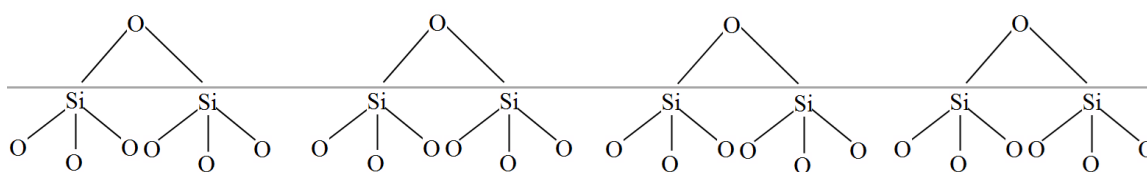


**Figure 2.16:** Fully de-hydroxylated surface of silica, transition from stage 4 to 5 ( $1200^\circ\text{C} \leq T$ )

Bermudez [49] achieved complete de-hydration of a silica surface at 100°C. At this temperature the de-hydroxylation of some silanols was observed as well. Hail [50] concluded that the major adsorptive property of the silica surface corresponds to surface hydroxyl groups, according to his study, by using infra-red gravimetric adsorption. The adsorption sites could be either freely vibrating or hydrogen-bonded to each other depending on the pre-treatment and temperature. The chemical re-activity of the silanol groups on the silica surface were affected by a small amount of impurities. Voort [51] revealed weak surface heterogeneity on silica gel by the contribution of free and bridged hydroxyl groups. The investigation was carried out by using the temperature-programmed desorption (TPD) experiment via strong hydrogen-bonding interaction between surface hydroxyl groups (free and hydrogen-bonded) and the adsorbed pyridine molecule. Various energetic sites were observed. The observed activation energy of pyridine desorbed from free hydroxyl groups was higher than that of bridged hydroxyls. It was concluded that the bridged silanols were de-hydroxylated much easier than isolated silanols.

Chuang et al [52], in their investigation, considered the participation of different hydroxyl groups in hydrogen-bonding or either non-hydrogen bonding, depending on surface segment type, relative hydroxyl groups orientation, as well as their local structural environments. He performed this study based on a generalized  $\beta$ -cristobalite surface model of silica. The de-hydroxylation temperatures and conditions of isolated and geminal silanols were considered in this study. In addition, yielding of highly strained siloxanes through de-hydroxylation at a higher temperature was also examined. The model enabled the explanation of de-hydroxylation/re-hydroxylation processes as well as re-hydration/de-hydration behaviours of the silica surface which take places under specific conditions.

## 2.5 *Catalyst formulation and reaction engineering in the F-T process*

### 2.5.1 *F-T catalyst formulation*

The product selectivity in F-T synthesis can be varied over a wide range. Catalyst formulation, the system which performs the synthesis process and reaction conditions, is the key factor that affects the product distribution in F-T synthesis. Chain growth probability ( $\alpha$ ) in F-T synthesis is influenced by the catalyst selected for the hydrogenation process. In addition to catalyst type, the chain growth probability mechanism on the catalyst surface is affected by the catalyst's promoter level and temperature and composition of feedstock gas as well. It should be mentioned that the probability of the chain growth is independent of both the chain length and reactor type. [53]. Cobalt, iron, ruthenium and nickel are considered as commercial catalysts in bio-fuel generation. These metals in their metallic form have the capability like all elements of VIII B group in the periodic table [54] to dissociatively adsorb carbon monoxide to form metal carbide on the catalytic surface and hydrogenate the adsorbed carbides. Ruthenium is not of interest for commercial application because of its high cost; despite the fact that it is one of the most active catalysts for F-T synthesis. Nickel does not have industrial relevance in F-T technology. The low average molecular weight of nickel prevents the usage of this metal for the F-T process. The small particle size of nickel leads to higher hydrogenation activity power compared to its chain growth power [54] Water Gas Shift (WGS) reaction activity over an iron catalyst in the F-T process is more than that of cobalt, which can lead to loss of carbon monoxide as a raw material by the formation of carbon dioxide. The activity of the WGS reaction produces more water as a co-product of this process, which is the kinetic inhibition of an iron catalyst. On the other hand, the higher activity of the WGS reaction over an iron catalyst allows the utilization of synthesis gas

which contains carbon dioxide or hydrogen depleted syngas [55]. A cobalt-based catalyst is of interest for industrial applications due to its significant specifications. The high selectivity of a cobalt catalyst to long chain alkanes, its low selectivity to oxygenate products and alkene as well as high deactivation resistance, long-life time and the relatively low price of this catalyst make it appropriate to be utilized for F-T bio diesel generation [56]. A cobalt-based catalyst is considered as an efficient and capable catalyst for this project due to its high activity at low temperature [17]. In addition, a cobalt catalyst has durability of up to 5 years on stream compared to 6 months in the case of an iron catalyst [55]. A cobalt catalyst generally yields in higher production of long-chain synthetic hydrocarbon [24]. The FTS process over a cobalt catalyst at normal pressure and temperature of 200 – 300 °C produces linear olefins ( $\alpha$ -olefins) as the main products. A small amount of non-linear products consisting mainly of mono-methyl branched compounds are produced at this temperature. High pressure Fischer-Tropsch Synthesis over a cobalt catalyst produces less olefins in favour of an alkanes' content due to the increase of molecular weight [31]. Chain growth probability is 0.5-0.7 for an iron catalyst and 0.7-0.8 for a cobalt catalyst. Chain growth probability can be maximized up to a value of 0.95 for a cobalt catalyst. It works well when the  $H_2/CO$  ratio is near to two [55].

Fischer-Tropsch synthesis in an iron-based fixed-bed reactor produces naphthenes and aromatics in small amounts; it is the case that cobalt and ruthenium-based fixed-bed reactors usually produce none of these compounds [30]. In comparison with iron and ruthenium catalysts, cobalt has a low rate of carbon monoxide activation, while low hydrogenolysis and low shift activity at a high  $H_2/CO$  ratio make it reasonable for synthetic diesel production ( $Fe < Co < Ru$ ). This catalyst has high hydrogenation activity when alkanes are preferred as the main product ( $Ru > Co > Fe$ ). The cobalt-based catalyst is not affected by steam practically in the F-T reaction regime [57].

### 2.5.2 *Catalyst carrier materials*

Support material and its nature are relevant significant parameters that influence the catalytic activity and products' selectivity in F-T synthesis. Metal-support interaction strength, resistance to attrition (mechanical properties), thermal stability and support's porosity are the features that influence the reaction and transfer phenomenon in the F-T process. Diffusion limitation for reactant and produced hydrocarbons caused by catalyst liquid-filled pores and capillary condensation of heavier hydrocarbons, influence the overall F-T reaction rate [58]. Under F-T synthesis conditions, the pores are filled with liquid/wax products. The reactants at the external surface of the catalyst dissolve in the waxes. The dissolved reactants diffuse inside the pores through the wax. Hydrogen possesses a higher diffusion coefficient compared to carbon monoxide. These phenomena result in a higher concentration of hydrogen inside the porous catalyst. The increase in H<sub>2</sub>/CO ratio accelerates the chain termination step and negatively affects the product selectivity and chain length of the products by pore diffusion limitation [59]. Usage of an eggshell catalyst in the F-T process could enhance the desired product selectivity by decoupling the severe transport restriction.

In addition to all the above mentioned, the properties of metal particles' size and active phase dispersion are considered to be affected by the pore size located inside [58]. Catalyst support plays a significant role in the catalytic behaviour of supported metal by changing the charge and size of metal particles, the particle shape and crystallographic structure, as well as the formation of active sites [60]. Said et al [61] studied the effect of support pore diameter on the performance of F-T synthesis and observed different adsorption properties of cobalt particles and cobalt crystalline size located in narrow and wide pores. Different types of metal oxide supports such as aluminium oxide (Al<sub>2</sub>O<sub>3</sub>), silicon dioxide (SiO<sub>2</sub>), titanium dioxide (TiO<sub>2</sub>), or

zeolite are employed as the carrier of catalyst materials, especially when the active sites are more expensive, like cobalt.

Combinations of remarkable characteristics such as large surface area, high surface/mass ratio as well as ultra-low density of silica, make it a marvellous support for F-T catalyst preparation. The high porosity degree of silica, its pores network and open pores volume rather than bulk volume, make it an attractive candidate for F-T catalyst support. This support facilitates the internal mass transfer due to its interconnected three dimensional networks which could form up to 99.8 % of its bulk volume [62]. The application of eggshell distribution of a catalyst could result in faster diffusion of higher molecular weight hydrocarbons, due to the deposition of an active phase in the outer region of the catalyst's pellets. This distribution of the catalyst lowers the intra-particle mass transport and yields to higher selectivity of middle distillate hydrocarbons [63] which are the desired products of this investigation. In addition, cobalt is highly active compared to iron, nickel and ruthenium when supported with silica, due to the fact that the nature of the support affects the catalyst's behaviour [64].

Gaderzi et al [65] examined the effect of calcination conditions on the performance of a cobalt/silica catalyst and also considered the metal crystallites distribution affected by solvent, during catalyst preparation via solution impregnation; they achieved higher active surface area and better dispersed metal, in the case of alcohol as a primary solvent compared to water. Song et al [66] considered the effect of support pore size on catalyst characterization and its activity in the F-T hydrogenation process; and concluded higher activity and productivity for the catalyst with pore sizes ranging 6 – 10 nm. Girardon et al [67] studied the effect of a cobalt precursor impregnated to silica support via incipient wetness impregnation and

achieved higher active site concentration and catalytic activity for the catalyst prepared by cobalt nitrate. Zhang et al [68] observed the best catalytic performance for the cobalt catalyst supported by silica gel prepared from dehydrated ethanol. The application of absolute ethanol resulted in a decrease in solvent polarity as well as prevention of the formation of an immobilized glassy water layer. As a result, higher interaction between more cobalt complex and the silica gel surface was provided. In that case, formation of highly dispersed small particles of cobalt species was obtained; these particles were activated at higher temperature.

Jae-Sun Junga [69] showed in his work that pore diameter and pore size distribution, which depends on the mesoporous support structure affects the cobalt particle size and significantly influences the catalytic activity of a cobalt catalyst in the F-T hydrogenation process. Anna Maria Venezia [70] enhanced the activity of a sol-gel prepared silica supported cobalt catalyst by adding a small amount of titania which was examined at different space velocities and high space velocity and resulted in higher Fischer-Tropsch reaction conversion and higher selectivity of heavier hydrocarbons. Shouli Sun et al. [71] was successful in increasing the activity of a cobalt catalyst, supported by silica gel support prepared by incipient wetness impregnation of cobalt (II) nitrate and cobalt (II) acetate employed for F-T synthesis. Yi Zhang [72] applied different solvents (acetic acid and ethanol) to prepare a highly active Co/SiO<sub>2</sub> catalyst for Fischer Tropsch synthesis and reported higher dispersion of the cobalt active site and reducibility, for a catalyst prepared with ethanol solvent; which resulted in higher activity of this catalyst in the F-T process. Hui Ming [73] studied the effect of different rare earth promoters on hydrogenation performance of a cobalt supported silica gel catalyst and realized praseodymium as the most effective promoter.

### 2.5.3 *F-T reactor technology*

Different kinds of reactors are employed to convert syngas to synthetic fuel, such as multi-tubular, slurry bubble column and fluidized bed reactors. Multi-tubular fixed-bed and slurry phase reactors are the types of reactors that are employed for low-temperature ( $T < 530$  K) Fischer-Tropsch synthesis [74]. Fixed bed reactor's technology is known as the most efficient reactor to maximize the synthesis driving force of the F-T process in the absence of heat transfer limitations [29]. There are some disadvantages in these reactors. High pressure drop occurs in a fixed-bed reactor and also low catalyst utilization can be achieved. Insufficient heat removal and limited diffusion are two other drawbacks of fixed-bed reactors. A fixed-bed reactor is employed to produce synthetic fuel due to its significant features in this project. The ease of scale up from single-bed to pilot plant, the ease of catalyst loading and replacement are two leading features of fixed bed reactors [75]. F-T reaction is highly exothermic ( $\Delta H_{298K} = -140$  to  $-160$   $\text{kJ}\cdot\text{mol}^{-1}$  CO converted, depending on the products) and produces waste heat that must be removed from the reactor. Heat transfer limitation is a major disadvantage of a fixed bed reactor and may lead to more activity of the methane formation reaction, low product selectivity and a shorter lifetime of the catalyst [76]. Radial heat transfer to the wall of a fixed-bed reactor and cooling medium is one of the aspects which should be taken into account. F-T synthesis is an exothermic reaction which produces waste heat. Nitrogen efficiently removes the produced heat of the exothermic F-T reaction and minimises the temperature's runaway probability. The application of nitrogen in feedstock leads to a cost-effective synthesis process due to the increase in the reactor's tubes diameter [77].

S. Chambrey et al [76] performed a comparative study of FTS in three different reactors. The results of this research showed higher hydrocarbon productivity for a mili-scale fixed-bed

reactor, compared to the two other reactors. Slow catalyst deactivation took place in the fixed-bed reactor and 0.92 chain growth probability was obtained. In this investigation, the fixed-bed reactor was employed to maximise the synthesis driving force, which is known as the most efficient reactor technology for synthesis of heavier hydrocarbons in the absence of heat and mass transfer limitations. This reactor produces more hydrogenated, less oxygenated and alkene products, compared to fluidize and slurry bed reactors. There is no restriction in the reaction phase of fixed-bed synthesis [78].

#### ***2.5.4 Overview of previous works regarding the Fischer-Tropsch synthesis process***

González et al [79] studied the behaviour of a cobalt catalyst supported on different meso-structured supports based on silica in the Fischer-Tropsch Synthesis process and observed highest activity of the catalyst in terms of carbon monoxide conversion; as well as heavy hydrocarbon product selectivity for the catalyst supported with 5 nm average pore diameter. He concluded that the average pore size of the mesoporous support highly impacted on the reducibility of the cobalt particles by forming a different size of supported cobalt clusters irrespective of higher dispersion.

Osakoo et al [80] increased the activity of a cobalt catalyst supported by SiO<sub>2</sub> by improving the cobalt particle size (using impregnation method) and subsequently its reducibility (by creating larger cobalt particle size); as well as by promoting the catalyst with 0.2 wt% palladium (Pd). He enhanced the formation of alkanes by adding the Pd as the promoter, which resulted in higher selectivity of heavy alkanes, methyl-branched paraffins as well as alcohols. Wu et al [81] concluded from their work that adding a small amount of TiO<sub>2</sub> could enhance the reducibility of a cobalt catalyst supported with silica gel by affecting the support-

catalyst interaction and subsequently could result in higher FTS reaction activity. The dispersion of active metal was improved as well by the addition of  $\text{TiO}_2$ . Khodakov et al [82] examined cobalt dispersion as well as its reducibility affected by the meso-porous structure of silica support (narrow and broad pore sized distribution in silica support) and concluded that the catalytic performance of a narrow pore sized catalyst was better than that of a broad pore size due to higher dispersion of the active site over this support.

Dunn et al [62] concluded the increase in the loading of cobalt content supported with silica aerogel up to 10 wt% resulted in higher activity of this catalyst in the Fischer-Tropsch Synthesis process. Ma et al [83] observed that the decrease in the average cobalt cluster diameter by about 30% (from 38.4 nm for a catalyst containing 15 wt% metal content to 27 nm for a catalyst containing 25 wt% metal content) in a cobalt catalyst supported by silica, resulted in an increase in the intrinsic reaction rate constant by about 102 %, due to the increase in the density of active  $\text{Co}^0$  on the surface site. Hong et al [84] enhanced the reducibility and catalytic activity of cobalt supported silica in F-T synthesis by adding organic additive (sorbitol,  $\text{HOCH}_2(\text{CHOH})_4\text{CH}_2\text{OH}$ ) to the impregnation solution during the preparation step. This enhancement was due to stabilizing of  $\text{Co}^{2+}$  due to the adding of the sorbitol. The sorbitol caused the cobalt complexes to decompose at a higher temperature and therefore higher dispersion in cobalt oxide was achieved.

Gnanamani et al [85] produced hcp (hexagonal close-packed) and fcc (face-centred cubic) cobalt metal particles over silica support by employing different pre-treatments and observed higher carbon cobalt dispersion (5.06% in the case of hcp and 3.84 % in the case of fcc) for the catalyst containing the hcp metallic phase; and subsequently higher carbon monoxide conversion (about 28 mol%) was achieved in this study, compared to that of fcc. Since the

cobalt catalyst used in Fischer-Tropsch synthesis is expensive, hence, Loosdrecht et al [86] investigated the oxidation of nano-sized metallic cobalt during realistic F-T synthesis to cobalt oxide and concluded that this type of oxidation is independent of the support materials and could prevent the correct combination of reactor partial pressure of H<sub>2</sub>O and H<sub>2</sub> ( $P_{H_2O}/P_{H_2}$ ). The cobalt crystalline size was 6 nm in this study. Storsæter et al [87] characterized un-promoted and rhenium-promoted cobalt catalysts supported with titania, silica and alumina in Fischer-Tropsch synthesis. This investigation showed a relatively higher activity of a Re-promoted cobalt catalyst when it was supported with TiO<sub>2</sub>.

Hunpinyo et al [88] performed a kinetic study in both a laboratory-scale and pilot-scale BTL process using a fixed bed reactor, to examine the performance of a ruthenium-based alumina supported catalyst in the F-T synthesis process at atmospheric pressure; they observed higher activity of this catalyst towards the formation of the desired heavy molecular weight hydrocarbons (CO conversion @ temperature = 220 °C and space velocity=3600 hr<sup>-1</sup>). Similar results in terms of product selectivity as well as distribution of hydrocarbon products were achieved in the cases of both the laboratory and pilot scale BTL processes.

Elbashir et al [89] presented an integrated approach in the designing of an advanced multiphase F-T reactor. Three parameters were identified in order to systemize the designing process, including: (i) process synthesis, (ii) process simulation and (iii) tailored experiments. The process configuration was generated from various building blocks within the process synthesis (e.g. reaction, separation, recycling, recovery). The process simulation evaluated the synthesized system performance and finally the generated design was verified experimentally. The study was successful to optimise the F-T reactor technology for near/super critical operation conditions. Guettel et al [90] derived a mathematical model to compare the

performance of different types of reactors (fixed-bed reactor, slurry bubble reactor, micro- and monolith reactors) in the Low-Temperature Fischer-Tropsch (LTFT) synthesis process. The lowest specific catalytic productivity in the simulation study was observed for the fixed-bed reactor operating at a trickle-flow regime due to severe resistances in mass transfer. However, the ease of separation of the catalyst from liquid products is still a significant advantage for the fixed-bed reactor to be employed in commercial-scale plant F-T synthesis. Schulz [91] presented a history of the Fischer-Tropsch synthesis process as well as its trends, by generalising some individual investigations including the development of the F-T reactor and process, F-T catalyst formulation, micro kinetic modelling of F-T reactions etc.

Chu et al [92] considered the effect of calcination temperature during catalyst preparation steps as well as platinum (Pt) promotion of a cobalt catalyst supported with alumina on the interaction of metal oxide ( $\text{Co}_3\text{O}_4$ ) with support materials. It was concluded that unlike the calcination temperature and promoting material, which had no significant influence in the size of the generated metal oxides crystallite size in the supported gamma-alumina, the particle size and subsequently its dispersion was greatly affected by pore size distribution. The rate of the F-T reaction was significantly increased by promoting the catalyst with a small amount of platinum. In contrast with the reaction rate, a slight decrease in the production of heavy hydrocarbons was observed in this study.

Zhang et al [93] considered the performance of a cobalt-based alumina supported F-T catalyst by modification of the support by magnesia. The performance of the magnesia-modified catalyst was examined in F-T synthesis and it was concluded that the activity of the catalyst in terms of carbon monoxide conversion was increased due to improvement in reducibility of the catalyst. It was observed that the increase in magnesia content resulted in a decrease in

catalyst activity, heavy hydrocarbon selectivity, as well as higher selectivity of co-products; due to the formation of MgO-CoO solution.

Itkulova et al [94] studied the production of ceresin (mixture of high molecular-weight hard hydrocarbons including n- and iso-alkanes) under pilot scale F-T synthesis, using a cobalt catalyst modified with platinum (Pt) and observed that promotion of the catalyst with 0.25 wt% of the second metal resulted in 77 % selectivity to ceresin fraction in the reactor output. The liquid synthesis process was optimised in this investigation in order to find the most selective reaction conditions for the production of ceresin. The best combination of cobalt catalyst and fixed bed reactor was found at 170-180 °C and space velocity of 100 hr<sup>-1</sup>.

Schulz [95] performed a comparative investigation on the dynamics of the structure and the function of cobalt and iron based catalysts in Fischer-Tropsch synthesis of liquid hydrocarbons, to obtain a deep understanding of the specific behaviours of these two catalysts in the F-T process. It was concluded that the active sites of a cobalt-based F-T catalyst are of a dynamic nature. Thus, the elemental reaction's relative rates correspond to the time on stream, reaction temperature and partial pressure of reactants (mainly hydrogen and carbon monoxide), While statics' structural function was observed for the iron-based catalyst, which means that the rate of F-T reaction is increased during catalyst re-assembling (dissociative hydrogenation of carbon monoxide with iron to create active surface carbide); whereas the selectivity didn't change. In the case of the iron catalyst, the final product's average molecular weight was controlled by a change in temperature, which means that only the temperature parameter had a significant influence.

Jacobs et al [96] performed a comparable work to examine the effect of co-fed water on a cobalt catalyst prepared with variable supports (Al<sub>2</sub>O<sub>3</sub>, TiO<sub>2</sub>, SiO<sub>2</sub>). A positive influence of

co-fed  $\text{H}_2\text{O}$  was observed for the silica supported cobalt catalyst which resulted in an increase in conversion of carbon monoxide as well as  $\text{C}_{5+}$  hydrocarbons' selectivity. At the same time, the methane selectivity was decreased while the carbon dioxide selectivity remained low. The rate of catalyst deactivation was accelerated with the increasing of the water content at the inlet. In contrast, the activity of the cobalt catalyst in terms of carbon monoxide conversion was decreased when the metal was supported with  $\text{TiO}_2$  and  $\text{Al}_2\text{O}_3$  with a strong cobalt oxide–support interaction.

Pichler et al [31] studied the product composition of the F-T synthesis as a function of residence time on the catalyst at low pressure (normal pressure) and low temperature ( $200\text{ }^\circ\text{C}$ ) over cobalt/thorium oxide/kieselguhr catalyst ( $\text{H}_2/\text{CO} = 2$ ) and concluded that the shorter the residence time leads to a larger  $\alpha$ -olefin fraction of the product. In addition, it was concluded that at low space velocity, the primarily formed  $\alpha$ -olefins are transformed within the secondary reactions into  $\beta$ -olefin, linear paraffins and methyl branched products.



---

# Chapter 3

---

## CATALYST PREPARATION AND DEVELOPMENT OF EXPERIMENTAL SET-UP

The catalyst preparation procedures to derive the supported catalyst are described in this chapter. Different characterization experiments involving methods and tools, which are used to examine the supported catalyst characteristics, are discussed intensively. The development of the experimental set-up to analyse the specific variables, including the effect of support variables and F-T reaction conditions, are also outlined. In addition, the chapter covers the methods applied widely to analyse the Fischer-Tropsch synthesis process involving the chemical reactions. The Design of Experiment (DOE) as a structured approach to identify the important parameters in the F-T process, determine their significance, as well as achieve the optimum reaction condition, is discussed.

### ***3.1 Catalyst preparation and characterization experiments***

#### ***3.1.1 Impregnation technique to deposit active metal over the support***

The supported catalysts are derived from several different procedures. The catalysts are classified based on the preparation procedures in three different broad categories: (i) bulk catalyst and supports, (ii) impregnated catalyst and (iii) mixed-agglomerated catalyst. Supported catalysts are the most preferred for this project due to the high dispersion of active agents over the support's surface, as well as the component's higher thermo-stability degree in supported catalysts. In this kind of catalyst, the supporting materials are required to be much more resistant to the sintering than the catalytic agents; due to the preparation process and the reaction conditions in which they are applied.[97]. The qualities of raw materials along with the steps of the preparation process greatly influence the catalytic properties of heterogeneous catalysts (gas/liquid phase process) in F-T synthesis. In heterogeneous catalysts, which are a surface phenomenon, the performances of the catalysts are determined by the exposed surface area.

The commercially available silica support was selected to stabilize the catalytic particles (metal oxides) in F-T synthesis based on its considerable characteristics such as inertness, high mechanical strength (resistance to attrition, hardness etc.), stability under re-generation and reaction conditions, and morphology (surface texture and its notable high porosity degree) [97]. In addition, the sphere supports have low manufacturing costs. The effective silica supports were provided by Fuji Silysia™ Chemical Ltd in different grades. Table 3.1 gives a full specification of the silica supports' structural properties provided by the company. A wide range of silicas varying in surface area, pore diameter and pore volume were provided in order to consider the effect of support variables in the F-T synthesis process.

**Table 3.1:** Certificate of analysis provided by Fuji Silysia Chemical Ltd. for different silica supports

Characterized items	Grade of supports			
	SUP-Q-3	SUP-Q-6	SUP-Q-10	SUP-Q-30
Bulk density (g/ml)	0.76	0.48	0.38	0.37
Water content (wt%)	1.7	0.1	0.6	0.1
pH	3.8	7.2	7.3	7.2
Pore volume (ml/g)	0.42	0.83	1.20	1.27
Surface area (m <sup>2</sup> /g)	663	536	257	107
Particle size distribution of silica supports with different grades				
On 150 $\mu\text{m}$ (wt%)	0.2	2.1	0.1	0.0
75-150 $\mu\text{m}$ (wt%)	93.6	91.3	98.8	98.0
Thru 75 $\mu\text{m}$ (wt%)	6.2	6.6	1.1	2.0

The supports were chemically and mechanically stable due to their high purity. They were not broken during the impregnation in solution because the water resistance of the supports had been improved. The quality of whether they were particularly good or worthy for the F-T process was determined based on the behaviour of the catalyst in the carbon monoxide hydrogenation activity. The supports exhibited excellent attrition resistance. The average pore diameter of the supports had been precisely controlled.

As the cost and preparation time were regarded as more significant priorities in the catalyst preparation and also due to the physico-chemical properties of proposed catalyst, the impregnation method was decided to be employed as a laboratory technique to prepare the desired catalyst for this project [97]. Impregnation of the active phase with the pre-shaped solid silica supports formed the impregnated supported-catalysts. In this method, the pores of

the silica support were filled with the solution of cobalt salt from which the alcohol solvent was subsequently evaporated [98]. The metal loading was achieved by adding the support materials to a metal salt solution. Two different methodologies carry out the catalyst preparation process in the impregnation technique: dry and wet impregnation. The dry impregnation is also referred to as “pore volume impregnation”, in which the impregnation solution’s volume is equivalent to the porous support’s pore volume. Hence, the pore volume of the support is estimated before impregnation. Thereafter, the support is in contact with the liquid which exactly fills the pore volume of the support. Within the second methodology, which is known as wet impregnation, the excess quantity of the solution containing the metal precursor is put into contact with the porous support [99]. The required weight percentage of impregnated active site is dependent on the molar concentration of the cobalt constituent. Contacting the support materials together with the impregnating solution, removing the imbibed liquid, followed by thermal decomposition to generate the active phase over the amorphous surface, were three major steps followed in the impregnation method [97]. In the case of wet impregnation, the soluble catalysts’ precursors are fixed by exchange with surface OH groups. Hence, the pre-treatment of the catalyst is a crucial process which determines the density of the surface hydroxyl groups [99].

A series of four cobalt catalysts were synthesized via one-step wetness impregnation or the dual-step method, with repeated applications of impregnation solutions in ambient conditions [97]. In a typical catalyst synthesis, the active metal precursor (cobalt (II) nitrate hexahydrate) was dissolved in absolute ethanol solvent (Fisherbrand<sup>®</sup>) using a one-necked Duran<sup>®</sup> laboratory bottle with a lid. A stirrer was employed for 15 minutes with a constant stirring speed to incorporate the salt into the liquid so as to form the metal salt solution. During all the preparation time, the bottle was sealed with a lid to prevent the evaporation of the liquid.

**Table 3.2:** Characteristics of wetness impregnation solutions and impregnation processes for the catalysts prepared to perform the catalyst-characterization experiments

Sample	Impregnation solution		Impregnation process	
	Precursor <sup>a</sup> (g)	Solvent <sup>b</sup> (ml)	Support <sup>c</sup> (g)	Repeating <sup>d</sup>
CAT-Q-3	15	20	SUP-Q-3: 12.5	Dual-step
CAT-Q-6	8.2	15	SUP-Q-6: 6.3	One-step
CAT-Q-10	7.5	17	SUP-Q-10: 6.3	One-step
CAT-Q-30	17	35	SUP-Q-30: 13	One-step

a. Precursor: Cobalt (II) nitrate hexahydrate, Linear formula:  $\text{Co}(\text{NO}_3)_2 \cdot 6\text{H}_2\text{O}$ , Molecular weight: 291.03 (g/mol), Impurities:  $\leq 0.01\%$  insoluble, pH: 4.0 at 100 g/l at 20 °C, Melting point: 55 °C –lit., Bulk Density: 8,000 (kg/m<sup>3</sup>)

b. Solvent: Ethanol absolute, Linear Formula:  $\text{C}_2\text{H}_6\text{O}$ , Molecular weight: 46.07 (g/mol), Relative density: 0.791 (g/cm<sup>3</sup>) at 25 °C.

c. Repeating: number of times that impregnation was repeated to achieve the desired metal loading

The cobalt salt was purchased from Sigma Aldrich<sup>®</sup> Co. Absolute ethanol was applied as a solvent to promote the dispersion and reduction degree of the supported cobalt catalyst, as well as its activity [72] on different spherical silica samples including various grades. Different solutions of various cobalt compositions were employed to synthesise the catalysts in the wetness impregnation. The series of supported cobalt catalysts, impregnation soluble characteristics, as well as impregnation process, are shown in Table 3.2.

Prior to the impregnation, the supports were pre-treated by drying at 473 K for 14 h (ramp-up rate: 5 K/min) using a chamber furnace. This action resulted in the complete removal of the physically adsorbed multi-layer of water while keeping the amorphous silica surface in a maximum hydroxylation state [47]. Following the drying, the supports were subjected to heat treatment at 773 K for 2 h with temperature ramping of 10 K/min; this treatment stage decreased the vicinal bridged OH group concentrations while the concentration of isolated

single and geminal OH groups were increased [39]. Afterwards, the impregnation solutions with appropriate precursor concentration were put into contact with the pre-treated supports for a certain period of time (solutions: CAT-Q-3: 2.58 M, CAT-Q-6: 1.88 M, CAT-Q-10: 1.51 M and CAT-Q-30: 1.67 M). The impregnation processes lasted 4 hours for each of the catalysts. All of the processes were carried out under constant stirring by a stirrer as shown in Figure 3.1

Consequently, to segregate the insoluble solid phase from the liquid phase, a complete suction filtration shown in Figure 3.1 was employed to achieve the impregnated support materials. The filter system was connected to a vacuum bolt neck filter flask. The top opening of the suction flask accommodated a single-hole rubber stopper which in turn supported a Buchner funnel assembled on top. The joint between the rubber stopper and the suction flask was air-

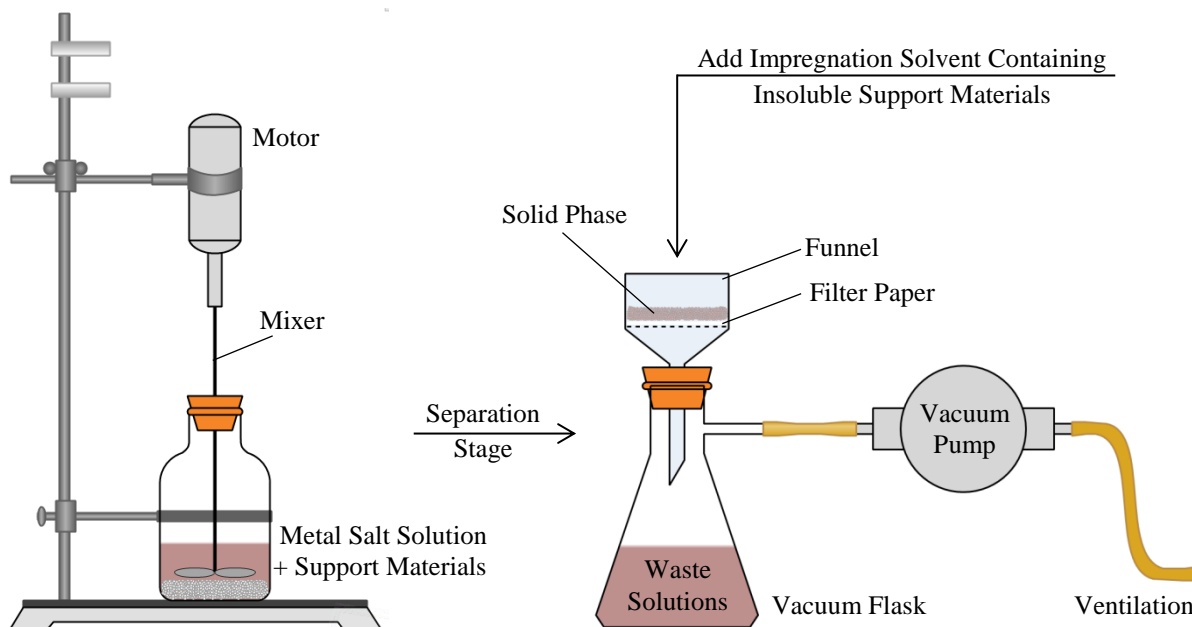


**Figure 3.1:** Laboratory set-up for impregnation of silica supports to wetness solution of cobalt precursor and filtration process of solid phase from waste liquid phase

tight. The side arm of the flask was connected to the source of reduced pressure using the heavy-walled rubber tubing for connections. A piece of filter paper (Fisherbrand®, qualitative, range: QL100, diameter: 240 mm), centred and completely flat, consistent with the size of the funnel, was placed inside it against the perforated surface. A vacuum pump enabled the vacuum system to separate the phases. Before each operation, the filter flask and top part of the Buchner funnel were rinsed with distilled water to make sure they were clean.

To start the separation, the pump was turned on and subsequently the impregnation solution containing the support materials was poured from the bottle into the funnel. The glass bottle contents were poured slowly and a stirring rod was used to direct the solution and precipitates to the centre of the filter paper. A sample spoon was used to keep the accumulating solid phase in the centre of the funnel to minimize the chances of the precipitate to pass around the filter paper and go into the vacuum flask. The pump was operated for four minutes to suck the whole liquid phase and make sure that the precipitated solids were as dry as desired.

*Figures refereed from [100]*

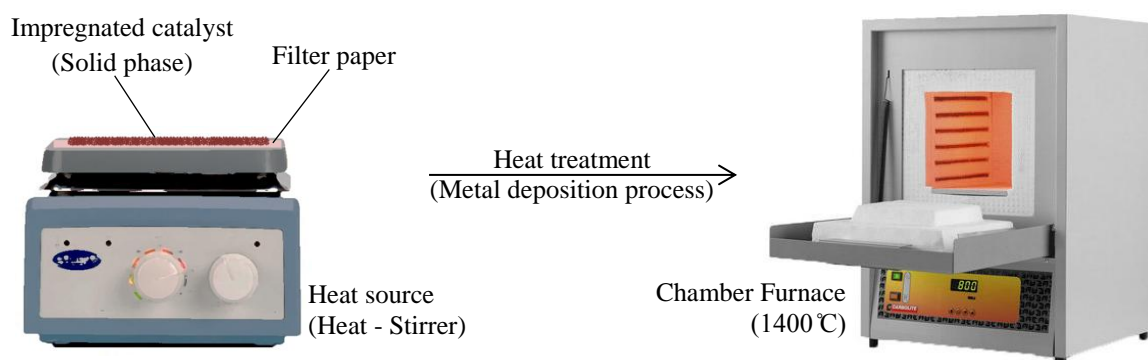


**Figure 3.2:** Separation of precipitated solid phase from filter paper and catalyst heat treatment (drying and calcination) to generate the active phase over the silica surface

The filter paper along with the contents on the top of it were transferred and put over the heat source (Stuart<sup>®</sup> CB162 magnetic heat-stirrer). This action resulted in the sticky precipitated solid phase being separated from the filter paper. The filter paper was heated at about 70 °C for 2 minutes. Then a double-ended sample spoon was used to separate the solid phase from the filter paper. Thereafter, the catalysts were transferred to a container to be put in the furnace. The magnetic stirrer was used sometimes in the impregnation process as well. The next stage was to convert the supported metal salt to the oxide state. This action was followed by drying and calcination of the catalyst in the chamber furnace. To remove the imbibed solution, the samples were treated at 473 K for 14 h (temperature ramping rate: 5 K/min). This action derived off the volatile components within the solution. The temperature ramping rate was adjusted relatively low to prevent the collision of the porous structure of the supports. Although this issue is more of a concern in pellet-shaped catalysts, nevertheless care was taken. Consequently, the furnace temperature was ramped continuously from 473 to 723 K with the ramping rate of 10 K/min and held for 4 h for further heat treatment in the air to generate the active phase and stabilize the mechanical properties. Then the catalyst was left to cool from 723 K to a temperature below 323 K and collected and stored in glass sample tube.

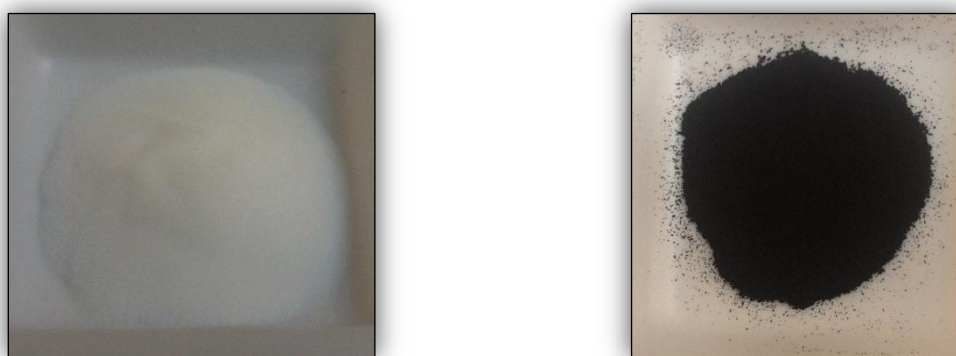


**Figure 3.3:** Silica support (left) and derived supported cobalt catalyst (right)

**Table 3.3:** Characteristics of wetness impregnation solutions and impregnation processes for the catalysts prepared to perform the metal-loading optimization experiments

Sample	Impregnation solution		Impregnation process	
	Precursor <sup>a</sup> (g)	Solvent <sup>b</sup> (ml)	Support <sup>c</sup> (g)	Repeating <sup>d</sup>
CAT-Q-15	3.0	23	SUP-Q-10: 8.0	One-step
CAT-Q-22	4.2	23	SUP-Q-10: 8.0	One-step
CAT-Q-29	6.5	23	SUP-Q-10: 8.0	One-step
CAT-Q-36	7.5	17	SUP-Q-10: 6.3	One-step

a. Precursor: Cobalt (II) nitrate hexahydrate, Linear formula:  $\text{Co}(\text{NO}_3)_2 \cdot 6\text{H}_2\text{O}$ , Molecular weight: 291.03 (g/mol), Impurities:  $\leq 0.01\%$  insoluble, pH: 4.0 at 100 g/l at 20 °C, Melting point: 55 °C –lit., Bulk Density: 8,000 (kg/m<sup>3</sup>)

b. Solvent: Ethanol absolute, Linear Formula:  $\text{C}_2\text{H}_6\text{O}$ , Molecular weight: 46.07 (g/mol), Relative density: 0.791 (g/cm<sup>3</sup>) at 25 °C.

c. Repeating: number of times that impregnation was repeated to achieve the desired metal loading

To optimise the deposition of the active sites over the silica support, a series of four cobalt-based catalysts were prepared by employing different concentrations of active metal over the support surface in order to maximise the conversion of the reactants per pass. The silica support SUP-Q-10 was selected as the unit support for the proposed catalysts. Table 3.3 summarizes the characteristics of wetness impregnation solutions as well as the required process to prepare the catalysts with different metal loading. To examine the effect of cobalt cluster size on the kinetics of Fischer-Tropsch synthesis, the loading of the metal precursors was varied from about 15 wt% to about 37 wt%. Except the impregnation solution, the other catalyst preparation steps, including the impregnation method, materials, drying and calcination conditions, were followed as in the same procedure which was explained for preparation of the catalyst in the catalyst-characterization experiments. The obtained catalysts were named based on the concentration of the cobalt metal over the support surface.

### 3.1.2 Characterization of catalysts

#### 3.1.2.1 X-Ray Fluorescence (XRF) spectrometry

A Wavelength-Dispersive X-Ray Fluorescence (WDXRF) spectrometer (Bruker<sup>®</sup> S8 Tiger) was employed to perform the quantitative and qualitative analysing of different elements in the samples. The XRF technique is based on the fluorescence radiation emitted by specific substances as a result of a shorter wavelength incident radiation such as X-rays (shown in Figure 3.4). The advantage of the XRF method is that it is economical and non-hazardous as well, as each sample could directly be analysed without destroying it.

In the XRF technique, the primary X-ray beam bombards the sample with X-rays. The individual electrons are shot out of the inner atomic shells K and L. The electrons from higher energy shells fill the resulting vacancies. At this moment, the X-ray fluorescence is generated from the excess energy of the electron transition from a higher energy atomic shell to the lower one to fill the vacancies in the inner shells. The radiation of X-ray fluorescence differs -

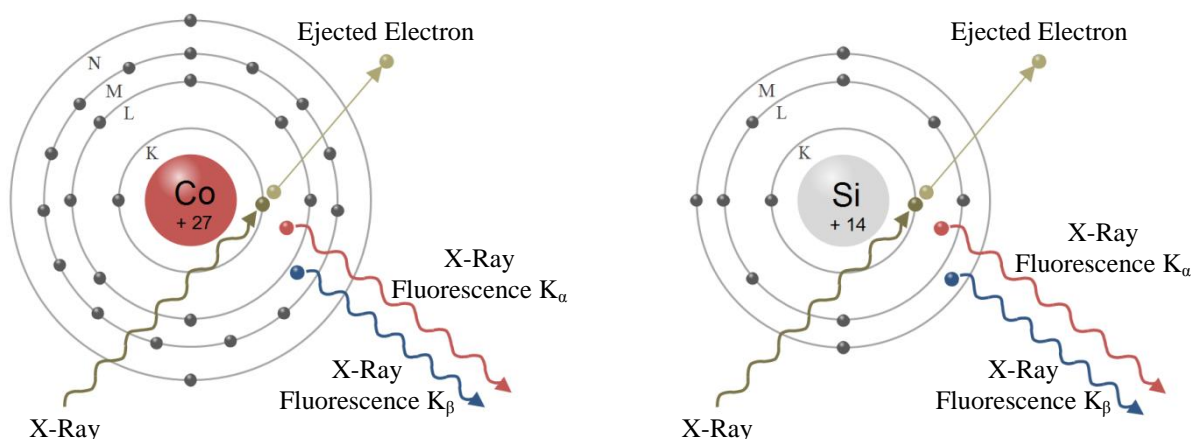


**Figure 3.4:** Configuration of electrons within different energy shells in cobalt and silicon (electron shell 027 cobalt 014 silicon) along with the X-ray fluorescence generations due to X-ray bombardment

**Table 3.4:** Characteristics' wavelength of energy for cobalt and silicon along with their specifications

Atomic Number		Atomic Weight	
<b>27</b>		<b>58.93</b>	
<b>Co</b>			
<b>Cobalt</b>		Density (g/cm <sup>3</sup> )	
		<b>8.56</b>	
Spectral Line	Energy (keV)	Bragg Angle (2 $\theta$ )	
K $\alpha$ 1.2	6.9	52.79	
K $\alpha$ 1.2	6.9	77.89	
K $\beta$ 1	7.7	44.46	
L $\alpha$ 1	0.8	33.77	
L $\beta$ 1	0.8	33.12	

Atomic Number		Atomic Weight	
<b>14</b>		<b>28.09</b>	
<b>Si</b>			
<b>Silicon</b>		Density (g/cm <sup>3</sup> )	
		<b>2.33</b>	
Spectral Line	Energy (keV)	Bragg Angle (2 $\theta$ )	
K $\alpha$ 1.2	1.7	109.21	
K $\alpha$ 1.2	1.7	14.890	
K $\beta$ 1	1.8	101.67	
K $\alpha$ 1	1.7	30.040	

for each element. The fluorescence radiation has a characteristic wavelength or energy for each element, such as a fingerprint and does not depend on the chemical bond of the atoms (Table 3.4). The elemental analyses of samples are carried out based on the differences in characteristic wavelengths. The concentrations of different elements in the samples are determined based on the intensity of the radiation. The simultaneous multi-elemental analysing is one of the key advantages in the XRF technique [101].

The WDXRF (Figure 3.5) was utilized combined with an X-ray source (end-window 4-kW Rh X-ray tube) operated at 60 kV, 50 mA (Co) and 30 kV, 100 mA (Si). The X-ray tube and beam path were shielded against contamination. The sensitive components in the spectrometer chamber were protected by a high transmission vacuum seal which separated the sample chamber from the goniometer chamber. The operation condition (high intensity X-ray source) along with the radiation filter provided the specific excitation energy for each of the existing elements in the sample and subsequently guaranteed that each element was optimally excited.

The characteristic wavelengths were separated in WDXRF with a very high degree of resolution using a collimator. The emitted X-rays were separated and counted under optimal measurement conditions using a high performance optimized analyser crystal (Co: LiF 200 crystal and Si: PET crystal). The analyser crystal plays a crucial role in breaking the multiple frequency fluorescence spectrums down into the specific wavelength for the elements. After diffraction by the analyser crystal, the X-ray signal was collected by a sophisticated scintillation counter. The primary X-ray beam has an irradiation diameter of 10 mm. Prior to each experiment the goniometer sample chamber was flushed by helium gas. All operations were performed under a helium atmosphere with flow rate of 0.7 l/min to avoid bursting the powder sample. In addition, helium gas prevents the air from absorbing as well as attenuation of the fluorescence X-ray of the analytes by the elements in air [102]. For each experiment, a powder sample of 0.4 g was weighted to be analysed. The weighted amount of the powder sample was poured into the sample cup. The bottom of the powder cup was covered with transparent film (Chemplex ®, Mylar: 2.5 µm thin and 63.5 mm diameter). Then the sample cup was mounted in the small mask (8 mm). Thereafter, the sample cup was fixed with the clamp and the mask was positioned on the sample tray. The sample was loaded and the measurement of the sample was started. The method was run for loose powder and the data was collected and analysed by the software, in person.

*Figure refereed from [103]*

**Figure 3.5:** Bruker® S8 Tiger Wavelength Dispersive X-Ray Fluorescence (WDXRF) spectrometer used for elemental analysis of the samples



### 3.1.2.2 Nitrogen adsorption/desorption

Sequences of reactions take place in the F-T heterogeneous catalysis process involving the exposed surface layer of the solid catalyst and fluid-phase reagents. The morphology of the solid catalyst (spherical porous silica powder), estimated by the total surface area of the catalyst, determines the potential accessibility of the catalyst to gas-liquid phase reactants as well as its general activity [104]. The physical adsorption method on the solid surface could characterize the porous solids due to gas adsorption and determines the specific surface area. The value is measured by calculating the amount of adsorbate gas corresponding to a monomolecular layer on the surface. The porous materials are most widely characterized by using nitrogen as an adsorptive at 77 K. The values derived from this method are not effective for the ultra-micro-porous materials which contain pores of molecular-dimensions. Otherwise this method is established for macro-meso porous materials [105].

The single-point pore capacity estimation and Brunauer-Emmett-Teller (BET) surface area analysis were carried out to evaluate pore size distribution, pore volume and surface area by analysis of the adsorptive ( $N_2$ ) physisorption on solid surface using Micromeritics<sup>®</sup> ASAP 2010 instrument (V5.03 G). Figure 3.6 indicates the instrument used to analyse the specific surface area as well as pore size distribution of

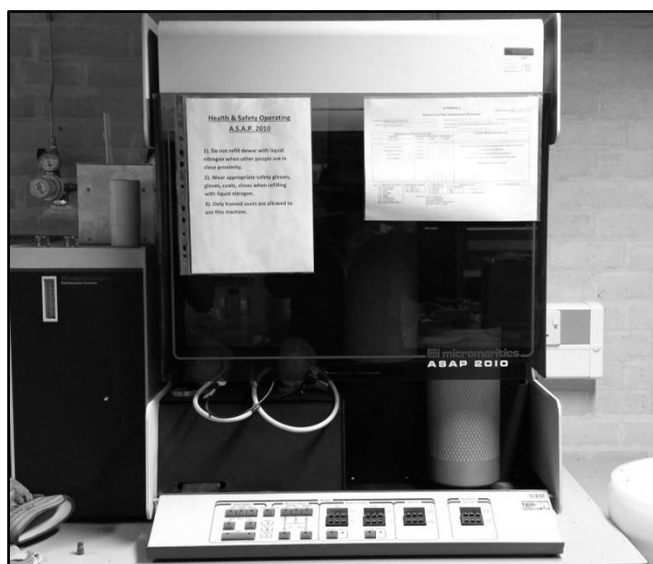


**Figure 3.6:** Micromeritics<sup>®</sup> ASAP 2010 instrument to analyse the surface area and pore size distribution

the samples. The surface area was calculated by employing the Brunauer–Emmett–Teller (BET) equation [106] by explaining the physisorption of N<sub>2</sub> molecule as the most current adsorbate (Gas: N<sub>2</sub>, boiling point: -195.795 °C, 77.355 K) on the catalyst surface. The amount of nitrogen adsorbed was measured between a vast relative pressure range (equilibrium vapour pressure ( $P$ )/saturation vapour pressure ( $P_0$ )) as well as an invariant temperature (liquid nitrogen, 77 K) to achieve the adsorption isotherm. Thereafter, desorption isotherm was obtained by reducing the pressure to measure the removed gas.

Prior to the experiments, 1.1 g of the samples was degassed for 4h at 363 K in flowing helium (30 ml/min) and the data were accumulated at 77.24 K. Equation 3.1 expresses the BET equation [107]:

$$\frac{P/P_0}{V_{ads} \cdot (1 - P/P_0)} = \left( \frac{1}{V_{ads} \cdot C_{BET}} + \frac{C_{BET} - 1}{V_{ml} \cdot C_{BET}} \right) \cdot \left( \frac{P}{P_0} \right) \quad (3.1)$$

$P/P_0$ : Relative pressure (equilibrium pressure/saturation pressure of nitrogen as adsorbate at the adsorption temperature)

$V_{ads}$ : adsorbed volume of gas

$V_{ml}$ : adsorbate monolayer volume

$C_{BET}$ : BET constant

Equation 3.2 expresses the BET constant. The resulting parameter,  $C_{BET}$  is positive.

$$C_{BET} = \exp\left(\frac{E_1 - E_L}{RT}\right) \quad (3.2)$$

$E_1$ : first layer's heat of adsorption

$E_L$ : second and higher layers' heat of liquefaction

At least, three data points are required to plot the straight-line multiple BET plot with  $\left(\frac{1}{V_{ads}}\right) \cdot \left(\frac{P/P_0}{1-P/P_0}\right)$  on the y-axis and relative pressure  $\left(\frac{P}{P_0}\right)$  on the x-axis based on the results obtained from analyzer (shown in Figure 3.7). The BET constant as well as the quantity of monolayer adsorbed gas are calculated by using the

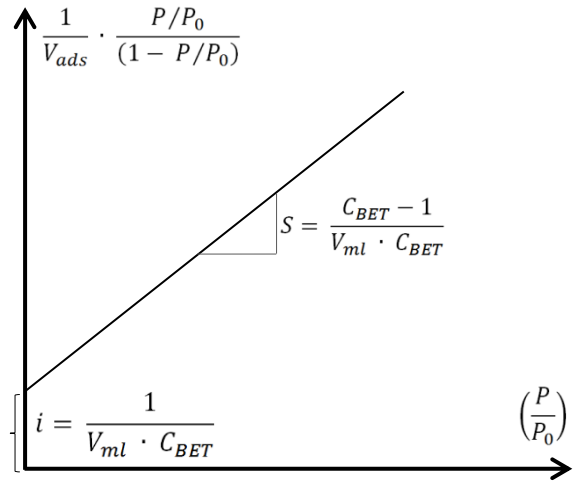


**Figure 3.7:** Multipoint BET plot

slope value and y-intercept line. Equations 3.3 and 3.4 describe these parameters [108]:

$$V_{ml} = \frac{1}{S + i} \quad (3.3)$$

$$C = 1 + \frac{S}{i} \quad (3.4)$$

Total surface area ( $S_{BET,total}$ ) was calculated by employing Equation 3.5 [108]

$$S_{BET,Total} = \frac{V_{ml} \cdot N \cdot A_{CS}}{M} \quad (3.5)$$

**N:** Avogadro's number ( $6.023 \times 10^{23}$ )

**M:** Molecular weight of adsorbate (28.0134 g/mol)

**A<sub>CS</sub>:** cross-sectional area of the adsorbate ( $A_{N_2} = 0.1620 \text{ nm}^2$ )

Finally, Equation 3.6 was used to determine the Specific BET surface area ( $S_{BET}$ ),

$$S_{BET} = \frac{S_{total}}{a} \quad (3.6)$$

**a:** mass of adsorbent (in g)

As mentioned previously, adsorption of the nitrogen molecule's mono-layer (adsorbate isotherm) onto the porous sample is used to determine the surface area of the materials. At low pressure, the nitrogen gas molecules are adsorbed onto the isolated sample sites. A monolayer of adsorbed nitrogen is formed by increasing the gas pressure which results in coverage of the solid sample with a gas monolayer. By extending the process, the nitrogen molecules are allowed to be

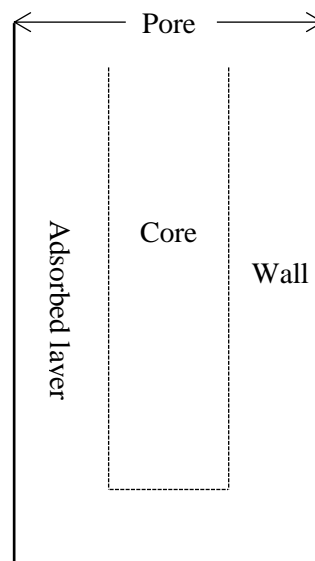


**Figure 3.8:** Different existing zones of a pore

condensed inside the pores. The multi-layer coverage is achieved by further increasing the gas pressure. By increasing the pressure, first the small dimensioned pores are filled with condensed nitrogen. The condensation process is increased by continually increasing the pressure until saturation is reached; at which point all of the sample's pores are filled with liquid nitrogen. At this stage, the complete coverage of the sample occurs. Thereafter, the analyser reduces the pressure of adsorptive nitrogen incrementally so that the condensed nitrogen evaporates from the system. The pore distribution is determined by using the Barrett, Joyner, and Halenda (BJH) method [109]. The average pore sizes are related to the amount of adsorbate lost in the desorption step, by using the desorption branch of the isotherm.

Figure 3.8 indicates the different zones of a pore, including the core and adsorbed layer formed during the multi-layer adsorption and then evaporation during desorption. Each of these two processes depends on a particular relative pressure (vapour pressure). The core of the pore is defined as the loss of condensed liquid adsorbate at a particular relative pressure

related to the core radius. After evaporation of the core of the pore, an adsorbate layer remains on the pore wall. At a particular relative pressure, the thickness of this layer could be calculated after desorption due to a decrease in the pressure. The pore volume of a sample is composed of the quantities of the gases desorbed from two different zones of a pore (core and adsorbed layer) during different steps in pressure reduction. The evaporated liquid of the cores are equivalent to the measured quantity of the gas desorbed in the first step [110].

The explained process was used to calculate the pore volume, pore size distribution and pore diameter of the prepared catalyst. The observed hysteresis of nitrogen physisorption type IV isotherm (restricted multi-layer isotherm) as a consequence of capillary condensation of liquid nitrogen in the complex porous network of the catalyst was used. The adsorption branch was traversed by increasing the relative pressure  $P/P_0$  from about 0.05769 to about 0.9864 to form the multi-layer of nitrogen physically adsorbed on the porous structure. Thereafter, the evaporation of the condensed nitrogen was begun due to desorption by decreasing the relative pressure  $P/P_0$  to about 0.1168. The core radius was measured by using the Kelvin equation [111, 112] represented in Equation 3.7.

$$\ln \frac{P}{P_0} = \frac{-2\gamma V_L}{RT r_c} \quad (3.7)$$

$P/P_0$ : relative pressure (actual vapor pressure/saturated vapor pressure)

$\gamma$ : surface tension

$V_L$ : molar volume of the liquid

$R$ : universal gas constant

$T$ : temperature

$r_c$ : radius of the curvature

### 3.1.2.3 *X-Ray powder Diffraction (XRD)*

The crystallographic structure of different substances can be obtained by using the multifunctional/non-destructive X-Ray Diffraction (XRD) method. In condensed matter physics, the solid materials are described as non-crystalline (amorphous) and crystalline materials. In the case of amorphous materials, the atoms are arranged in a random pattern (e.g. glass); while in the crystalline solids, which describes about 95 percent of the solid materials, the atoms are arranged in a regular pattern. The atoms' organization in the crystalline structure specifies the properties of the materials [113].

The X-rays as electromagnetic radiations have exactly the same nature as light but are of a very much shorter wavelength. The boundary of X-rays is defined in the region between gamma-rays and ultraviolet rays in the electromagnetic spectrum. The wavelengths of the X-rays used in an XRD diffractometer are approximately in the range of 0.5 – 2.5 Å. While the visible light wavelength is of the order of 6000 Å [114]. Most of the X-rays' techniques are based on the portion of the X-ray elastically scattered by the electrons [115]. The charges of all electrons of an atom interact with the electric field of such waves [116]. The electromagnetic radiations with a certain frequency go into the materials. These radiations are ridden by the electrons in the materials and are oscillated in the polarization direction of the incident light by those electrons. The electromagnetic radiations are created due to accelerated electrons; the oscillating electrons emit lights with the same frequency and in spherical distribution [115]. The almost spherical waves are emitted with the same wavelength as incident radiation, as a result of the diffraction event [116]. The intensity of X-rays is decreased due to energy transfer during the oscillation of the electrons in the materials. The spherically scattered X-rays experience constructive interactions in particular directions with

a material showing a periodicity in the distribution of electrons comparable to the wavelength ( $\lambda$ ) of X-rays [115]. Hence, the number of electrons in the atom is proportional to the outgoing wave amplitude. The atomic number is in accordance with it as well. The atom form factor  $f$ , describes the scattered wave amplitude. The amplitude of the outgoing wave varies due to the interference within the individual atom, especially the larger one. Subsequently the scattering angle along with the atom form factor is varied as well [116].

The theoretical method of XRD was explained by Bragg's law who discovered the characteristic X-ray lines. The description of diffraction by a crystal in Bragg's method is used to compute the diffraction directions. X-ray beam reflection by the crystallographic planes defined by indices  $hkl$  describes the diffraction in Bragg's representation. Incident waves reflected by equivalent planes with characteristic separation  $d_{hkl}$  (the distance  $d$  is varied for different materials) are in phase if the difference in their travel ( $a_1 + a_2$ ) is equal to an integral number of wavelengths,  $n$  (shown in Figure 3.9) [115].

$$n\lambda = a_1 + a_2 \quad (\text{where } a_1 = a_2) \quad (3.8)$$

$$n\lambda = 2a_1 \quad (3.9)$$

$$\sin \theta = a_1/d \quad (3.10)$$

$$a_1 = d_{hkl} \sin \theta \quad (3.11)$$

$$n\lambda = 2d_{hkl} \sin \theta_{hkl} \quad (3.12)$$

Where  $\lambda$  is the radiation wavelength,  $n$  is an integer number,  $\theta$  is the angle between the incident beam and the lattice planes.  $d$  is the distance of the lattice planes for which the peak occurs. A diffraction peak is generated from the  $d$ -spacing of the set of planes. The function of this technique is the diffracted beam intensity. As the electrons are the objects scattering X-

rays, hence, the intensity of the diffracted beams depends on the density of the distributed electrons within the crystal [115]. He also derived that the atomic number of the emitter influences the wavelength of any particular line. The increase in atomic number results in a decrease in line wavelength [114]. When a periodic crystalline structure (phase) interacts with X-rays, a diffraction pattern is produced. Every crystalline substance gives a pattern. This pattern is characteristic for each crystalline substance, like a fingerprint. Hence, in the case of polycrystalline phases, X-ray diffraction is an ideal method to characterize and identify the different crystalline substances [113].

The X-ray diffraction measurements of un-reduced/calced catalysts were carried out at ambient temperature employing Inel EQUINOX 3000 motorization-free diffraction system (Figure 3.10) with monochromatized Cu-K $\alpha$  radiation [117]. The scans ranged from 0° to 115°. Each experiment lasted 10 minutes and the 2 $\theta$  diffraction patterns were measured in

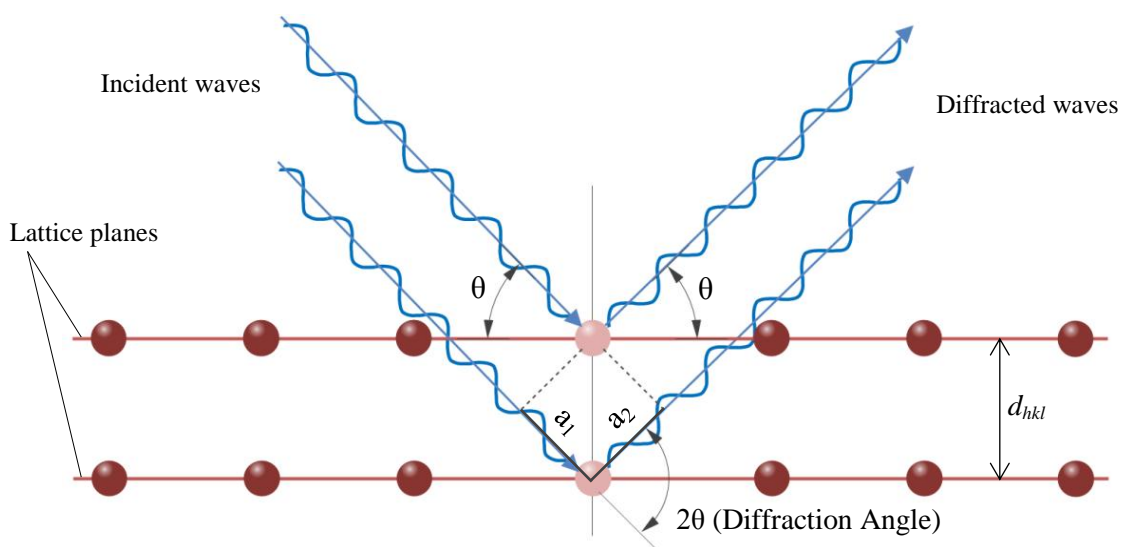


**Figure 3.9:** Representation of Bragg's law, diffraction condition (constructive interference) as the reflection of X-rays from lattice (atomic) planes (h k l)

real-time. The diffractometer was equipped with a curved detector with asymmetric acquisition mode. The samples were scanned in their original powder forms. Cobalt phases were analysed by comparing the obtained diffraction patterns with those in the standard XRD Powder Diffraction File (PDF), combined by the Joint Committee on Powder Diffraction Standards (JCPDS), published by the International Centre for Diffraction Data (ICDD) [118]. The average crystallite sizes of  $\text{Co}_3\text{O}_4$  were calculated from the Scherrer equation [114] using the (3 1 1) peak located at  $2\theta = 36.65^\circ$ .

$$d = \frac{k \cdot \lambda}{B \cdot \cos \theta} \times \frac{180^\circ}{\pi} \quad (3.13)$$

Where  $d$  is the mean crystallite diameter (nm),  $\lambda$  the X-ray wavelength ( $1.54056 \text{ \AA}$ ), and  $B$  is the Full-Width Half-Maximum (FWHM) of the  $\text{Co}_3\text{O}_4$  diffraction peak. A  $k$  factor of 0.89 was used in the Scherrer equation.

*Figure refereed from [119]*

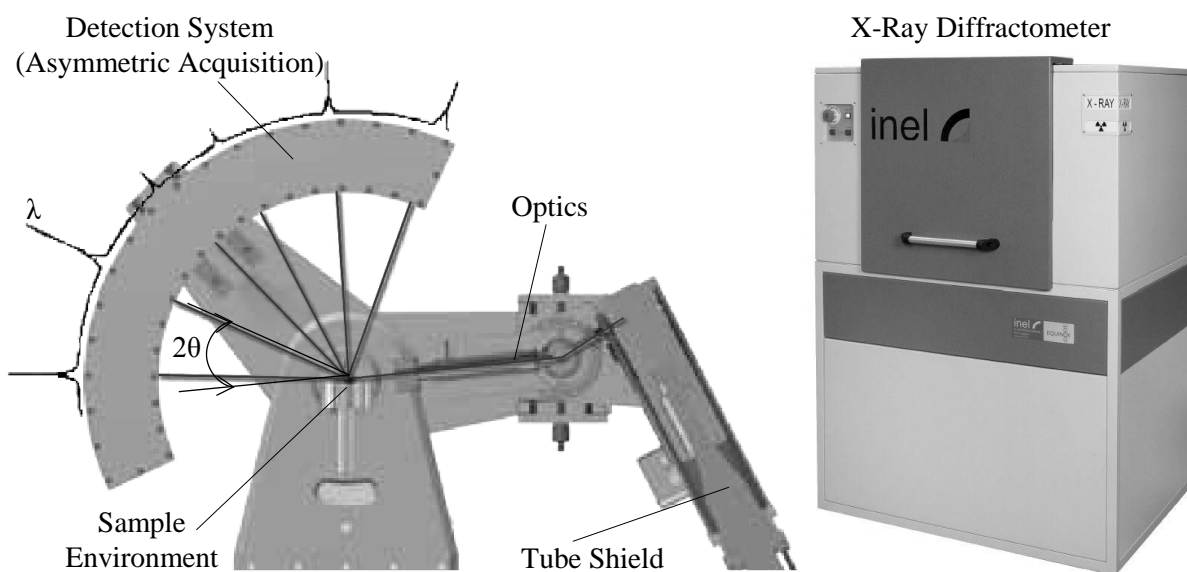


**Figure 3.10:** X-Ray diffractometer with motorization free curved detector (Inel® EQUINOX 3000)

### 3.1.2.4 Scanning Electron Microscopy – Energy Dispersive X-Ray Spectroscopy

The micro-structural characteristics of a solid catalyst were examined and analysed by using the Scanning Electron Microscope (SEM) instrument. The primary function of this technology is to make the micro-structural features visible to the human eye. The SEM uses a focused beam of electrons for imaging, which enables the observation of very fine details at high magnification as well as features of large samples at low magnification. The three-dimensional appearance of the specimen is obtained by offering the large depth of field by SEM technology.

The SEM instrument consists of electron guns, a lens system, electron detector and an imaging system. The electron gun in the JEOL 6060 instrument contains a tungsten filament. The filament is heated with a power supply and maintained at a high negative voltage (typically 10-20 kV) during operation. As a result of tungsten heating, electrons are emitted from the tip and subsequently accelerated to the ground by the 10-20 kV potential between the filament and the anode. The emitted and accelerated electrons from the gun are controlled and directed to the specimen by a series of electromagnetic

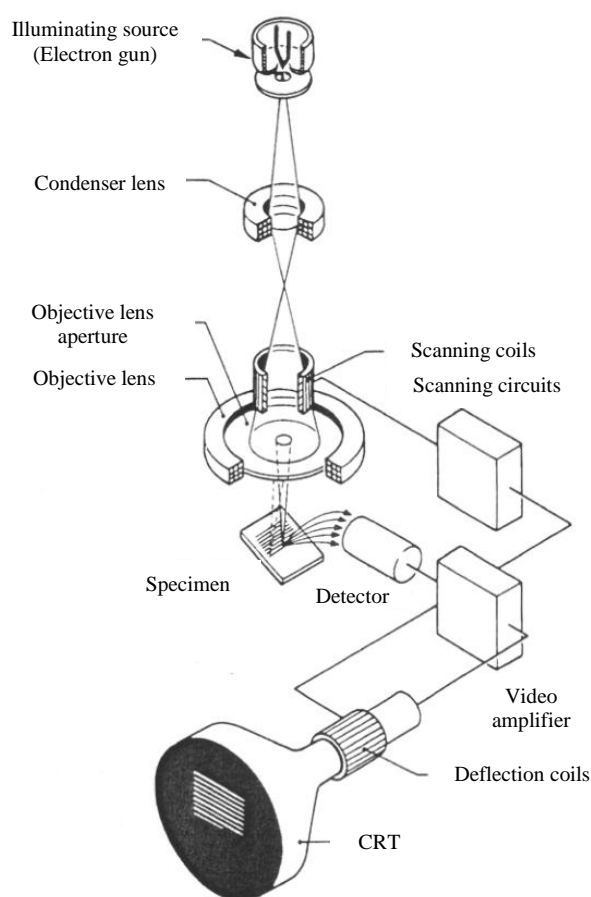


**Figure 3.11:** Basic image formation in a Scanning Electron Microscope (SEM)

lenses and apertures. When the electrons of the electron beam hit the specimen, a number of electron-specimen interactions including elastic scattering of electrons, secondary electron emissions (emissions of loosely bound electrons of the conduction band), ionization of inner shell electrons (produces x-rays and Auger electrons), and excitation of phonons (causes heating of the specimen) may occur. Different materials and samples' geometries produce different amounts or different types of secondary electrons, backscattered electrons, Auger electrons, transmitted electrons, and x-rays. All of these interactions may be used for imaging or analysis of the sample. Secondary Electron Imaging (SEI) involving a Secondary Electron Detector (SED) was employed for imaging in SEM as it is the most common type. The secondary electrons, along with some backscattered electrons emitted from the sample's surface, were collected and subsequently converted into a video signal in the SEI [120].

The samples were prepared with a coating prior to the SEM imaging, utilizing a sputter deposition process (thin film deposition through the Physical Vapour Deposition (PVD) method) to enable and improve the sample's imaging. The coating was required to create a conductive layer of metal on the sample.

Accordingly, the charging of the specimen caused by static electric fields' accumulation by the electron beam was inhibited by the metal thin layer; as well as thermal damage being reduced. In addition, the emitted amount of secondary electron signals were increased, which were required for topographic examination in the SEM



**Figure 3.12:** Sputter coating of Au before imaging in Scanning Electron Microscopy (SEM)

(heavy metals are good secondary electron emitters) [121]. Emscops<sup>®</sup> SC500 sputtering apparatus (Figure 3.12) was employed for applying an ultra-thin coating of electrically-conducting gold (Au) onto non-conducting or poorly-conducting samples. The sputtered films typically had the thickness range of 2–20 nm. A conductive adhesive tab was used to hold the samples on the sample holder surface. The samples were positioned on the adhesive tabs and then the holder was put in a sputter chamber and the chamber lid was fitted correctly. The chamber was vacuumed to 0.07 Torr and subsequently was purged by using Argon gas. Thereafter the chamber vacuum was dropped to 0.1 Torr and the coating was started. Position control was adjusted to give a reading of 25 mA. The coating lasted for 3 minutes using a timer control and then the ventilation took place. This procedure was repeated two times to make sure that all the porous surfaces had been deposited with a thin layer of gold.

The morphological properties of the species over the texture of the surfaces were analysed by utilizing a Jeol<sup>®</sup> JSM 6060 Scanning Electron Microscope (SEM) operating (accelerating voltage) at 0.5 to 30 kV (resolution at high voltage mode: 3.5 nm @ 30 kV). The samples were handled by gloves just to make sure that the area was kept clean. The sample holder including the prepared samples was slid onto the stage dovetail. The sample height (working distance) was adjusted in 10 mm which is the working distance for EDS as well. A 10 mm working distance enables high magnification

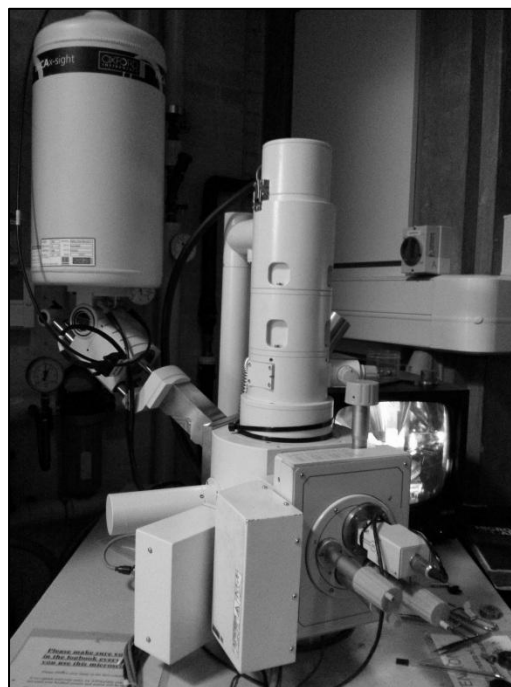


**Figure 3.13:** JEOL 6060 instrument

imaging. The samples were not tilted during the imaging. The system was vacuumed to minimize the interference of air particles with the electron beam and to prevent rapid oxidation of the tungsten filament. Then the accelerating voltage was set at 10 kV. The signal was set to SED. The imaging was performed at different magnifications. The structure of the cobalt catalysts was considered at nano-scale by using FEI strata<sup>®</sup> XP 235 dual beam SEM.

The Jeol 6060 instrument was fitted with an Oxford instrument Inca 300 Energy-Dispersive X-ray Spectroscopy (EDS) system to construct the elemental concentration maps and metal distribution. The identification of particular elements as well as their atomic proportions over the surface of different samples was the main purpose for exploitation of the EDS technique. A specified acquisition of X-ray data on a user-defined area of an image was applied for all of the samples. The elemental analyses were performed to determine the distribution and relative proportions of previously defined elements (cobalt and silica) over the scanned surfaces (spectrums). The data was acquired from different sites of interest. The accelerating voltage was chosen as 20 kV, to make sure most X-ray lines would be excited from most elements. The concern of working at a higher kV was that the higher penetration into the sample would increase the absorption correction. In contrast, high accuracy of quantification was achieved at high kV. The live time for which the system was processing counts into the spectrum was set 140 to 150 seconds to terminate acquisition. The process time (the length of time spent to reduce noise from the X-ray signal coming from the ED detector) was selected to 5 out of 6. The longer the process time resulted in the lower the noise. Resolution of the peaks displayed in the spectrum was improved by minimising the noise. In addition, the longer process time prevented the overlapping of the peaks. The desired working distance (the distance between the lower pole piece of the objective lens and the plane at which electrons were focused) to perform the micro-analysis was set at 10 mm, the spot size was 71.

### 3.1.2.5 Temperature-Programmed Reduction (TPR) analysis

A Temperature-Programmed-Reduction (TPR) technique was employed to determine the number of reducible species along with the temperature at which the reduction of each of the present species over the catalyst surface occurs. The solid catalysts are characterized by using the TPR technique. The Micromeritics<sup>®</sup> AutoChem II 2920 chemisorption analyser (shown in Figure 3.14) was used to conduct the comprehensive temperature-programmed reactions. Valuable information could be acquired by TPR analysis regarding the heterogeneous catalyst containing reducible metals. For example, the most efficient reduction conditions of oxidized catalysts could be achieved by TPR analysis. The following steps were followed to perform a typical TPR analysis.

For each of the experiments, 0.2 g of the calcined sample was obtained. Then the weighted sample was loaded into the U-shaped tubular quartz reactor. Quartz wool was used to support the sample in the U-shaped tube. Afterwards the sample tube was installed on the analyser. The tube was positioned in an electric furnace equipped to the temperature controller. The sample target temperature could range from ambient to 1100 °C. A sample thermocouple was used to measure the sample temperature. For more accuracy in temperature reading, the bare thermocouple end was placed inside the sample.

*Figures refereed from [122]*

**Figure 3.14:** Micromeritics<sup>®</sup> AutoChem II 2920 chemisorption analyser to characterize the heterogeneous catalysts by the TPR analysis



Prior to the experiment, the sample was purged by flowing helium gas (sample preparation step). The gas flow rate was 10 ml/min and the sample temperature was increased by 10 °C/min from ambient temperature to 110 °C and held for 40 minutes. After completing the purging step, the sample temperature was cooled down to 60 °C and the sample was held at this temperature for 10 minutes so that the temperature in the reaction zone was stabilized. Then, the helium line was closed and the TPR analysis was begun by flowing the pure hydrogen (analysis gas) through the sample with a flow rate of 10 ml/min. While the hydrogen was flowing, the temperature of the sample was increased linearly with time (ramping rate: 5 °C/min). The sample's target temperature was set at 900 °C and the sample was held for 30 minutes at the target temperature. During the TPR, the metal oxides were reacted with hydrogen gas to form pure metal. At critical temperatures, hydrogen atoms in the gas flow reacted with the sample forming water molecules. The H<sub>2</sub>O molecules were removed from the gas stream using a cold trap. In some cases, the cold trap was not required as only a trace of water was formed as a product of the reduction. In addition, the internal analyser temperature zones were maintained at 100 °C or even higher during the entire experiments.

The consumption of hydrogen by reaction was monitored by using a Thermal Conductivity Detector (TCD). The detector contains a heated filament. TCD measures the difference in gas thermal conductivity sensed between the gases flowing over the sample and reference filament. The hydrogen flowing past the detector cools the filament by extracting heat. When the sample reacted with the hydrogen, it caused changes in the composition of the hydrogen and consequently, changed the thermal conductivity of the gas. Changes in the concentration of the hydrogen downstream from the reaction cell were determined this information yielded the volume of hydrogen uptake. The experiment was started at 60 °C (lower than the reduction temperature) so that it established a baseline based on collected data.

## 3.2 *Fischer-Tropsch synthesis measurements*

### 3.2.1 *Development of experimental set-up (bio-diesel generator)*

The F-T plant consists of two major units: a downdraft fixed-bed gasifier and an F-T bio-fuel generator. The experimental work of this project concentrated on developing a miniaturised version of the plant that could accomplish the preliminary investigation regarding the F-T process, before scale up to pilot plant and building of a pilot scale bio-fuel generator. For this purpose, a small scale F-T bio-diesel generator via the Fischer-Tropsch synthesis process was designed, built and commissioned (eventually on the scale suitable to produce bio-diesel in milli scale per day) in a laboratory of the School of Mechanical Engineering of the University of Birmingham. A mini structured downdraft fixed-bed reactor was employed in order to examine hydrogenation activity of different catalysts, find the optimum reaction conditions for maximum production of synthetic fuel, as well as to convert the syngas into the synthetic bio-fuel. No re-cycling system was devised to recycle the unreacted feed.

Figure 3.15 indicates the schematic diagram of the experimental set-up along with the Process Path Flow (PPF), which describes the path of implementation in converting the syngas into the liquid hydrocarbons. A simulated nitrogen-rich syngas bottle was employed to simulate the outlet product of the gasification process. Nitrogen and hydrogen bottles were used to purge and activate the catalytic bed respectively. Each of the bottles comprised a high accuracy compressed gas pressure regulator to reduce the pressure of gases from the cylinders to a lower value needed by other devices in the next stages (Figure 3.17(d)). Two flashback arrestors were installed in the gas lines and on the outlet of the flammable gas cylinders (syngas and hydrogen bottles) to stop a flame in its tracks. The check valves (one-way valves) were used to prevent backward flow of gases to the gas sources (Figure 3.16(e)).

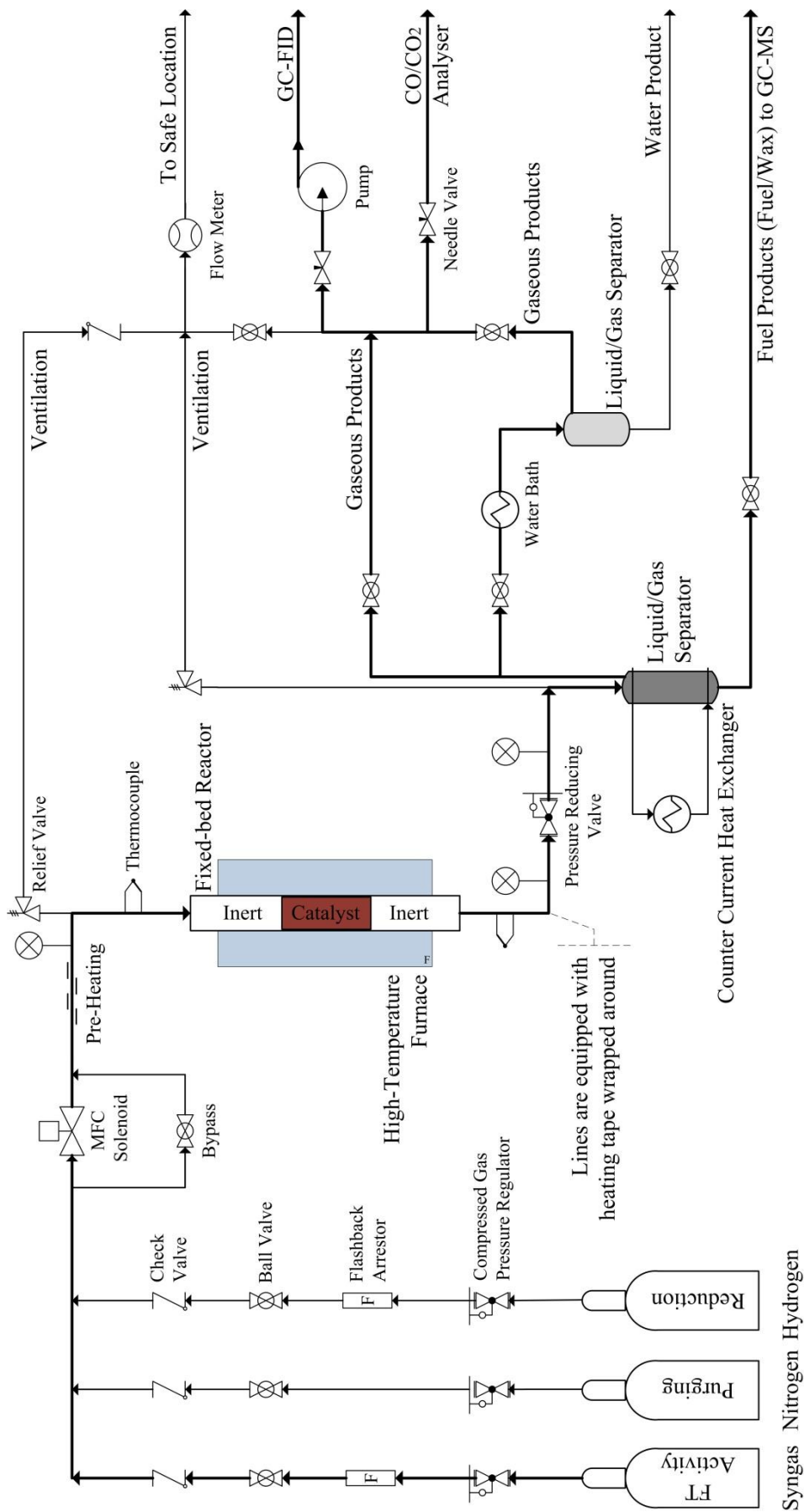


**Figure 3.15:** Schematic diagram of small scale bio-diesel generator via Fischer-Tropsch Synthesis (FTS) process and utilized equipment along with Process Path Flow (PPF) to implement conversion of synthesis gas into the liquid heavy hydrocarbons (shown with thicker line)

The volumetric flow rate of the feedstock was regulated using a calibrated smart Mass Flow Controller (MFC) shown in Figure 3.17(c). A bypass line shown in Figure 3.17(c) was improvised to allow the gases to bypass the MFC and release the pressure after the experiments were over. To generate and raise the temperature of inlet gas before the reactor, a flexible heat tape with an electrical heating element was run in physical contact along the length of the inlet pipe to the reactor to maintain the flow temperature constantly at a higher degree. The heat tape was covered with thermal isolation to retain heat losses from the pipe (Figure 3.16(f)). The system pressure was monitored using a pressure gauge before and after the reactor (shown in Figure 3.16(b)). A proportional relief valve (Figure 3.17(f)) was applied before the reactor so that in the case of system failure it would be opened gradually and release the pressure. The valve was set at 40 bar. The inlet and outlet temperature of the flow was measured by using a thermocouple connected to a thermometer (shown in Figure 3.17(f)).

Carbon monoxide hydrogenations were carried out in an F-T unit consisting of a single-channel downdraft fixed-bed reactor (tubular seamless stainless steel, 0.75 in. inner diameter, 0.065 in. wall thickness and 20.87 in. length) shown in Figure 3.16(b). The reactor was surrounded by a metal jacket to achieve a uniform wall temperature along the reactor length. A tube furnace controlled by a thermocouple positioned along the reactor centreline was used to provide heating. The thermocouple end was generally located approximately 60-80 mm inside the catalytic bed. The microprocessor-based Proportional-Integral-Derivative (PID) temperature controller was used to control the temperature in different regimes (pre/after-heating and catalyst bed (reactor)). To get the best possible control of temperature for the catalytic bed, the proportional, integral and derivative were set by auto-tuning of the controller at a simulated F-T reaction condition before the running of the main experiments. The reactor temperature fluctuation during the experiments was  $\pm 1$  °C.

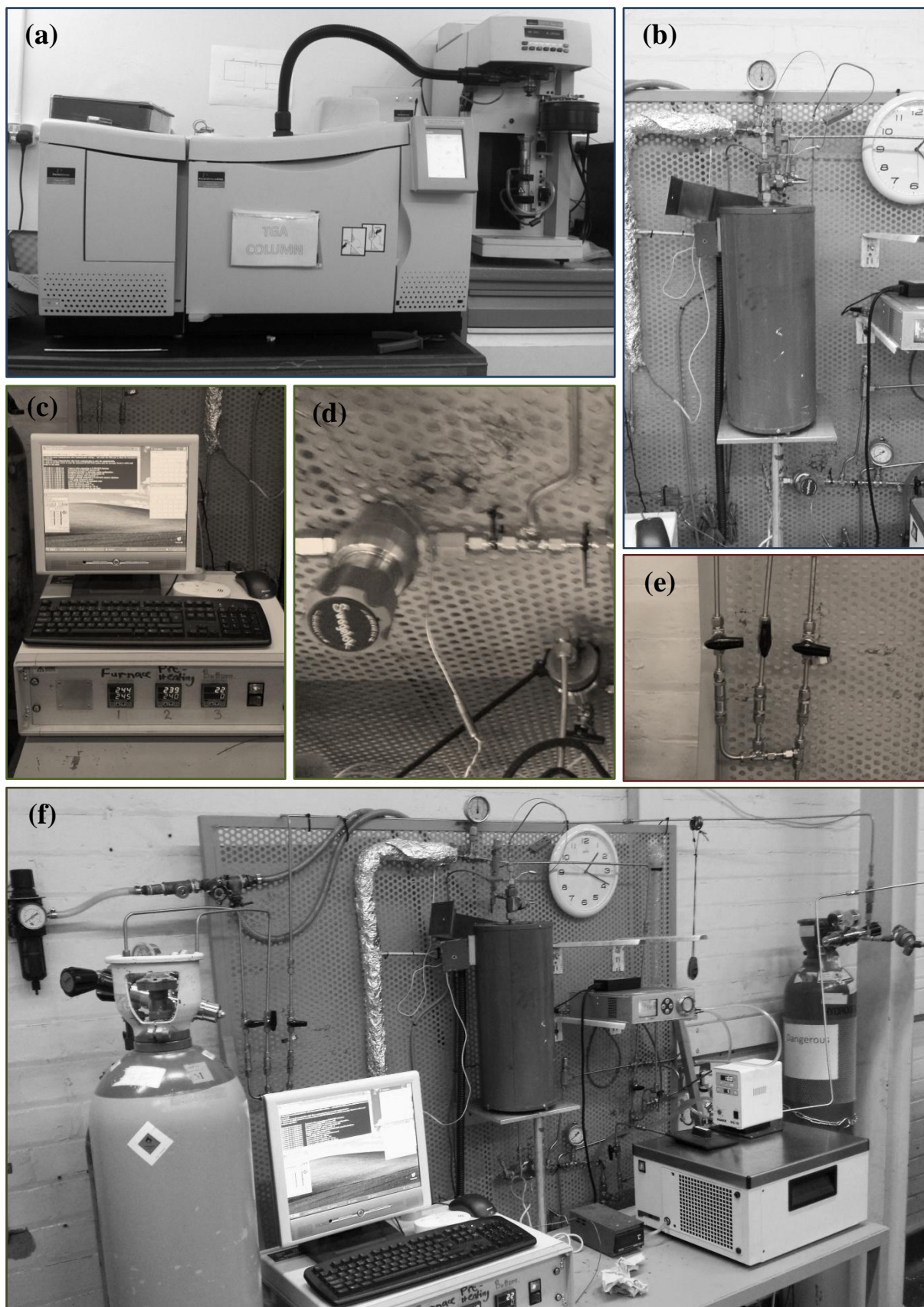


**Figure 3.16:** Different components of mini bio-diesel generator in Fisher-Tropsch Synthesis process

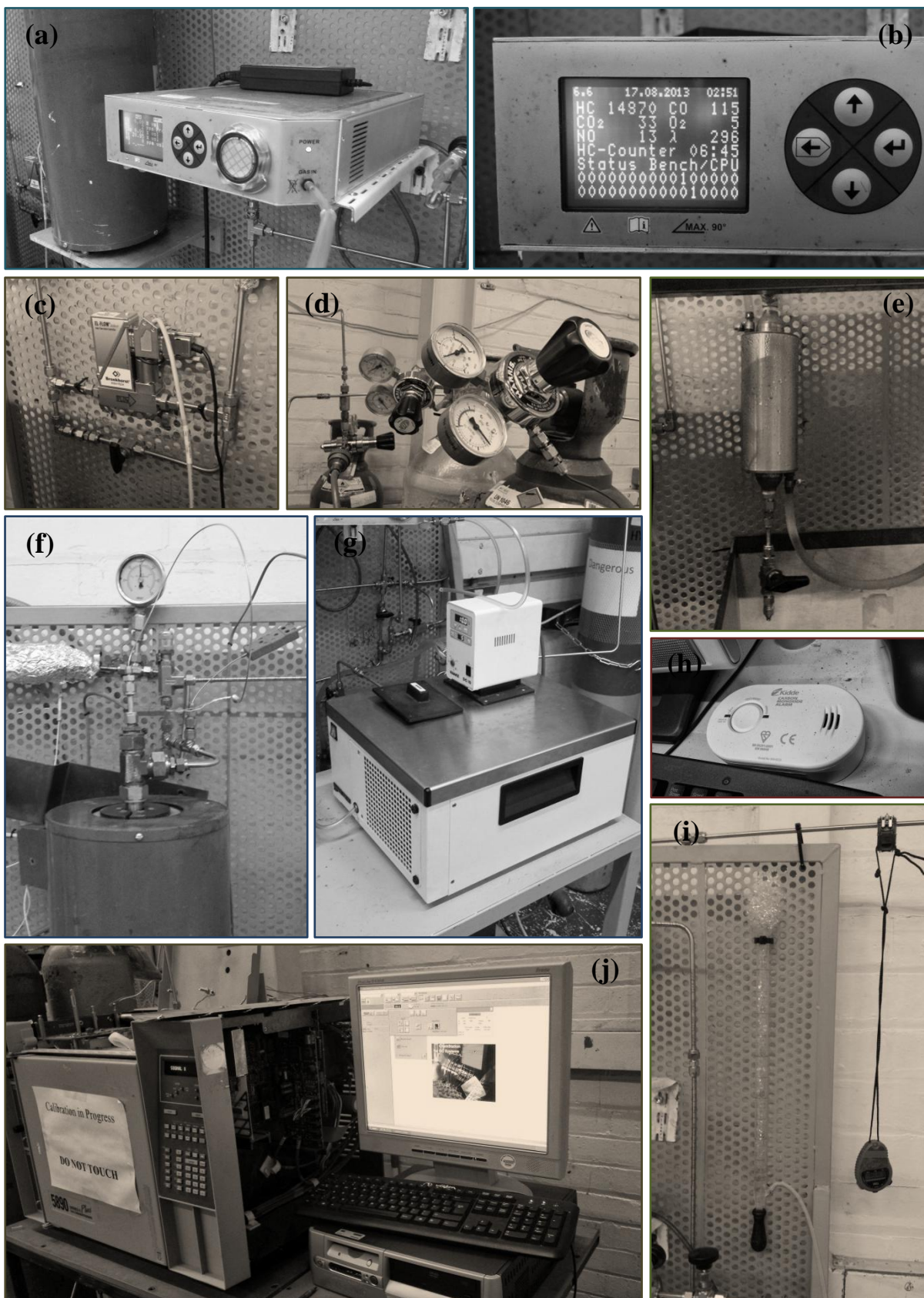


**Figure 3.17:** Different components of mini bio-diesel generator in Fisher-Tropsch Synthesis process

After the reaction regime, to reduce the pressure of the system as well as to control the pressure of the downstream system to keep it as constant as possible, while the inlet pressure and the flow may vary, a pressure reducing regulator was used (shown in Figure 3.16(d)). The lines after the reactor were equipped with heating tape wrapped around them to prevent the condensation of liquid products before the separation systems. A relief valve was installed before the separators so that in the case of blockage, it would release the pressure of the system (Figure 3.16(b)). The mixture of product streams was separated into two, a liquid hydrocarbon stream and an unreacted gaseous stream, by using the vapour-liquid separation system. The condensed liquid products were flown downward inside the column and collected from time to time. The gaseous stream left from the top of the column (shown in Figure 3.17(e)). A counter current heat exchanger was used to reduce the temperature around and inside the column. A refrigerated laboratory water bath was utilized to keep the coolant fluid at a constant temperature (shown in Figure 3.17(g)). The temperature was set at 10°C during all of the experiments.

The volumetric based outlet flow rate was measured by using a volumetric bubble flow meter. The flow was determined by measuring the required time for a volume of a gas stream in millilitres (ml) to move a soap bubble through a specific volume per unit of time in minutes (shown in Figure 3.17(i)). Since the outlet flow rate of the system was much lower to run the gas chromatogram, a pump was utilized as a mechanical device to move and force the gaseous stream into the gas-chromogram (GC), extract the remaining air from the gas loop and fill the loop with test gas. The reactor temperature was cooled down by using compressed air connected to the central air compressor line (shown in Figure 3.16(f)).

Different items used to develop the F-T experimental rig, along with the purposes of utilization, its specification as well as the product suppliers, are listed in Table 3.5.

**Table 3.5:** List of different components in experimental rig, specifications and products' suppliers

<b>Item</b>	<b>Purpose of Application</b>	<b>Technical Specifications</b>	<b>Supplier</b>
Syngas Bottle	Simulated synthesis gas bottle to carry out the F-T activity	<ul style="list-style-type: none"> <li>• Composition: 17% Carbon Monoxide, 33% Hydrogen and balanced Nitrogen (Volume %)</li> <li>• Cylinder size: L (50L water capacity)</li> <li>• Pressure (bar): 200</li> </ul>	BOC <sup>®</sup>
Nitrogen Bottle	To purge the catalytic bed and F-T synthesis system	<ul style="list-style-type: none"> <li>• Grade: Zero N4.8 (99.998%)</li> <li>• Cylinder size: L (50L water capacity)</li> <li>• Pressure (bar): 200</li> </ul>	BOC <sup>®</sup>
Hydrogen Bottle	To reduce the catalyst for activating	<ul style="list-style-type: none"> <li>• Grade: Chemically pure zero grade N5.0 (99.999%)</li> <li>• Cylinder size: L (50L water capacity)</li> <li>• Pressure (bar): 200</li> </ul>	BOC <sup>®</sup>
Compressed Gas Pressure Regulator	To cut off the flow of compressed gas from the bottle at a certain pressure	<ul style="list-style-type: none"> <li>• M/stage 0.10 bar</li> </ul>	HARRIS <sup>®</sup>
Flashback Arrestor	To stop the flame from burning back up into the bottles and equipment	<ul style="list-style-type: none"> <li>• Connections: 3/8 BSP Female/GAS x 3/8 BSP LH ACET, PROP, HYDRO</li> </ul>	Gas ARC <sup>®</sup>
Ball Valve	On and off valve for high pressure and temperature supporting	<ul style="list-style-type: none"> <li>• 1-Piece 316 stainless steel Ball Valve</li> <li>• Connections: 1/4 in.</li> <li>• Maximum Temperature Pressure rating: 148 °C @ 172 bar</li> <li>• Flow pattern: standard (2-way)</li> </ul>	Swagelok <sup>®</sup>
Check Valve	To allow the gas flow through it in only in one direction	<ul style="list-style-type: none"> <li>• Poppet 316 stainless steel Check Valve</li> <li>• Connections: 1/4 in.</li> <li>• Maximum Temperature Pressure rating: 190 °C @ 150 bar</li> </ul>	Swagelok <sup>®</sup>

*Continued on the next page*

---

Mass Flow Controller	Digital device to measure and control the flow of the gases calibrated by the company	<ul style="list-style-type: none"> <li>• Range: 4 – 200 mln/min</li> <li>• Inlet pressure: 50 bar (g)</li> <li>• Outlet pressure: 40 bar (g)</li> <li>• Connections: 1/4 in. OD compression</li> <li>• Temperature: 20 °C</li> <li>• Orifice: Ø 0.05 mm</li> </ul>	Bronkhorst®
Heater Tape	To raise and maintain the temperature of the pipes with electrical heating element	<ul style="list-style-type: none"> <li>• Voltage: 240 V</li> <li>• Length: 6 foot</li> <li>• Power: 250 W</li> </ul>	OMEGA®
Pressure Gauge	To measure the pressure	<ul style="list-style-type: none"> <li>• Pressure range: 40 bar</li> <li>• End connections: 1/4 in.</li> </ul>	Swagelok®
Relief Valve	To control and limit the pressure in the system in the case of equipment failure	<ul style="list-style-type: none"> <li>• Medium-Pressure stainless steel Proportional Relief Valve</li> <li>• Connections: 1/4 in.</li> <li>• Maximum Temperature Pressure Rating: 121 °C @ 338 bar</li> <li>• Size: 1/8 in.</li> </ul>	Swagelok®
Thermocouple	To measure the temperature	<ul style="list-style-type: none"> <li>• Type: K type</li> <li>• Probe diameter: 1/16 in.</li> </ul>	RS®
Pressure Reducing Valve	To regulate the gas pressure before separation system	<ul style="list-style-type: none"> <li>• Body material: 316 stainless steel</li> <li>• Pressure control range: 0 - 34.4 bar</li> <li>• Port configuration: 1/4 in. female NPT</li> </ul>	Swagelok®
Solid Glass Beads	Spherical material used to pack the catalytic bed	<ul style="list-style-type: none"> <li>• Material: borosilicate</li> <li>• Diameter: 3 mm</li> </ul>	Sigma Aldrich®
Glass Wool	Insulating material to pack the catalytic bed into the reactor	<ul style="list-style-type: none"> <li>• Silanized glass wool</li> </ul>	Sigma Aldrich®

---

*Continued on the next page*

---

Glass Bubble Flow Meter	A volumetric flow measurement at ambient pressure and temperature	<ul style="list-style-type: none"> <li>• Materials: Glass</li> <li>• Soap film flow meter 5 ml</li> </ul>	Thermo®
Needle Valve	To allow precise regulation of flow capable for low flow rate	<ul style="list-style-type: none"> <li>• 316 stainless steel bonnet needle valve</li> <li>• Connections: 1/4 in.</li> <li>• Maximum Temperature Pressure rating: 232 °C @ 2362 bar</li> <li>• Flow pattern: standard (2-way)</li> </ul>	Swagelok®
Carbon Monoxide Detector	To detect the presence of carbon monoxide in order to prevent poisoning	<ul style="list-style-type: none"> <li>• Temperature range: 4.4-37.8 °C</li> <li>• At 100 ppm, alarm within 10-40 mins</li> <li>• At 300 ppm, unit alarm before 3 mins</li> </ul>	Kidde®
K15Water Bath with DC10 Circulating	To gradually cool the heat transfer fluid and keep it at constant temperature over the period of time	<ul style="list-style-type: none"> <li>• Working temperature range: -28 °C to 100 °C</li> <li>• Cooling capacity (at 0 °C): 200 W</li> <li>• Pump flow rate: 12.5 l/min</li> </ul>	HAAKE®
Oil-less diaphragm Pump	To move and force the gaseous products into the GC gas loop	<ul style="list-style-type: none"> <li>• Max. flow: 400 l/min</li> <li>• Motor nominal voltage: 240 V</li> </ul>	Thomas®
Stainless Steel Tube	Used to load the catalytic bed and carry out the reaction	<ul style="list-style-type: none"> <li>• Seamless stainless steel tube</li> <li>• Tube outer diameter: 3/4 in.</li> <li>• Tube wall thickness: 0.65 in.</li> <li>• Allowable working pressure: 227 bar</li> </ul>	Swagelok®
Silicon carbide	To dilute the catalyst to prevent the formation of heat spots in the reaction regime	<ul style="list-style-type: none"> <li>• Form: powder</li> <li>• Mesh particle size: 200-450 mesh</li> <li>• Melting Point: 2700 °C (lit.)</li> <li>• Density: 3.22 g/ml at 25 °C (lit.)</li> </ul>	Sigma Aldrich®
Temperature Controller	To control the temperature in different experimental zones	<ul style="list-style-type: none"> <li>• Vertex VT4810</li> <li>• Microprocessor based Control loop feedback mechanism system</li> <li>• Featured with auto PID tuning</li> </ul>	Vertex®
Coolant Liquid	Added to the water of water bath to lower the freezing point	<ul style="list-style-type: none"> <li>• Advanced antifreeze</li> <li>• Effective down to -34 °C</li> <li>• Water/coolant ratio 50:50</li> </ul>	Diall®

### ***3.2.2 Measurement of hydrogenation activity***

A protocol was defined to govern the F-T experimental procedures including reactor loading, catalyst activation and hydrogenation process; so that it would enable the comparison of the results for different experiments. The protocol was followed for all the experiments including catalyst characterization and optimisation experiments. The following are the different procedures in running the F-T experiments.

#### ***3.2.2.1 Loading of the reactor***

The conversions of reactants in exothermic heterogeneous catalytic reactions are greatly influenced by diluters due to the difference in catalyst and inert particles' distributions in laboratory and industrial scale chemical processes [123]. The dilution of a solid catalyst (in this case powder) with an inert diluent (silicon carbide) is a common practice in the laboratory scale F-T process to make the heat removal more easier as well as for effective use of the catalyst bed [124]. For this purpose, for each experiment, 2 g of the pre-calcined catalyst was weighted and then diluted with 12 g of inert silicon carbide (mesh particle size 200-450), in order to improve the temperature distribution along the catalytic beds and minimize the formation of heat spots. The weighted amount of the catalyst and diluter were mixed until smooth together. Smaller diluent particles prevent catalyst particles moving down along the reactor. The catalyst beds were packed using glass beads (3 mm diameter) and glass wool. To load the catalyst into the reactor, the reactor tube was placed in upside down in the vice. A clamp was used to hold the reactor tube. First of all, glass beads were inserted at the top of the reactor in the pre-heating zone, then insulating glass wool was loaded to avoid movement of the glass beads. The reactor was loaded with the pre-mixed catalyst with diluent materials.

After the catalyst was loaded, a thick layer of glass wool was inserted at the bottom side of the catalytic bed to keep it at the specified position. Then the glass beads were added to fill the remaining space of the reactor. As different catalysts have different densities, the length of the catalytic bed was varied slightly for different loading in the characterization experiments.

### 3.2.2.2 *Start-up procedures of F-T experiments*

Prior to the catalyst activation, the samples were purged to completely remove the water vapour as well as other impurities. This action was performed by passing nitrogen gas for 2 hours at 413 K and atmospheric pressure. The entering volumetric flow rate of nitrogen per weight of the catalytic bed was 4.2 NL/h.g<sub>cat</sub>. The catalyst bed's temperature was increased from ambient temperature to 413 K and the ramp rate of the temperature was about 3.3 K/min. Afterwards, the catalysts were reduced *in situ* based on the TPR profile obtained from a chemisorption analyser in three different steps [66]. After completing the purging step, the reactor temperature was cooled down to 333 K to begin the catalyst activation step. The nitrogen gas line was closed and the reduction was begun by flowing pure hydrogen (zero grades) through the samples starting at 333 K. While the hydrogen gas was flowing, the bed temperature was increased linearly with time to 473 K and held for 1 h. The ramp rate of the temperature was 3.3 K/min at this reduction step. Then the temperature was ramped to 613 K and held for 1 h (temperature ramping: 2.5 K/min). The final temperature ramping was targeted to 723 K with the rate of about 2 K/min and the catalysts were held at this condition for 14 h with a volumetric hydrogen flow rate of 3.6 NL/h.g<sub>cat</sub>. The flow rate was the same for all three reduction steps. The hydrogen space velocity was adjusted too high to avoid the catalyst sintering by removing the produced water. After the reduction, the samples were

flushed with nitrogen while the temperature was lowered to 443 K. The temperature reducing step lasted about 40 minutes. The temperature was adjusted lower than the F-T reaction temperature, to prevent temperature run-away and catalyst de-activation during the F-T reaction start-up. After the preparation steps, the F-T reaction conditions were established one after another. The synthesis gas was then introduced into the reactor and the system was pressurized to the desired pressure to perform the F-T process. The syngas inlet flow rate was 4.2 NI/h.g<sub>cat</sub>. During the system pressurizing, the bed temperature was increased by about 4 °C to 8 K for different experiments. Afterwards, the bed temperature was adjusted based on the different experiment conditions. The temperature was increased to the reaction temperature very slowly to prevent temperature runaway and catalyst deactivation. The F-T activity was started after the inlet flow rate was regulated to the desired reaction space velocity. The catalytic performances were considered as a function of time on stream for 12 h.

### ***3.2.2.3 Liquid and gas products analyses***

A modified AVL Digas<sup>TM</sup> 440 instrument was used to monitor the changes in concentration of carbon monoxide and carbon dioxide production (shown in Figure 3.17(a)). The diagnostic module (AVL DiOBD 820) of the device was calibrated by the Company before the experiments so that it would be able to detect the carbon monoxide (measurement range: 0 – 20 vol%), carbon dioxide (measurement range: 0 – 20 vol%), oxygen (measurement range: 0 – 22 vol%), NO<sub>x</sub> (measurement range: 0 – 5000 ppm) and HC (0 – 20000 ppm). The device was an emission test module; hence the configuration was modified to be operated at low flow rate as well as being able to measure the carbon monoxide at a higher concentration. Figure 3.17(b) indicates the reading of the mentioned compounds during one of the experiments. The

readings were carried out at ambient conditions (pressure: atmospheric, temperature: 15-20 °C). The effluent gaseous products were analysed for C<sub>1</sub> to C<sub>8</sub> hydrocarbons employing a HP<sup>®</sup> 5890 gas chromatograph equipped with a Flame Ionisation Detector (FID) (Figure 3.17(J)) and Pora-Plot Q column to separate hydrocarbons. 250 µL of the sample was injected into the GC using helium as carrier gas. The initial oven temperature was adjusted at 278 K while the temperature was ramped at 7.5 K/min to reach 498 K and then held for 8 minutes. The detector temperature was set at 593 K. Quantitative analysis was carried out to measure the concentration of different compounds in the sample gas. Prior to each experiment, the standard sample gases listed in Table 3.6 with known concentrations were injected into the instrument. The standard samples' peak retention time (appearance time) and areas were compared to the test sample to calculate the concentration of different constituents of the test gas. Figure 3.18 indicates the GC pattern of standard gas analysed by GC-FID. The areas under each of the peaks are proportional to the amount of each compound that was passed the detector. Liquid hydrocarbon products were collected in a cold trap cooled externally at 283 K using a counter current heat exchanger. The product distributions were analysed off-line -

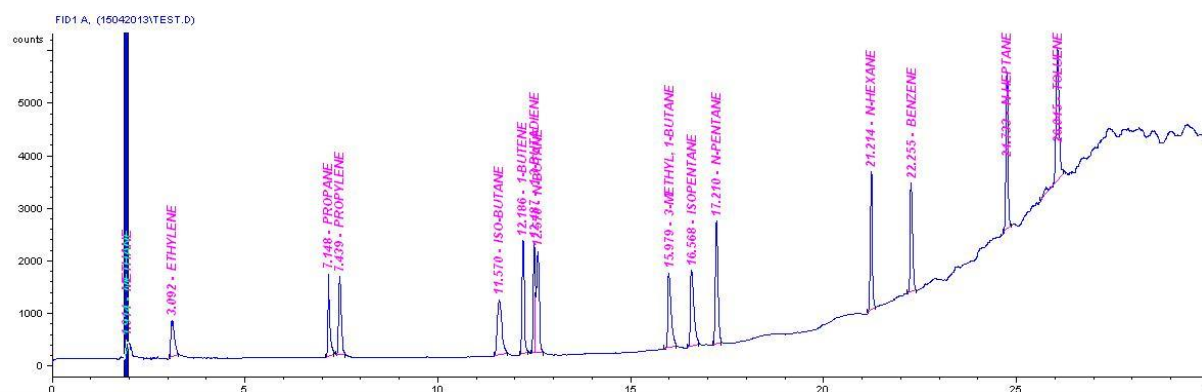


**Figure 3.18:** GC chromatogram of standard gas (image directly taken from HP<sup>®</sup> 5890 software), the time taken for lighter hydrocarbons to travel through the column to the detector are shorter

**Table 3.6:** Different constituent of standard gas bottle for quantitative analysis of gaseous products

<b>Component</b>	<b>Molecular Formula</b>	<b>Retention Time</b>	<b>Area</b>	<b>PPM</b>
<b>Methane</b>	CH <sub>4</sub>	1.932	3009.6	50.4
<b>Ethylene</b>	C <sub>2</sub> H <sub>4</sub>	3.097	4829.5	50.5
<b>Ethane</b>	C <sub>2</sub> H <sub>6</sub>	3.501	5199	50.5
<b>Propene</b>	C <sub>3</sub> H <sub>6</sub>	7.15	7067.8	50.4
<b>propane</b>	C <sub>3</sub> H <sub>8</sub>	7.44	7431.8	50.4
<b>Isobutane</b>	C <sub>4</sub> H <sub>10</sub>	11.571	9100.8	50.4
<b>1 - butane</b>	C <sub>4</sub> H <sub>10</sub>	12.187	9523.1	50.4
<b>1,3-Butadiene</b>	C <sub>4</sub> H <sub>6</sub>	12.488	7468.5	50.4
<b>n-butane</b>	C <sub>4</sub> H <sub>10</sub>	12.57	9675.1	50.4
<b>3-Methyl 1-butene</b>	C <sub>5</sub> H <sub>8</sub>	15.98	9574.3	49.9
<b>Iso-pentane</b>	C <sub>5</sub> H <sub>12</sub>	16.568	10133.7	49.9
<b>n-pentane</b>	C <sub>5</sub> H <sub>12</sub>	17.211	10202.9	49.9
<b>n-hexane</b>	C <sub>6</sub> H <sub>14</sub>	21.215	10744.5	49.9
<b>Benzene</b>	C <sub>6</sub> H <sub>6</sub>	22.257	9405.35	49.9
<b>n-heptane</b>	C <sub>7</sub> H <sub>16</sub>	24.734	12125.6	49.8
<b>Toluene</b>	C <sub>7</sub> H <sub>8</sub>	26.045	12801.9	49.9

- employing a DB1 column combined with Gas chromatography-mass spectrometry (GC-MS) PerkinElmer shown in Figure 3.16(a). A 1  $\mu$ L portion of each sample containing the mixture of gasoline, diesel and waxes was injected into the GC with a split ratio of 34:1. Non-reactive inert helium gas was used to carry the gases' samples through the instrument. The injection port was heated to 573 K; the oven temperature was increased at 8 K/min from 303 K to 493 K and held at this temperature for 5 minutes. For liquid samples, the qualitative analysis was performed to identify the constituents (elements of functional groups).

### 3.2.2.4 Reactor performance characterization

In this section, some intensive dimensionless quantities are expressed to characterize the operation of the F-T reactor and present the methods used for reactor performance measurement and analysis. The conversion of reactant A in a plug flow reactor operating at steady state is defined by Equation 3.14 [125],

$$f_{A_{out}} = \frac{\text{Rate reactant A is consumed in the system}}{\text{Rate reactant A is fed to the system}} = \frac{F_{A_{in}} - F_{A_{out}}}{F_{A_{in}}} \quad (3.14)$$

The conversion is related to the composition of the reactant and was defined only for carbon monoxide; which by definition has a value between 0 and 1. Therefore, Equation 3.15 was employed to quantify the fraction of carbon monoxide that has been consumed in the F-T reactor. The conversion only depends on the boundaries of the system, “in” and “out” [66]. It should be mentioned that the conversion was not defined on the basis of any particular F-T reaction in which multiple co/main reactions take place. It is important to note that none of the reactions in the F-T synthesis process produce carbon monoxide.

$$X_{CO} \text{ (CO Conversion \%)} = \frac{\text{moles of inlet CO} - \text{moles of outlet CO}}{\text{moles of inlet CO}} \times 100 \quad (3.15)$$

Various simultaneous chemical reactions take place in F-T synthesis producing both desired and undesired products. Product selectivity expresses the amount of product V produced when reactant A is consumed within the desirable chemical reaction [125].

$$\sigma_V(t) \equiv \left( \begin{array}{c} \text{Stoichiometric} \\ \text{factor} \end{array} \right) \frac{\text{Rate product V is formed in the reactor}}{\text{Rate reactant A is consumed in the reactor}} \quad (3.16)$$

Hence, Equations 3.17-19 were used to measure the portion of reactant converted to desired and undesired products in the F-T process. Since the carbon dioxide is the only co-product which consumed the carbonaceous reactant to be produced, Equation 3.18 was defined to quantify the amount of this by-product produced relative to the amount of carbon monoxide consumed when reacted within the WGS reaction.

$$S_{CO_2} (CO_2 \text{ selectivity } \%) = \frac{\text{moles of } CO_2 \text{ produced}}{\text{moles of inlet } CO - \text{moles of outlet } CO} \times 100 \quad (3.17)$$

$$S_{x(1-4)} \% = \frac{\text{moles of } C_x \text{ produced}}{(\text{moles of } CO_{in} - \text{moles of } CO_{out}) - \text{moles of } CO_{2\text{produced}}} \times 100 \quad (3.18)$$

In Equation 3.18, the desired products' selectivity was determined relative to the amount of carbon monoxide reactant converted to hydrocarbon products; hence, in the denominator the moles of carbon monoxide converted to carbon dioxide were subtracted. The numerical values of products' selectivity are between 0 to 100 % based on their definitions. The summation of all products' selectivity must be equal to 100 %.

Equation 3.19 describes how to determine the selectivity of the heavy hydrocarbons (carbon number  $\geq 5$ ). As some of the compounds in the standard gas bottle used for quantitative analysis of gaseous products by GC-FID were not available, the measurement of the quantities of particular constituents presented in the gaseous products downstream of the reactor was not possible; therefore the product selectivity of detailed hydrocarbons were measured up to hydrocarbons with a carbon number  $\leq 4$ .

$$S_{5+} = 100 - S_{C_1} - S_{C_2} - S_{C_3} - S_{C_4} \quad (3.19)$$

### 3.2.3 Design of Experiments (DOE), the Taguchi method

In this study, the Taguchi method involving an orthogonal array [126] was applied to design an experiment in which different influential parameters (temperature, pressure and space velocity) were organized, for investigating the effect of each of them in process optimisation and also reduce the variation with considering a reliable Design of Experiment. The main advantage of this method is that it allows estimating the significant effects with a minimum number of experimental runs. Hereupon, many different parameters could be analysed without any preventative factors (e.g. high number and subsequently cost of experiments). In addition, the closest mean performance characteristics' value to the target value is emphasize in the Taguchi method, rather than a value within certain specification limits [127]. The objectives of the experiments are to achieve the optimum condition of liquid fuel production as well as a cost effective process in a single pass F-T operation. For this purpose, the effort was made to reach the highest conversion and product selectivity in a single pass F-T process with maximum precursor loading and utilization of support surface area.

Two different optimization studies were performed at low and medium pressure F-T reaction conditions. For low pressure optimisation study (temperature (T factor): 503 – 528 K, pressure (P factor): 2 – 10 bar, WHSV (W factor): 2.4 – 3.6NL/h.  $g_{catalyst}$ ), three operating factors in three levels were considered in an  $L_9$  orthogonal array; the Taguchi method with nine runs. Table 3.7 summarizes the list of different factors and control levels. For optimisation study at medium range pressure reaction conditions (temperature: 503 – 543 K, pressure: 10 – 25 bar, WHSV: 1.8 – 3.6NL/h.  $g_{catalyst}$ ), three operating factors in four levels were considered in an  $L_{16}$  orthogonal array; the Taguchi method with 16 runs. Table 3.7 summarizes the list of factors and different control levels for this study as well.

**Table 3.7:** Control factors and levels for different optimisation studies at different pressure conditions

Parameters	Low pressure reaction conditions			Medium pressure reaction conditions			
	Control levels			Control levels			
	Level 1	Level 2	Level 3	Level 1	Level 2	Level 3	Level 4
T (K)	503	518	528	503	518	528	543
P (bar)	2	6	10	10	15	20	25
W (NI/h.g <sub>cat</sub> )	2.4	3.0	3.6	1.8	2.4	3.0	3.6

Table 3.8 indicates the experimental layout derived by orthogonal arrays and factor settings.

**Table 3.8:** Factor settings for Taguchi L<sub>9</sub> design (left) for optimisation study at low pressure F-T reaction conditions and Taguchi L<sub>16</sub> design (right) for optimization study at high pressure F-T reaction conditions

DOE for low-pressure reaction conditions				DOE for medium-pressure reaction condition			
Exp Run	T	P	W	Exp Run	T	P	W
EXP01	503 <sub>(1)</sub>	2 <sub>(1)</sub>	2.4 <sub>(1)</sub>	EXP01	503 <sub>(1)</sub>	10 <sub>(1)</sub>	1.8 <sub>(1)</sub>
EXP02	503 <sub>(1)</sub>	6 <sub>(2)</sub>	3.0 <sub>(2)</sub>	EXP02	503 <sub>(1)</sub>	15 <sub>(2)</sub>	2.4 <sub>(2)</sub>
EXP03	503 <sub>(1)</sub>	10 <sub>(3)</sub>	3.6 <sub>(3)</sub>	EXP03	503 <sub>(1)</sub>	20 <sub>(3)</sub>	3.0 <sub>(3)</sub>
EXP04	518 <sub>(2)</sub>	2 <sub>(1)</sub>	3.0 <sub>(2)</sub>	EXP04	503 <sub>(1)</sub>	25 <sub>(4)</sub>	3.6 <sub>(4)</sub>
EXP05	518 <sub>(2)</sub>	6 <sub>(2)</sub>	3.6 <sub>(3)</sub>	EXP05	518 <sub>(2)</sub>	10 <sub>(1)</sub>	2.4 <sub>(2)</sub>
EXP06	518 <sub>(2)</sub>	10 <sub>(3)</sub>	2.4 <sub>(1)</sub>	EXP06	518 <sub>(2)</sub>	15 <sub>(2)</sub>	1.8 <sub>(1)</sub>
EXP07	528 <sub>(3)</sub>	2 <sub>(1)</sub>	3.6 <sub>(3)</sub>	EXP07	518 <sub>(2)</sub>	20 <sub>(3)</sub>	3.6 <sub>(4)</sub>
EXP08	528 <sub>(3)</sub>	6 <sub>(2)</sub>	2.4 <sub>(1)</sub>	EXP08	518 <sub>(2)</sub>	25 <sub>(4)</sub>	3.0 <sub>(3)</sub>
EXP09	528 <sub>(3)</sub>	10 <sub>(3)</sub>	3.0 <sub>(2)</sub>	EXP09	528 <sub>(3)</sub>	10 <sub>(1)</sub>	3.0 <sub>(3)</sub>
				EXP10	528 <sub>(3)</sub>	15 <sub>(2)</sub>	3.6 <sub>(4)</sub>
				EXP11	528 <sub>(3)</sub>	20 <sub>(3)</sub>	1.8 <sub>(1)</sub>
				EXP12	528 <sub>(3)</sub>	25 <sub>(4)</sub>	2.4 <sub>(2)</sub>
				EXP13	543 <sub>(4)</sub>	10 <sub>(1)</sub>	3.6 <sub>(4)</sub>
				EXP14	543 <sub>(4)</sub>	15 <sub>(2)</sub>	3.0 <sub>(3)</sub>
				EXP15	543 <sub>(4)</sub>	20 <sub>(3)</sub>	2.4 <sub>(2)</sub>
				EXP16	543 <sub>(4)</sub>	25 <sub>(4)</sub>	1.8 <sub>(1)</sub>

To examine the effect of each of the variables on the output, the Signal-to-Noise ratio (SN) was calculated for each experiment with respect to various responses conducted [128]. Equation 3.20 indicates the formula employed to determine the target value of the performance characteristics. In this equation,  $y_i$  is the mean value (value of performance characteristics for an experiment) and  $S_i$  is the variance.

$$SN_i = 10 \log \frac{\bar{y}_i^2}{S_i^2} \quad (3.20)$$

Where,

$$\bar{y}_i = \frac{1}{N_i} \sum_{u=1}^{N_i} y_{i,u} \quad (3.21)$$

$$S_i^2 = \frac{1}{N_i - 1} \sum_{u=1}^{N_i} (y_{i,u} - \bar{y}_i)^2 \quad (3.22)$$

$i = \text{Experiment number}$

$u = \text{Trial number}$

$N_i = \text{Number of trials for experiment } i$

The Signal-to-Noise ratio derived from above equation depends on the criterion for the quality characteristics to be optimised. For the case of minimising the performance characteristic (smaller-is-better quality characteristic), the data sequences were pre-processed as per Equation 3.23:

$$SN_i = -10 \log \left( \sum_{i=1}^n \frac{(1/y_i^2)}{n} \right) \quad (3.23)$$

The data sequences for higher-the-better performance characteristics were pre-processed as Equation 3.24 to maximise the performance characteristic by the following definition of the SN ratio:

$$SN_i = -10 \log \left( \sum_{i=1}^n \frac{y_i^2}{n} \right) \quad (3.24)$$

One-way Analysis of Variance (ANOVA) was performed to determine the influence of any given control factors affecting output values [128]. The effect of input parameters (in this study: T parameter (temperature), P parameter (pressure) and W parameter (space velocity)) are determined from a series of experimental results by designing the experiments for the Fischer-Tropsch synthesis process. A comprehensive interpretation of the experimental data could be achieved by employing ANOVA analysis [129].

The deviation of the experimental data from the mean value of the data is measured by using the Sum of Squared (SS) expressed in Equation 3.25. This equation represents the total variation ( $SS_{total}$ ).

$$SS_{total} = \sum_{ij=1}^n (X_{ij} - \bar{X})^2 \quad (3.25)$$

Where  $\bar{X}$  represents the grand mean which is calculated by  $\bar{X} = \sum x/N$ . Equation 3.25 measures the SS of all the observations, regardless of which treatment produced them from the grand mean. The deviation of the means of groups ( $X_j$ ) from the grand mean ( $\bar{X}$ ) is calculated by using Equation 3.26 which represents the Sum of Squares ( $SS_{treat}$ ).

$$SS_{treat} = n \sum_{j=1}^n (X_j - \bar{X})^2 \quad (3.26)$$

The sum over the sums of squared deviations of scores around their group's mean is measured by using Equation 3.27. The  $SS_{error}$  also is obtained from subtraction of  $SS_{total}$  from  $SS_{treat}$  ( $SS_{error} = SS_{total} - SS_{treat}$ ) expressed in Equation 3.28.

$$SS_{error} = \sum_{ij=1}^n (X_{ij} - \bar{X}_j)^2 \quad (3.27)$$

$$SS_{error} = SS_{total} - SS_{treat} \quad (3.28)$$

Degree of Freedom ( $f$ ) is the measure of the amount of information that can be uniquely determined from a given set of data. Degree of freedom for data concerning a factor equals one less than the number of levels [128]. The data distribution about the data mean is measured by variance. The variance is measured by division of sum of squared over DOE of each factor.

$$V \text{ (Variance)} = \frac{\text{Sum of Squared}}{\text{Degree of Freedom}} = \frac{SS}{f} \quad (3.29)$$

Table 3.9 represents the generalized format of the Analysis of Variance table. This table summarizes the Sum of Squared ( $SS$ ), Degree of Freedom ( $f$ ), Mean Squares ( $MS$ ) as well as variance ratio ( $F$ ). The variance ratio (generally called  $F$  statistic) is employed to determine the importance of the factor under study with respect to all the factor's variance. To interpret the variation percentage in a response variable, Equation 3.30 is used to apportion the total Sum of Squares ( $SS_{total}$ ) between different sources of variable within the ANOVA technique.

$$R^2 \text{ (R - squared)}(\%) = \left(1 - \frac{SS_{error}}{SS_{total}}\right) \times 100 \quad (3.30)$$

**Table 3.9:** Analysis of Variance (ANOVA) table

Source	Sum of Squares ( $SS$ )	Degree of Freedom ( $f$ )	Variance (Mean Squares)	$F$ ratio
<b>Treat</b>	$SS_{treat}$	$K - 1$	$MS_{treat} = \frac{SS_{treat}}{K - 1}$	$\frac{MS_{treat}}{MS_{error}}$
<b>Error</b>	$SS_{error}$	$N - K$	$MS_{error} = \frac{SS_{treat}}{K - 1}$	
<b>Total</b>	$SS_T = SS_{treat} + SS_{error}$	$N - 1$		

**K:** number of factor levels (Taguchi  $L_9$  ( $3^{**3}$ ) = 3, Taguchi  $L_{16}$  ( $3^{**4}$ ) = 4)

**N:** number of trials (Taguchi  $L_9$  ( $3^{**3}$ ) = 9, Taguchi  $L_{16}$  ( $3^{**4}$ ) = 16)



---

# Chapter 4

---

## EFFECT OF SUPPORT VARIABLES ON CATALYTIC PERFORMANCE

In the present chapter, the effect of the silica supports' texture on the physicochemical characteristics of cobalt catalysts was considered by utilizing X-ray Fluorescence (XRF) analysis, nitrogen-sorption analysis, X-ray Diffraction (XRD) and Scanning Electron Microscopy (SEM) fixed with Energy Dispersive X-Ray Spectroscopy (EDS) experiments. The activity and selectivity of in-house prepared Co/SiO<sub>2</sub> catalysts were examined in the Fischer-Tropsch Synthesis process by using a mini-single channel downdraft fixed-bed reactor. Different observations regarding the interaction of a cobalt catalyst and silica support were reported in the previous works. This study concentrated on the influence of high cobalt loading using ethanol solution over dissimilar porous supports.

#### 4.1 X-ray Fluorescence (XRF) analysis of Si and Co in derived catalysts

The XRF technique was applied to analyse the oxide particles and Co/Si contents in the prepared supported catalysts. Table 4.1 shows the analytical results of the quantified and normalized elemental and oxide compositions of Co/Si and CoO/SiO<sub>2</sub> respectively. Figures 4.1-4.4 indicate the typical wavelength dispersive X-ray Fluorescent spectrums of CAT-Q-3, CAT-Q-6, CAT-Q-10 and CAT-Q-30 respectively in the vicinity of Co K<sub>α</sub>, Co K<sub>β</sub>, Co L<sub>β</sub>, Si K<sub>α</sub> and Si K<sub>β</sub>. The transition of an electron from “L” shell to the innermost “K” shell results in an emission line of K<sub>α</sub>; K<sub>β</sub> is the result when an electron transitions from “M” shell to “K” shell and likewise, the M→L transition of electrons is called L<sub>α</sub>. Each of these connecting transitions from initial to final orbitals yields a fluorescence photon with characteristics’ energy. The values of different transition energies for different elements are provided by the National Institute of Standards and Technology (NIST) X-ray Transition Energy database [130]. In Figures 4.1-4.4 the x-axis shows the value of transition energies in which the peak positions specify the type of element. The Y-axis indicates the amount an element existing in the sample.

**Table 4.1:** Analytical results for Co and Si acquired by XRF in prepared supported cobalt catalysts

Catalysts	Elemental compositions		Oxide compositions	
	Si (%)	Co (%)	SiO <sub>2</sub> (%)	CoO (%)
<b>CAT-Q-3</b>	61.70	36.03	77.6	20.2
<b>CAT-Q-6</b>	62.61	36.54	78.8	20.4
<b>CAT-Q-10</b>	62.51	35.75	78.6	19.7
<b>CAT-Q-30</b>	63.06	34.94	79.4	19.6

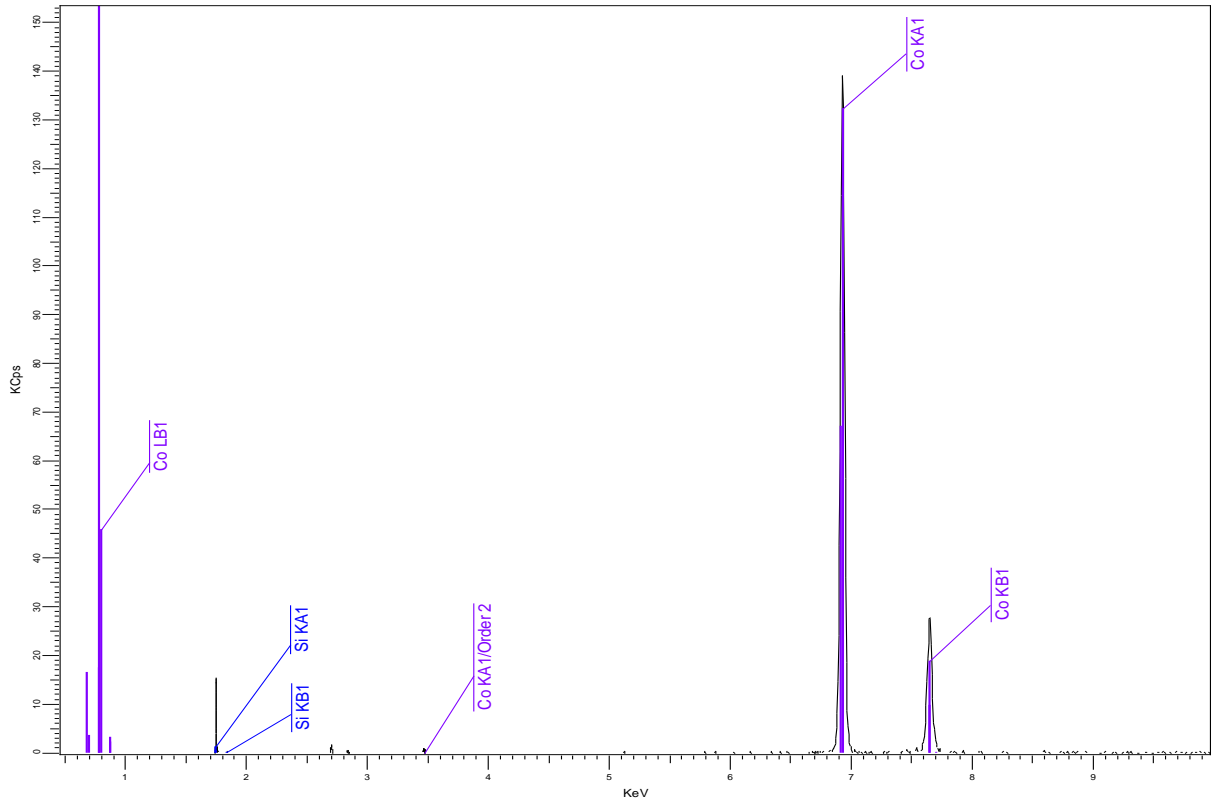


**Figure 4.1:** X-ray Fluorescent spectra of CAT-Q-3 in the vicinity of Co  $K_{\alpha}$ , Co  $K_{\beta}$ , Co  $L_{\beta}$ , Si  $K_{\alpha}$  and Si  $K_{\beta}$

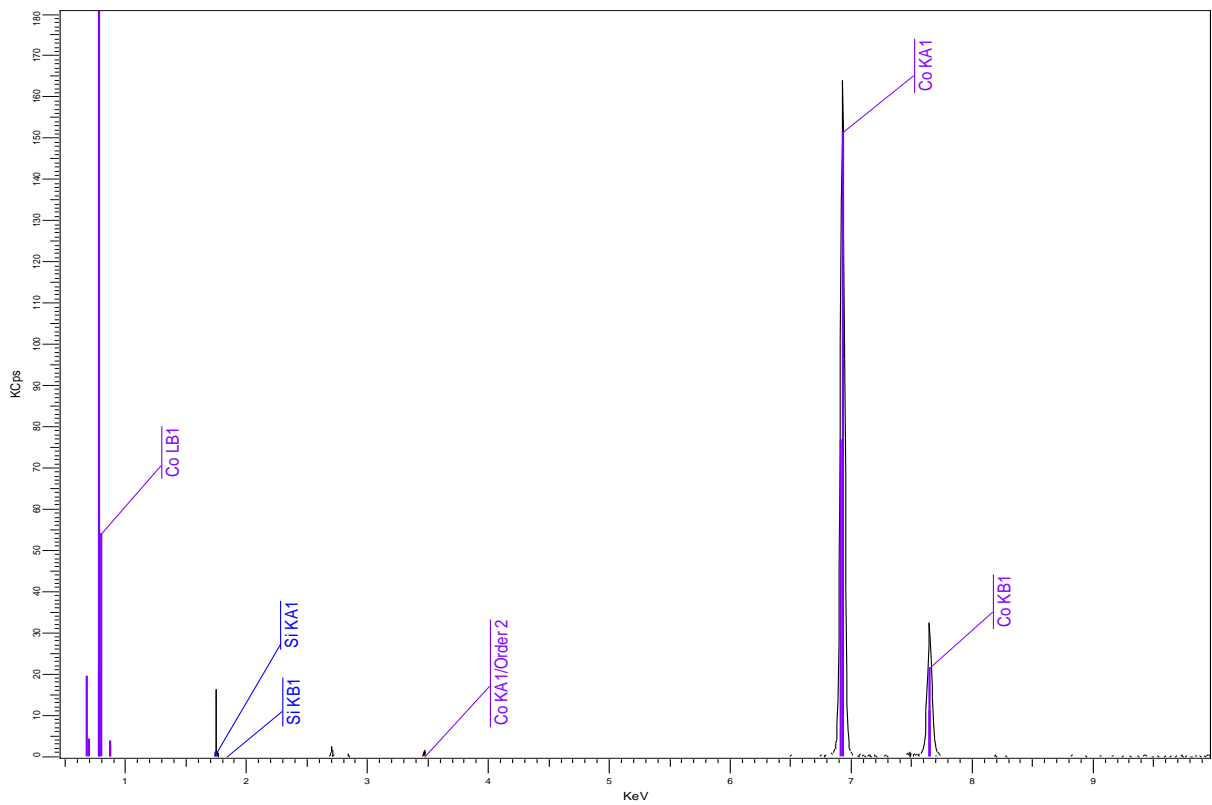


**Figure 4.2:** X-ray Fluorescent spectra of CAT-Q-6 in the vicinity of Co  $K_{\alpha}$ , Co  $K_{\beta}$ , Co  $L_{\beta}$ , Si  $K_{\alpha}$  and Si  $K_{\beta}$

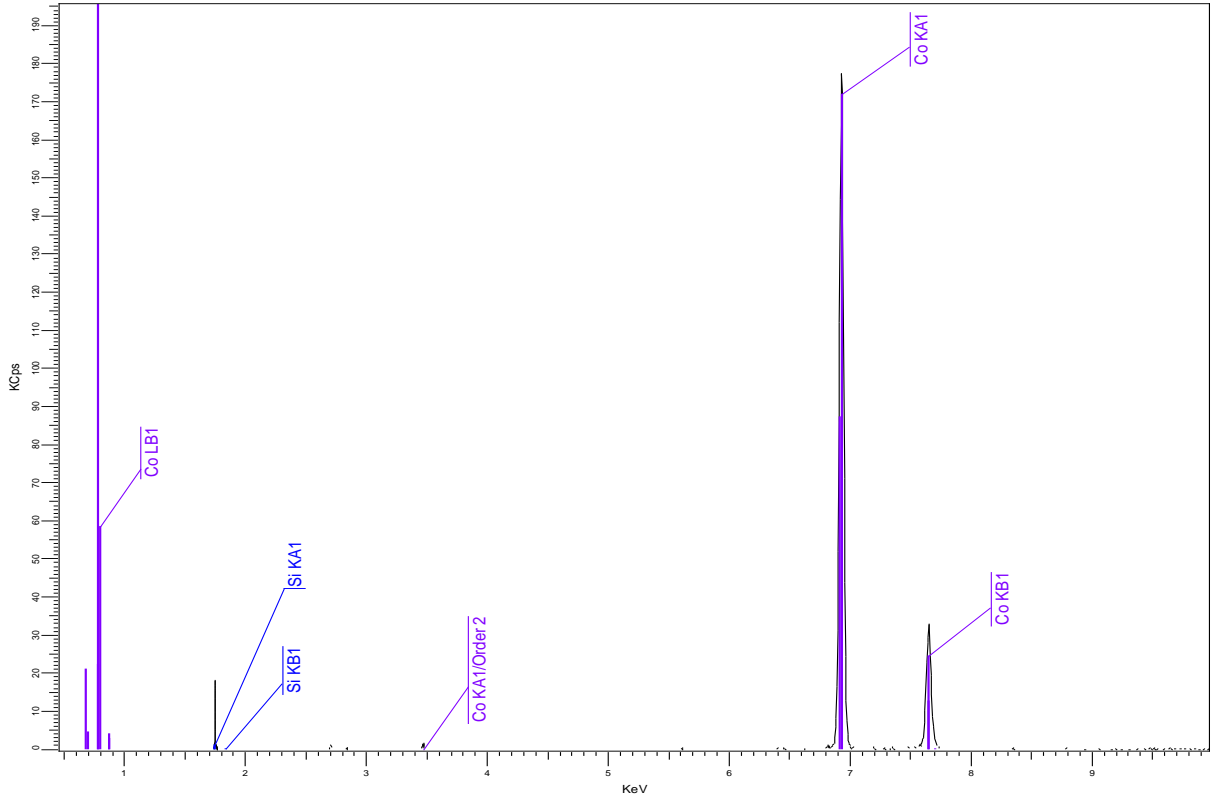


**Figure 4.3:** X-ray Fluorescent spectra of CAT-Q-10 in the vicinity of Co  $K_{\alpha}$ , Co  $K_{\beta}$ , Co  $L_{\beta}$ , Si  $K_{\alpha}$  and Si  $K_{\beta}$

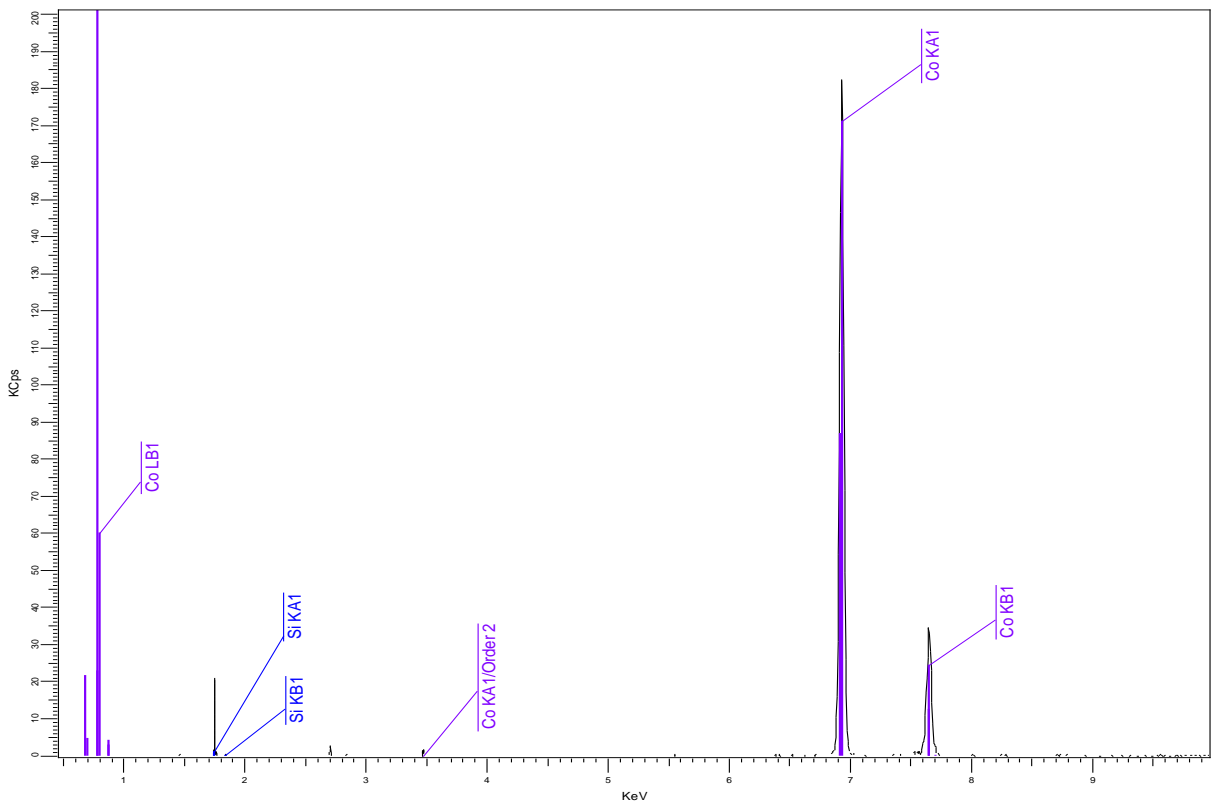


**Figure 4.4:** X-ray Fluorescent spectra of CAT-Q-30 in the vicinity of Co  $K_{\alpha}$ , Co  $K_{\beta}$ , Co  $L_{\beta}$ , Si  $K_{\alpha}$  and Si  $K_{\beta}$

## 4.2 Nitrogen physisorption measurements

The measurements of the catalyst's surface area and porosity were carried out by nitrogen physisorption analysis. The BET multi-layer equation (Equation 3.1) was used to calculate the mono-layer sorption values for different catalysts. These data were used to obtain the specific surface area. During the experiments, both adsorption and desorption of the nitrogen were recorded. Table 4.2 lists different variables used to perform the BET surface area analysis to evaluate the total surface area of the catalysts. The nitrogen adsorption/desorption measurement results for supports and catalysts are listed in Table 4.3. This table shows the single-point estimation of the pore capacity of the catalysts and the support's materials for total pore volume as well as pore diameter. The results of surface area and pore volume for the supports were well matched with those provided by the company.

It is clear that the support's pore diameter is increased with the decreasing of the surface area. The highest pore size was reported for the catalyst with the lowest surface area (CAT-Q-30); while the lowest pore diameter was seen for the catalyst with the highest surface area (CAT-Q-3). As shown in Table 4.3, the surface area and the average pore volume for all the catalysts are decreased. This is due to the impregnation, drying and calcination process utilized in the preparation steps. The reduction in the surface area and pore volume ranged from 16.16% to 31.56% and from 13.92% to 33.33% respectively. A slight decrease in the surface area of catalysts CAT-Q-10 and CAT-Q-30 were observed; while significant reductions were reported for CAT-Q-3 and CAT-Q-6. The only unexpected trends corresponded to the increase in the average pore diameter of CAT-Q-6 and CAT-Q-30 after deposition of cobalt metal. These could be related to the 16.16% reduction in the CAT-Q-6 surface area as well as the 31.285% reduction for CAT-Q-30.

**Table 4.2:** Variables derived from nitrogen physisorption to measure the total surface area

CAT-Q-3			CAT-Q-6		
<b>Slope (S g/cm<sup>3</sup> STP)</b>	0.009069		<b>Slope (S g/cm<sup>3</sup> STP)</b>	0.009206	
<b>Y-intercept (i g/cm<sup>3</sup> STP)</b>	0.000048		<b>Y-intercept (i g/cm<sup>3</sup> STP)</b>	0.000118	
<b>BET Constant (C<sub>BET</sub>)</b>	189.041603		<b>BET Constant (C<sub>BET</sub>)</b>	79.023024	
<b>V<sub>ml</sub> (cm<sup>3</sup>/g STP)</b>	109.682532		<b>V<sub>ml</sub> (cm<sup>3</sup>/g STP)</b>	107.253735	
<b>Adsorbate Cross-section (nm<sup>2</sup>)</b>	0.1620		<b>Adsorbate Cross-section (nm<sup>2</sup>)</b>	0.1620	
<i>P/P<sub>0</sub></i>	<i>V<sub>ads</sub></i> (cm <sup>3</sup> /g STP)	$\frac{P/P_0}{V_{ads}(1 - P/P_0)}$	<i>P/P<sub>0</sub></i>	<i>V<sub>ads</sub></i> (cm <sup>3</sup> /g STP)	$\frac{P/P_0}{V_{ads}(1 - P/P_0)}$
0.057245935	106.3268	0.000571	0.057978678	94.8481	0.000649
0.076400349	111.4464	0.000742	0.077817923	100.9122	0.000836
0.119108392	120.4488	0.001123	0.116780277	110.6055	0.001195
0.160907435	127.6668	0.001502	0.158953390	119.5666	0.001581
0.197456113	133.3252	0.001845	0.197316912	127.1328	0.001934
CAT-Q-10			CAT-Q-30		
<b>Slope (S g/cm<sup>3</sup> STP)</b>	0.019070		<b>Slope (S g/cm<sup>3</sup> STP)</b>	0.056430	
<b>Y-intercept (i g/cm<sup>3</sup> STP)</b>	0.000203		<b>Y-intercept (i g/cm<sup>3</sup> STP)</b>	0.000291	
<b>BET Constant (C<sub>BET</sub>)</b>	95.00675		<b>BET Constant (C<sub>BET</sub>)</b>	194.984492	
<b>V<sub>ml</sub> (cm<sup>3</sup>/g STP)</b>	51.886338		<b>V<sub>ml</sub> (cm<sup>3</sup>/g STP)</b>	17.630083	
<b>Adsorbate Cross-section (nm<sup>2</sup>)</b>	0.1620		<b>Adsorbate Cross-section (nm<sup>2</sup>)</b>	0.1620	
<i>P/P<sub>0</sub></i>	<i>V<sub>ads</sub></i> (cm <sup>3</sup> /g STP)	$\frac{P/P_0}{V_{ads}(1 - P/P_0)}$	<i>P/P<sub>0</sub></i>	<i>V<sub>ads</sub></i> (cm <sup>3</sup> /g STP)	$\frac{P/P_0}{V_{ads}(1 - P/P_0)}$
0.057569098	46.9291	0.001302	0.060309883	17.2234	0.003726
0.079682113	50.1593	0.001726	0.077190605	17.9175	0.004668
0.118571037	54.6777	0.00246	0.118575169	19.4971	0.006900
0.160379606	58.6985	0.003254	0.161966823	20.5223	0.009418
0.199343249	62.0799	0.004011	0.198841592	21.4825	0.011553

**Table 4.3:** Textural characteristics of meso-macro porous silica supports and cobalt supported catalysts measured by nitrogen physisorption technique

Sample	Nitrogen adsorption/desorption		
	BET surface area (m <sup>2</sup> /g)	Average pore diameter (nm)	Pore volume (cm <sup>3</sup> /g)
CAT-Q-3	477.5	2.37	0.28
SUP-Q-3	697.6	2.39	0.42
CAT-Q-6	466.9	5.76	0.68
SUP-Q-6	556.9	4.96	0.79
CAT-Q-10	225.9	16.4	0.92
SUP-Q-10	277.4	17.2	1.20
CAT-Q-30	76.75	46.9	0.90
SUP-Q-30	111.7	42.9	1.20

### 4.3 X-Ray Diffraction (XRD) analysis

The crystallite size of the generated cobalt oxides over different support materials were measured from X-ray diffraction patterns obtained from a diffractometer. The XRD spectra of various catalysts after drying and the calcination process are illustrated in Figure 4.5. The presence of a spinal phase of Co<sub>3</sub>O<sub>4</sub> with 2θ values of 36.65, 38.44, 44.93, 65.46 and 78.80 were found in all of the diffractograms. The patterns clearly show that the narrow pore size based catalysts had a smaller crystallite size than those prepared over the wide pore based catalysts. The broad diffraction peak shown for the unreduced sample, CAT-Q-3 with weak signal detected at 2θ=36.65° is due to the presence of small Co<sub>3</sub>O<sub>4</sub> crystalline ( $d(\text{Co}_3\text{O}_4) = 9.4$  nm) formed over an essentially meso-porous silica support [131]. From Figure 4.5, it can be concluded that with an increase in the catalyst pore diameter, the detected peaks for spinal

$\text{Co}_3\text{O}_4$  crystallite become sharper, which corresponds to the larger particle sizes. Similar results have been reported by Ghampson et al [132]. The increase in cobalt content could result in an increase in the  $\text{Co}_3\text{O}_4$  mean particle size. This explains the fact that distinct peaks are presented in diffractograms of catalysts' crystallographic phases [133]. The application of highly dispersed nano-sized  $\text{Co}_3\text{O}_4$  clusters and formation of amorphous cobalt silicates are the reason that no diffraction signal can be observed from the diffractometer. It was reported that the large metal particles are formed through the interaction of supported cobalt species with vicinal silanols. The interactions of metal species with isolated silanols result in the formation of the smaller Co particles [134].

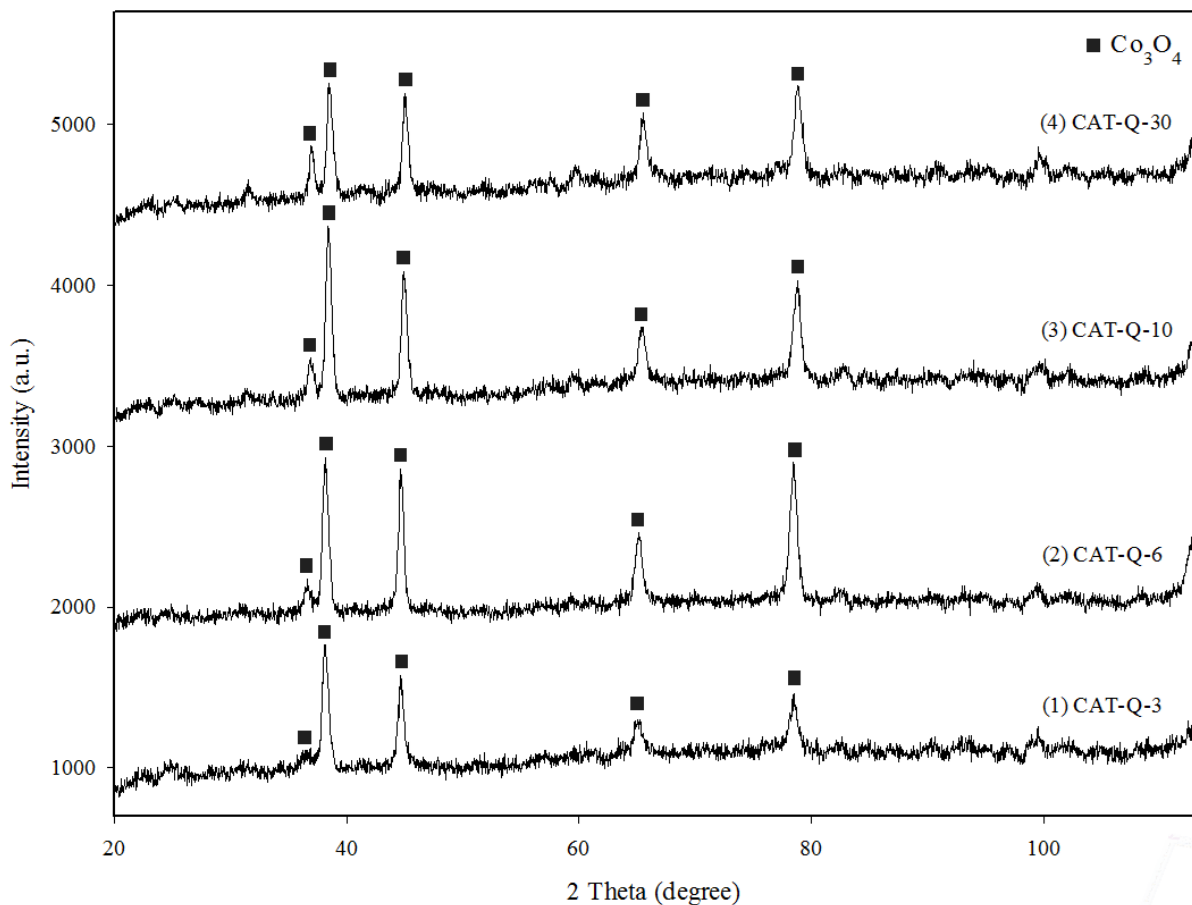


**Figure 4.5:** X-Ray diffraction spectrogram of different calcined and unreduced supported catalysts

**Table 4.4:** Average  $\text{Co}_3\text{O}_4$  crystallite size, estimated  $\text{Co}^0$  particle diameter and estimated cobalt dispersion for different supported catalysts

Sample	$\text{Co}_3\text{O}_4$ crystallite diameter (nm)	Estimated $\text{Co}^0$ particle diameter (nm)	Estimated cobalt dispersion %
CAT-Q-3	9.40	7.05	10.21
CAT-Q-6	13.63	10.22	7.043
CAT-Q-10	16.04	12.03	5.985
CAT-Q-30	22.74	17.05	4.221

The average crystallite sizes of oxidized cobalt calculated by using the Scherrer equation are listed in Table 4.4. It should be taken into account that the size of the metallic cobalt is proportional to its  $\text{Co}_3\text{O}_4$  crystallite size [135]. Holmen et al [136] derived the corresponding reducing factor to convert cobalt crystallite diameter to cobalt metal particle diameter in order to compare cobalt oxide particle size with metal dispersion. The resulting size reduction factor according to the relative molar volumes of cobalt crystallite and metallic cobalt is calculated by using Equation 4.1:

$$d(\text{Co}^0) = 0.75 \cdot d(\text{Co}_3\text{O}_4) \quad (4.1)$$

By assuming spherical uniform cobalt particles with site density of  $14.6 \text{ at/nm}^2$ , the related cobalt metal dispersion could be calculated by employing Equation 4.2:

$$D (\%) = 96/d_{\text{Co}_3\text{O}_4} \quad (4.2)$$

Where  $d$  is the average metal particle size (nm). Accordingly, the metal particle size and dispersion were estimated by employing the  $\text{Co}_3\text{O}_4$  crystallite diameter. The measurements for the cobalt metal particle size along with the cobalt particle dispersion are listed in Table

4.4. The average spherical crystalline size of  $\text{Co}_3\text{O}_4$  for the samples CAT-Q-3 and CAT-Q-6 were significantly larger than the meso-porous diameter ( $d_{(\text{Co}_3\text{O}_4)}(\text{CAT-Q-3}) = 9.4 \text{ nm}$  and  $d_{(\text{Co}_3\text{O}_4)}(\text{CAT-Q-6}) = 13.63 \text{ nm}$ ). This is due to the highly branched structure of silica support which enables the cobalt metals to be formed and interconnected to other neighbouring pores existing inside the silica support. This causes most of the cobalt particles to be placed on the external surface of the supports [137]. The larger crystallite size obtained from XRD measurements, compared to the catalyst pore diameter from the BJH method, could be attributed to other reasons. Some very small cobalt particles being missed in the XRD measurements, due to significant XRD line broadening and also the over-estimated measuring of the crystalline diameter, calculated by the Full Width at Half Maximum (FWHM), could be ascribed to this as well [58].

#### ***4.4 Micro-structural and morphological structure of the catalysts***

The SEM-EDS surface analysis was performed to evaluate the heterogeneity of the particle size as well as metal repartition over the surface of various catalysts. The representative SEM images of all the prepared catalysts are shown in Figures 4.6 to 4.9. In addition to the morphology of the catalysts, the cobalt mappings obtained from EDS micro-analysis have been represented in these figures as well, for each of the samples. The concentration of cobalt particles in the area-scan method are demonstrated in the white colour while the dark colour represents the silica support surface. The acquisition conditions for X-ray acquisition including livetime (140 s) as well as process times (5 out of 6) were selected for all scanning to enable the comparison between different samples.

**Table 4.5:** Elemental analysis of catalysts' surface by SEM-EDX to characterize metal content

Sample	Element (weight %)		Element (atomic %)	
	Si K	Co K	Si K	Co K
<b>CAT-Q-3</b>	59.76	40.24	75.70	24.30
<b>CAT-Q-6</b>	65.33	34.67	79.82	20.18
<b>CAT-Q-10</b>	63.24	36.76	78.31	21.69
<b>CAT-Q-30</b>	65.12	34.88	79.66	20.34
<b>Total</b>	100	100	100	100

For all of the catalysts, ploy-dispersed spherical particles were observed [138]. The figures exhibit that the metals are deposited on the external surface of the supports in the eggshell catalyst. The average cobalt contents over the catalysts' surface were measured by EDS in different spectrums over different samples. The results are listed in Table 4.5 which are in agreement with the overall cobalt content measured by the XRF machine. This is in case there were some deviations from the average metal content that were observed at different sides/spectrums. Despite having a higher metal content, the cobalt distribution appeared qualitatively uniform in CAT-Q-3 (shown in Figure 4.6 C). Figure 4.7 C illustrates that cobalts are properly deposited on the periodic meso-porous silica surface for the sample CAT-Q-6 [69]. Inconsistent mass distributions of cobalt metal over the supports' surface were reported for the sample CAT-Q-10 (shown in Figure 4.8 C) and particularly for the sample CAT-Q-30 (shown in Figure 4.9 C). The accumulations of deposited cobalt are clearly observed in the mapping images for the sample CAT-Q-30. Based on surface micro-analysis and according to the metal dispersion listed in Table 4.4, it could be concluded that the poorly dispersed catalyst was yielded by employing low surface area supports; while high surface area supports resulted in a well and highly dispersed catalyst [139].

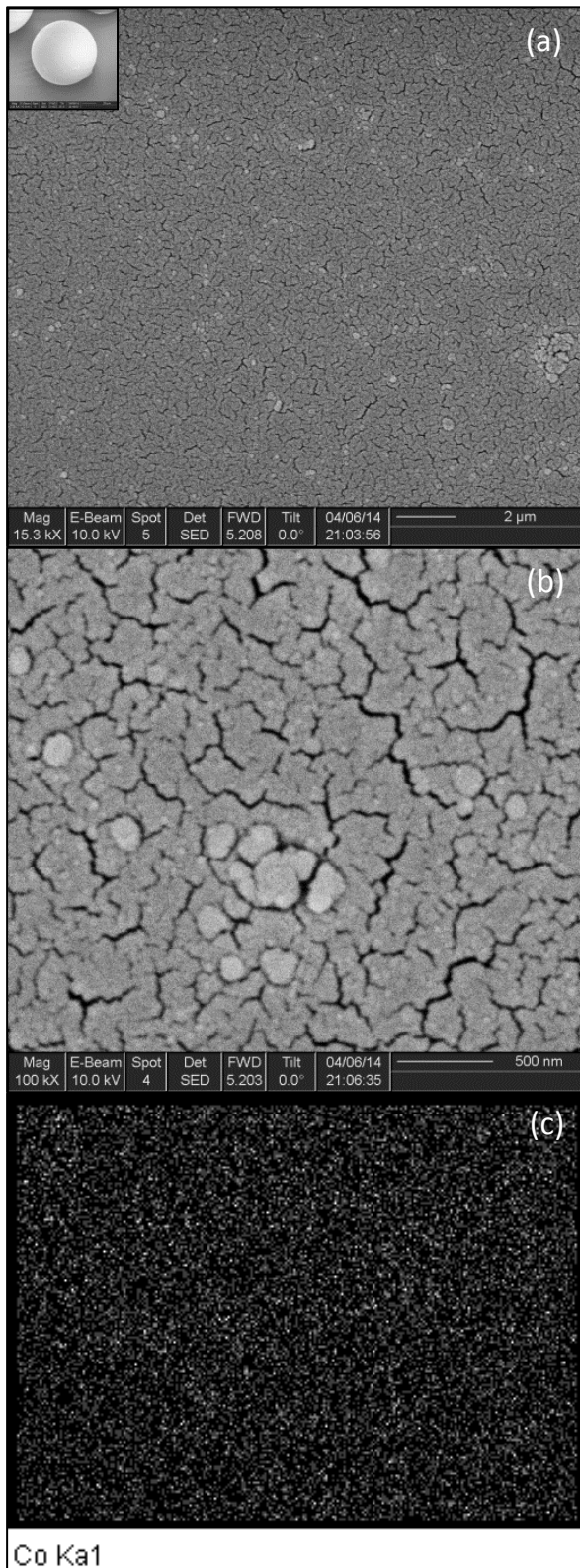


**Figure 4.6:** SEM micrographs (Figures 4.6.a and 4.6.b) and EDX micro-analysis (Figure 4.6.c) of sample CAT-Q-3

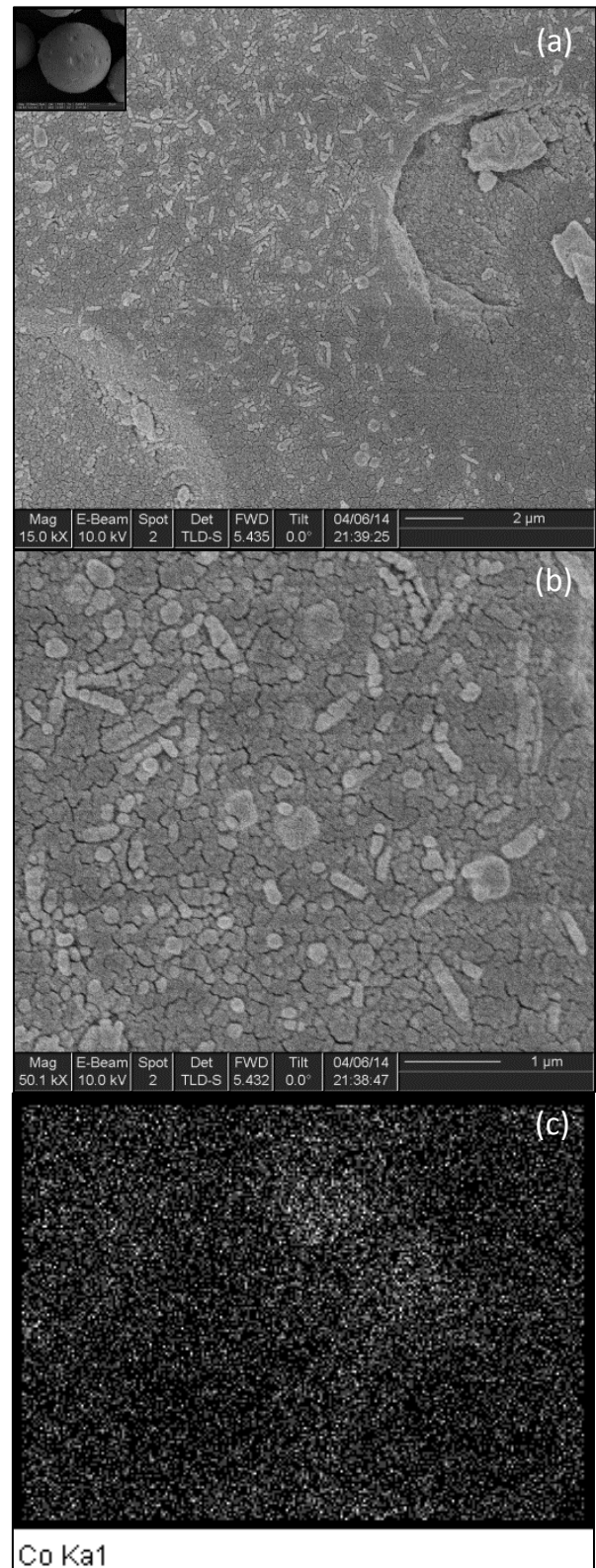


**Figure 4.7:** SEM micrographs (Figures 4.7.a and 4.7.b) and EDX micro-analysis (Figure 4.7.c) of sample CAT-Q-6

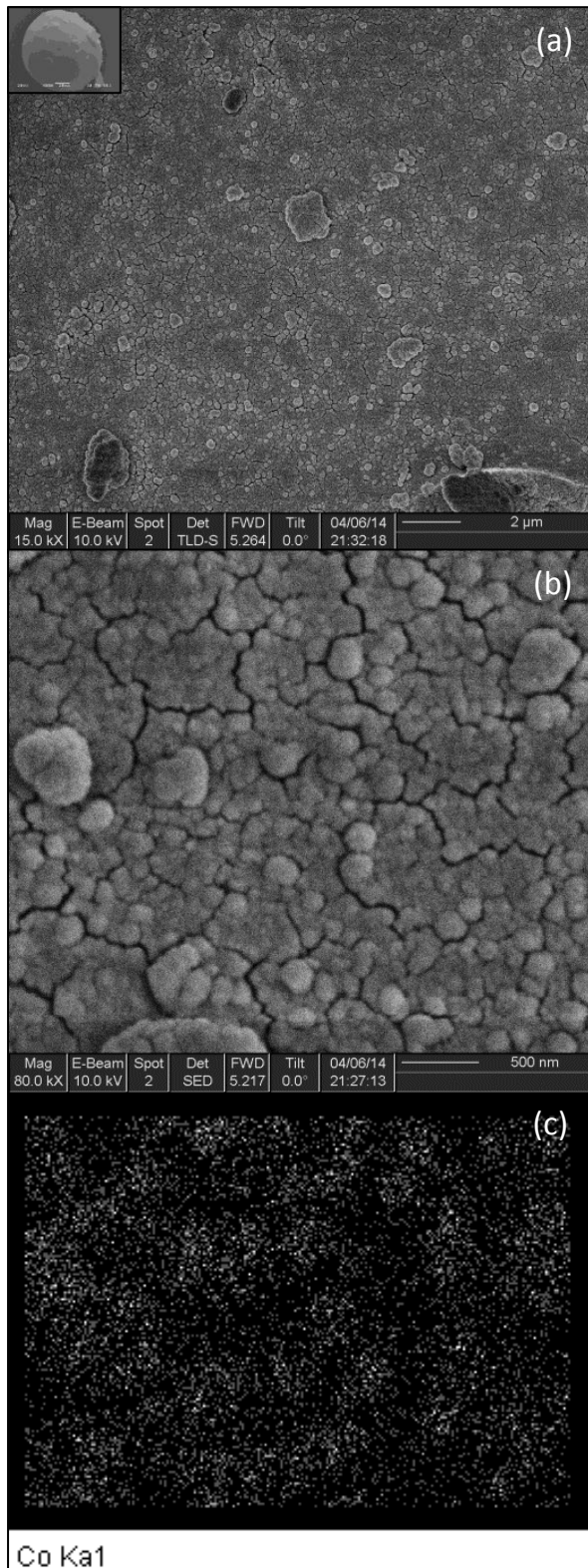


**Figure 4.8:** SEM micrographs (Figures 4.8.a and 4.8.b) and EDX micro-analysis (Figure 4.8.c) of sample CAT-Q-10

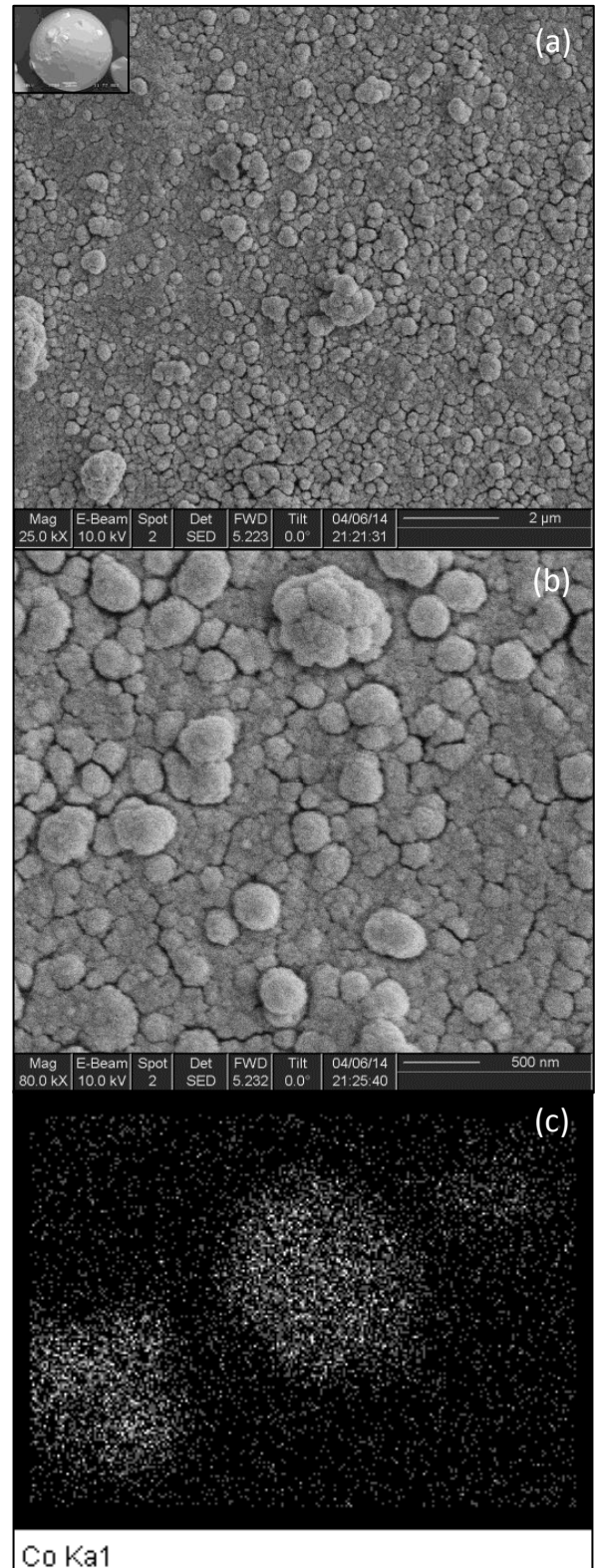


**Figure 4.9:** SEM micrographs (Figures 4.9.a and 4.9.b) and EDX micro-analysis (Figure 4.9.c) of sample CAT-Q-3

#### 4.5 Catalyst activity and selectivity in the FTS process

The F-T performances of the different catalysts were considered at 503 K, 20 bar and 3.0  $\text{Nl/h.g}_{\text{cat}}$ . To achieve a strict control and precise comparison of F-T synthesis, the different samples' catalytic performances were examined in a same reactor set-up and gaseous environment. The results of the catalysts' activity and selectivity after 12 hours on stream are listed in Table 4.6.

The results provided evidence that the catalyst pore size highly influenced not only the catalytic activity of cobalt, but also its products' selectivity. The catalyst activity in terms of carbon monoxide conversion was at its maximum ( $X_{(\text{CO})}=92.84 \text{ mol}\%$ ) when the catalyst pore size was 5.76 nm. The lowest conversion of carbon monoxide was achieved for the catalyst with the largest pore size (average pore size: 46.9 nm) and smallest surface area ( $76.75 \text{ m}^2/\text{g}$ ). To obtain accurate results during the experiments, the F-T regime temperature was kept constant to prevent the formation of hot-spots which enhance the catalytic activity. The catalysts prepared over the wide pore size support ranging from 5.76 to 16.4 nm could make the active site of the catalyst more accessible and enhance the reactant consumption. Therefore, the CAT-Q-6 catalyst revealed the highest activity compared to the others. CAT-Q-30 had the lowest surface area and biggest cobalt crystalline diameter, which couldn't deposit highly concentrated metal over the surface to be exposed to the reactant; therefore at the same space velocity, the CO conversion, which is a function of metal dispersion, was decreased to 50.55 mol%. Saib et al found that the increase in support pore diameter results in an increase in obtained crystalline size of cobalt and as a result a decrease in metal dispersion [61]. Borg et al reported that small cobalt particles formed in narrow pore size are less active than those created in wide pore size [140]. No such difference was found in this study.

**Table 4.6:** Catalytic performance of the different catalysts in FT synthesis: CO conversion ( $X_{CO}$ ), hydrocarbon selectivity ( $S_{CO_2}$ ,  $S_{CH_4}$ ,  $S_{C_2-C_4}$ ,  $S_{C_{5+}}$ ) and mass fraction of liquid phase's products

Catalyst	Selectivity of gas phase products (mol%)							LP (ml)
	$X_{CO}$	$S_{CO_2}$	$S_{CH_4}$	$S_{C_2}$	$S_{C_3}$	$S_{C_4}$	$S_{C_{5+}}$	
<b>SG Q-3</b>	68.48	3.10	52.43	3.78	6.26	5.36	32.17	3.3
<b>SG Q-6</b>	92.84	7.22	25.71	2.03	3.52	3.64	65.10	4.7
<b>SG Q-10</b>	85.50	4.61	11.18	0.89	1.54	1.40	84.99	4.4
<b>SG Q-30</b>	50.55	1.87	30.72	2.41	3.76	2.96	60.15	2.6

It was found that the methane selectivity of the catalyst with small pore diameter (sample: CAT-Q-3) was higher than that of the catalyst with a wider pore diameter. This is due to the fact that the adsorption rates of linear type carbon monoxide formed on the small cobalt crystalline, are much lower than those of the bridged type CO formed on the larger cobalt crystalline [137]. The weaker CO adsorption favoured the formation of methane. The hydrogen diffusion rate inside small pores filled with liquid is greater than carbon monoxide; the carbon monoxide diffusion limitation resulted in an increase in the hydrogen to carbon monoxide ratio in the vicinity of the active site and the catalyst pore; it could alter the product selectivity to methane and light hydrocarbons [141]. Narrow pore diameter in mesoporous silicas leads to formation of smaller  $Co_3O_4$  particles which are barely reducible. The presence of this unreducible oxides phase could catalyze the WGS reaction and yield to higher carbon dioxide and methane production [67]. CAT-Q-30 demonstrated the lowest WGS reaction activity due to its easily reducible cobalt particles created in the wide pores.

The product distribution of the cobalt catalyst is greatly affected by the support's porosity and the metal particle size distribution [66]. The increase in the catalyst's pore diameter resulted

in an increase in the cobalt particle size. The  $C_{5+}$  selectivity was also strongly increased with this enlargement, most strongly for cobalt particles  $\geq 10$  nm. This corresponded to the higher chain growth probability of wide pore based catalysts compared to that of catalysts with a narrow pore diameter. Figure 4.10 supports this explanation by showing the CO conversion and  $C_{5+}$  hydrocarbons' selectivity corresponding to the average catalyst pore diameter. The  $C_{5+}$  selectivity of the sample CAT-Q-3 was lower than the corresponding selectivity of the other catalyst (32.17 %). The small crystalline size of the cobalt species located in the narrow pores leads to higher hydrogenation activity power compared to its chain growth power. The catalyst supported by silica with an average pore diameter of 17.2 nm was the most selective for heavy hydrocarbon compounds. The maximum  $C_{5+}$  selectivity was reported for the sample CAT-Q-10 ( $S_{C_{5+}} = 84.99$  mol %). The interpretation of higher chain growth probability for this catalyst is related to a higher elementary polymerization rate affected by larger cobalt particle size. Some of the previous investigations expressed that cobalt dispersion does not affect the rate of chain growth probability. Utilization of a different precursor such as cobalt nitrate for CO hydrogenation over wide-pore supports, could enhance the paraffin/olefin ratio exponentially with chain growth probability. This enhancement in secondary reactions, which is a function of cobalt particles' cluster sizes, results in a high re-activity of  $\alpha$ -olefins to be re-hydrogenated or re-polymerized due to easily re-adsorption into the catalyst. This caused the higher paraffin content in the product stream. The  $\alpha$ -olefins' compounds are produced by the breaking of linear surface alkyl chains by  $\beta$ -hydrogen abstraction; while the  $n$ -paraffins are yielded by  $\alpha$ -hydrogenation [142, 143]. For the catalyst CAT-Q-6 and CAT-Q-10, the increase in reactant conversion leads to production of more water in the F-T regime. This increase in water content could be ascribed as another reason for higher selectivity of  $C_{5+}$  hydrocarbons [144]. This is in case that the  $C_{5+}$  selectivity is greatly impacted by the change

in the mesoporous based catalyst's diameter [137]. The increase in carbon monoxide conversion as a result of a decrease in feed space velocity increases the co-produced water. This should take into account that excessive water production is a challenging problem particularly for a Co supported  $\text{SiO}_2$  catalyst; affecting its lifetime by accelerating the deactivation trend of this catalyst [145]. The sample CAT-Q-30, despite having the lowest F-T activity, allocated a high selectivity in  $\text{C}_{5+}$  hydrocarbons. The presence of macro-pore diameter in its structure facilitated reactant accessibility to active phases, as well as boosted the heavy hydrocarbons to diffuse out from the pores. The results are in good agreement with those obtained from the investigation by Borg [144]. Accessible cobalt particles of this catalyst shortened the possible residence time of olefin re-adsorption as well.

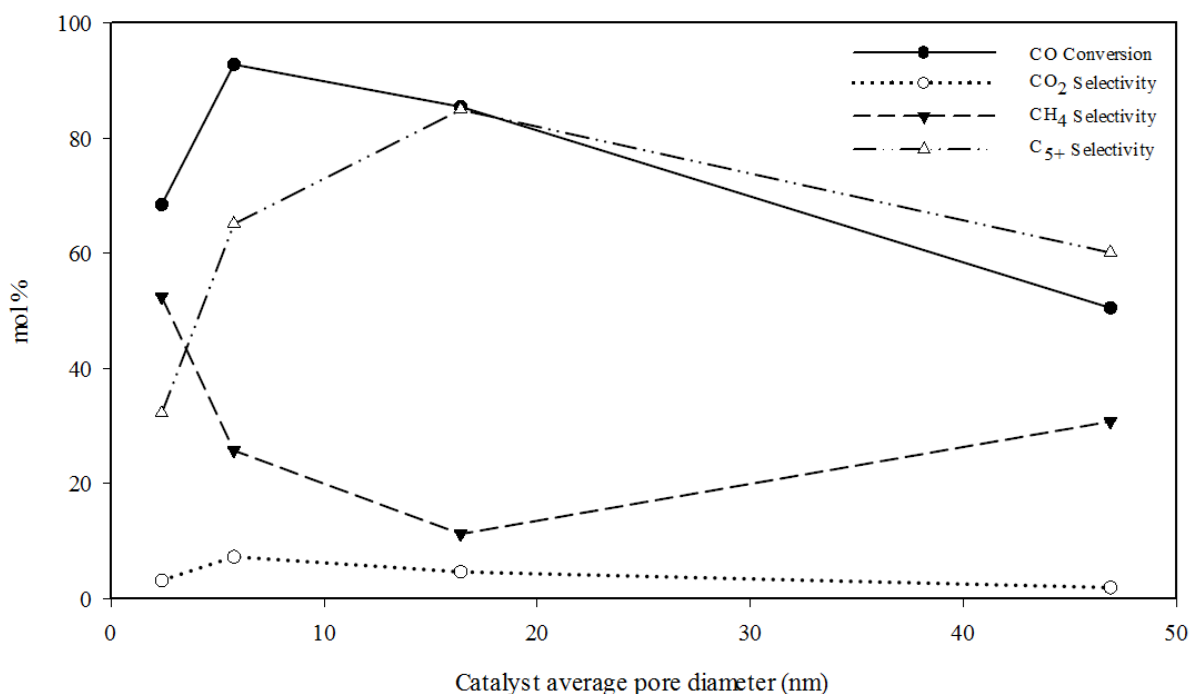


**Figure 4.10:** Effect of average pore diameter of catalyst on CO conversion,  $\text{CO}_2$ ,  $\text{CH}_4$  and  $\text{C}_{5+}$  selectivity. Reaction conditions; P: 20 bar, T: 510 K, WHSV: 3.0 NL/h.gcat

#### ***4.6 Deactivation of a cobalt-based catalyst during FT synthesis***

The deactivation mechanism of different catalysts over the reaction time depends on their type and use [146]. In this section, the responsible mechanisms for the short-term catalyst deactivation in the cobalt-based LTFT process are discussed within the first reaction cycle.

Tsakoumis [147] summarized corresponding mechanisms for cobalt-based catalyst decay in the F-T synthesis in his review. The physical blockage of the catalyst's active site for the reaction by strongly adsorbed sulphur poisons on the metallic cobalt phase is not ascribed to deactivation of the Co/SiO<sub>2</sub> catalyst in this study. Poisoning compounds (hydrogen sulphide (H<sub>2</sub>S) and organic sulphur (COS)) are usually presented in raw synthesis gas derived from biomass and coal. This is in case that the F-T activity was performed by employing a highly purified simulated syngas bottle and there was no trace of permanent poisoning sulphur compounds and possibly nitrogen-containing contaminants (e.g. ammonia (NH<sub>3</sub>) and hydrogen cyanide (HCN)) in the feed gas [29]. Irreversible deactivation by syngas sulphur contaminants leads to lower carbon monoxide adsorption, hydrogenation capability and higher methane formation [148]. Carbon deposition and fouling by carbon species are significant deactivation mechanisms ascribed for Co-LTFT catalysts. Accumulations of high molecular weight/inactive polymeric hydrocarbons from the fluid phase on the surface and/or pores of the catalyst caused the reactants' diffusion inhibition and lowered the rate of reaction. This reversible deactivation which less likely occurs from strong carbon species chemisorption, just resulted in lower activity of the catalyst and not complete deactivation [147]. Re-activation of the catalyst could be carried out by regeneration treatment. Carbon deposition influences extremely the Co-LTFT catalyst activity as well as its selectivity; however, the cobalt-based F-T synthesis is considered as a carbon in-sensitive process [149].

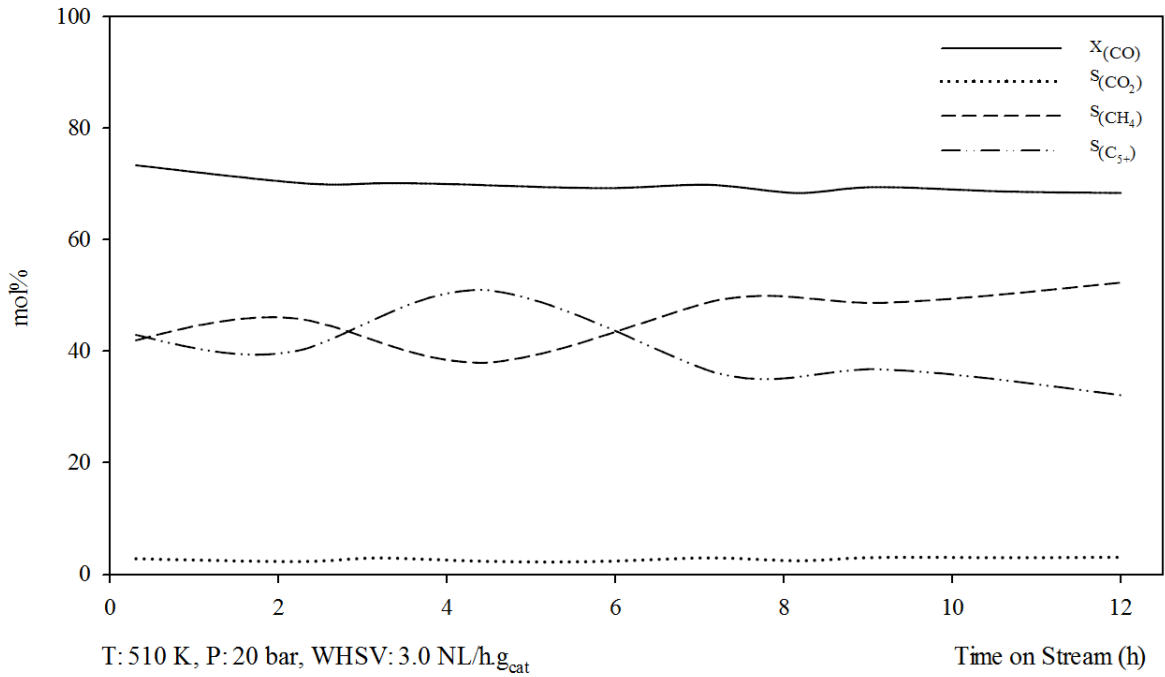


**Figure 4.11:** Performance of sample CAT-Q-3 in F-T synthesis regime, trend of CO conversion, CO<sub>2</sub>, CH<sub>4</sub> and C<sub>5+</sub> selectivity as a function of time on stream over cobalt catalyst supported silica

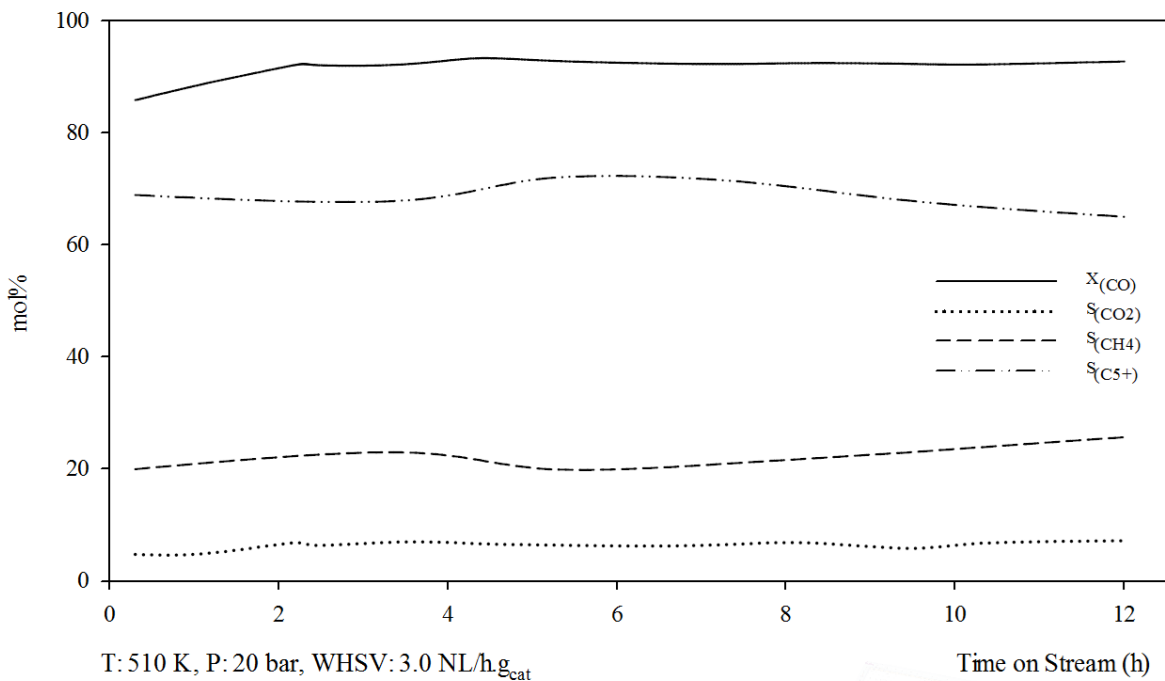


**Figure 4.12:** Performance of sample CAT-Q-6 in F-T synthesis regime, trend of CO conversion, CO<sub>2</sub>, CH<sub>4</sub> and C<sub>5+</sub> selectivity as a function of time on stream over cobalt catalyst supported silica

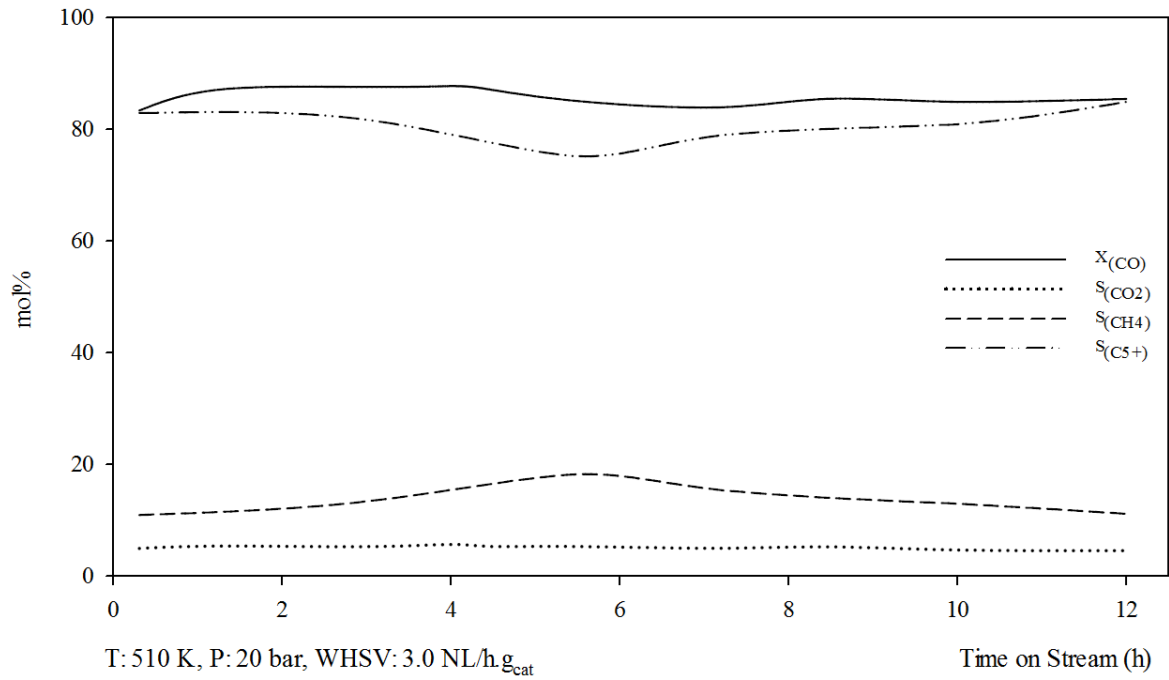


**Figure 4.13:** Performance of sample CAT-Q-10 in F-T synthesis regime, trend of CO conversion, CO<sub>2</sub>, CH<sub>4</sub> and C<sub>5+</sub> selectivity as a function of time on stream over cobalt catalyst supported silica

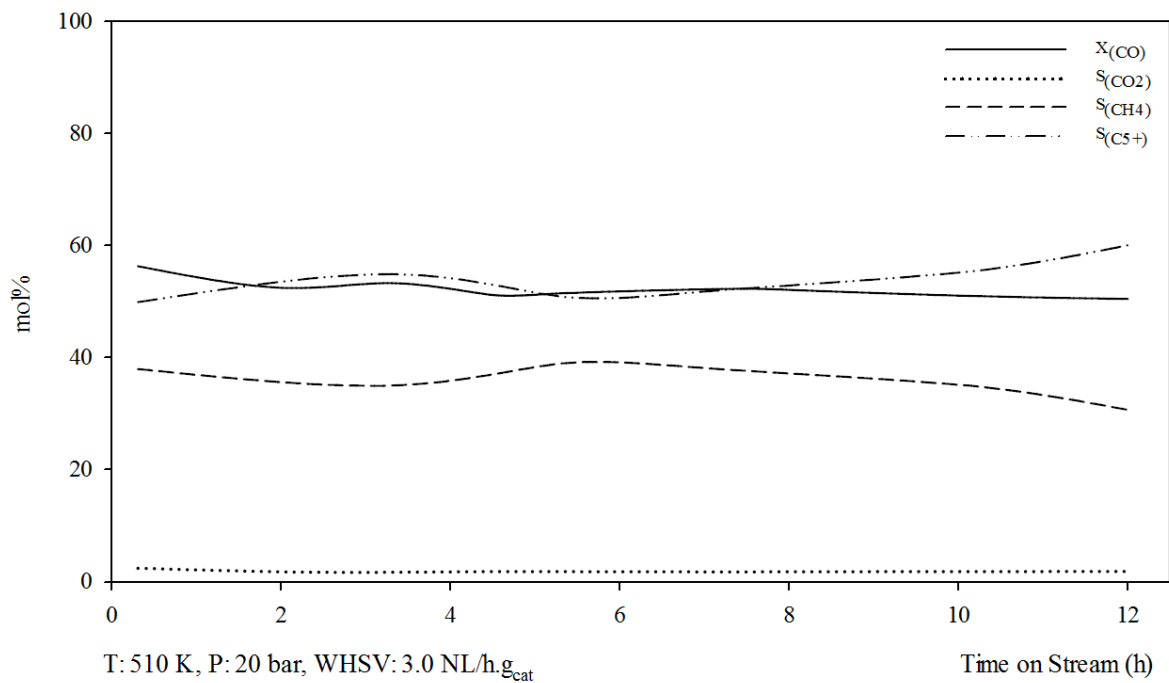


**Figure 4.14:** Performance of sample CAT-Q-30 in F-T synthesis regime, trend of CO conversion, CO<sub>2</sub>, CH<sub>4</sub> and C<sub>5+</sub> selectivity as a function of time on stream over cobalt catalyst supported silica

The catalysts' activities in terms of CO conversion as well as hydrocarbons selectivity as a function of exposure time to syngas, are represented in Figures 4.11 to 4.14. The relative activity of CAT-Q-3 was decreased from 73.46 to 68.49 mol%, which is corresponding to a 0.58% deactivation rate per hour. In addition to the above reasons, this might be ascribed to the contribution of the small cobalt crystallite's surface energy to re-oxidize active metal by residual oxygen of dissociative carbon monoxide adsorption to inactive cobalt oxides [150]. The relative selectivity to methane kept increasing at a rate of 2.07% per hour; while the selectivity to heavy hydrocarbons was decreased from 43.1 mol% to 23.17 mol% at the end of the experiment. The observed trend might be explained by the poisoning of the active site by carbonaceous deposition; while the formation of methane on non-specific sites was not as affected [151]. The activity of CAT-Q-6 in terms of CO conversion was increased in the first two hours and then became relatively stable. This might be explained by more production of water due to an increase in conversion at relatively low space velocity, which promotes the activity of the catalyst. It should be taken into account that the excessive water partial pressure occurring at high conversion per pass could cause a deactivation. The investigation of Huber et al [152] demonstrated that this kind of deactivation is not reversible through re-oxidation and re-reduction treatment, due to collapse of the support and formation of cobalt silicates. It should be mentioned that formation of cobalt silicates via the aqueous deposition method in the preparation stage is unavoidable. On the other hand, the selectivity of this catalyst did not present a similar steady state. The selectivity to methane and C<sub>5+</sub> hydrocarbons followed the same trend as CAT-Q-3. It seems likely that the slight deactivations caused by sintering and oxidation of the moderate pore diameter catalyst CAT-Q-10, might increase the average cobalt particle size. It is probable that this increase resulted in higher C<sub>5+</sub> selectivity despite having a negative trend in the CO conversion [144]. The

same catalytic behaviour was observed for CTA-Q-30. The experiments were carried out at an operational pressure lower than 30 bar to prevent the reaction of the catalyst metal with carbon monoxide to form metal carbonyl [153].

The agglomeration of small cobalt particles due to their high surface free energy is caused by a reduction in catalyst active surface sites [153]. Sintering is energetically favoured as a result of support, or either active phase crystalline growth, due to the crystallites' surface energy minimization on various catalysts [147]. Atomic migration and crystalline migration are two significant sintering mechanisms that are accelerated by an increase in reaction temperature (diffusion coefficient) and water vapour content (partial pressure). For the cobalt, the Hüttig temperature at which the atoms become mobile at defects is 526 K ( $T_{Hüttig} = 0.3T_{melting}$ ), when it reaches to its Tamman temperature ( $T_{Tamman} = 877\text{ K}$  ( $0.5T_{melting}$ )), the atoms from the bulk exhibit mobility [154]. To avoid the temperature-dependent surface diffusion of largely aggregate mobility, the experiments were carried out at a relatively low temperature ( $T_{reaction} < T_{Hüttig} < T_{Tamman}$ ). Saib et al [155] concluded that the catalyst deactivation caused by sintering is mostly reversible by the oxidative regeneration method.

The observed trends of the reactant consumption from the catalyst's exposure time to the syngas were found to be close to the usage ratio of H<sub>2</sub>/CO in the reactor. This could eliminate the concerns regarding the increasing of the conversion per pass due to an increase in metal content. Since the F-T synthesis over cobalt catalyst is a WGS active reaction, the change in hydrogen to carbon monoxide ratio (partial pressure) with increasing the conversion might result in insufficient productivity and catalyst deactivation. The increase in per pass conversion could lead to a change in WGS compounds and affect the catalytic behaviours while no alteration in CO<sub>2</sub> selectivity is demonstrated. In addition, this extent in reactant conversion could influence many aspects in the reactor design as well as gas loop design [29].

#### **4.7 Conclusion**

In this study the meso-macro porous silica supports were used to prepare supported cobalt catalysts. The average pore diameter varied from 2.37 nm to 46.9 nm. The physicochemical properties of the cobalt catalysts were greatly influenced by the change in support texture and porosity. The performances of the catalysts were considered in F-T synthesis employing a mini-single channel downdraft fixed-bed reactor. Higher conversion in carbon monoxide, higher C<sub>5+</sub> selectivity as well as lower by-products selectivity, were observed for the catalysts featuring medium sized pore (5.76 - 16.4 nm) and crystallite (13.63 - 16.04 nm). In addition, the catalyst allocating a 16.04 nm pore diameter demonstrated a negative catalyst deactivation trend, i.e. there is no loss of activity. Three separate parameters resulted in highly dispersed small cobalt particles over the surface of the supports: (i) increase in cobalt content; (ii) using dehydrated ethanol solvent and (iii) application of meso-porous silica support. The resulting cobalt oxides were activated at a relatively high temperature (20 K) compared to previous works. Despite this fact, greater production of long chain hydrocarbons at the same time was achievable.



---

# Chapter 5

---

## PROCESS OPTIMIZATION AT

### LOW-PRESSURE REACTION CONDITION

In this work, an experimental scheme was utilized based on the Taguchi method to investigate the effect of different operational parameters (Pressure= 2-10 bar, Temperature= 503-528 K and Weight Hourly Space Velocity (WHSV) = 2.4-3.6  $\text{NI/h.g}_{\text{cat}}$ ) and their interactions in F-T performance of an in-house prepared cobalt catalyst supported by silica and a single-channel fixed-bed reactor. The objectives of the experiments were to achieve the optimum condition of liquid fuel production; make the process cost-effective in a single pass F-T operation; minimise the methane formation and Water Gas Shift (WGS) reactions' activities. For this purpose, an effort was made to reach the highest conversion, selectivity and productivity in a single pass F-T process with maximum precursor loading and support surface area utilization. The optimum levels for controllable system parameters were concluded using the mean of the Signal to Noise (SN) ratio by considering the impact of each level on response variables. In addition, the interactions of control factors were recognized using the Analysis-of-Variance (ANOVA) to determine the most significant control factor.

### 5.1 Experimental results

The kinetic study of the F-T chemical process and hydrogenation activity is a principal investigation for industrial practice, simulation and the optimisation process of fuel generation. In order to optimise the reactant conversion and bio-diesel production, the effect of operating conditions was investigated at low pressure/temperature reaction conditions using Taguchi  $L_9$  (discussed in Chapter 3, section 3.2.3). Table 5.1 shows the experimental data collected from nine experiments run based on the Taguchi DOE and for each of the experiments, the conversion of carbon monoxide ( $X_{CO}$ ), selectivity of carbon dioxide ( $S_{CO_2}$ ), methane selectivity ( $S_{CH_4}$ ),  $C_1 - C_4$  and  $C_{5+}$  hydrocarbons' selectivity ( $S_{C_{5+}}$ ) have been illustrated. After each experiment, nitrogen gas was flushed into the reactor to extract the produced liquid; the amount of Liquid Produced (LP) is tabulated in Table 5.1 as well.

**Table 5.1:** Experimental data: changes in CO conversion ( $X_{CO}$ ), hydrocarbon selectivity ( $S_{CO_2}$ ,  $S_{CH_4}$ ,  $S_{C_2-C_4}$ ,  $S_{C_{5+}}$ ) for 9 experiments run

Exp. Run	Selectivity of gas phase products (mol %)							LP (ml)
	$X_{CO}$	$S_{CO_2}$	$S_{CH_4}$	$S_{C_2}$	$S_{C_3}$	$S_{C_4}$	$S_{C_{5+}}$	
EXP1	34.99	2.89	51.43	4.78	7.66	6.57	29.56	1.1
EXP2	47.65	1.81	33.82	2.96	5.15	4.62	53.45	2.7
EXP3	43.79	2.29	26.60	2.10	3.82	3.48	64.00	2.8
EXP4	45.16	7.62	62.37	0.95	1.34	0.72	34.62	1.7
EXP5	62.09	8.52	68.94	6.94	10.22	8.84	5.058	3.2
EXP6	93.03	14.10	23.27	2.27	3.13	2.77	68.56	2.9
EXP7	45.02	10.24	71.43	1.02	1.19	0.53	25.83	0.9
EXP8	84.65	17.11	36.96	0.52	0.65	0.38	61.49	1.4
EXP9	90.78	16.38	40.29	3.85	5.37	4.62	45.87	2.2

## 5.2 Effect of the process conditions on the catalyst activity and products' selectivity

The change in carbon monoxide conversion and hydrocarbons' selectivity were measured during each of the experiments performed at different operating conditions and the results are plotted in Figures 5.1 to 5.5.

The dissociative adsorption rate of carbon monoxide, hydrogenation of carbon atoms of metal carbides to create monomer units, chain propagation and chain termination on the catalytic surface are greatly affected by reaction temperature in the F-T regime. As it is apparent from Figure 5.1 a, the increase of the bed temperature at low pressure enhances slightly the conversion of CO from 34.99 to 45.16 mol% at 2 bar and strongly increases the conversion from 43.79 to 90.78 mol% at 10 bar, when the concentration of reactants is appropriate at higher pressure. From Figure 5.1 b, keeping constant WHSV, an increase in CO conversion from 34.99 to 93.03 mol% at WHSV: 2.4 NL/h.g<sub>cat</sub> and from 47.65 to 90.78 mol% at WHSV: 3.0 NL/h.g<sub>cat</sub> respectively, were observed with an increase in temperature from 503 to 528 K and a slight decrease occurring at the higher space velocity because of the increase in concentration of reactants in these circumstances.

Chain termination is deeply impacted by temperature, since the hydrocarbons' desorption from the catalyst surface is an endothermic process; the increase in the temperature favours the methane production, more oxygenated and alkenes selectivity and less hydrogenated products (alkanes) [151]. The increase in temperature favours the re-adsorption and inter-conversion of the oxygenates' reaction rate as well [29]. As shown in Figure 5.4 b, an increase in the temperature from 503 to 528 K at lower space velocity resulted in an increase in C<sub>5+</sub> selectivity from 29.56 to 61.49 mol%. In contrast, this increase in temperature at a higher space velocity resulted in a decrease from 64.00 to 25.83 mol% in C<sub>5+</sub> selectivity.

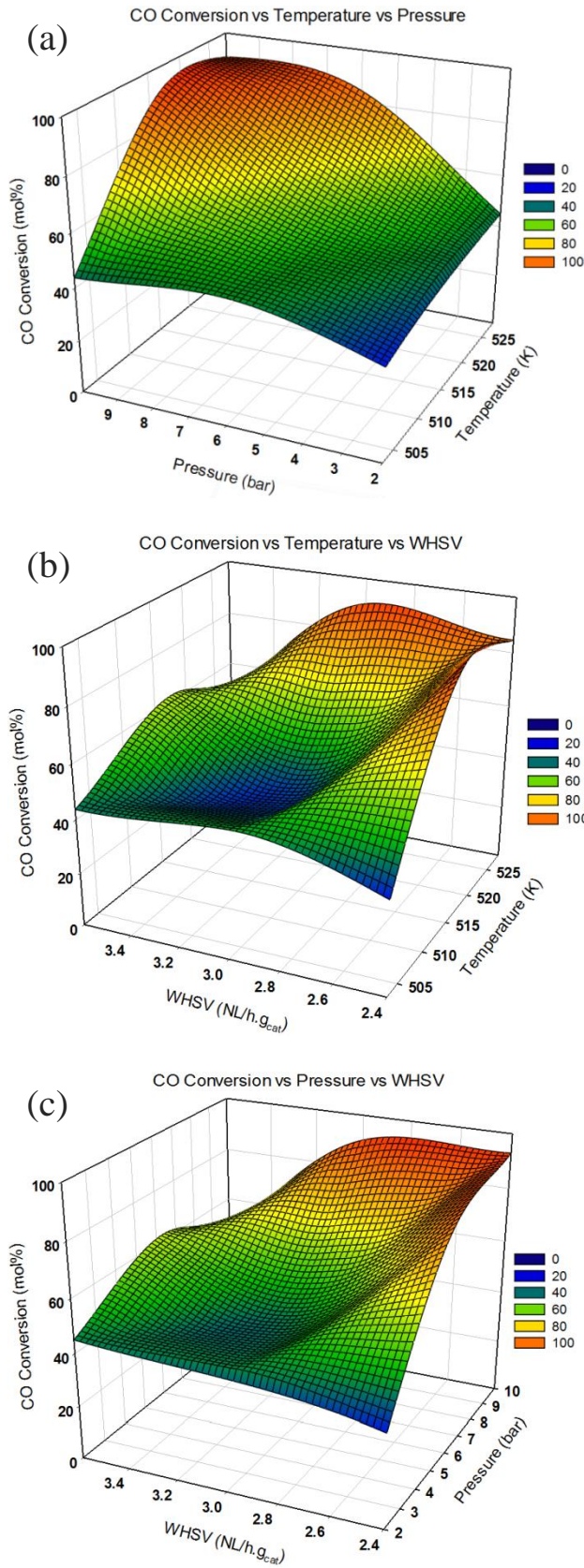


**Figure 5.1:** Effect of synthesis reaction conditions (Temperature, Pressure and space velocity) on CO conversion

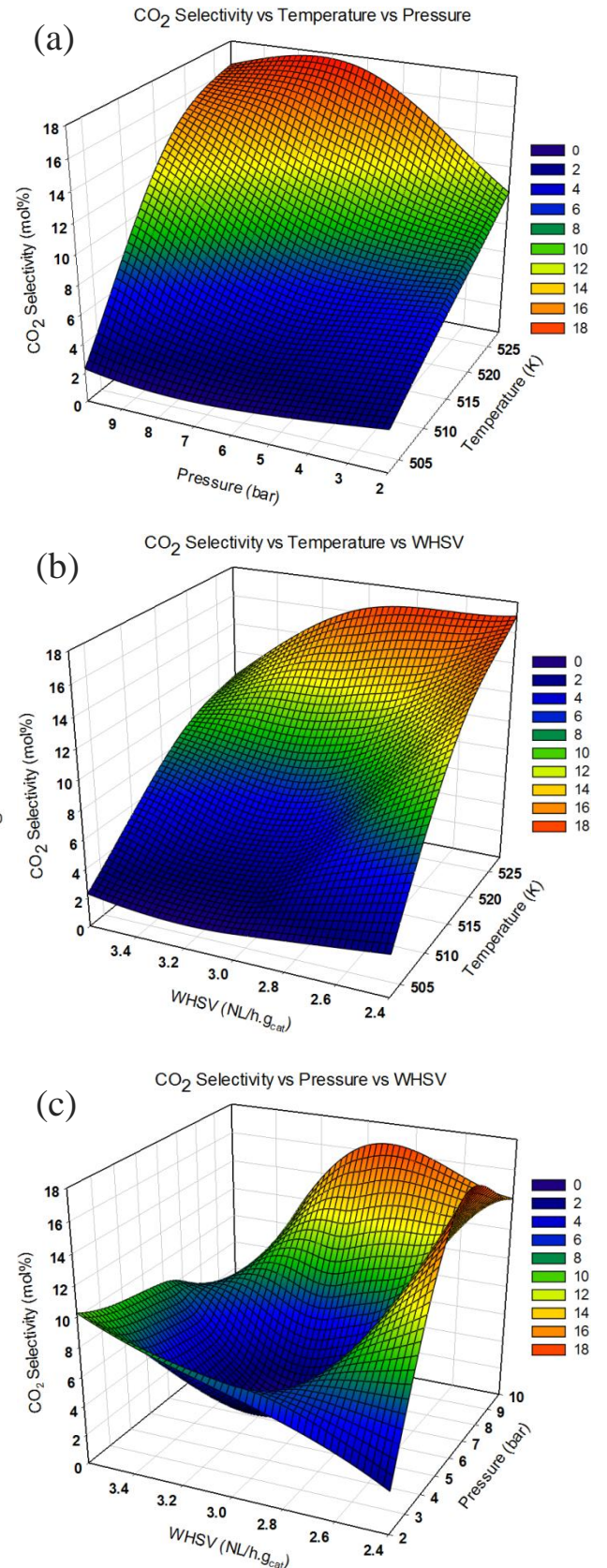


**Figure 5.2:** Effect of synthesis reaction conditions (Temperature, Pressure and space velocity) on CO<sub>2</sub> selectivity

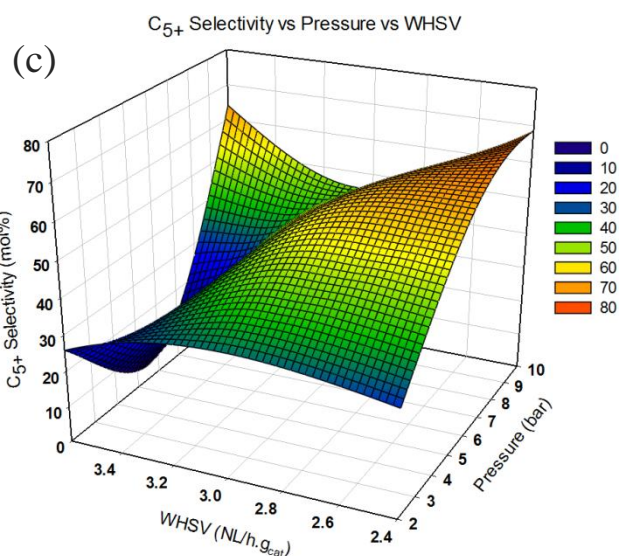
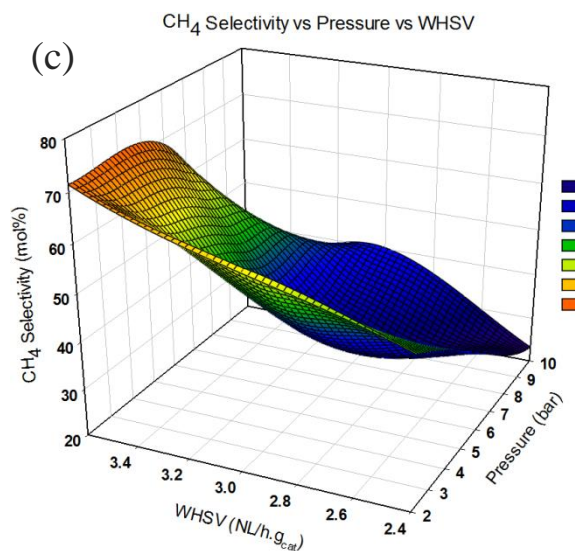
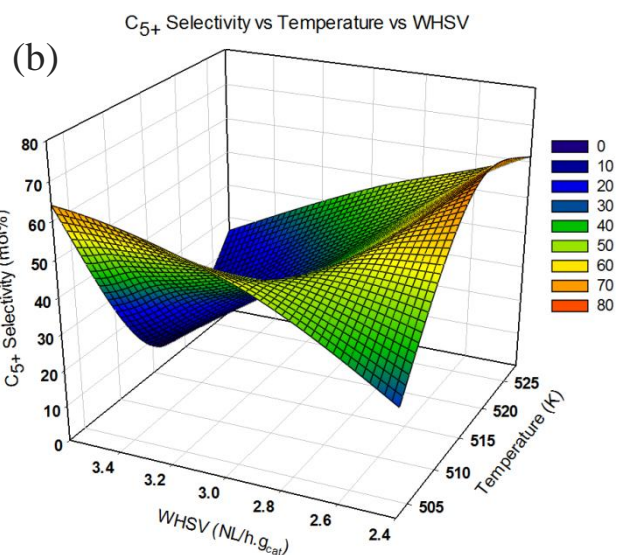
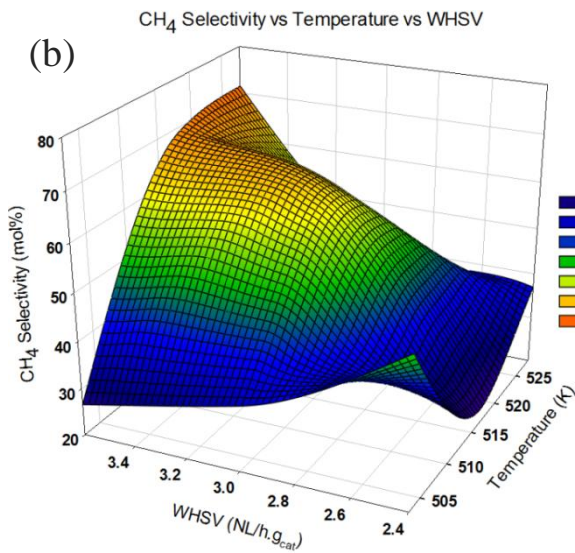
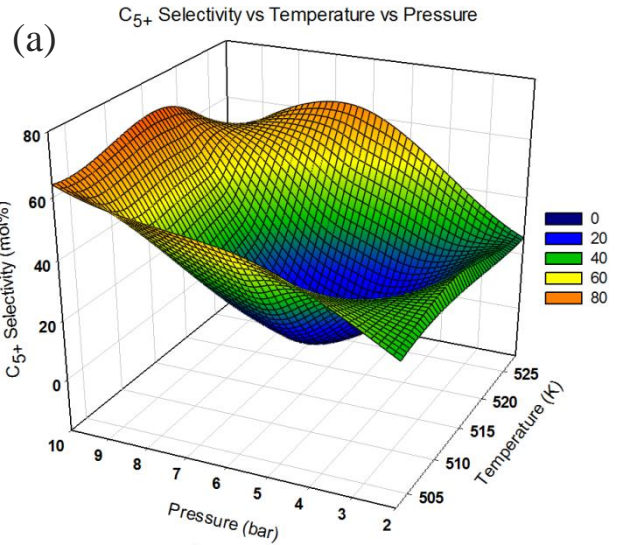
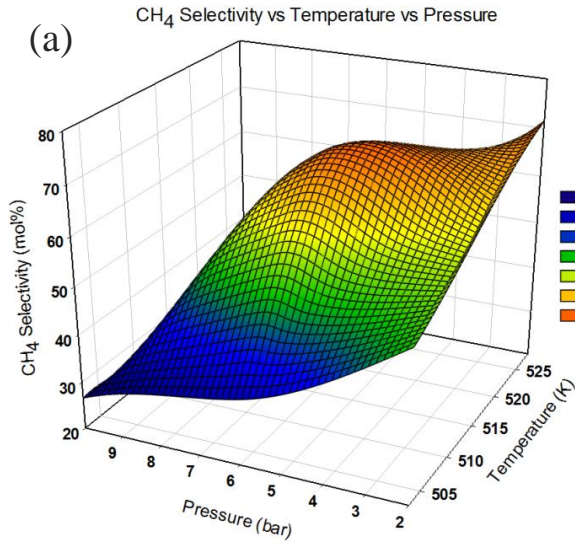


**Figure 5.3:** Effect of synthesis reaction conditions (Temperature, Pressure and space velocity) on CH<sub>4</sub> selectivity

**Figure 5.4:** Effect of synthesis reaction conditions (Temperature, Pressure and space velocity) on C<sub>5+</sub> hydrocarbons selectivity

Each catalyst possesses its own operating pressure. With cobalt-based F-T process, operating at pressure above 30 bar leads to the formation of metal carbonyl through the catalyst's metals reaction by carbon monoxide [153]. The increase in partial pressure enhances the reactant's concentration on the catalyst surface and favours the conversion of carbon monoxide, as it is more forcefully adsorbed onto the surface of the catalyst than hydrogen and promotes the chain propagation and chain growth probability; taking into account that a higher concentration of CO could be conducted to the production of more oxygenates [29]. As shown in Figure 5.1 a, the conversion of CO is enhanced by increasing the total pressure from 34.99 mol% at 2 bar to 43.79 mol% at 10 bar at a lower temperature and from 45.02 mol% at 2 bar to 90.78 mol% at 10 bar at a higher temperature. The increase in reaction temperature, hydrogen partial pressure and H<sub>2</sub>/CO ratio, results in a higher hydrogen concentration on the catalytic surface and enhances the hydrogenation degree of highly concentrated monomers. This increase accelerates the chain termination which causes a decrease in the monomer unit's propagation, chain growth probability and production of the heavy hydrocarbons and governs the F-T product selectivity to lighter synthetic hydrocarbons [156].

The hydrogen to carbon monoxide ratio was kept at 2:1 during all of the experiment to prevent a higher concentration of H<sub>2</sub> and also prevent a change in the usage ratio during the synthesis reaction, as it is the appropriate ratio to produce heavy hydrocarbons [29]. The effect of F-T reaction parameters on Water Gas Shift (WGS) and methanation reactions' activity are shown in Figures 5.2 and 5.3 respectively, as a function of temperature, pressure and space velocity. The data plotted in Figure 5.2 a clearly illustrates that CO<sub>2</sub> selectivity slightly decreases upon increasing the total pressure at a lower temperature from 2.89 mol% at 2 bar to 2.29 mol% at 10 bar. In contrast, the selectivity to the carbon dioxide strongly increases at a higher temperature with increasing the pressure from 10.24 mol% at 2 bar to

16.28 mol% at 10 bar keeping the temperature constant. The data plotted in Figures 5.2 and 5.3 clearly illustrate that carbon dioxide and methane selectivity increase upon increasing the temperature. Lower activity of the cobalt catalyst in the WGS and methanation reaction at optimal H<sub>2</sub>/CO ratio is an extraordinary advantage of this catalyst. Carbon dioxide is the final product from the cobalt-based F-T synthesis [56].

The surface polymerization of -CH<sub>2</sub>- intermediates created by dissociation and hydrogenation of adsorbed carbon monoxide on the cobalt catalyst, results in hydrogenation of the produced residual oxygen atoms and forms water as a co-product. This should take place at the same rate of CO dissociation to prevent cobalt oxidation as a reason for catalyst deactivation, which occurs under specific circumstances. With cobalt based F-T synthesis, the produced water has no inhibiting effect and is even able to promote the conversion of reactants and lowers the methanation activity. The previous investigations demonstrate that smaller crystalline size cobalt could provide a sufficient surface energy contribution to be re-oxidised [150]. The increase in the concentration of carbon dioxide, which acts as a diluter in the F-T regime, causes a reduction in concentration and partial pressure of the carbon monoxide content and results in a change in the products' composition from the proposed F-T synthetic hydrocarbons to a methanation reaction product, due to selective inhibition dominating the F-T regime [157]. The highest methane selectivity was reported for EXP7 which was carried out at 528 K, 2 bar and 3.6 NL/h.g<sub>cat</sub> and allocated a higher WGS reaction activity rate by consuming 10.24 mol% of converted CO. It was found that an increase in the bed temperature from 503 to 528 K resulted in an increase in carbon dioxide and methane selectivity from 1.81 to 17.11 mol% and from 26.60 to 71.43 mol% respectively.

A higher space velocity resulted in a slight increase in CO conversion due to an increase in the reactant concentration in the F-T synthesis regime from 34.99 to 43.79 mol%. In contrast,

this increase in space velocity caused a sharp decrease in CO conversion at a higher temperature; due to an increase in the reactants' concentration, the catalyst desorption rate and a decrease in residence time. Generally, high space velocity is associated with low reactant residence time [24]. The outcomes demonstrated that at low space velocity, the CO conversion was high (93.03 and 84.65 mol% at 518 and 528 K respectively) due to a high residence time. The CO consumption was decreased with an increase in WHSV for both circumstances. The results of the experiments, in terms of CO conversion and hydrocarbons selectivity, are shown in Figures 5.1-5.4 b as a function of temperature and space velocity.

An increase in space velocity in the Co-based catalyst and the constant reactants' ratio (H<sub>2</sub>:CO = 2:1) had a negative influence in methane and carbon dioxide selectivity at a lower temperature. As it is apparent from Figure 5.3 b, the CH<sub>4</sub> selectivity is decreased with an increase in space velocity (CH<sub>4</sub> selectivity alteration at 503 K from 51.43 to 26.60 mol %). In contrast, by increasing the space velocity at a higher temperature, the direct carbon monoxide hydrogenation to produce methane seems to be increased, as observed from Figure 5.3 b. The increase in space velocity resulted in an increase in CH<sub>4</sub> selectivity at 518 K from 23.27 to 68.94 mol% and from 36.96 to 71.43 mol% at 528 K. Figure 5.2 b illustrates that the catalyst activity in terms of CO<sub>2</sub> selectivity was at maximum (17.11 and 14.10 mol%) at the lowest space velocity (WHSV=2.4 NL/h.g<sub>cat</sub>) and at a minimum (7.62 and 10.24 mol%) at a higher space velocity (WHSV=3.0 and 3.6 NL/h.g<sub>cat</sub>), keeping the temperature constant at 518 and 528 K respectively.

The variation in selectivity of light hydrocarbons (C<sub>2</sub> – C<sub>4</sub>), C<sub>5+</sub> and produced liquid with operational parameters are given in Table 5.1. Figure 5.5 b represents the variation of produced heavy hydrocarbons with syngas space velocity. It could be concluded that by increasing the synthesis gas space velocity, the amount of liquid fuel collected is increased,

due to the fact that this increase results in the elimination of mass transfer limitation and causes the removal of hydrocarbons from the catalyst surface and pores due to the dominant diffusion effect [158]. The maximum amount of liquid was reported for experiment EXP5 which was run at 3.6 NL/h.g<sub>cat</sub>. A longer residence time of higher molecular mass hydrocarbons increases the re-adsorption rate of  $\alpha$ -olefins and water partial pressure; which is another reason for the proposed increase in heavy hydrocarbon selectivity under typical conditions [24]. The results documented in Table 5.1 demonstrate that the increase in syngas space velocity in some particular conditions resulted in an enhancement in higher molecular weight hydrocarbon's propagation of surface species and favoured the production of long chain heavier compounds (EXP1:  $S_{C_{5+}} = 29.56$  mol% at 2.4 NL/h.g<sub>cat</sub>, EXP3:  $S_{C_{5+}} = 64$  mol%

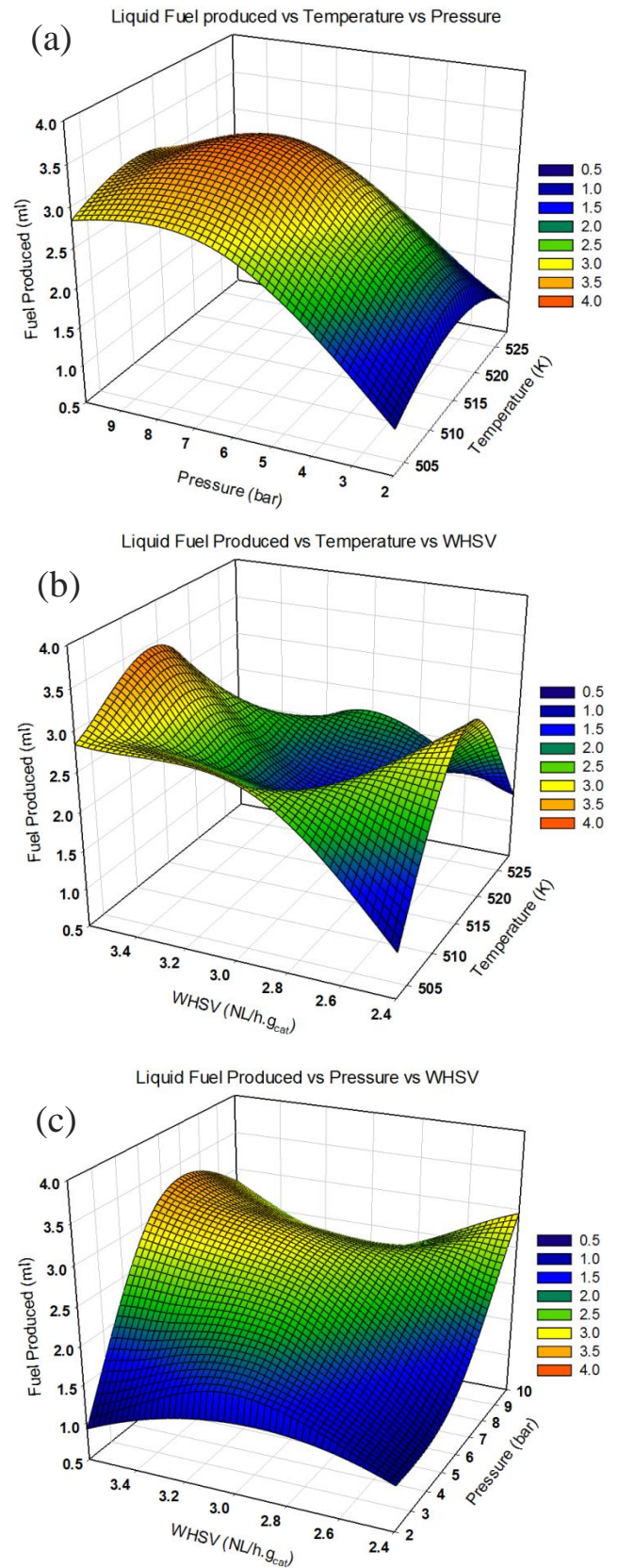


**Figure 5.5:** Effect of synthesis reaction conditions on liquid production

at 3.6 NL/h.g<sub>cat</sub> keeping the temperature constant). From Table 5.1, the C<sub>2</sub>, C<sub>3</sub> and C<sub>4</sub> selectivity were varied by -56.06, -50.13 and -47.03 % by increasing the WHSV from 2.4 to 3.6 NL/h.g<sub>cat</sub> respectively. The increase in the feed space velocity results in the contribution of reactants in the chain growth polymerization step to yield heavy hydrocarbons; whereas the lower syngas space velocity leads to higher activity of greatly exothermic methanation and coke formation reactions, in which case the formation of a heat spot and catalyst deactivation are inevitable [75]. Nitrogen plays a remarkable role in removing the waste heat produced by the exothermic F-T reaction and prevents temperature runaway in the F-T regime. Utilization of nitrogen-rich synthetic gas (50 vol%) to produce heavy hydrocarbons enables the application of large diameter reactor tubes and leads to a notable reduction in the number of tubes, which makes the production process cost-effective [77].

### 5.3 Cobalt-based F-T deactivation mechanisms

The responsible F-T catalyst deactivation mechanisms are discussed in this section. The trend in CO consumption, selectivity to CO<sub>2</sub>, CH<sub>4</sub>, and C<sub>5+</sub> products and the catalyst's deactivation trend as a function of reaction time for various experiments are illustrated in Figure 5.6. The catalysts' deactivations were considered within the first period of the reaction cycle. Each catalyst was put for 12 h on stream and the performance was monitored during this time.

Different deactivation mechanisms have been proposed for Co-based catalysts in the F-T process. The investigations demonstrated that a cobalt catalyst with a larger crystallite size than 6 nm and when  $P_{H_2O}/P_{H_2}$  is varied from 1 to 1.5, could prevent the oxidation of active metal to inactive metal oxide by residual oxygen and water co-product respectively; therefore, the reversible Co oxidation deactivation rate could be lowered or increased by cobalt

crystallite size distribution [33, 39]. Synthesis gas feed related poisons (generally sulphur, halides and  $\text{NH}_3/\text{HCN}$ ), which are strongly chemisorbed to the active phase could not be the reason for deactivation in this study, as a highly pure simulated syngas bottle was employed to perform the F-T activity. This deactivation occurred by the physical blockage of the cobalt active sites, modification of the metal's nearest neighbour, and/or catalyst surface reconstruction by reversible or irreversible poisons [40].

The Co-LTFT deactivation in this study could be ascribed to carbon deposition and fouling (physical deposition) by wax products, or from the fluid phase species which results in blockage of the pores and leads to lower selectivity towards desired products and higher selectivity towards methane. The performance of the catalyst could be affected by irreversible adsorption of carbon on the metal surface, which acts as poison and might influence the dissociative adsorption of neighbouring species [29-30]. The worst deactivation trend was observed for experiment EXP5, in which the deactivation rate of the catalyst was significantly high. In this experiment, the  $\text{C}_{5+}$  selectivity was decreased with time by 84.08 % (deactivation rate: 7% per hour) as the selectivity to methane kept increasing. Li et al [41] considered the stability of a Pt promoted  $\text{Co}/\text{Al}_2\text{O}_3$  catalyst and concluded that higher space velocity leads to lower water partial pressure and stable activity of the catalyst, which is in good agreement with the results of this investigation in some specific circumstances. Figure 5.6 (EXP6) illustrates that after exposure of the catalyst to syngas at 518 K, 10 bar and 2.4  $\text{NL}/\text{h.g}_{\text{cat}}$  running for 12 hours, the catalyst's relative activity in terms of  $\text{C}_{5+}$  selectivity was lowered by about 11%; which corresponded to a deactivation of about 0.9% per hour. The catalyst's activity as a function of exposure time to syngas kept increasing for the other experiments.

The increase in reactants' conversion could affect many aspects in the F-T fuel generator's design. Dissociative chemisorption of carbon monoxide is much stronger than hydrogen. The

composition and synthetic gas flow rate at the inlet; reactants' ( $H_2/CO$ ) usage ratio, based on F-T primary products; the extent in the WGS reaction activity, which is negligible in a cobalt-based F-T process; are some of the factors that influence the reactants' partial pressure and their concentration on the catalytic surface; and limited the increase in conversion per pass of carbon monoxide [42]. The trend in carbon monoxide consumption and products' selectivity are illustrated over the time on stream in Figure 5.6, in order to examine the effect of an increase in Co loading on the F-T process' stability. All of the experiments have shown a stable profile in F-T and WGS reaction activity.

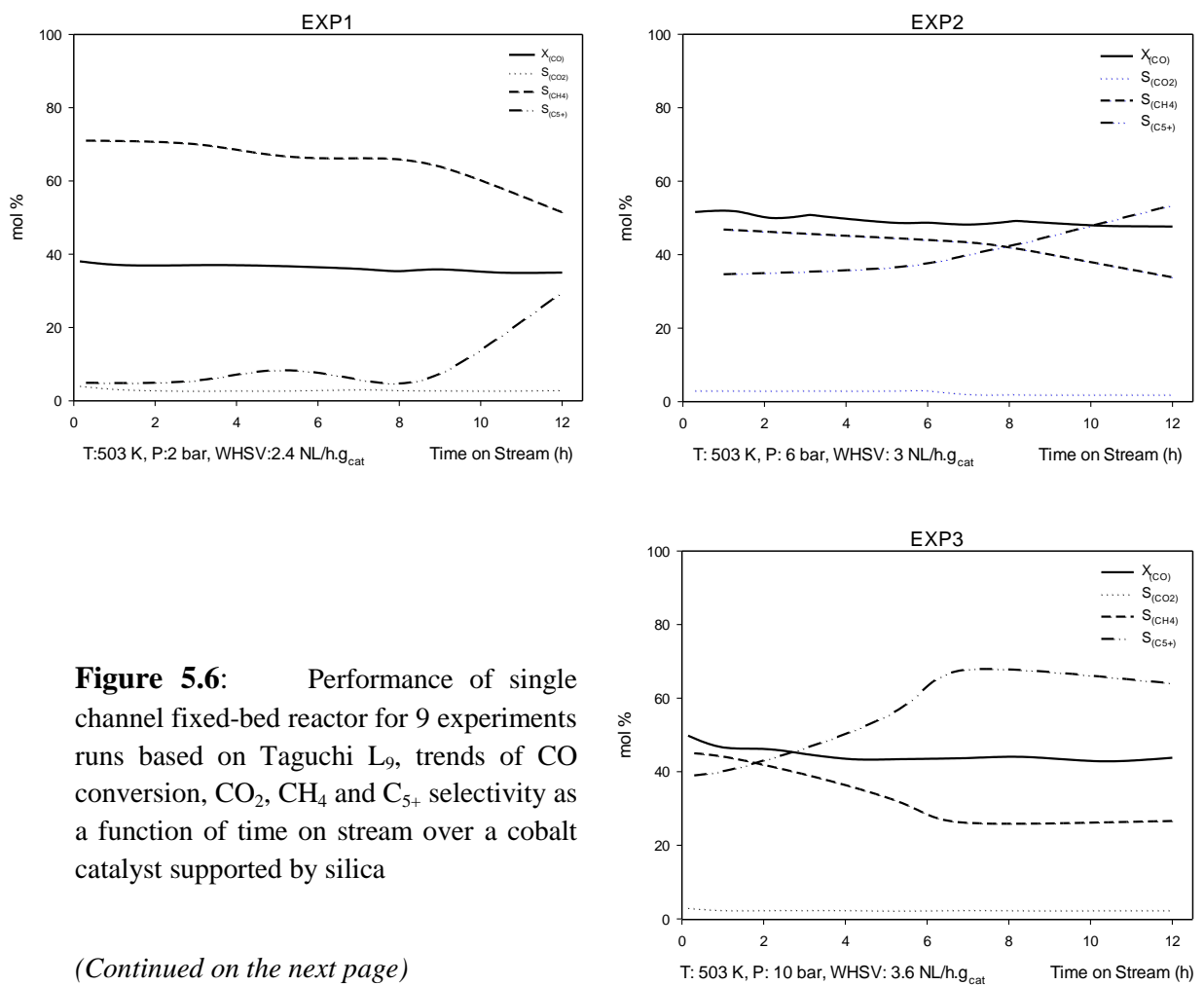
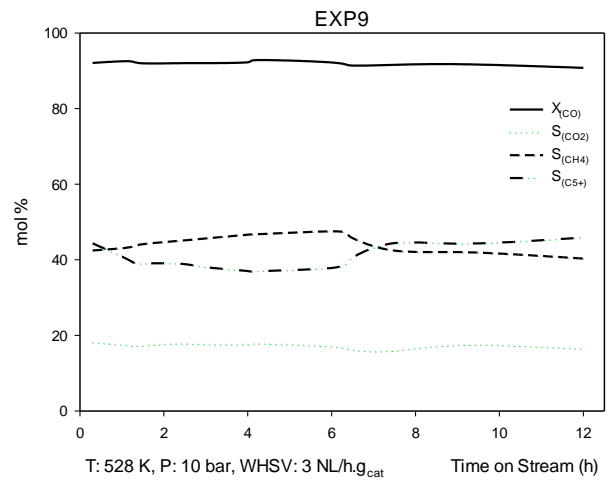
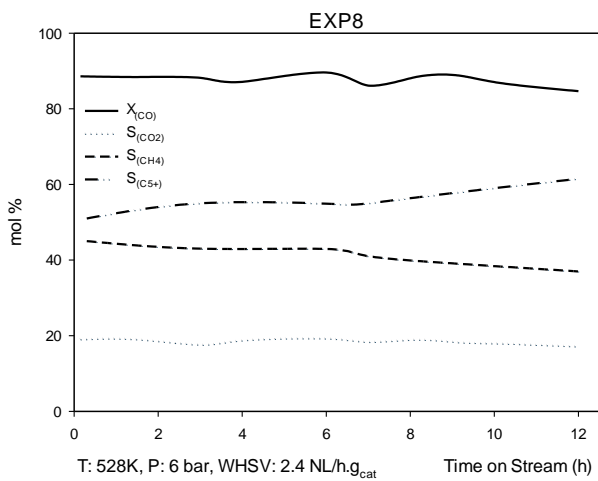
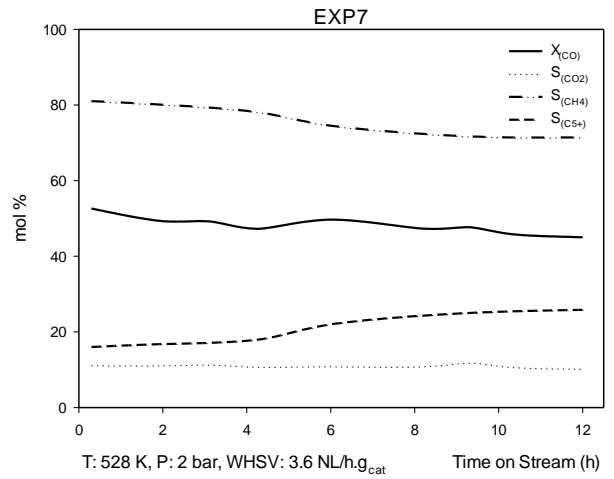
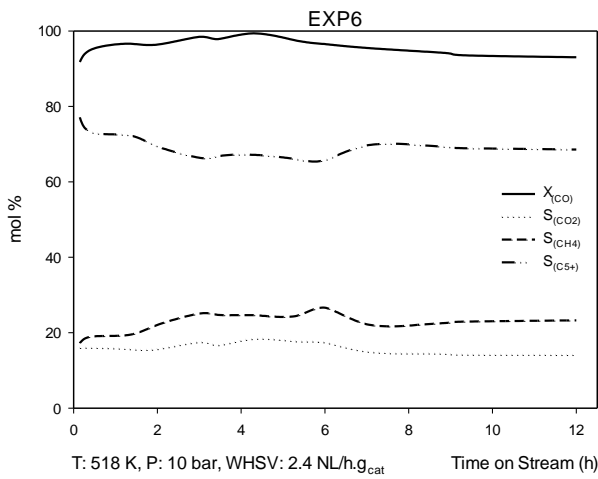
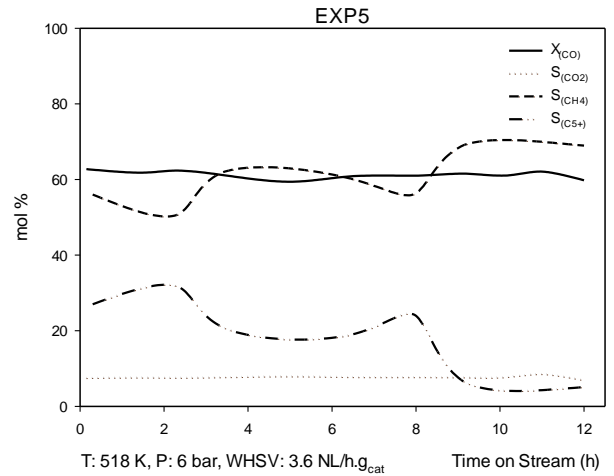
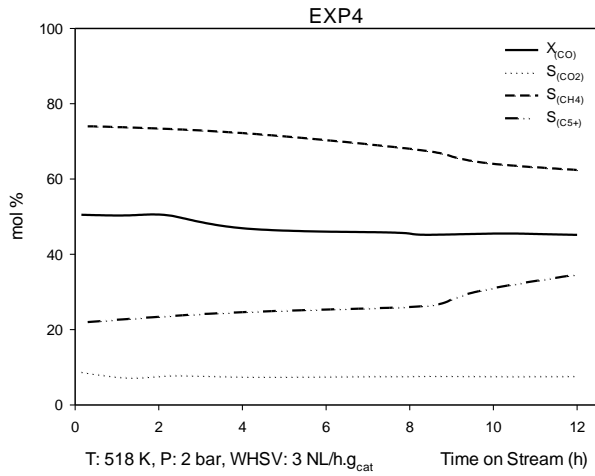


**Figure 5.6:** Performance of single channel fixed-bed reactor for 9 experiments runs based on Taguchi L<sub>9</sub>, trends of CO conversion, CO<sub>2</sub>, CH<sub>4</sub> and C<sub>5+</sub> selectivity as a function of time on stream over a cobalt catalyst supported by silica

(Continued on the next page)

Continuance of Figure 5.6



#### 5.4 Signal to Noise (SN) ratio, Analysis of Variance (ANOVA)

Table 5.2 summarizes the SN ratios for various runs with respect to different responses. The objective of this section is to select the optimum levels for the controllable system parameters. The Taguchi method was employed to estimate the main effect of temperature, followed by total pressure and space velocity, on the system's performance and approach the best combination of control factors to optimise the quality characteristics using SN ratio.

Figure 5.7 represents the mean of the SN ratio's plots for different control parameters (Temperature: T, Pressure: P, WHSV: W) studied at three control levels with respect to different responses; and also illustrates the value for R-Squared (R-Sq) determined by ANOVA, to examine the contribution percentage of individual parameters and their effect on the entire process.

**Table 5.2:** Significance of control factors on responses utilizing Signal-to-Noise ratio

Run	SNRA1** R: $X_{(CO)}$	SNRA2* R: $S_{(CO_2)}$	SNRA3* R: $S_{(CH_4)}$	SNRA4** R: $S_{(C_5^+)}$	SNRA8** R: $LP$
EXP1	30.8789	-9.2180	-34.2243	29.4141	0.7406
EXP2	33.5613	-5.1536	-30.5835	34.5590	8.7328
EXP3	32.8275	-7.1967	-28.4976	36.1236	9.0511
EXP4	33.0951	-17.6391	-35.8995	30.7865	4.6243
EXP5	35.8604	-18.6088	-36.7694	14.0796	10.1409
EXP6	39.3725	-22.9844	-27.3359	36.7214	9.3964
EXP7	33.0681	-20.2060	-37.0776	28.2425	-0.7716
EXP8	38.5525	-24.6650	-31.3546	35.7761	2.7850
EXP9	39.1598	-24.2863	-32.1039	33.2306	6.8603

\* Smaller is better

\*\* Larger is better

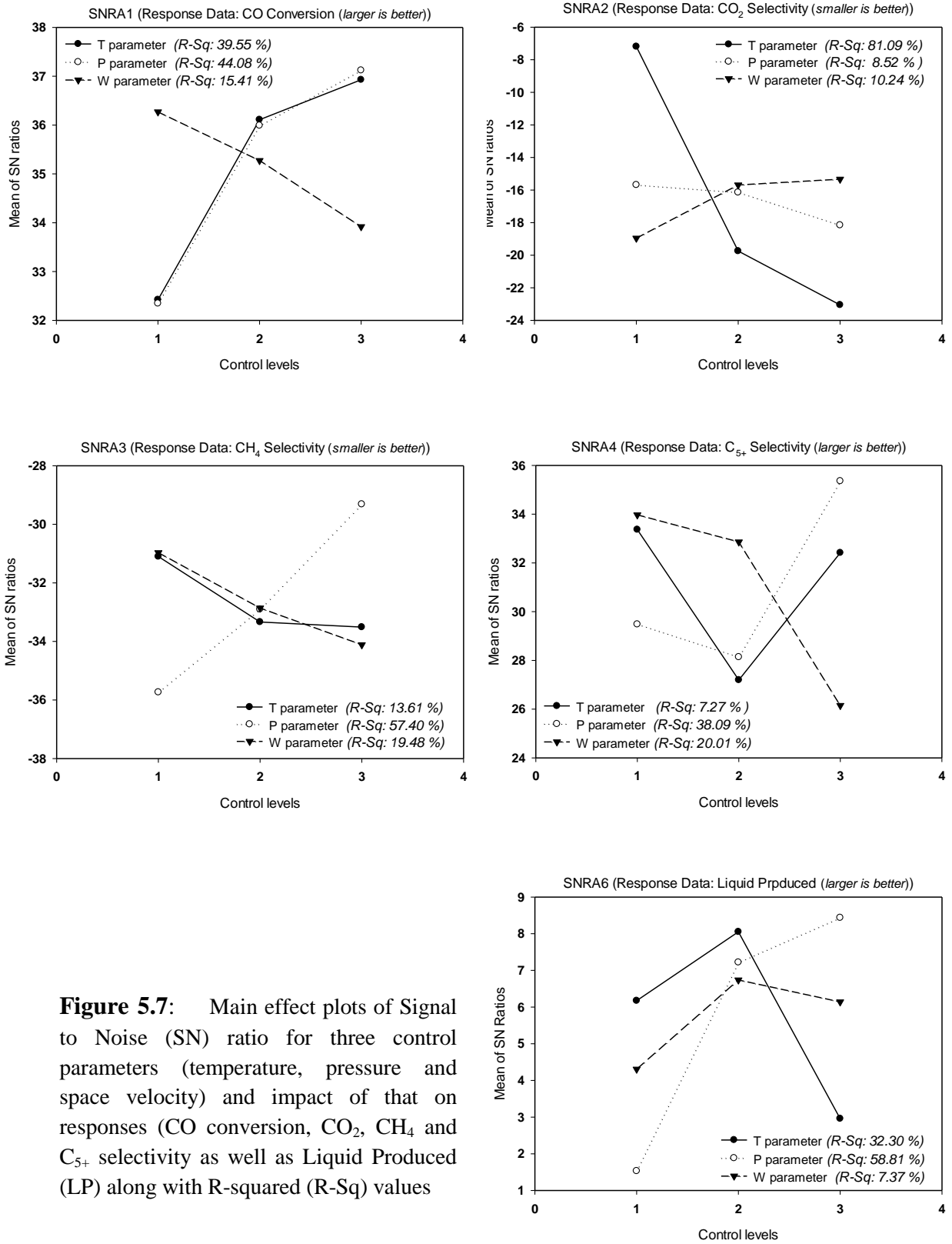


**Figure 5.7:** Main effect plots of Signal to Noise (SN) ratio for three control parameters (temperature, pressure and space velocity) and impact of that on responses (CO conversion, CO<sub>2</sub>, CH<sub>4</sub> and C<sub>5+</sub> selectivity as well as Liquid Produced (LP) along with R-squared (R-Sq) values

Examination of the SN ratio's plots reveal that the increases in parameter level settings for the T and P parameters had a very positive influence on the quality characteristics of  $X_{(CO)}$ ; whereas the mean of the SN ratio decreased for W parameter in general (Figure 5.7: SNRA1). As shown in Figure 5.7, the parameter level setting for P3 (mean: 37.1199) had the largest effect on the  $X_{CO}$  response. In terms of  $X_{CO}$  response, clearly all of the parameters should be set at T3, P3 and W1 to optimise the CO conversion (mean of SN ratio: 36.9268, 37.1199 and 36.2680 respectively). The P and T parameters had the most percentage contribution on the output value, allocating 44.08 % and 39.55 % R-Sq values respectively.

As shown in Figure 5.7 (SNRA2 and SNRA3), in terms of  $S_{CO_2}$  and  $S_{CH_4}$ , the best responses for the SN ratios can be concluded when the factors are set at level T1, P1 and W3 and T1, P3 and W1 to minimise the impact of these responses as undesirable co-products' selectivity, respectively. The responses are deeply impacted by the variation in T (mean of SN ratio for T1: -7.1894 and T3: -23.0524) and P (mean of SN ratio for P1: -35.7338 and P3: -29.3125) control factors respectively.

The R-Squared of the parameters indicate that temperature and pressure significantly contribute towards  $CO_2$  and  $CH_4$  selectivity. Figure 5.7 (SNRA4 and SNRA5) demonstrates the main effect plots of the SN ratio with respect to  $S_{C_{5+}}$  and LP responses. The optimum levels for the control factors should be set at T1, P3 and W1 to reach the highest quality characteristics of  $S_{C_{5+}}$  response. Clearly it is observed from the figure that the highest and lowest liquid products were yielded by the variation in the P parameter (P1: 1.53109 and P3: 8.43593). The best parameter for liquid production was found for space velocity (R-Sq: 58.81 %). The results are well-matched with the Taguchi method's results obtained from experiments.

## 5.5 Conclusion

An optimisation study on synthetic gas conversion to F-T synthetic fuel was carried out in order to find optimum reaction conditions and the best combination of fixed bed reactor, cobalt catalyst supported by silica and operating philosophy at low pressure (P: 2-10 bar) and temperature (T: 503-528 K), to maximise diesel fuel generation. The Taguchi method ( $L_9$  ( $3 \times 3$ )), with a combination of Signal to Noise (SN) ratio and ANOVA, were used to design an experiment and furthermore find the optimum operational parameters and their impact and contribution in various responses respectively. The catalyst's deactivation trend was considered within the first reaction cycle for each experiment to examine the catalyst's performance over the time.

It was concluded that operating at low pressure could increase the direct CO conversion to  $\text{CH}_4$ ; whereas the WGS activity is decreased. With respect to reactant conversion, product selectivity and liquid fuel production, the optimum reaction conditions were found to be at 518 K, 10 bar and 2.4 NL/h.g<sub>cat</sub> and 503K, 6 bar and 3 NL/h.g<sub>cat</sub>. These conditions demonstrated a stable F-T performance and negative catalyst deactivation rate over the time exposed to the reactants and liquid/gas products' species. This study was accomplished to reach a cost effective F-T process, with an optimal combination of F-T operational parameters, in order to scale up the process to produce transportable fuel for individual consumption, as future work.



---

# Chapter 6

---

## PROCESS OPTIMIZATION AT

### HIGH-PRESSURE REACTION CONDITION

The aim of this study was to achieve the most efficient combination of a fixed-bed reactor and cobalt catalysts at a medium-range pressure reaction condition. Hence, the attempt was made to optimize the FTS process using cobalt catalysts supported by silica. The optimization variables were pressure (10 - 25 Bars), temperature (503 - 543 K) and space velocity (1.8 – 3.6NL/h.g<sub>catalyst</sub>), to examine the effect of these parameters on product distribution. A thermodynamic study of the FTS process will result in an effective use of cobalt catalysts, taking into consideration the high cost of the cobalt precursor. The optimization study gives an understanding into the effect of reaction thermodynamics in selectivity and productivity, in terms of carbon number, with optimization parameters using nitrogen-rich syngas with a volumetric ratio of 17% carbon monoxide, 33% hydrogen and 50% nitrogen. In this study, it was decided to utilize the maximum capacity of the silica support to load the cobalt precursor, so that it reached a higher conversion of carbon monoxide as well as higher productivity of liquid hydrocarbons.

## 6.1 *Experimental results*

The aim of this investigation was to find the best combination of Co/SiO<sub>2</sub> catalyst, fixed bed reactor and operating conditions to attain the particular objective; this was to achieve the optimal F-T technology with a combination of operating regime and catalyst formulation to produce bio diesel from syngas for individual consumption. Fischer-Tropsch Synthesis is a very sensitive process towards operational parameters. Synthesis conduction as well as the Fischer Tropsch catalyst could manipulate the syncrude composition. In fact, the synthesis step within an efficient F-T refinery process could directly influence the product quality and selectivity. The attempt was made to reach the highest conversion of carbon monoxide per pass of syngas simultaneously with higher selectivity of heavy hydrocarbon and productivity of liquid hydrocarbons. This achievement could influence many aspects of reactor and gas loop design and make the process cost-effective.

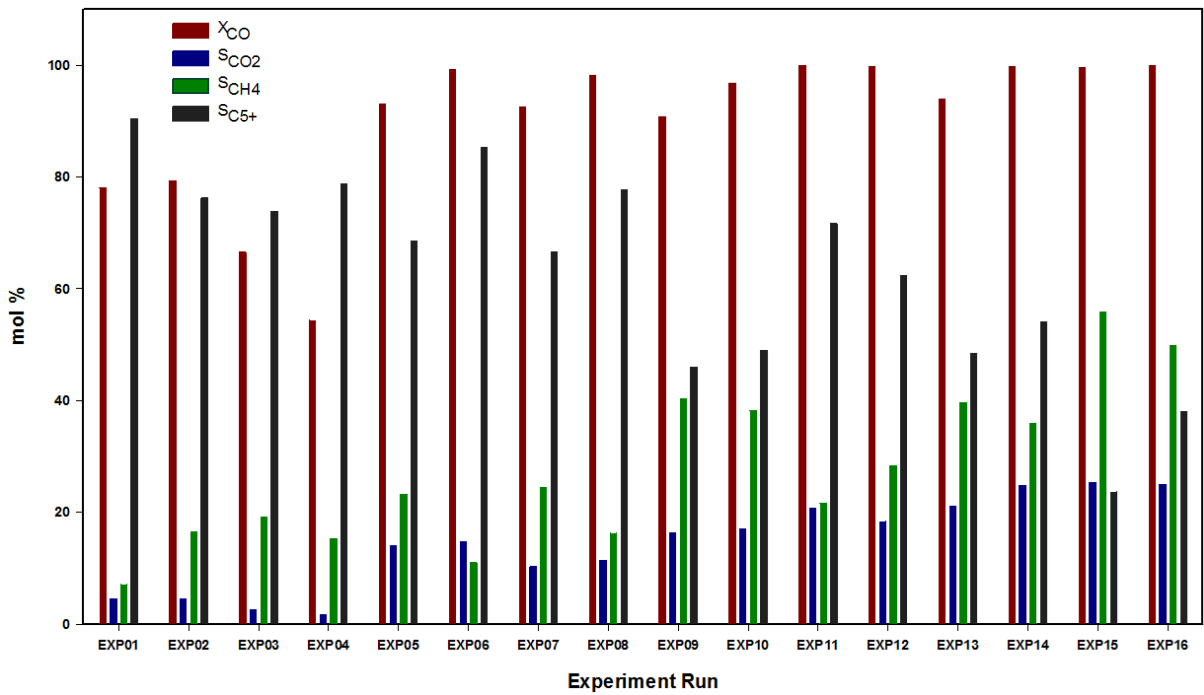
Table 6.1 shows the experimental data collected from 16 experiments run based on the Taguchi L<sub>16</sub> DOE (discussed in Chapter 3, section 3.2.3); and for each of the experiments, the conversion of carbon monoxide ( $X_{(CO)}$ ), selectivity of carbon dioxide ( $S_{(CO_2)}$ ), methane selectivity ( $S_{(CH_4)}$ ), C<sub>1</sub> – C<sub>4</sub> and C<sub>5+</sub> hydrocarbons' selectivity ( $S_{(C_{5+})}$ ) have been illustrated. The gaseous products were analysed quantitatively using GC-FID. The liquid products were analysed qualitatively by GC-MS and the mass fraction for the cut of C<sub>7</sub> - C<sub>11</sub> (gasoline part), C<sub>12</sub> - C<sub>22</sub> (diesel products) and C<sub>23+</sub> (wax products) have been represented in Table 6.1. After each experiment, nitrogen gas was flushed into the reactor to extract the remaining produced liquid; the amount of liquid produced (LP) in each experiment is tabulated in Table 6.1. The rates of reactions are given in this table as well to describe the carbon monoxide consumption rate. Figures 6.1 and 6.2 support Table 6.1 by providing comparative bar charts.

**Table 6.1:** Experimental data, changes in CO concentration ( $X_{CO}$ ), carbon dioxide selectivity ( $S_{CO_2}$ ), methane selectivity ( $S_{CH_4}$ ) as well as hydrocarbon selectivity, liquid phase mass fraction ( $W_i$ ), rate of reaction and Liquid Produced (LP) for 16 experiments run based on Taguchi  $L_{16}$

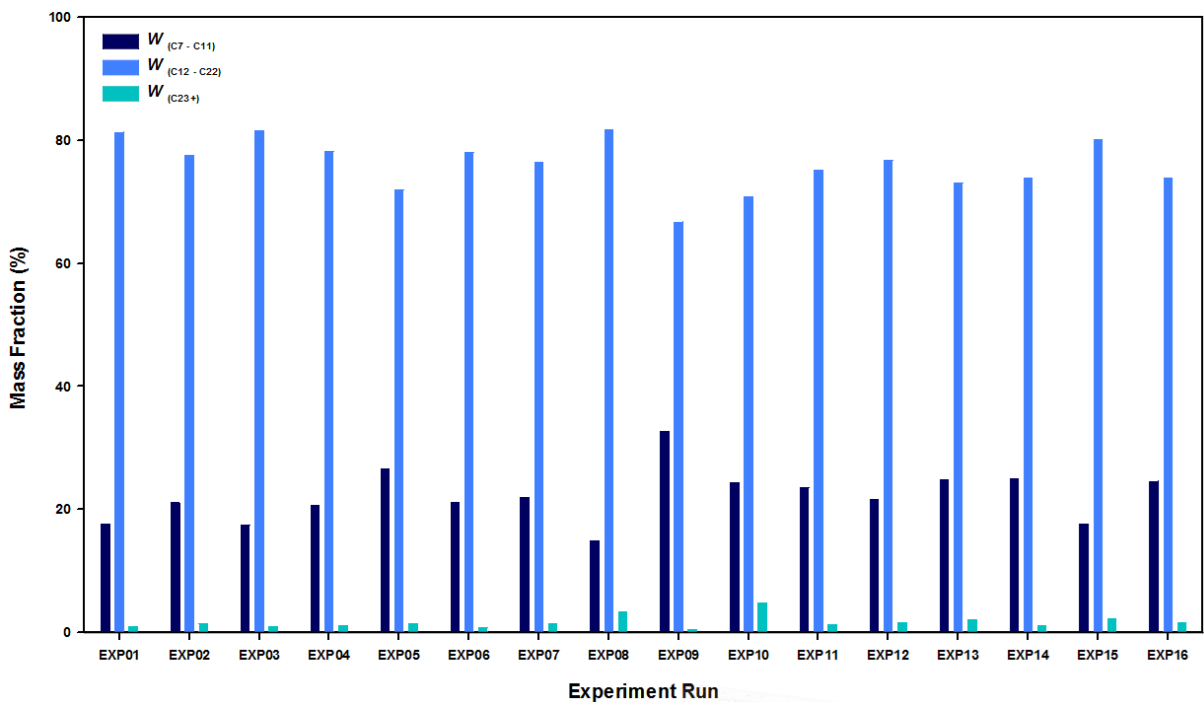
Exp. Run	Selectivity of gas phase products (%)						
	$X_{CO}$	$S_{CO_2}$	$S_{CH_4}$	$S_{C_2}$	$S_{C_3}$	$S_{C_4}$	$S_{C_{5+}}$
EXP01	78.04	4.52	7.062	0.582	1.001	0.9009	90.454
EXP02	79.34	4.46	16.58	1.465	2.785	2.934	76.236
EXP03	66.55	2.63	19.20	1.517	2.901	2.531	73.851
EXP04	54.34	1.72	15.32	1.274	2.512	2.176	78.708
EXP05	93.03	14.1	23.27	2.277	3.138	2.743	68.569
EXP06	99.15	14.68	10.96	1.053	1.475	1.218	85.310
EXP07	92.52	10.25	24.38	2.376	3.477	3.241	66.526
EXP08	98.22	11.45	16.24	1.584	2.411	1.970	77.783
EXP09	90.78	16.38	40.29	3.856	5.372	4.600	45.878
EXP10	96.81	17.05	38.24	3.891	4.660	4.274	48.924
EXP11	99.96	20.70	21.61	2.053	2.532	2.141	71.656
EXP12	99.74	18.34	28.25	2.777	3.521	3.039	62.407
EXP13	93.95	21.01	39.65	3.738	4.607	3.621	48.376
EXP14	99.74	24.75	35.88	3.450	3.640	2.995	54.025
EXP15	99.59	25.36	55.81	10.687	5.551	4.335	23.621
EXP16	99.88	24.93	49.79	4.535	4.320	3.442	37.982

Exp. Run	$W_i$ (liquid phase)			Rate of Reaction ( $mol/min.g_{cat}$ )	LP (ml)
	$C_7 - C_{11}$	$C_{12} - C_{22}$	$C_{23+}$		
EXP01	17.66	81.35	0.99	0.0001430	2.367
EXP02	21.06	77.55	1.39	0.0003040	2.360
EXP03	17.52	81.53	0.95	0.0005040	3.134
EXP04	20.69	78.19	1.12	0.0007580	2.125
EXP05	26.64	71.96	1.40	0.0002200	2.540
EXP06	21.12	78.08	0.80	0.0004730	2.440
EXP07	21.98	76.53	1.49	0.0007220	5.443
EXP08	14.91	81.70	3.39	0.0011980	4.450
EXP09	32.76	66.76	0.48	0.0002890	2.527
EXP10	24.35	70.89	4.76	0.0006244	3.821
EXP11	23.58	75.14	1.28	0.0010600	2.183
EXP12	21.56	76.78	1.66	0.0015920	3.470
EXP13	24.85	73.09	2.06	0.0004976	2.137
EXP14	25.035	73.93	1.04	0.0009234	2.314
EXP15	17.62	80.12	2.26	0.0015800	2.194
EXP16	24.59	73.84	1.57	0.0023760	1.060



**Figure 6.1:** A comparison in conversion of carbon monoxide ( $X_{CO}$ ), selectivity of carbon dioxide ( $S_{CO_2}$ ), methane ( $S_{CH_4}$ ) and heavy hydrocarbon ( $S_{C_5+}$ ) for 16 experiments run based on Taguchi  $L_{16}$



**Figure 6.2:** A comparison in composition of different hydrocarbons cuts ( $C_7-C_{11}$ ,  $C_{12}-C_{22}$ ,  $C_{23+}$ ) in liquid products analysed qualitatively by GC-MS for 16 experiments run based on Taguchi  $L_{16}$  DOE

### 6.1.1 The rate of reaction

A number of kinetic studies of the Fischer-Tropsch synthesis over cobalt catalysts have been performed [63, 159-161]. All of the expressions found to fit the rate data on these catalysts show that carbon monoxide inhibits the rate of synthesis. However, a wide array of proposed forms for the rate expression exist, which is partly a result of the considerable variation in reaction conditions studied. Furthermore, some studies, particularly the earlier work, were performed in fixed-bed reactors. Integral kinetic data from a complex reaction such as the Fischer-Tropsch synthesis cannot be interpreted easily and a fixed-bed reactor may be difficult to maintain isothermally. In other cases, data are reported only for very low conversions [162]. Various kinetic equations of FTS based on cobalt catalysts have been proposed and are summarized [163]. The equation which was used to describe the CO consumption rate, the lumped kinetic equation, is as follows:

$$R_{CO} = \frac{kP_{H_2}P_{CO}}{(1 + K_{H_2}P_{H_2} + K_{CO}P_{CO})^2} \quad (6.1)$$

$$K = 2.89 \times 10^{-5} \exp \left[ \frac{-59.3 \times 10^3}{R} \left( \frac{1}{T} - \frac{1}{503.15} \right) \right] \quad (6.2)$$

$$K_{H_2} = 1.56 \times 10^{-4} \exp \left[ \frac{26.9 \times 10^3}{R} \left( \frac{1}{T} - \frac{1}{503.15} \right) \right] \quad (6.3)$$

$$K_{CO} = 3.53 \times 10^{-2} \exp \left[ \frac{24.2 \times 10^3}{R} \left( \frac{1}{T} - \frac{1}{503.15} \right) \right] \quad (6.4)$$

It is worth noting that, although the simplified reaction rate may lead to an over- or under-estimation problem, this model with appropriately estimated kinetic parameters satisfactorily performs to predict the profiles of CO conversion and temperature in the present reactor. For

the development of the reactor model in the present study, kinetic parameters of the lumped model need to be estimated [163]. As this model is not a mechanistic description of the synthesis, a conclusion concerning the catalyst formulation could not be drawn. The lumped equation experiment's condition is a detailed three-dimensional modeling of a channel type reactor with a plate heat exchanger for cobalt-based FTS. In this study, a cobalt-based catalyst was carried out in a tubular mini-structured downdraft fixed bed reactor, which is similar to the lumped equation experiment's boundary conditions.

## ***6.2 Effect of reaction conditions on F-T synthesis process***

### ***6.2.1 Effect of temperature***

The performance of the Co/SiO<sub>2</sub> catalyst was detected during the experiment to investigate the effect of each of the parameters on the activity of the F-T synthesis as well as the WGS reactions. The experimental results show that the activities of these two reactions increased with the increase in temperature. The change in conversion and selectivity of carbon monoxide and carbon dioxide are represented in Figures 6.3 and 6.4 respectively, as the function of pressure, temperature and space velocity. The results confirm that F-T reaction is very sensitive to the reaction temperature and that of the syngas conversion is greatly affected by the temperature. The figures also demonstrate that activity of the catalyst in terms of CO conversion and CO<sub>2</sub> selectivity was at a maximum (99.96 and 25.36 mol% respectively) at higher temperature and at a minimum (54.34 and 1.72 mol% respectively) at the lower temperature (503 K). The amount of CO consumption was increased strongly from 503 K to 518 K (54.34 to 93.03 mol%) by an increase in CO adsorption rate and it increased slightly from 518 to 543 K (90.78 to 99.96 mol%). Lower activity of the cobalt catalyst in the WGS

reaction at optimal hydrogen to carbon monoxide ratio is a remarkable superiority of this catalyst. Carbon dioxide is the final product of cobalt-based F-T synthesis [56]. The increase in CO<sub>2</sub> content as a diluent decreases the CO content and leads to lower activity of the F-T reaction; higher activity of the methanation reaction; and changes the product composition, by dominating the F-T regime caused by selective inhibition [157]. The highest methane selectivity was reported for EXP15 which was carried out at 543 K, 20 bar and 2.4 NL/h.g<sub>cat</sub> and allocated the highest WGS reaction activity by consuming 25.36 mol% of converted CO. A higher F-T reaction temperature resulted in smaller mean chain length F-T products and produced more methane and lighter hydrocarbons as well as less liquid diesel fuels and wax products. Figures 6.5 (a) and (b), and 6.6 (a) and (b) support this elucidation and indicate the variation of methane and C<sub>5+</sub> selectivity with change in temperature. Product desorption rate in F-T reaction is affected by temperature. An increase in temperature results in an increase in chain termination, which is the consequence of the higher endothermic desorption process on the crystal surface [29].

Two significant trends are apparent from Figures 6.7 and 6.8, which represent hydrocarbon distribution of F-T synthesis on liquid products as a function of temperature, pressure and WHSV; and they corroborate this explanation. With an increase in the temperature, the F-T product composition was changed from C<sub>2+</sub> hydrocarbons to the methanation type product (only methane) given in Table 6.1. It was found that an increase in the bed temperature from 503 to 543 K resulted in an increase in methane selectivity from 7.062 mol% (EXP01) to 55.81 mol% (EXP15). The highest C<sub>5+</sub> selectivity was reported for EXP01 which was 90.454 mol%. It was also found that with an increase in methane formation reaction activity, the C<sub>5+</sub> selectivity was decreased and reached its lowest content at the highest temperature (23.621 mol %).

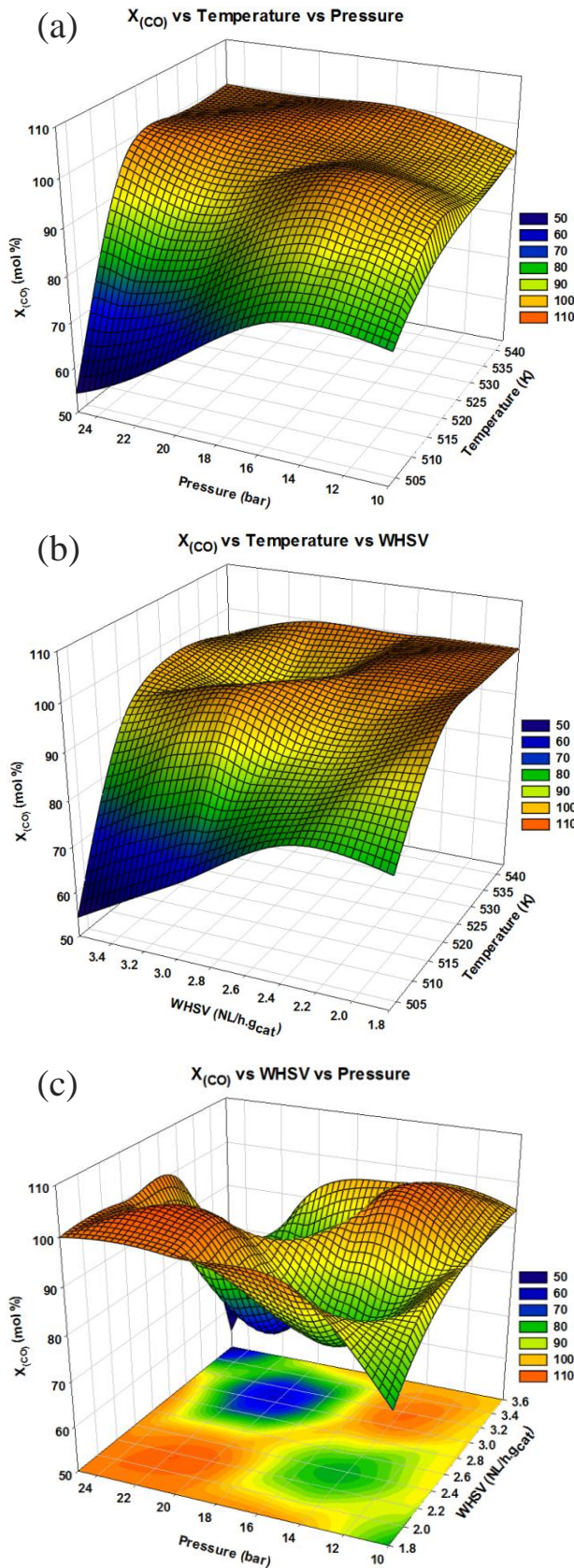


**Figure 6.3:** Effect of synthesis reaction conditions on CO conversion. Reaction conditions; P: 10 - 25 bar, T: 503 - 543 K, WHSV: 1.8 - 3.6 NL/h.g<sub>cat</sub>

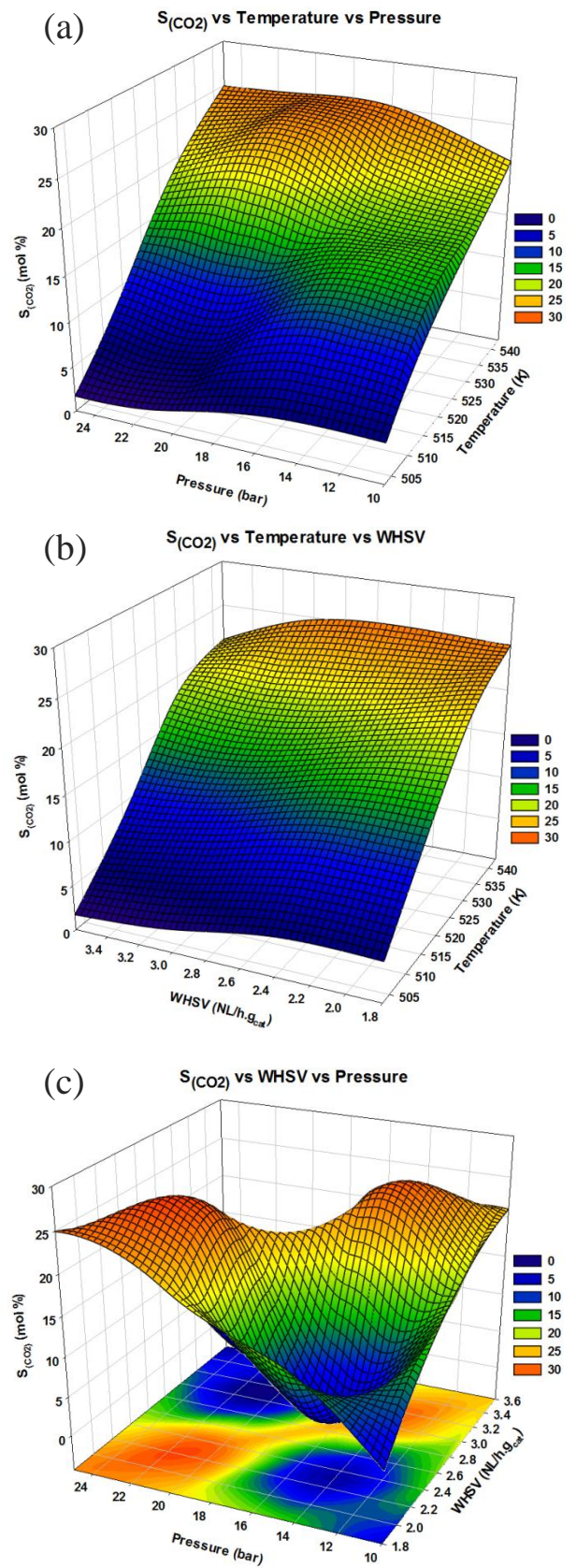


**Figure 6.4:** Effect of synthesis reaction conditions on CO<sub>2</sub> selectivity. Reaction conditions; P: 10 - 25 bar, T: 503 - 543 K, WHSV: 1.8 - 3.6 NL/h.g<sub>cat</sub>

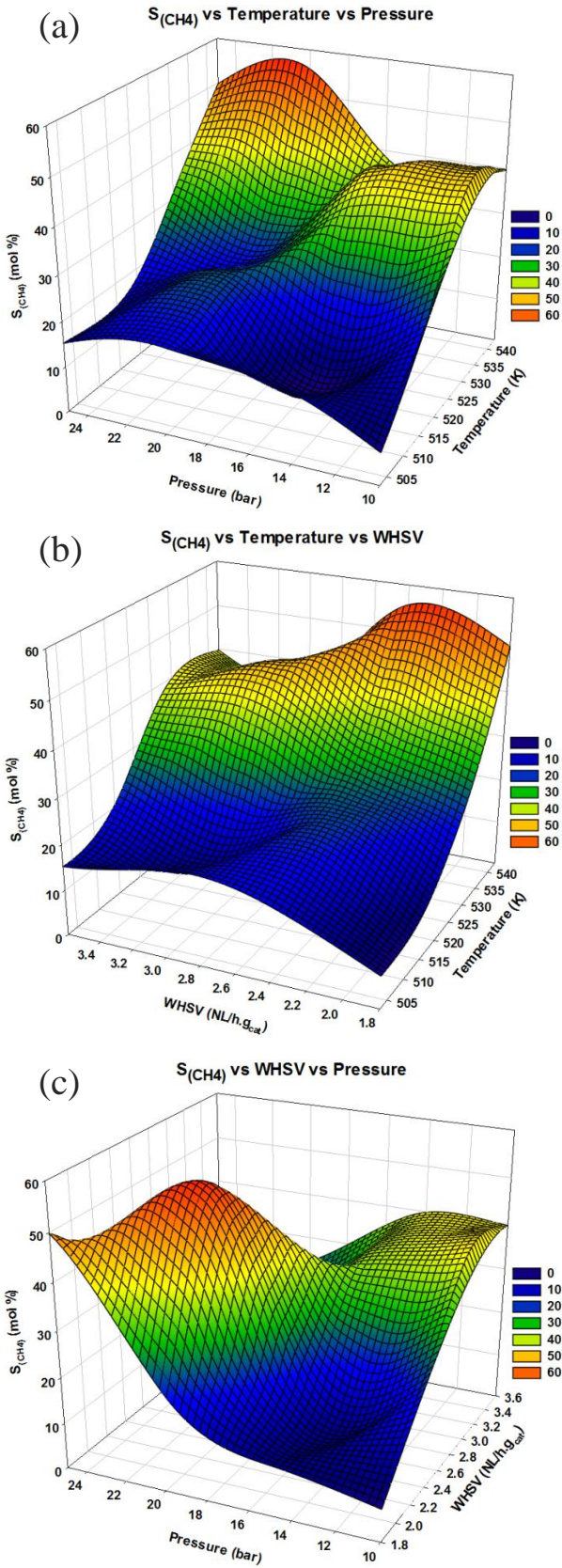


**Figure 6.5:** Effect of synthesis reaction conditions on methane selectivity. Reaction conditions; P: 10 - 25 bar, T: 503 - 543 K, WHSV: 1.8 - 3.6 NL/h.g<sub>cat</sub>

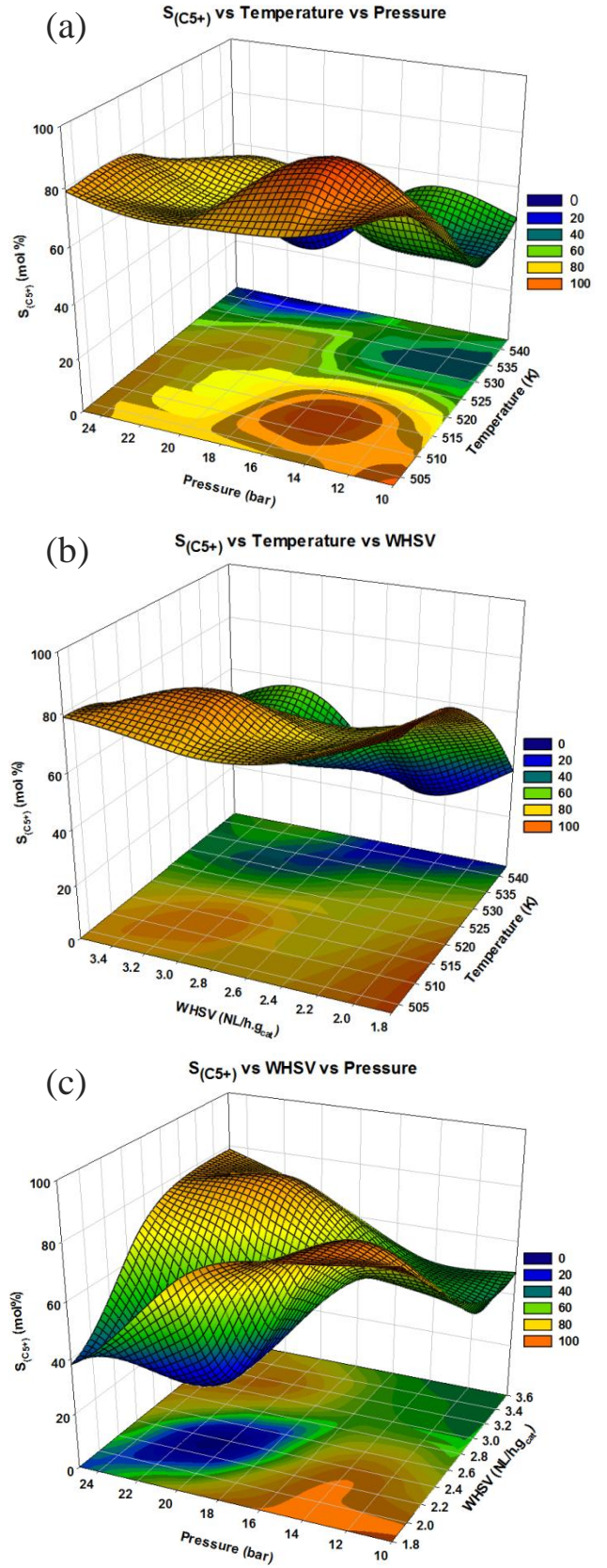


**Figure 6.6:** Effect of synthesis reaction conditions on C<sub>5+</sub> hydrocarbons selectivity. Reaction conditions; P: 10 - 25 bar, T: 503 - 543 K, WHSV: 1.8 - 3.6 NL/h.g<sub>cat</sub>

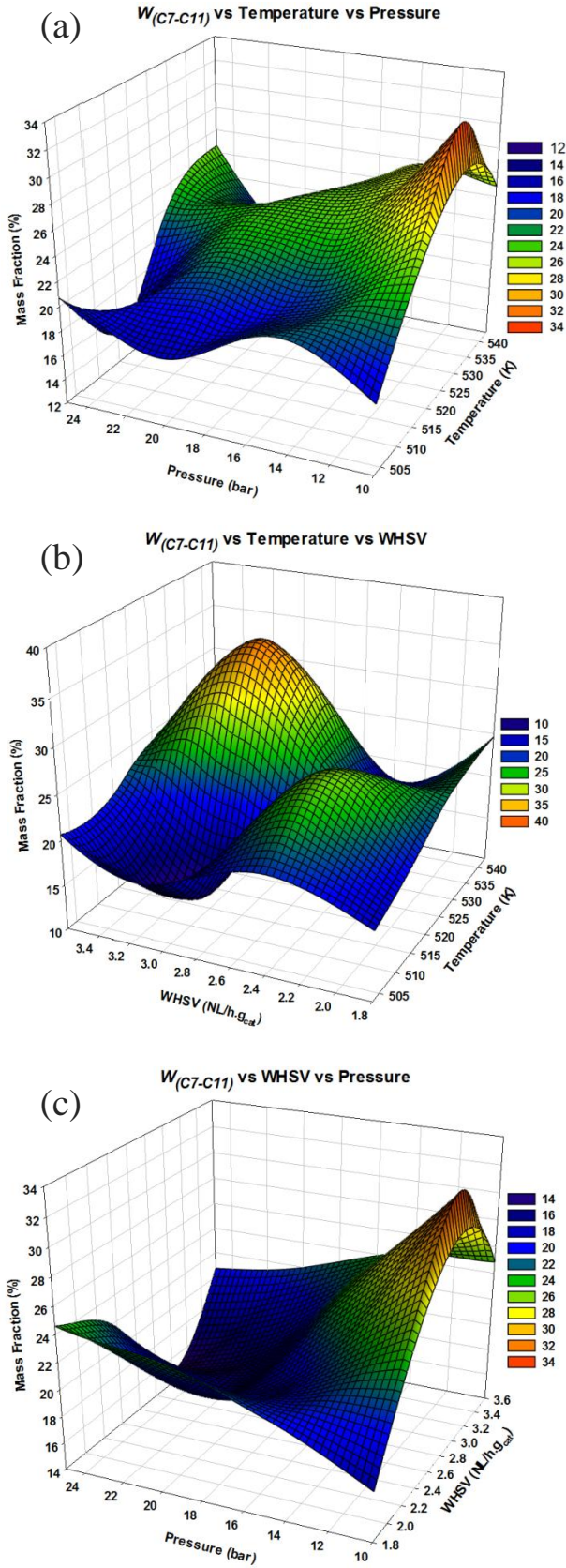


**Figure 6.7:** Effect of synthesis reaction conditions on C<sub>7</sub>-C<sub>11</sub> HC cut. Reaction conditions; P: 10 - 25 bar, T: 503 - 543 K, WHSV: 1.8 - 3.6 NL/h.g<sub>cat</sub>

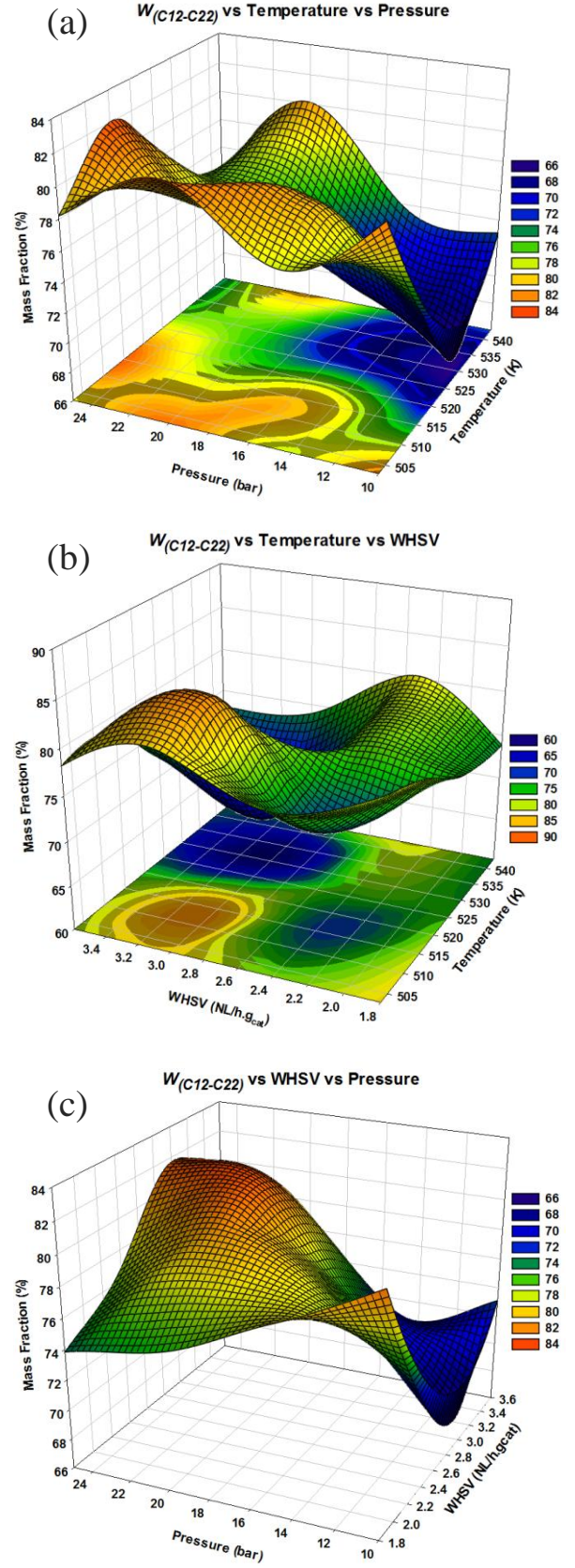


**Figure 6.8:** Effect of synthesis reaction conditions on C<sub>12</sub>-C<sub>22</sub> HC cut. Reaction conditions; P: 10 - 25 bar, T: 503 - 543 K, WHSV: 1.8 - 3.6 NL/h.g<sub>cat</sub>

This increase in temperature could lower the production of olefins and oxygenated products by controlling the initiation, growth of carbon chain and enhancing the chain termination. On the other hand, more hydrogenated products (alkanes) can be obtained as an impact of the temperature rise which causes chain termination influenced by the carbide carbon hydrogenation rate. Therefore, the reaction process should be governed so that the rate of desorption is increased and the  $\alpha$ -value is reduced to obtain qualified fuel [29].

The hydrogen to carbon monoxide ratio was 2 in this study, which was the desired usage ratio in the synthesis reactor to produce hydrocarbon with a carbon number ranging from 10 to 20; and the syngas was balanced with nitrogen to simulate bio syngas; the produced water could be converted to carbon dioxide at a higher temperature. Utilization of nitrogen-rich syngas (volumetric percentage of N<sub>2</sub>: 50) leads to a reduction in the production cost of diesel oil by eliminating the need for the application of gas recycling loop after production of syngas by air partial oxidation. The waste generated heat of the F-T reaction, could be removed effectively by nitrogen gas and this role of nitrogen as an inert in the F-T regime, could result in an increase in the tube diameter of the reactor and a decrease in the number of tubes of the F-T generator, without danger of temperature runaway [77]. For this purpose, the Water Gas Shift reaction activity must be lowered as much as possible to prevent usage of syngas and changing in partial pressure of WGS compounds, which could significantly affect the catalyst activity and stability. Otherwise, the increase in conversion will cause a change in the CO:H<sub>2</sub> ratio and catalyst deactivation would be inevitable [29]. The consumption ratio of hydrogen and carbon monoxide in the hydrogenation and polymerization process of F-T synthesis is dependent on the final products of the process. To produce bio-diesel, as the main product becomes heavier, the usage ratio of hydrogen to carbon monoxide is approximated to 2 [164]. The higher ratio of hydrogen to carbon monoxide resulted in lower alkenes and the

oxygenated product's selectivity, by decreasing the chain growth probability as a result of the increase in the hydrogenation driving force. The increase in this ratio could cause higher activity of the methane formation reaction and result in higher selectivity of this co-product. The literature shows that the cobalt catalyst works well when the H<sub>2</sub>/CO ratio is near 2 and yields in the production of long chain HCS [29, 164].

### **6.2.2 Effect of pressure**

Adsorption of carbon monoxide on the catalyst surface initiates the F-T reaction. Carbon monoxide is chemisorbed initially in a bridge mode, involving two surface sites of the catalyst and also is equilibrated with a linear mode, involving only one site of the surface. Hydrogen is chemisorbed and dissociated on the surface site [26]. Carbon monoxide is adsorbed more forcefully than the hydrogen on the catalytic surface sites [29].

Each of the catalysts owns its particular operating pressure range. Cobalt-based LTFT process is catalysed at a pressure ranging from 1 to 60 bar. Cobalt catalyst forms metal carbonyl at above 30 bar pressure by the reacting of carbon monoxide with the metal surface because of the strong reaction of the metal surface with carbon monoxide [153]. F-T reactions are greatly affected by pressure. The increase in the total pressure of reagents, hydrogen and carbon monoxide, specifies the partial pressure of each of the reactants and results in a higher concentration of carbon monoxide on the catalytic surface. The results indicate that the increase in total pressure at the lower temperature resulted in lower conversion of carbon monoxide. It is the case that this increase at low space velocity, increased the conversion of carbon monoxide by increasing the concentration of reactants, as shown in Figure 6.3 (a, b

and c) and is explained by the fact that the change in partial pressure of carbon monoxide leads to an alteration in space velocity at the same time, due to the change in total flow [165].

The methane selectivity declined at high space velocity and was enhanced at low space velocity with the increasing of the pressure (Figure 6.5). The yields of the diesel range and wax products from the low-temperature F-T generator were improved when the pressure was increased. The higher partial pressure and concentration of carbon monoxide at lower temperature resulted in a higher production of long chain heavy hydrocarbons and lowered the production of light hydrocarbons, which is illustrated in Figures 6.7 and 6.8. Therefore, with the increasing of the total pressure, it has been noticed that product selectivity was shifted to heavier hydrocarbons. By this increase in partial pressure, which is combined with the composition of feedstock and hydrogen to carbon monoxide ratio, the chain growth and the catalyst's observed  $\alpha$ -value are promoted, which are a consequence of high CO concentration and leads to production of more oxygenated products [29]. It has been reported that the catalyst's lifetime is increased by increasing the operating pressure range of the F-T process from normal-pressure synthesis to medium-pressure synthesis (10 – 30 bar), caused by the condensed products' solvent action in the F-T reactor [166].

### **6.2.3 Effect of WHSV**

The results show that enhancement of space velocity has a considerable influence on reactants' conversion, by-products' selectivity, as well as light and heavy hydrocarbons' productions, which are in accordance with the kinetics and thermodynamics of F-T synthesis. The reactants' conversion was decreased by the increasing of WHSV, which is related to the lower residence time of carbon monoxide at higher pressure. The results provided evidence

that at low pressure, the increase in space velocity resulted in a slight increase in CO conversion, because of the higher concentration of CO on the catalytic surface given in Figure 6.3 c. It was found that there was a slight increase in the conversion of carbon monoxide at high temperature with the increase of space velocity. Figure 6.6 shows that high WHSV was caused by higher production of heavy hydrocarbons, particularly  $C_{5+}$ , by eliminating the mass diffusion limitation that leads to removal of heavier hydrocarbons from the catalyst surface by diffusion. Figures 6.7 and 6.8 indicate the alteration in the mass percent composition of gasoline and diesel liquid products. They also ascertain this phenomena, that the higher molecular weight compounds are enhanced by enhancing the surface species, as a result of the increase in WHSV and lowering the production of low molecular weight hydrocarbons at lower temperature and higher pressure [24].

The chain growth polymerization termination step takes place when the adsorbed chains  $-HC-(CH_2)_{n-2}-CH_3$  are combined with adsorbed surface  $CH_3$  or surface H and then released, which yields the alkanes' products and when the empty surface sites are released, yield the alkenes' products. Secondary reactions happen and cause the production of alkenes by dehydrogenation of alkanes, formation of iso-alkanes by isomerization of n-alkanes. Sometimes released hydrocarbon molecules are re-adsorbed from the catalytic surface sites and follow other secondary reaction paths, which cause them to be hydrogenolysed to lighter alkanes [26]. The secondary reactions are reduced by increasing the space velocity. High space velocity is associated with a low residence time that reduces the re-adsorption probability of released hydrocarbons and decreases their contact time with the catalyst. This reduction in residence time results in a reduction in alkenes and oxygenates' hydrogenation, as well as oxygenates' inter-conversion. By increasing the WHSV, the usage of carbon monoxide was decreased, which caused higher partial pressure of carbon monoxide at the

reactor outlet that aided the lower activity of the secondary reaction. Methane formation by direct hydrogenation of CO was reduced by increasing the space velocity at higher pressure as shown in Figure 6.5 c.

### **6.3 Effect of increase in conversion**

The extent of carbon monoxide conversion in the F-T process could affect many aspects of F-T synthesis, such as product selectivity and catalyst stability, by alteration in partial pressure of the reactants which causes the variation and instability in the ratio of hydrogen/carbon monoxide and inhibits the adequate productivity of the process. Figure 6.9 was sketched to illustrate the trend of carbon monoxide consumption and catalyst stability over the time on stream by indicating the trend of methanation reaction; WGS reaction and selectivity of long chain hydrocarbons; to derive the impact of this increase in carbon monoxide conversion. EXP04 has shown an unstable F-T procedure by an increase in partial pressure of the reactants which was ultimate to the excess amount of CO and H<sub>2</sub> in the F-T region. This experiment was run at 503 K, 25 bar and WHSV of 3.6 NL/h.g<sub>cat</sub>. As it is shown in Figure 6.9, the carbon dioxide production trend is constant with time, which means that WGS reaction was stable and did not affect the ratio of H<sub>2</sub>/CO; as this ratio was kept close to the usage ratio of the synthesis reactor. CO<sub>2</sub> selectivity was reported 1.72 mol% for this experiment that had the lowest WGS reaction activity among the other experiments. From the precarious profile for CO conversion, methane and C<sub>5+</sub> selectivity at this operational condition, the principle could be concluded that at low temperature, the F-T operation condition could not be higher than 25 bar and 3.6 NL/h.g<sub>cat</sub>; with taking into account that carbon monoxide adsorption rate is low at this temperature (503 K). The other experiments

followed a reasonable trend in carbon monoxide conversion, F-T reaction and by-products' selectivity as indicated in Figure 6.9. It was found that the conversion of carbon monoxide could be increased to the highest point without any change in stability of the process, in terms of selectivity of long chain hydrocarbons, which could affect the F-T process design. The investigation of the effect of enhancing cobalt loading and CO conversion under a laboratory scale F-T process as well as  $S_{(CH_4)}$ ,  $S_{(CO_2)}$  and  $S_{(C_{5+})}$  selectivity's profiles indicates that the CO consumption in the F-T region could reach the highest value by setting the operating conditions at 518 K, 25 bar and 3.0 NL/h.g<sub>cat</sub> (EXP08) using a fixed-bed reactor.

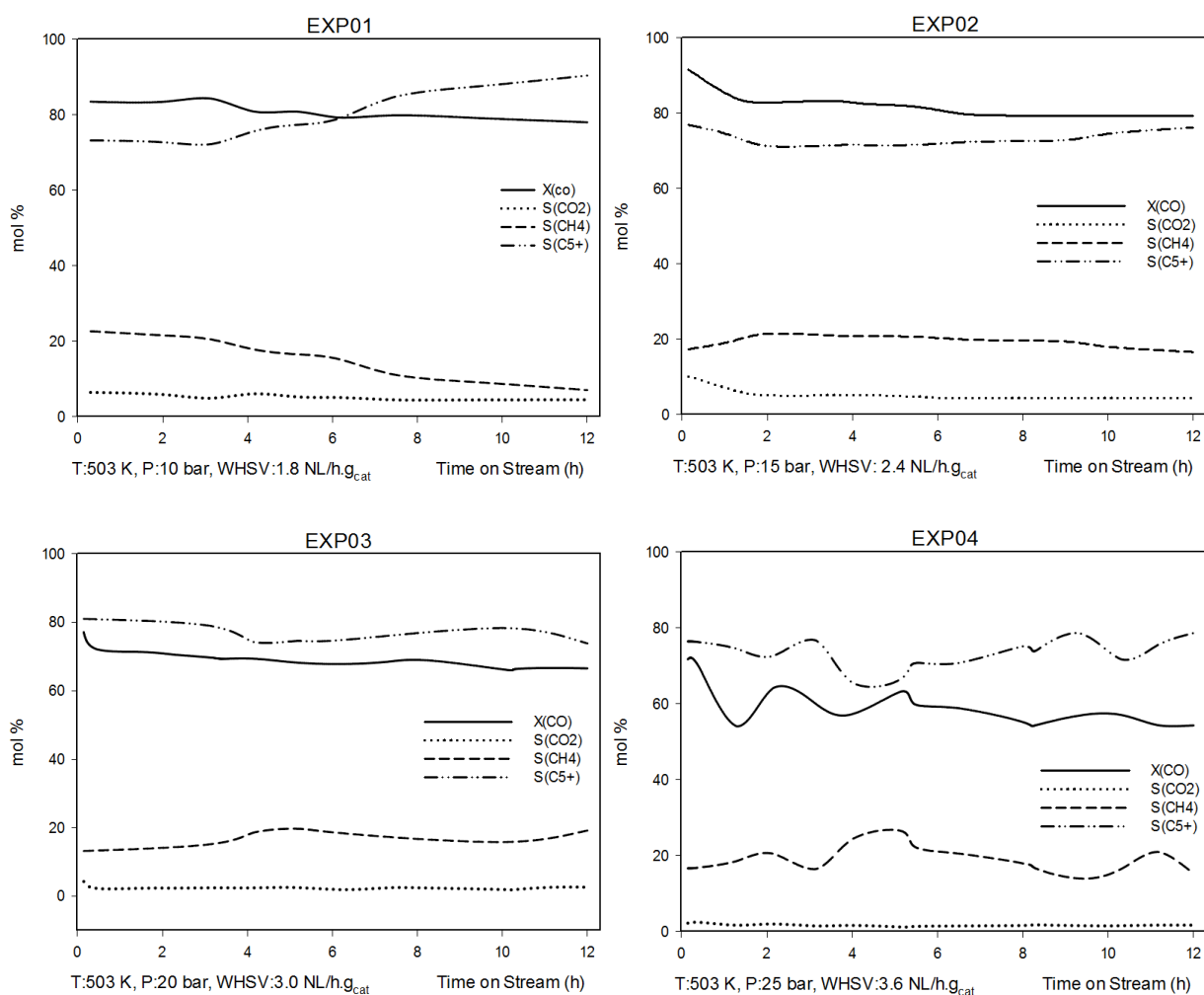
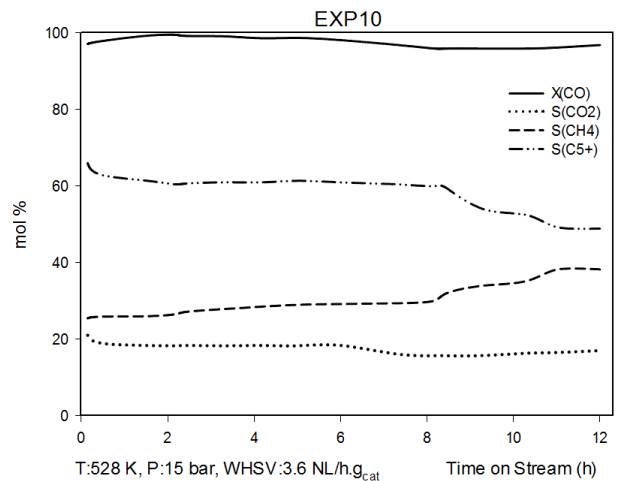
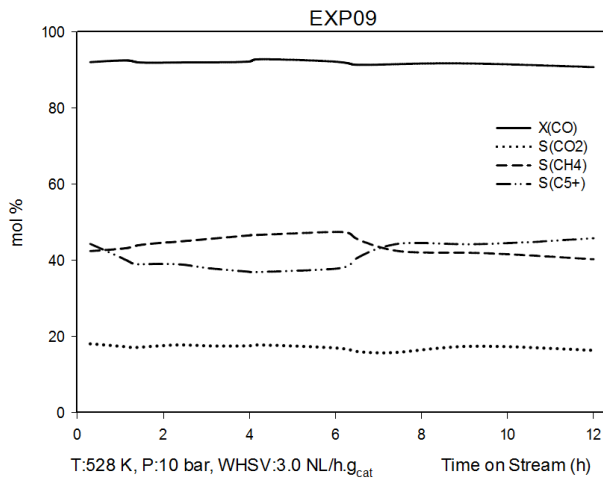
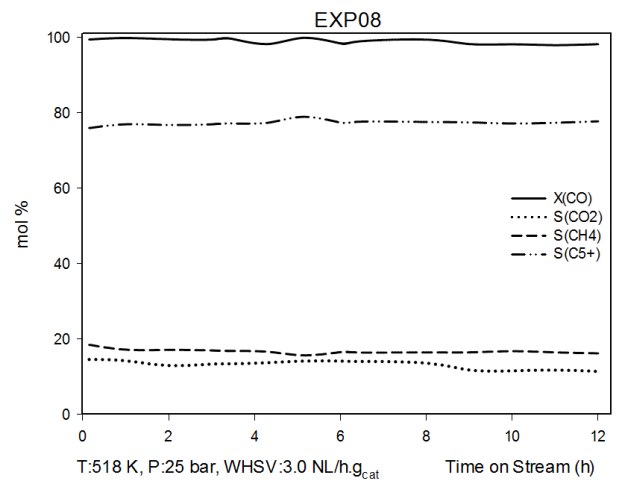
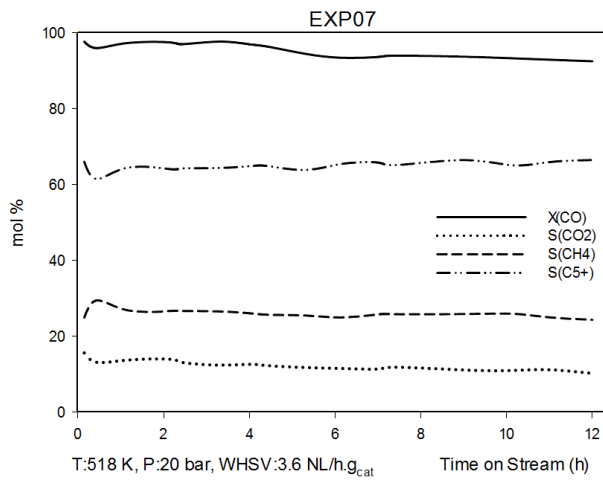
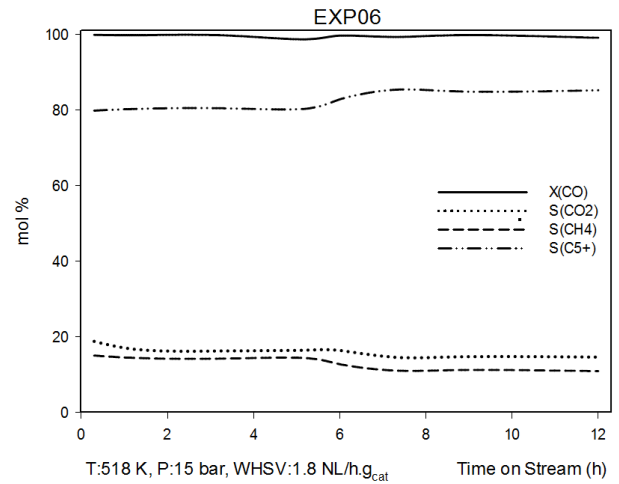
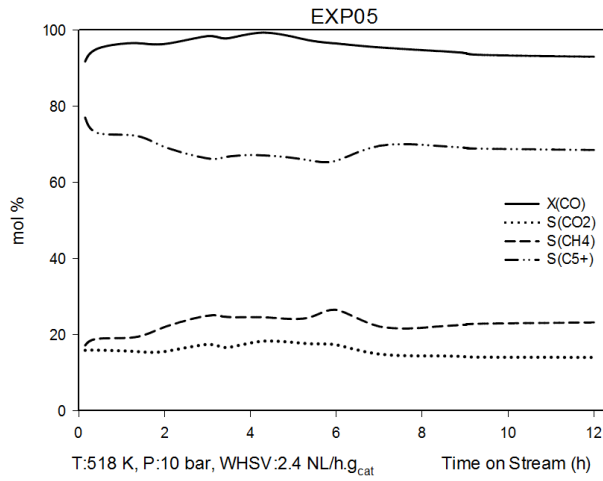
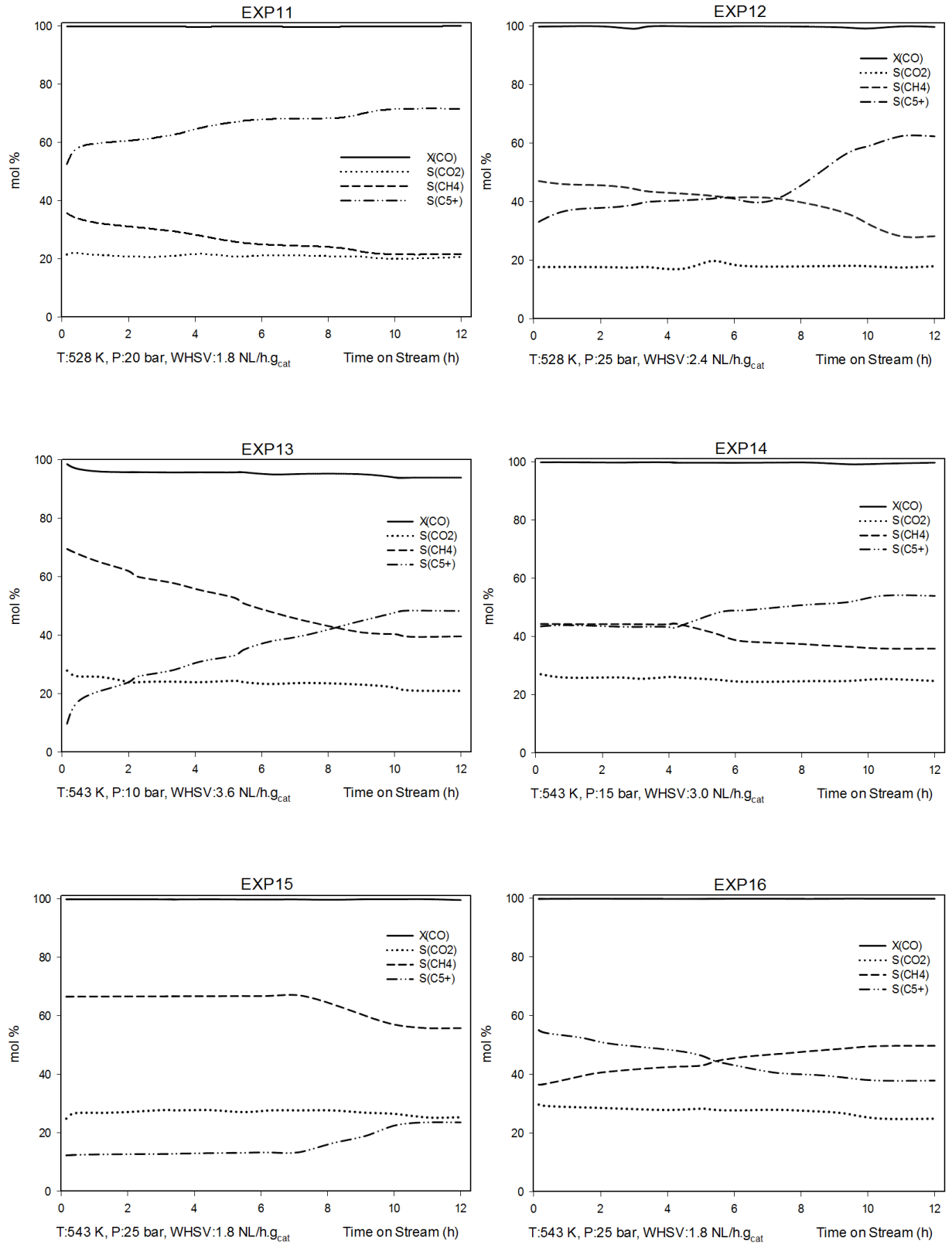


**Figure 6.9:** Performance of fixed bed reactor for 16 experiment runs, variation of CO conversion, CO<sub>2</sub>, CH<sub>4</sub> and C<sub>5+</sub> selectivity as a function of time on stream over cobalt catalyst supported silica

Continuation of Figure 6.9



Continuation of Figure 6.9



#### 6.4 *The Taguchi design of experiment*

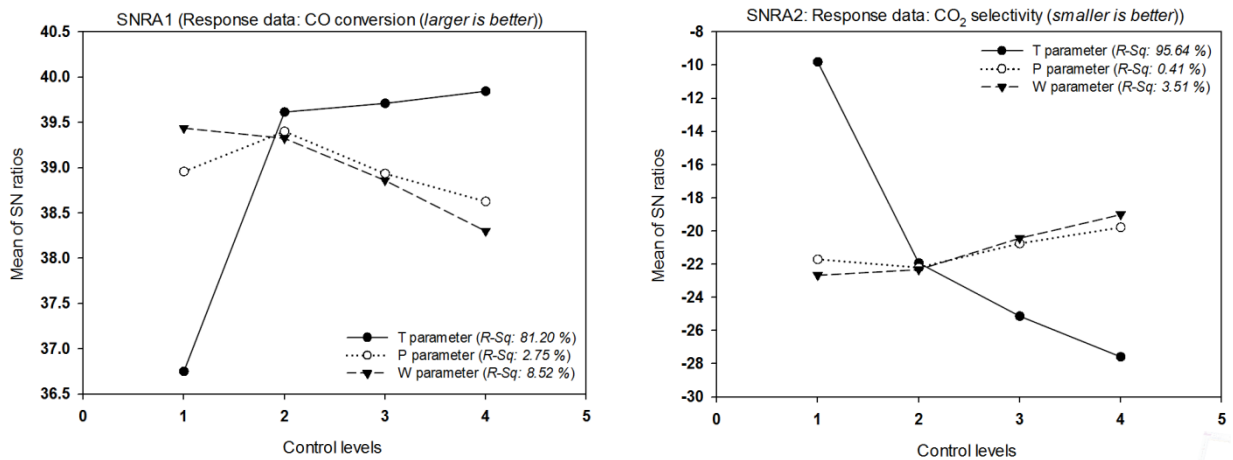
It has been concluded from the previous section that the F-T region temperature followed by total pressure and the space velocity are the three most significant parameters that influence the F-T synthesis process. According to the Taguchi method, the objective of this section is to select the optimum levels for the controllable system parameters. The results were analysed to select the best combination of control parameters so that the outputs are most optimized with respect to the noise factor. The first step is to determine the quality characteristics to be optimized which are the output or response variables that have been observed. Table 6.2 summarizes the Signal-to-Noise ratio (SN) for various parameters. The aim was to measure the relative effect of different control parameters within different levels on performance characteristics. Therefore the mean of the SN ratios for four different control levels of each control factor were calculated to examine the impact of each one on the responses shown in Figure 6.10. It also illustrates the value for R-Squared determined by ANOVA to examine the contribution percentage of individual parameters and their effect on the entire process.

Figure 6.10 (SNRA1) presents the plot of the mean of the SN ratios for the three control factors studied at four levels for the  $X_{(CO)}$  response. The examination of the SNRA1 plot reveals that the parameter level setting for T4 has the largest effect (mean: 39.8473) on the quality characteristic than the others. Clearly all of the parameters should be set at levels T4, P2 and W1 to optimise the quality characteristics for the response  $X_{(CO)}$ . The means calculated for these levels are 39.8473, 39.4029 and 39.4396 respectively. The increase in the levels of the T factor resulted in an increase in the mean of the SN ratios. The lowest impact in the  $X_{(CO)}$  response was reported for the T1 level (mean: 36.7504). The T parameter had the most percentage contribution on the output value allocating an 81.20 % R-Sq value.

**Table 6.2:** Significance of control factors (T, P and W) on responses ( $X_{(CO)}$ ,  $S_{(CO_2)}$ ,  $S_{(CH_4)}$ ,  $S_{(C_5+)}$ ,  $W_{(C_7-C_{11})}$ ,  $W_{(C_{12}-C_{22})}$ ,  $W_{(C_{23+})}$  and LP) utilizing Signal-to-Noise ratio

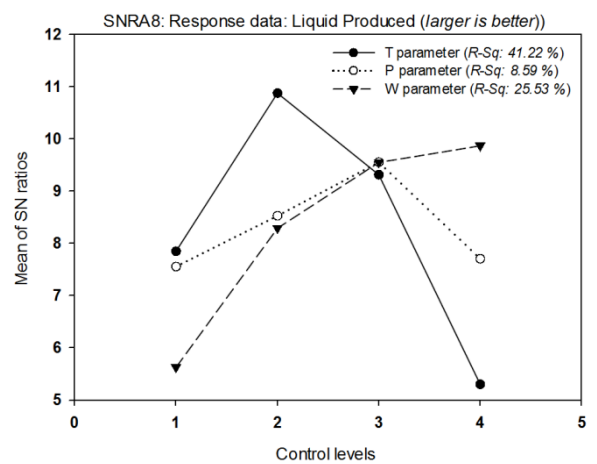
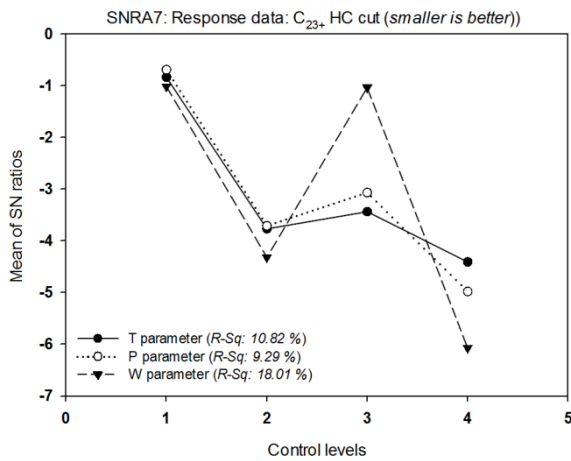
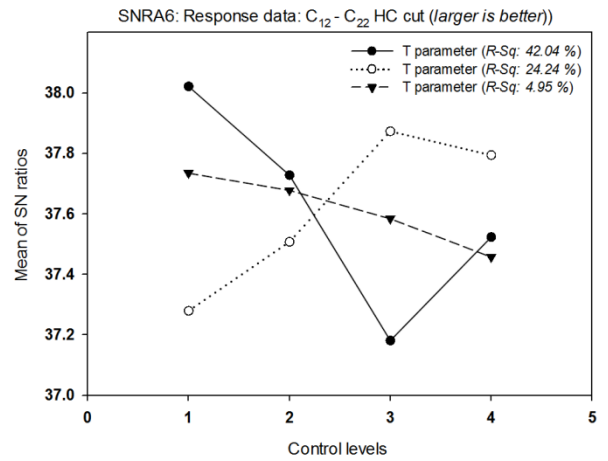
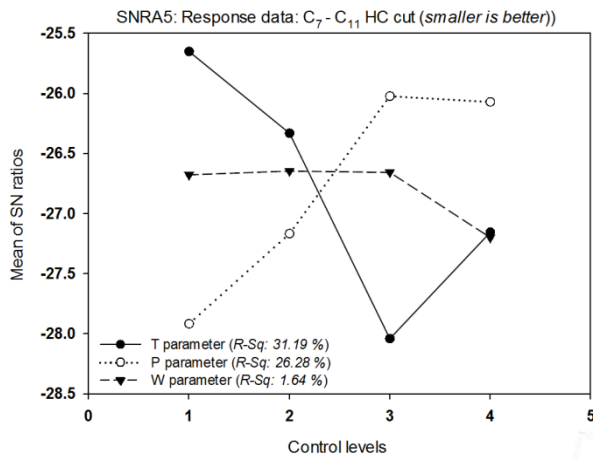
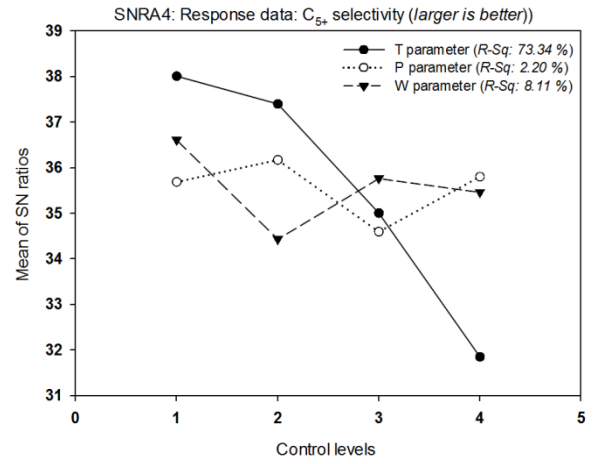
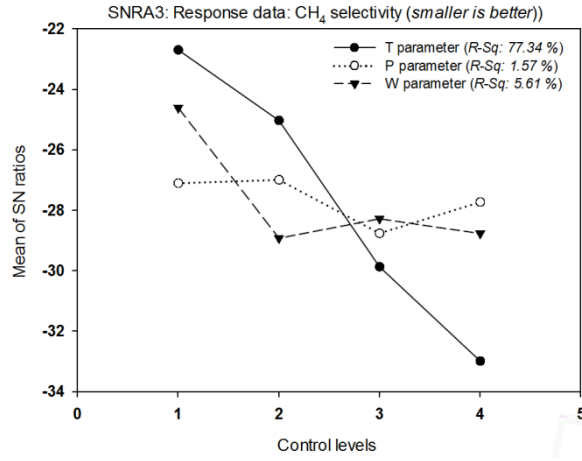
Run	SNRA1** R: $X_{(CO)}$	SNRA2* R: $S_{(CO_2)}$	SNRA3* R: $S_{(CH_4)}$	SNRA4** R: $S_{(C_5+)}$	SNRA5* R: $W_{(C_7-C_{11})}$	SNRA6** R: $W_{(C_{12}-C_{22})}$	SNRA7* R: $W_{(C_{23+})}$	SNRA8** R: LP
01	37.8463	-13.1028	-16.9786	39.1286	-24.9398	38.2072	0.0873	7.4840
02	37.9898	-12.9867	-24.3917	37.6432	-26.4692	37.7916	-2.8603	7.4582
03	36.4630	-8.3991	-25.6660	37.3671	-24.8707	38.2263	0.4455	9.9220
04	34.7024	-4.7106	-23.7052	37.9204	-26.3152	37.8630	-0.9844	6.5472
05	39.3725	-22.9844	-27.3359	36.7226	-28.5107	37.1418	-2.9226	8.0967
06	39.9259	-23.3345	-20.7962	38.6200	-26.4939	37.8508	1.9382	7.7478
07	39.3247	-20.2145	-27.7407	36.4598	-26.8406	37.6766	-3.4637	14.7168
08	39.8440	-21.1761	-24.2117	37.8177	-23.4696	38.2444	-10.6040	12.9672
09	39.1598	-24.2863	-32.1039	33.2321	-30.3069	36.4903	6.3752	8.0521
10	39.7184	-24.6345	-31.6504	33.7904	-27.7300	37.0117	-13.5521	11.6435
11	39.9965	-26.3194	-26.6931	37.1051	-27.4509	37.5174	-2.1442	6.7811
12	39.9774	-25.2680	-29.0204	35.9047	-26.6730	37.7050	-4.4022	10.8066
13	39.4579	-26.4485	-31.9649	33.6926	-27.9065	37.2772	-6.2773	6.5961
14	39.9774	-27.8715	-31.0970	34.6519	-27.9710	37.3764	-0.3407	7.2873
15	39.9643	-28.0830	-34.9342	27.4660	-24.9201	38.0748	-7.0822	6.8247
16	39.9896	-27.9344	-33.9428	31.5916	-27.8152	37.3658	-3.9180	0.5061

\* smaller is better, \*\* Larger is better



**Figure 6.10:** Main effect plots of SN ratio for three control parameters and impact on responses along with percentage of contribution of parameters in responses (R-Sq value)

Continuation of Figure 6.10



As shown in Figure 6.10 (SNRA2), the best response of the SN ratio can be concluded when the magnitude of the factors are set at levels T1, P4 and W4 respectively (means: -9.79979, -19.7723 and -19.0020 respectively) to minimise the impact of the  $S_{(CO_2)}$  response. The response is greatly impacted by the variation in the T parameter (mean of the SN ratio for T1: -9.79979 and T4: -27.5844). The R-Squared of the parameters indicates that the temperature is significantly contributing towards the  $CO_2$  selectivity (R-Sq: 95.64%). The variation for the main effects of the SN ratio of the response  $S_{(CH_4)}$  is largely impacted by the change in the T factor (mean<sub>(high)</sub>: -22.6854, mean<sub>(low)</sub>: -32.9847) and slightly affected by the change in the P and W factors (Figure 6.10 (SNRA3)). The R-Sq value for the T parameter is 77.34 %. To minimise the quality characteristic, the control parameters should be set at levels T1, P2 and W1 respectively for the  $S_{(CH_4)}$  response.

Figure 6.10 (SNRA8) represents the magnitude and the main effects' plot of the SN ratio for the LP (Liquid Produced) response within different levels and factors. It can be seen that the highest effect was conducted for level 2 of the T factor (mean: 10.8821). The magnitude of the response from level T1 to T2 increased and reached the highest point and then decreased to the lowest value at T4 (mean: 5.30355) by an increase in the level. It can be concluded that the highest and lowest impact on the product's yields resulted from the variation in the T factor. The optimum levels for the control factors should be set at T2, P3 and W4 (means 10.8821, 9.56114 and 9.87589 respectively) to yield the highest quality characteristics of the LP response. The optimum value of the LP response did not result in a desirable quality characteristic of the  $W_{(C_{12}-C_{22})}$  response; as the highest impact of W4 on the LP response resulted in the lowest impact of this control level on the  $W_{(C_{12}-C_{22})}$  response (mean: 74.675). Both of the responses are greatly impacted at the level of the P3 control factor. The predicted

analyse concluded that the combination of T2, P3 and W4 levels resulted in an optimised quality characteristic with respect to the responses of  $X_{(\text{CO})}$ ,  $S_{(\text{C5+})}$ ,  $W_{(\text{C12-C22})}$  and LP.

## 6.5 Conclusion

A cobalt-based silica supported fixed-bed reactor was utilized within a Low-Temperature F-T generator (LTFT) to convert bio-syngas to bio diesel. The investigation was performed to examine the effect of reaction variables (temperature (503 - 543 K), pressure (10 - 25 Bar) and, WHSV ( $1.8 - 3.6 \text{NL/h. } g_{\text{catalyst}}$ )) on product distribution to achieve an effective use of a cobalt catalyst, taking into consideration the high cost of cobalt precursors.

The investigation was successful to increase the conversion of carbon monoxide to the highest point ( $\sim 99.9 \text{ mol } \%$ ) by controlling the reactants' concentration on the catalytic surface with the stable activity of the catalyst. A comprehensive set of experiments was planned using the Taguchi method ( $L_{16}$ ) to evaluate the effect of different parameters on the performance of the F-T synthesis. It was concluded that the increase in reaction temperature was influenced by the CO conversion, by increasing the catalyst activity and it also enhanced the productivity of  $\text{C}_{5+}$  hydrocarbons. The excess temperature resulted in a higher product's desorption rate on the catalyst surface, lower production of heavy hydrocarbons and higher selectivity of by-products. An increase in WHSV resulted in a decrease in CO consumption as a result of the change in species residence time and an increase in collected liquid fuel, by eliminating the mass transfer diffusion limitation caused by removal of heavier hydrocarbons. The conversion of carbon monoxide increased with an increase in the pressure of the F-T regime and yielded to the production of diesel range hydrocarbons and also lowered the gasoline products.

The utilizing of the Taguchi method resulted in the optimum condition of the operating variables in T2 (518 K), P3 and P4 (20 and 25 bar respectively) and W3 and W4 (3.0 and 3.6 NL/h.g<sub>cat</sub> respectively).



---

# Chapter 7

---

## OPTIMIZATION OF METAL LOADING

This chapter covers the optimization study of active metal concentration over the surface of the support material in the Fischer-Tropsch Synthesis (FTS) process to produce heavy hydrocarbons. In this study, different amounts of cobalt metal varying from 15 to 36 weight % was loaded in four series of catalysts (metal loading: 15.49, 22.03, 29.34 and 35.75 wt%) in order to examine the effect of metal loading on catalytic performance of Co/SiO<sub>2</sub> catalysts during the operation of a fixed-bed reactor. The supported-catalysts were characterized by using X-Ray Fluorescence (XRF), Nitrogen physisorption, Temperature-Programmed Reduction (TPR), X-Ray Diffraction (XRD) and Scanning Electron Microscopy (SEM) fixed with Energy-Dispersive Spectroscopy (EDS) analysis as described in sections 7.1 to 7.5 respectively. The performances of the catalysts in the F-T synthesis are discussed in section 7.6. The reactor was operated at T=510 K, P=20 bar and WHSV=3.0 NI/h.g<sub>cat</sub>. The reaction conditions were kept constant during the F-T experiments. The active site's concentration was maximized by utilizing all the available surface area of the sphere's porous support in order to maximize the production of heavy hydrocarbons per unit of time, as well as minimize the production time of the desired products.

### 7.1 X-ray Fluorescence (XRF) elemental analysis of derived catalysts

The quantitative elemental analyses of the prepared catalyst were carried out by using a Wavelength-Dispersive XRF spectrometer. The results are listed in Table 7.1. The metal oxides are quantified and normalized in this table as well. The metal concentrations over the support's surface were controlled by changing the molarity of the cobalt precursor's constituents in the impregnation solutions discussed in Chapter 3, section 3.1.1. Figures 7.1 to 7.4 indicate the XRF spectras obtained from the analysis of different supported catalysts. A comparative elemental analysis of catalysts in the vicinity of Co ( $K\alpha$ ,  $K\beta$ , and  $L\beta$ ) and Si ( $K\alpha$ ,  $K\beta$ ) are represented in Figures 7.5 and 7.6. The mass fraction of cobalt metal in the XRF technique is proportional to the intensity of the analytical signals measured from the characteristics' radiations in kilo counts/seconds from which they originated in the samples being analysed [167]. The metal loading was maximised up to about 36 wt% since the higher cobalt deposition over the silica support required a much higher metal precursor in the impregnation process which was not cost-effective.

**Table 7.1:** XRF elemental analysis to determine the Co and Si concentrations in the derived catalysts

Catalysts	Elemental compositions		Oxide compositions	
	Si (%)	Co (%)	SiO <sub>2</sub> (%)	CoO (%)
CAT-Q-15	81.88	15.49	91.2	6.61
CAT-Q-22	76.10	22.03	88.1	10.3
CAT-Q-29	68.87	29.34	83.6	14.9
CAT-Q-36	62.51	35.75	78.6	19.7

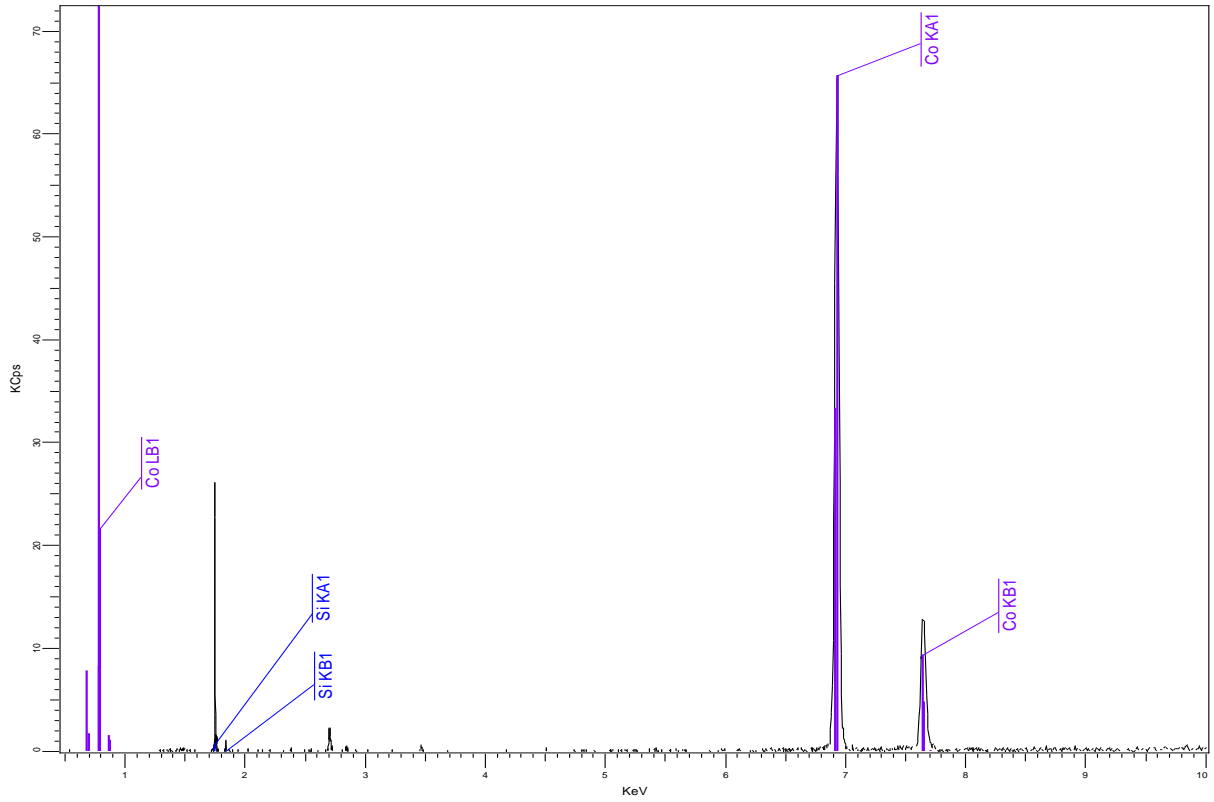


**Figure 7.1:** X-ray Fluorescent spectra of CAT-Q-15 in the vicinity of Co  $K\alpha$ , Co  $K\beta$ , Co  $L\beta$ , Si  $K\alpha$  and Si  $K\beta$

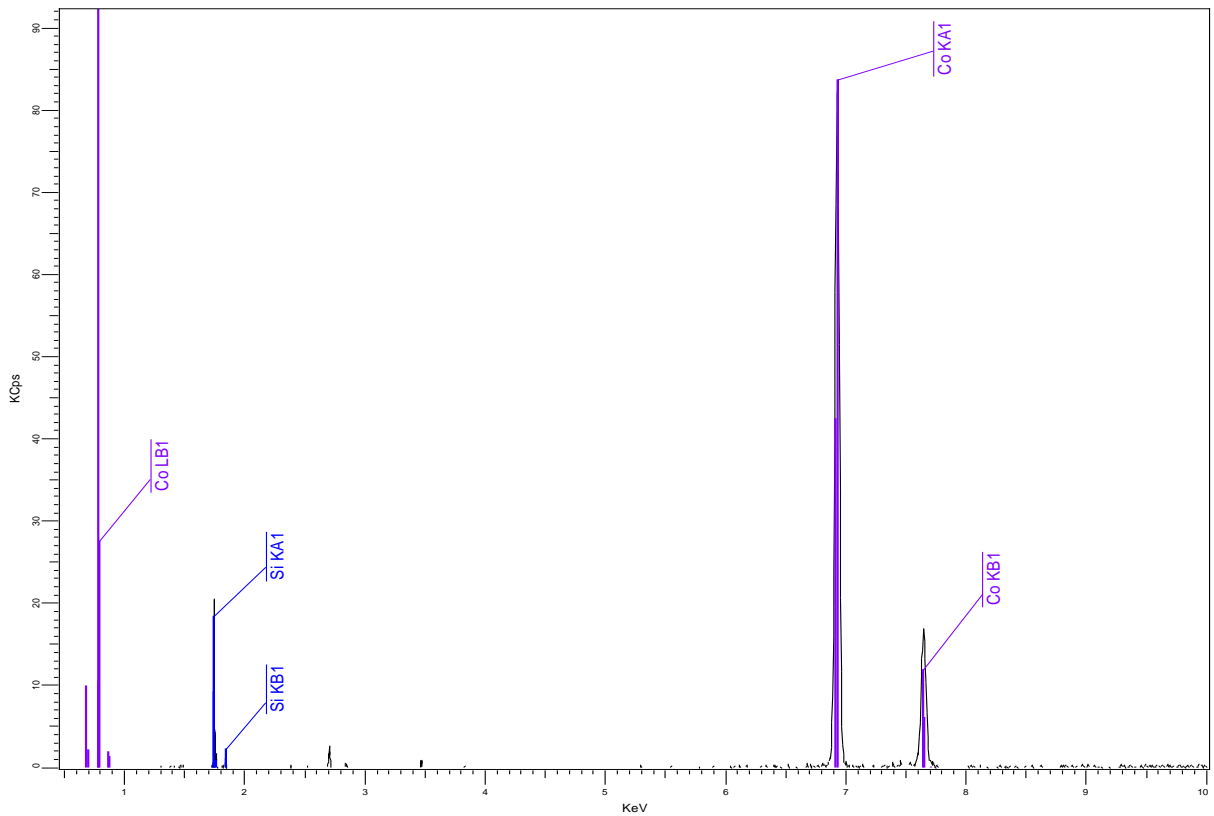


**Figure 7.2:** X-ray Fluorescent spectra of CAT-Q-22 in the vicinity of Co  $K\alpha$ , Co  $K\beta$ , Co  $L\beta$ , Si  $K\alpha$  and Si  $K\beta$

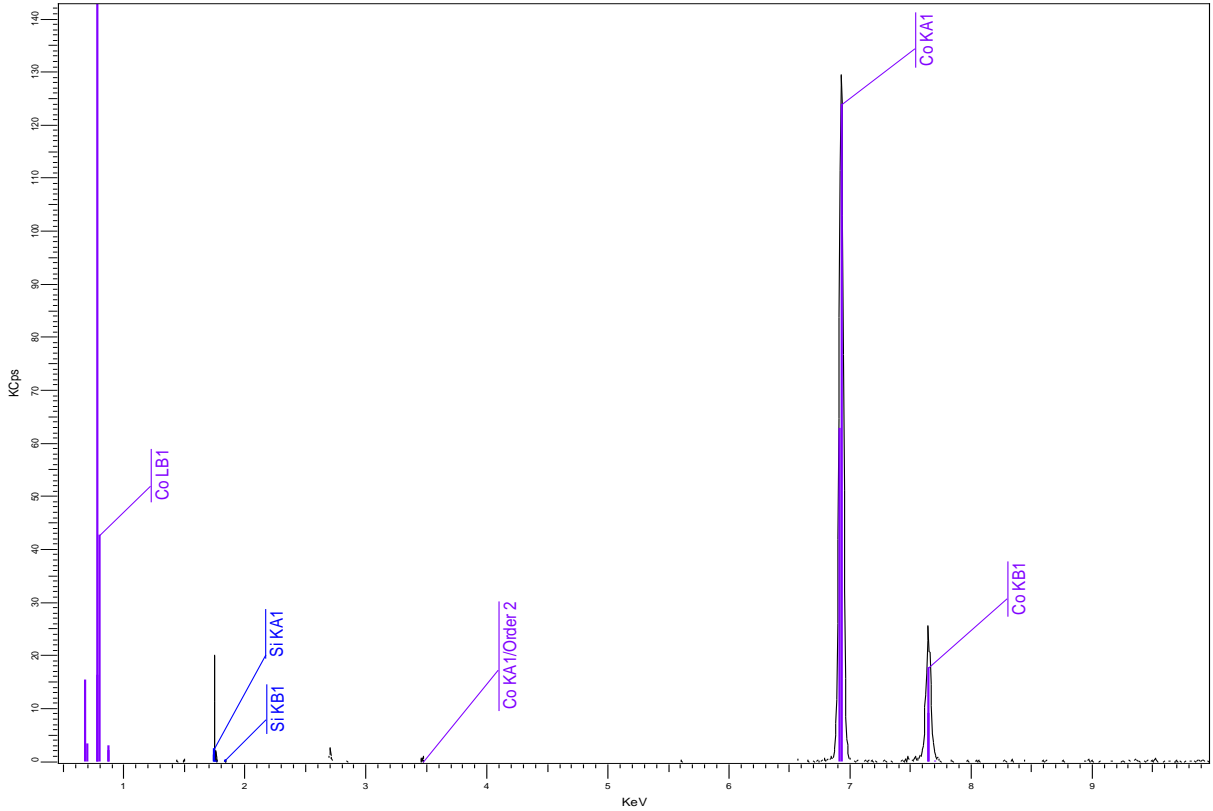


**Figure 7.3:** X-ray Fluorescent spectra of CAT-Q-29 in the vicinity of Co K $\alpha$ , Co K $\beta$ , Co L $\beta$ , Si K $\alpha$  and Si K $\beta$

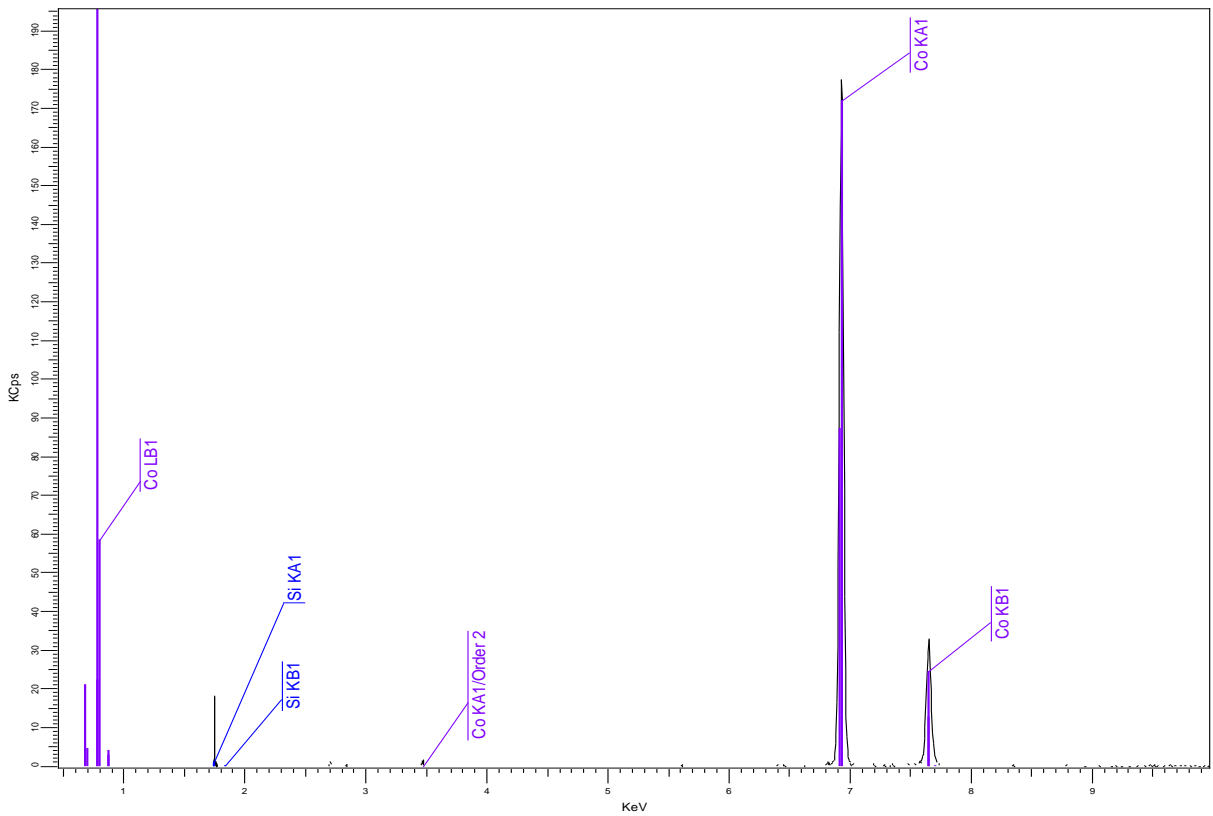


**Figure 7.4:** X-ray Fluorescent spectra of CAT-Q-36 in the vicinity of Co K $\alpha$ , Co K $\beta$ , Co L $\beta$ , Si K $\alpha$  and Si K $\beta$

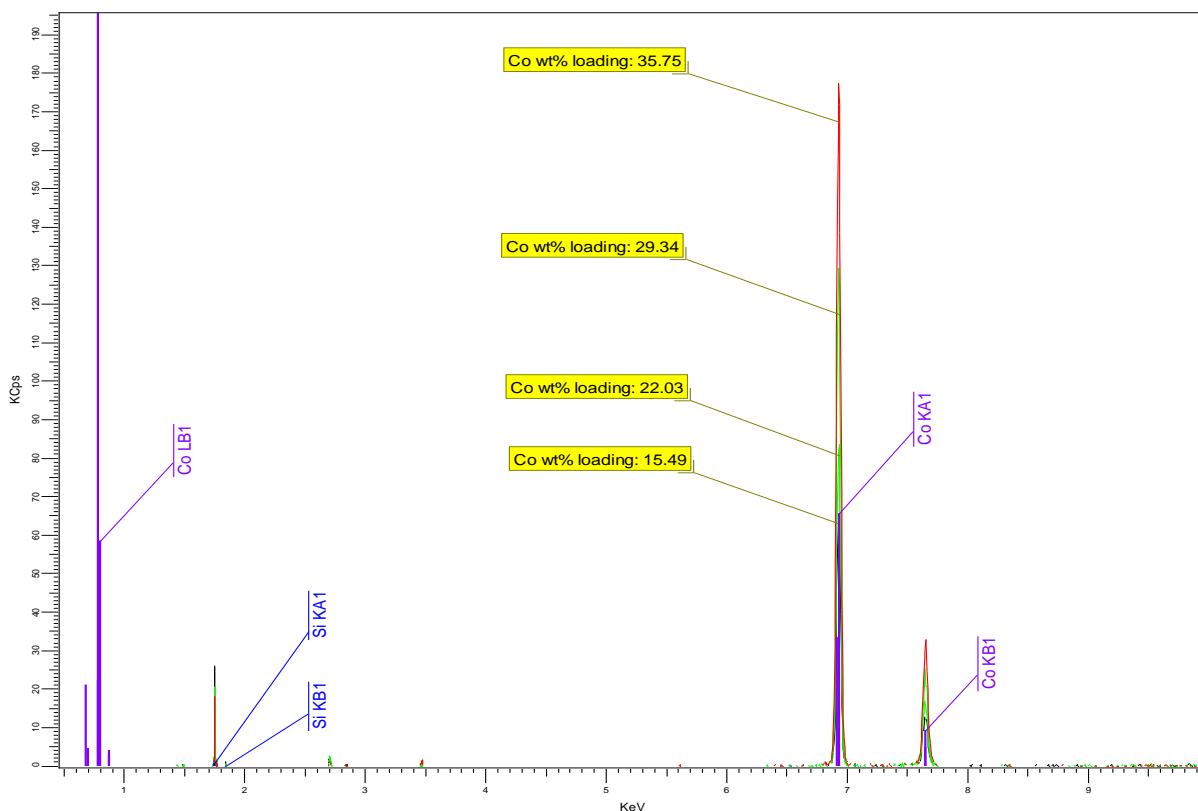


**Figure 7.5:** Comparative elemental analysis of catalysts in the vicinity of Co ( $K\alpha$ ,  $K\beta$ , and  $L\beta$ ) and Si ( $K\alpha$ ,  $K\beta$ )

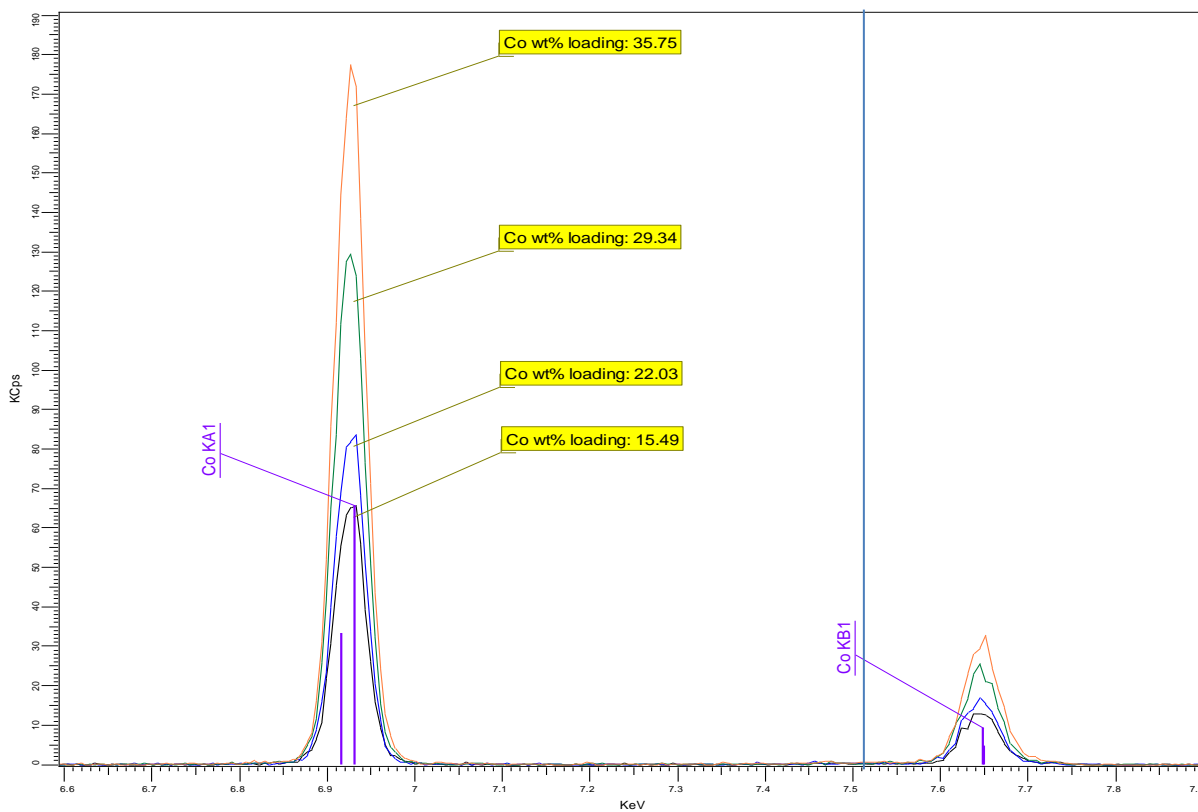


**Figure 7.6:** Comparative elemental analysis of four derived catalysts in the vicinity of Co  $K\alpha$  and Co  $K\beta$

## 7.2 Nitrogen adsorption/desorption analysis

The results of the surface area measurements as well as the pore volume and pore diameter are represented in Table 7.2. The results show that the BET surface area of the silica support (SUP-Q-10) was decreased from 10.63 % in CAT-Q-15 to 18.56 % in CAT-Q-36 after the impregnation process. The loading of the active metal over the porous support resulted in the blockage of some pores and subsequently a reduction in specific surface area and pore volume [168]. The highest reduction in pore volume was reported for the sample CAT-Q-36 (23.33 %) and the lowest decrease was seen in the sample CAT-Q-15 (10 %). The BET surface areas of CAT-Q-15, CAT-Q-22 and CAT-Q-29 are very close to each other, which means that the increase in amount of metal content from 15 to 29 wt% has no significant influence in the porous structure of the support. It is the case that the cobalt introduction to the support SUP-Q-10 by approximately 36 wt% resulted in a considerable decrease, in both surface area as well as pore volume of CAT-Q-36, due to more plugging of the pores of support by the active metal species, which led to in-accessible pores during the nitrogen adsorption.

**Table 7.2:** Textural characteristics of meso-macro porous silica supports and cobalt supported catalysts measured by nitrogen physisorption technique

Sample	Nitrogen adsorption/desorption		
	BET surface area (m <sup>2</sup> /g)	Average pore diameter (nm)	Pore volume (cm <sup>3</sup> /g)
CAT-Q-15	247.9	17.4	1.080
CAT-Q-22	249.7	16.7	1.046
CAT-Q-29	250.8	16.2	1.019
CAT-Q-36	225.9	16.4	0.92
SUP-Q-10	277.4	17.2	1.20

**Table 7.3:** Variables derived from nitrogen physisorption to measure the total surface area

CAT-Q-15			CAT-Q-22		
<b>Slope (S g/cm<sup>3</sup> STP)</b>	0.017396		<b>Slope (S g/cm<sup>3</sup> STP)</b>	0.017253	
<b>Y-intercept (i g/cm<sup>3</sup> STP)</b>	0.000160		<b>Y-intercept (i g/cm<sup>3</sup> STP)</b>	0.000177	
<b>BET Constant (C<sub>BET</sub>)</b>	109.516750		<b>BET Constant (C<sub>BET</sub>)</b>	98.559239	
<b>V<sub>ml</sub> (cm<sup>3</sup>/g STP)</b>	56.958140		<b>V<sub>ml</sub> (cm<sup>3</sup>/g STP)</b>	57.372225	
<b>Adsorbate Cross-section (nm<sup>2</sup>)</b>	0.1620		<b>Adsorbate Cross-section (nm<sup>2</sup>)</b>	0.1620	
<i>P/P<sub>0</sub></i>	<i>V<sub>ads</sub></i> (cm <sup>3</sup> /g STP)	$\frac{P/P_0}{V_{ads}(1 - P/P_0)}$	<i>P/P<sub>0</sub></i>	<i>V<sub>ads</sub></i> (cm <sup>3</sup> /g STP)	$\frac{P/P_0}{V_{ads}(1 - P/P_0)}$
0.059623829	52.8324	0.001200	0.061456633	52.8468	0.001239
0.081298147	56.0621	0.001578	0.080660198	55.7882	0.001573
0.118214355	60.6864	0.002209	0.118055088	60.6309	0.002208
0.160919005	64.9064	0.002955	0.161181287	65.1207	0.002951
0.198298409	68.3975	0.003616	0.200646289	68.8549	0.003646
CAT-Q-29			CAT-Q-36		
<b>Slope (S g/cm<sup>3</sup> STP)</b>	0.017166		<b>Slope (S g/cm<sup>3</sup> STP)</b>	0.019070	
<b>Y-intercept (i g/cm<sup>3</sup> STP)</b>	0.000189		<b>Y-intercept (i g/cm<sup>3</sup> STP)</b>	0.000203	
<b>BET Constant (C<sub>BET</sub>)</b>	92.026853		<b>BET Constant (C<sub>BET</sub>)</b>	95.00675	
<b>V<sub>ml</sub> (cm<sup>3</sup>/g STP)</b>	57.620653		<b>V<sub>ml</sub> (cm<sup>3</sup>/g STP)</b>	51.886338	
<b>Adsorbate Cross-section (nm<sup>2</sup>)</b>	0.1620		<b>Adsorbate Cross-section (nm<sup>2</sup>)</b>	0.1620	
<i>P/P<sub>0</sub></i>	<i>V<sub>ads</sub></i> (cm <sup>3</sup> /g STP)	$\frac{P/P_0}{V_{ads}(1 - P/P_0)}$	<i>P/P<sub>0</sub></i>	<i>V<sub>ads</sub></i> (cm <sup>3</sup> /g STP)	$\frac{P/P_0}{V_{ads}(1 - P/P_0)}$
0.060399122	52.4235	0.001226	0.057569098	46.9291	0.001302
0.077266094	55.1496	0.001518	0.079682113	50.1593	0.001726
0.116687552	60.3649	0.002188	0.118571037	54.6777	0.00246
0.161255848	65.1642	0.002950	0.160379606	58.6985	0.003254
0.200874631	69.0127	0.003642	0.199343249	62.0799	0.004011

The decrease in pore volume and surface area of the catalysts could be ascribed to the heat treatments during the preparation process of the catalysts (drying and calcination). Figure 7.7 shows the nitrogen adsorption and desorption isotherm calculated by employing the BJH method for different catalysts. The typical hysteresis loops for capillary condensation of nitrogen in the cobalt catalysts supported with meso-porous silica are exhibited by the isotherms in this figure. Table 7.3 indicates the variables derived from physisorption of nitrogen to calculate the specific surface area of the catalysts.

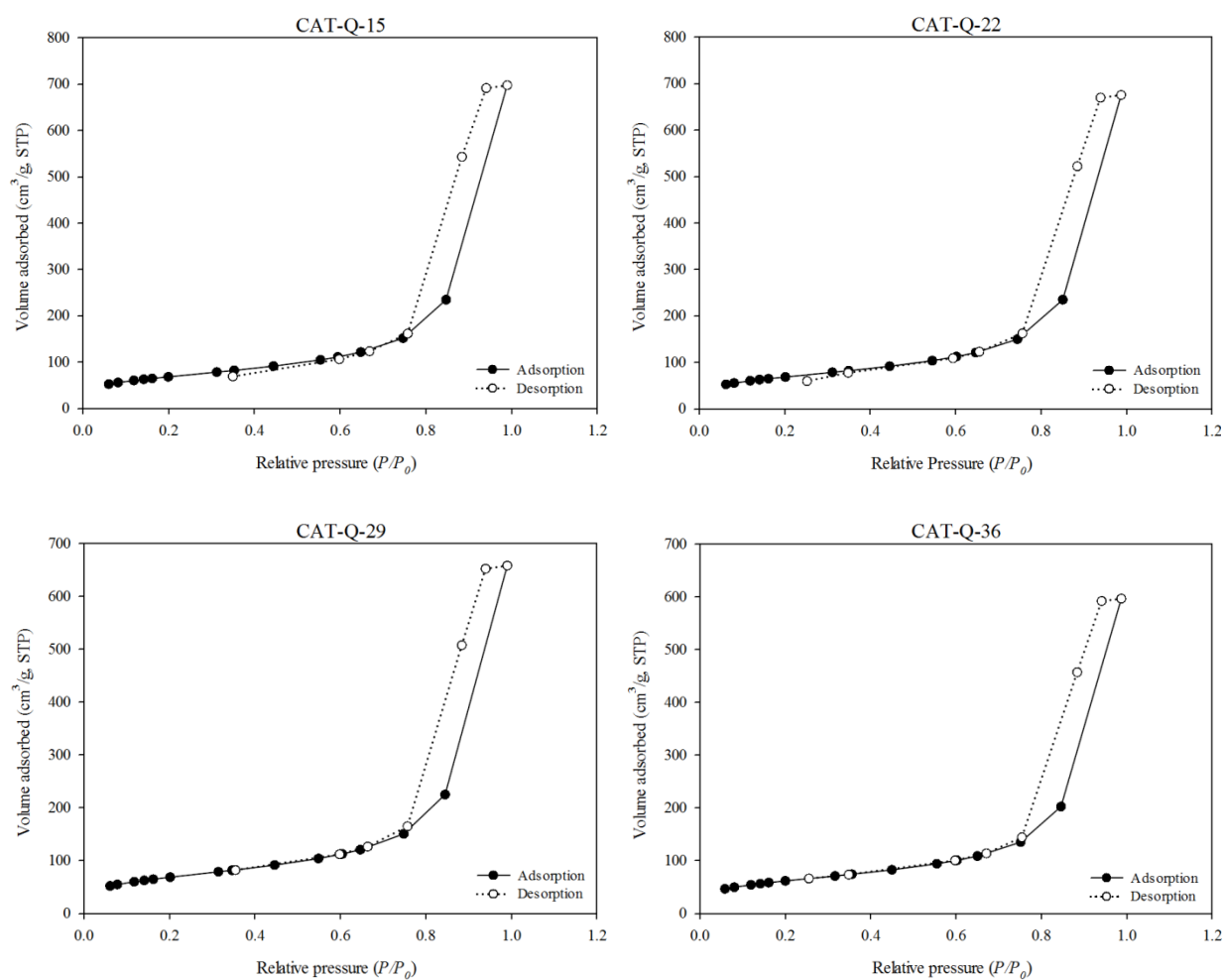
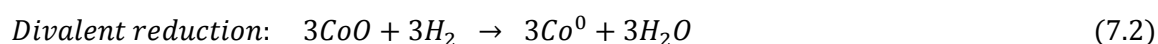
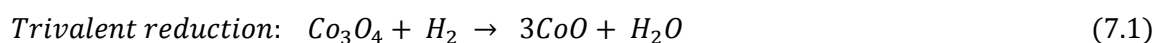


**Figure 7.7:** Nitrogen adsorption (filled circle) and desorption (empty circle) type IV isotherms for different catalysts obtained at 77 K

### 7.3 Temperature-Programmed Reduction (TPR) analysis

The Temperature-Programmed Reduction (TPR) technique was applied as a thermo-analytical method to characterize the prepared heterogeneous cobalt-supported catalysts. Characterization of the catalyst by using the TPR technique could result in an alteration in the structure of the original catalyst due to treatment at high temperature, which is known as one of the shortcomings of this technique [169]. Figure 7.8 indicates the reduction behaviour of the calcined silica-supported cobalt catalysts as a function of active metal loading in the presence of multiple reduction peaks. The TPR profiles of different catalysts as a function of time and temperature are given in this figure. Three reduction regions were observed for all of the catalysts. In some cases, four TPR peaks were detected. The reduction profile of each of the catalysts could be ascribed to two TPR peaks detected between 250 to 640 °C, due to two reduction phases of trivalent and divalent which occurred at this temperature period.



$\text{Co}_3\text{O}_4$  crystalline phase reductions to the  $\text{CoO}$  metal oxide are ascribed to the low temperature reduction peaks (CAT-Q-15: 368 °C, CAT-Q-22: 337 °C, CAT-Q-29: 335 °C, CAT-Q-36: 345 °C) for the four differently loaded cobalt catalysts. On the other hand, the reductions which occurred at 450, 440, 470 and 455 °C are ascribed to the reduction of  $\text{CoO}$  oxide to the free metallic  $\text{Co}^0$  in CAT-Q-15, CAT-Q-22, CAT-Q-29 and CAT-Q-36 respectively [70, 170-172]. The reductions of all of the catalysts were completed below 480 °C. As shown in the figure, all of the catalysts display a broad peak at temperatures higher than 750 °C (CAT-Q-15: 770 °C, CAT-Q-22: 804 °C, CAT-Q-29: 760 °C, CAT-Q-36: 758 °C), which could be attributed to the reduction of surface cobalt interacting with surface silicates [173, 174].

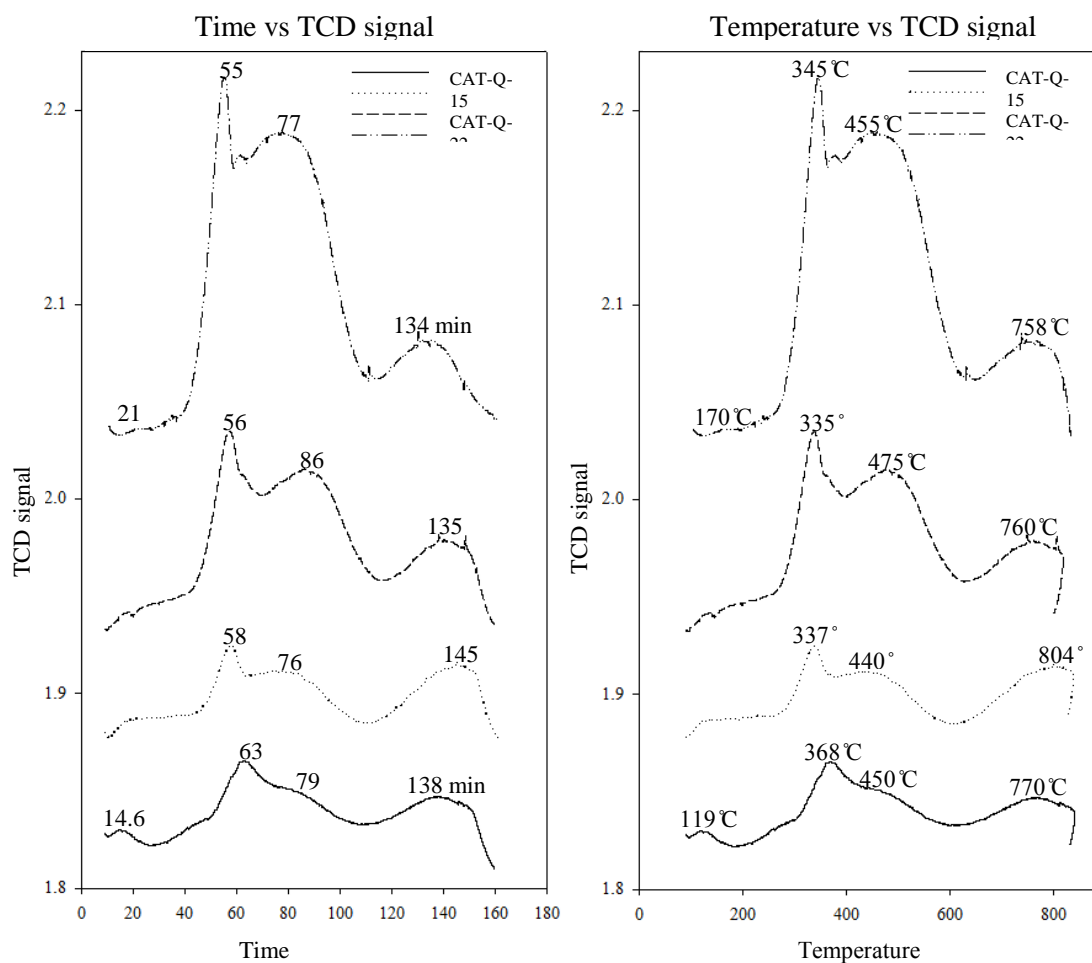


**Figure 7.8:** Temperature-Programmed Reduction (TPR) profiles of calcined catalysts with different concentrations of active sites (metal oxides) obtained from a chemisorption analyser

By taking the difference of the TPR spectra for four catalysts, it could be concluded that only a small fraction of the surface cobalt responsible for the broad peaks are reduced during the TPR procedure; in comparison to the trivalent and divalent reduction phases in CAT-Q-29 and CAT-Q-36. In contrast to these two catalysts, considering the TPR spectra of CAT-Q-15 and CAT-Q-22, it is observed that the amounts of responsible Co species for the broad peaks detected at temperatures higher than 750 °C are so considerable, in comparison to the reduction peaks obtained at lower than this temperature. Since the degree of interaction with the silica support varies as a function of the metal cluster size, hence different shoulders are observed

for different catalysts. A strong interaction of the cobalt-silica is the result; due to the formation of smaller cobalt oxides' clusters, which are difficult to reduce and are only reduced at a higher temperature [173]. For sample CAT-Q-22, the reduction peak occurred at a higher temperature (804 °C), indicating that the more Co-Si complex are formed during the preparation and calcination process; which are much more difficult to reduce compared to the other catalysts. The TPR profiles of CAT-Q-15 and CAT-Q-36 contain a low intensity low temperature peak at 119 °C and 170 °C respectively; which could be attributed to the reduction of residual cobalt remaining from the impregnation step. In these pre-calcined samples, at low temperature the residual cobalt nitrates are decomposed in the presence of H<sub>2</sub> gas [67]. As it is observed from Figure 7.8, the increase of the cobalt content in the catalysts from 15 wt% to 29 wt % affected significantly the reducibility of the catalysts due to the bulk reduction of cobalt oxide ( $Co^{3+} \rightarrow Co^{2+} \rightarrow Co^0$ ); and a slight shift in the TPR profiles to the low temperature is observed. The easier reduction in CAT-Q-29 compared to CAT-Q-15 is due to the weaker interaction of cobalt with silica [175]. The reduction of cobalt oxides are facilitated in CAT-Q-29 which results in an increase in the number of exposed Co<sup>0</sup> active sites that consequently results in the hydrogenation of CO in the F-T process [176]. The trend in the reduction profile of the catalysts is in agreement with the study of Dunn et al [62]. The bulk reduction of cobalt oxide is slightly shifted to the higher temperature in the CAT-Q-36, due to the stronger interactions of the Co species. The TPR profiles for the reduction of  $Co_3O_4$  obtained for the sample CAT-Q-36 have a much larger area than the other catalysts; which demonstrates the much higher consumption of hydrogen during the reduction procedure. The higher consumption of analysis gas suggests a much higher concentration of accessible active sites in CAT-Q-36 in comparison to the other catalysts. CAT-Q-15 showed the lowest H<sub>2</sub> consumption and CAT-Q-36 showed the highest consumption in hydrogen.

#### 7.4 X-ray Diffraction (XRD) analysis

The X-ray Diffraction (XRD) method was employed to identify and characterize the F-T active phases of heterogeneous cobalt supported silica catalysts. The ex-situ studies of cobalt sites situated on the surface of relatively large crystalline Co metal particles (> 10 nm) were performed to evaluate the crystalline size of the metal [177, 178]. The XRD spectra of differently cobalt-loaded catalysts after drying and the calcination process are illustrated in Figure 7.9. For all of the catalysts, the characteristics spinel  $\text{Co}_3\text{O}_4$  are shown by five sharp signals. The presence of  $\text{Co}_3\text{O}_4$  spinel phases with  $2\theta$  values of 36.69, 38.21, 44.74, 65.13 and 78.63 were observed in all of the diffractograms [58]. Among various unreduced oxidized cobalt phases created over porous support, ( $\text{Co}_3\text{O}_4$ ,  $\text{CoO}$ ,  $\text{Co}_3\text{O}_{4-x}$  (intermediate cobalt oxides), Co-Si (metal-support oxide phase) as well as non-decomposed residual cobalt precursor), cobalt oxide phases of  $\text{Co}_3\text{O}_4$  and  $\text{CoO}$  crystalline could be easily detected and observed by XRD patterns obtained from the diffractometer [169, 179]. Table 7.4 lists the average crystalline size of the oxidized cobalt calculated by employing the Scherrer equation [114]. The cobalt metal particle diameter, as well as the metal dispersion, was estimated by using the reducing factor derived by Holmen et al [136] discussed in Chapter 4, section 4.3.

**Table 7.4:** Average  $\text{Co}_3\text{O}_4$  crystallite size, estimated  $\text{Co}^0$  particle diameter and estimated cobalt dispersion for different supported catalysts

Sample	$\text{Co}_3\text{O}_4$ crystallite diameter (nm)	Estimated $\text{Co}^0$ particle diameter (nm)	Estimated cobalt dispersion %
CAT-Q-15	24.79	18.59	3.87
CAT-Q-22	19.47	14.60	4.93
CAT-Q-29	12.98	9.735	7.39
CAT-Q-36	16.04	12.03	5.98

Chen et al [135] concluded that the metallic cobalt crystalline size is proportional to the size of the  $\text{Co}_3\text{O}_4$  crystalline phase. It should be mentioned that in addition to the cobalt cluster size, the average size of supported  $\text{Co}_3\text{O}_4$  crystalline is greatly influenced by the porous silica support's structure as well [82, 131].

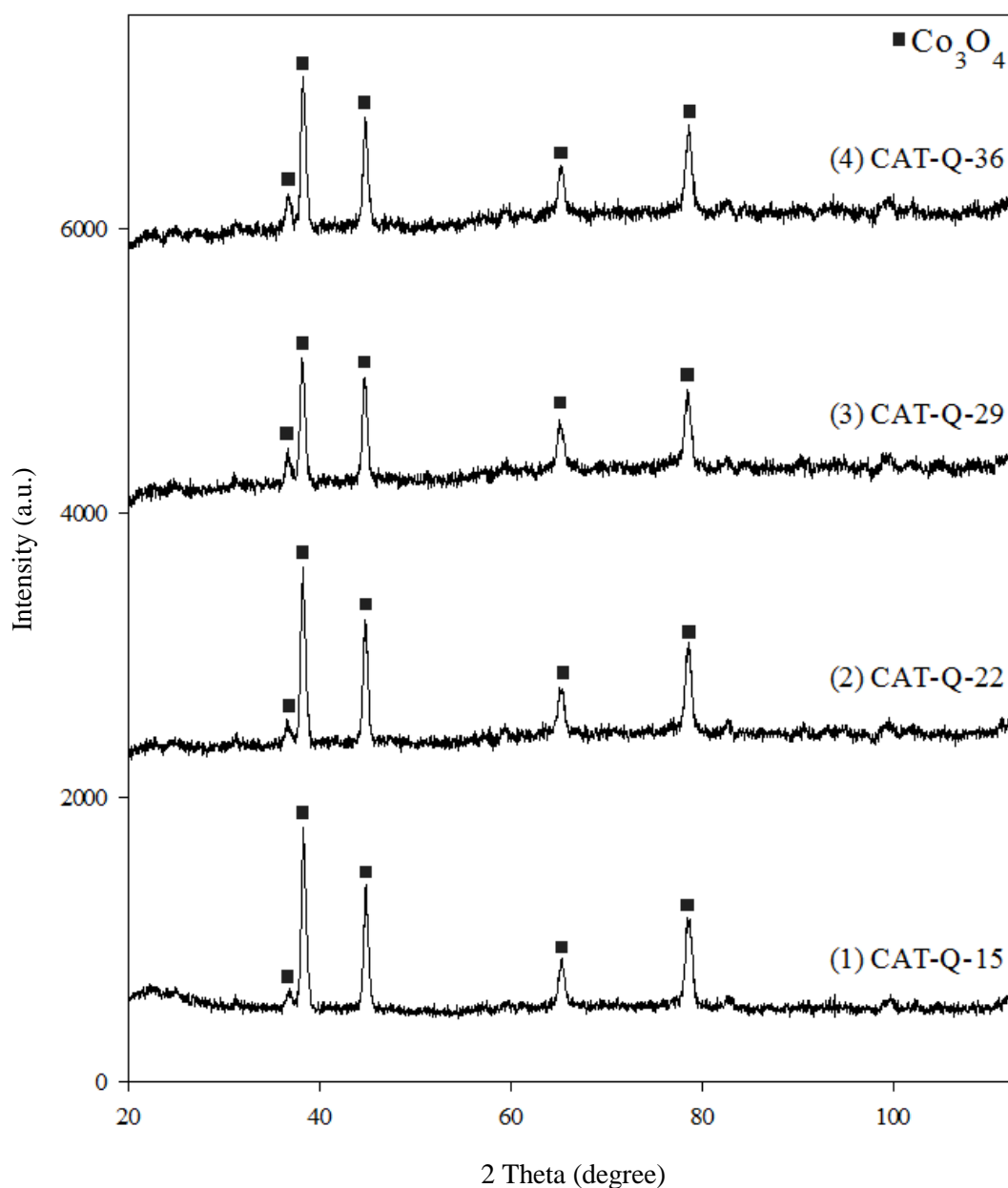


**Figure 7.9:** XRD diffraction spectrogram of different calcined and un-reduced supported catalysts

It is clearly observed that the increasing of the cobalt content resulted in  $\text{Co}_3\text{O}_4$  particles in samples CAT-Q-22 and CAT-Q-29 and were considerably smaller than for the sample CAT-Q-15 (by about 21.46 and 47.64 % respectively). The wide diffraction peaks illustrated for the unreduced sample, CAT-Q-29 with the weak signal detected at  $2\theta=36.69$ , are due to the presence of a small  $\text{Co}_3\text{O}_4$  crystalline phase formed over meso-porous silica support. From the figure, it could be concluded that by increasing the cobalt content up to 29%, the detected peaks for spinal  $\text{Co}_3\text{O}_4$  crystalline become sharper which corresponds to the smaller cobalt cluster size. In contrast, dissimilar results were reported by Lira et al [133]. In the sample CAT-Q-29, the cobalt oxide phase seems to be better dispersed with considering the same support structure. This sample assigns the highest estimated cobalt dispersion among the others. The average crystalline size of the  $\text{Co}_3\text{O}_4$  phase was increased by 19.07 % from 12.98 to 16.04 nm in CAT-Q-36, containing the highest cobalt concentration. The findings imply that the increase in cobalt content leads to most of the cobalt particles being placed on the external surface of the silica support.

Due to the higher cobalt content in the prepared catalysts, distinct peaks have been represented in diffractograms of catalysts' crystallographic phases [133]. In some cases (CAT-Q-15 and CAT-Q-22), the crystalline sizes calculated from the XRD measurements are larger than the pore diameter of the catalysts. This could be suggested by the highly branched structure of the silica supports, which able the cobalt metals to be formed and interconnected to other neighbouring pores and to be placed on the exterior surface of the supports [137]. When small sized particles are measured by using the XRD technique, the limitations and approximations of using the XRD peak width could result in overstating of the actual size of the particles by up to factor of 2 [180]; which could explain the observation of the larger particle size measured by XRD.

### 7.5 *Microstructural and morphological structure of the catalysts*

Heterogeneity of particle size as well as repartition of active sites over the surface of different eggshell catalysts were considered by employing the SEM instrument fixed with EDS. The SEM images of differently loaded cobalt-supported silica catalysts are exhibited in Figures 7.10 to 7.13 (a), (b). In addition to the morphology of the catalysts, typical micro-analysis of the surface of the catalysts was investigated by EDS and is represented in Figures 7.10 - 7.13 (c). These figures map the distribution of F-T active sites as well as the relative proportion (intensity) of previously defined elements (Co and Si) over the user-defined scanned areas. The concentration of cobalt particles in the area-scan method are demonstrated in the white colour while the dark colour illustrates the silica support surface. The acquisition conditions for X-ray acquisition including livetime (140-150 s) as well as process time (5 out of 6) were selected for all scanning to enable the comparison between different samples. The average metal content over the support surfaces were analytically measured and normalized by EDS in different spectrums over different granules. The results are listed in Table 7.5 which is in good agreement with the overall cobalt content measured by the XRF technique.

**Table 7.5:** Elemental analysis of catalysts' surface by SEM-EDX to characterize metal content

Sample	Element (weight %)		Element (atomic %)	
	Si K	Co K	Si K	Co K
<b>CAT-Q-15</b>	83.54	16.46	91.42	8.58
<b>CAT-Q-22</b>	79.63	20.37	89.13	10.87
<b>CAT-Q-29</b>	70.28	29.72	83.22	16.78
<b>CAT-Q-36</b>	63.24	36.76	78.31	21.69
<b>Total</b>	100	100	100	100

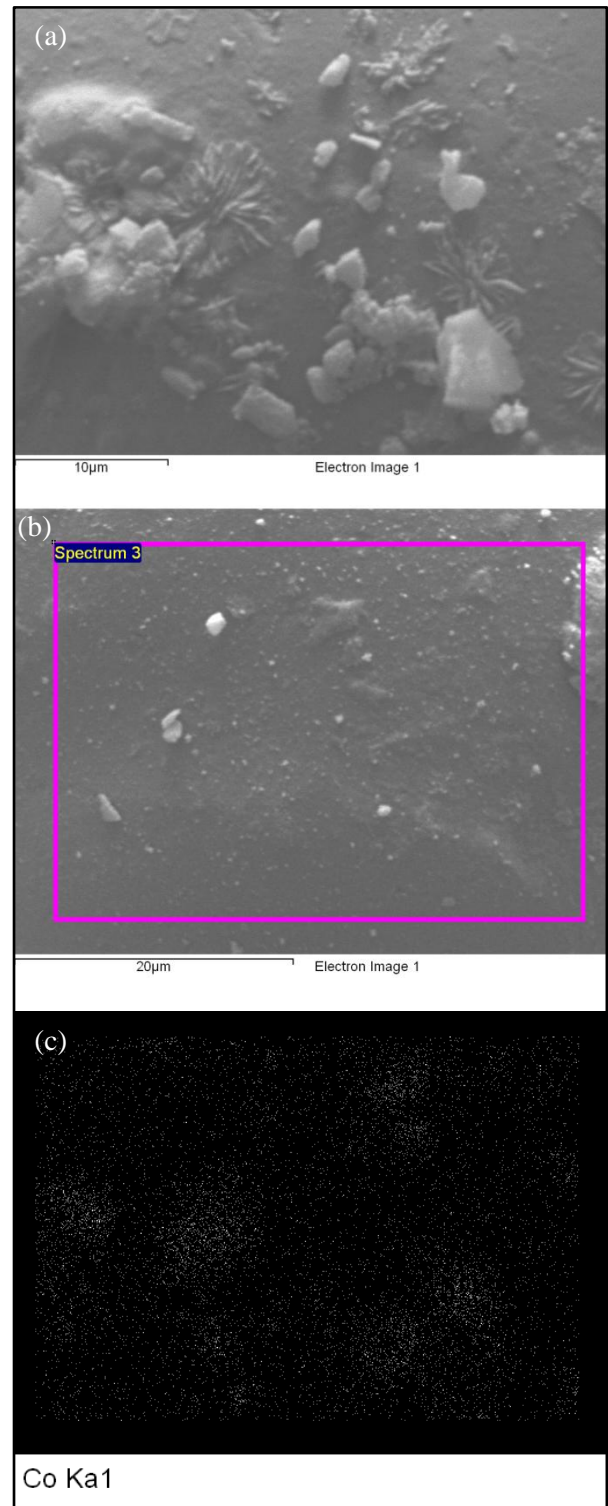
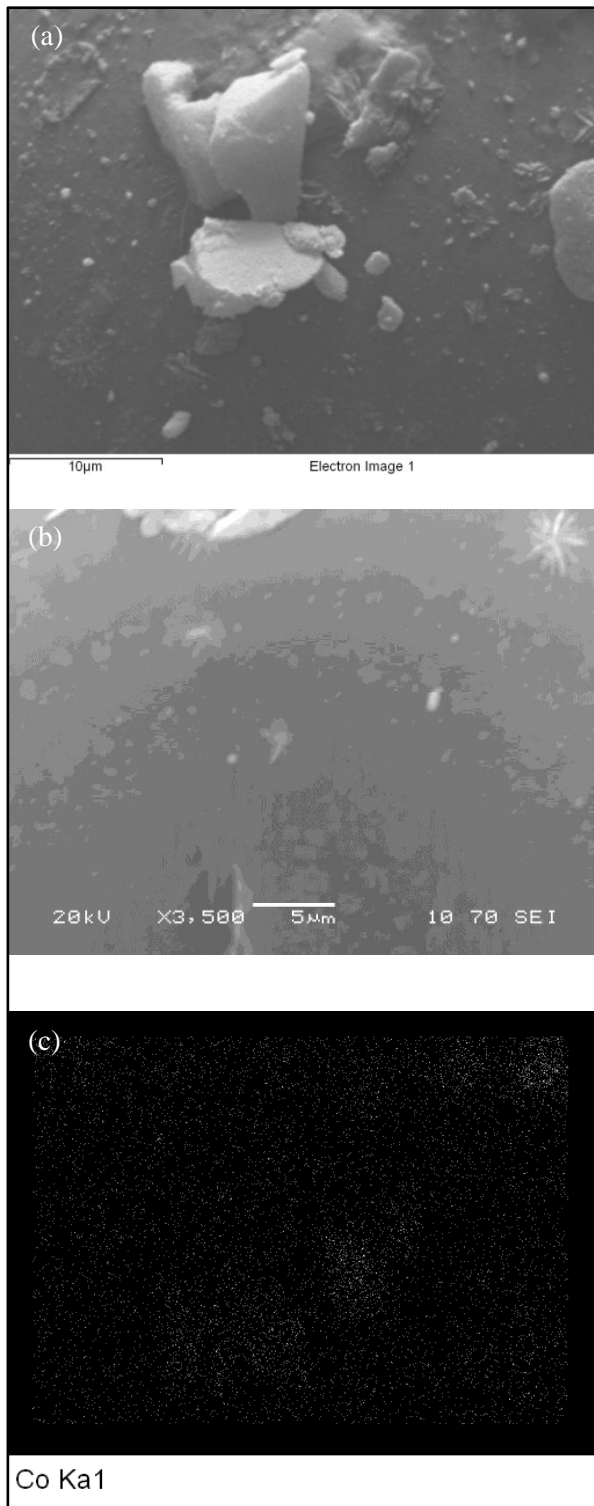


**Figure 7.10:** SEM micrographs (Figures 7.10.a and 7.10.b) and EDX micro-analysis (Figure 7.10.c) of sample CAT-Q-15

**Figure 7.11:** SEM micrographs (Figures 7.11.a and 7.11.b) and EDX micro-analysis (Figure 7.11.c) of sample CAT-Q-22

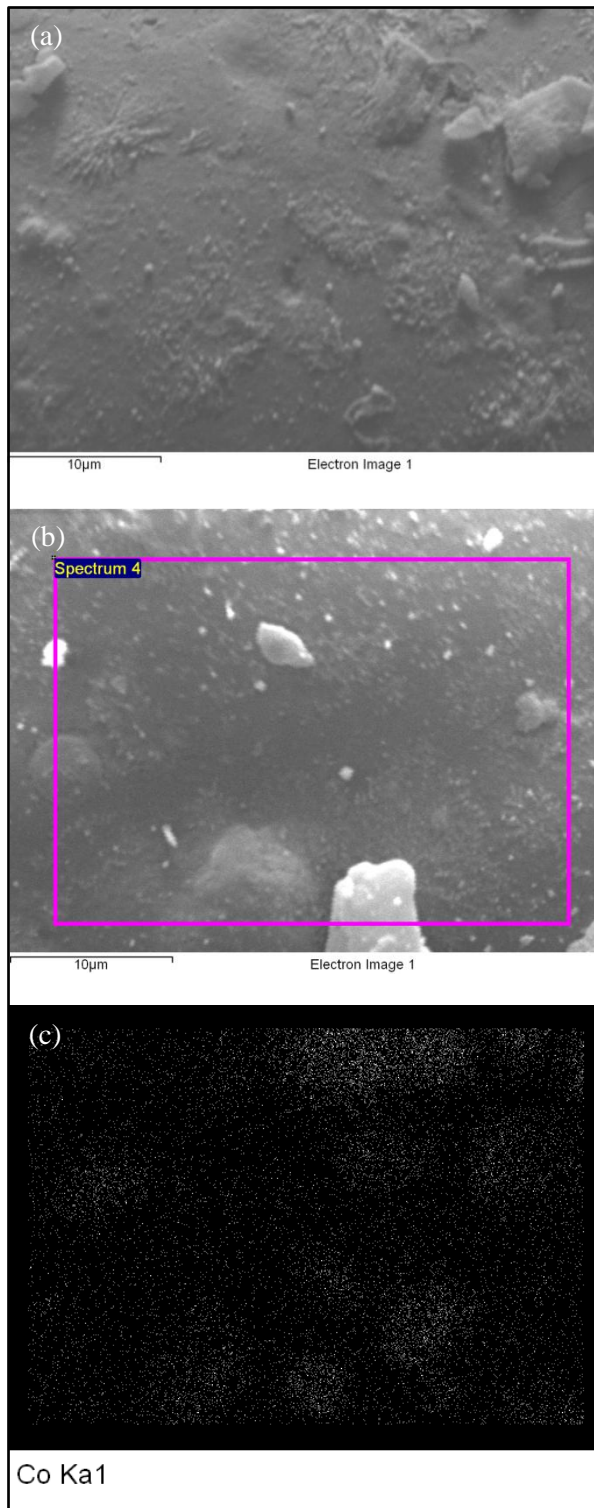


**Figure 7.12:** SEM micrographs (Figures 7.12.a and 7.12.b) and EDX micro-analysis (Figure 7.12.c) of sample CAT-Q-29

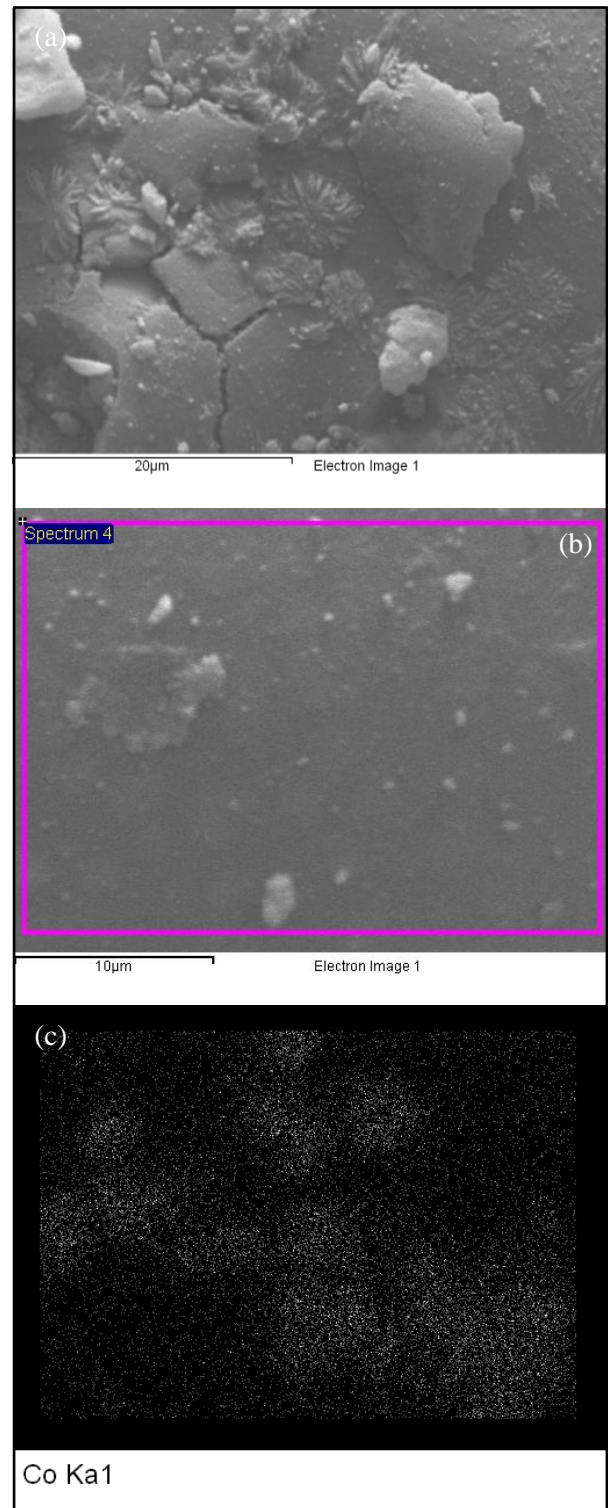


**Figure 7.13:** SEM micrographs (Figures 7.13.a and 7.13.b) and EDX micro-analysis (Figure 7.13.c) of sample CAT-Q-36

It should be mentioned that some deviation from average metal content measured by XRF analysis was observed at different spectrums of various sample sides. In the case of CAT-Q-29, the deviation in cobalt content was  $\pm 25$  wt%. The minimum deviation was observed in CAT-Q-15. The highest deviation was reported for CAT-Q-36 with the value of 29 wt%. The typical SEM imaging of the samples along with EDS mapping illustrates that the cobalt particles are distributed on the external surface of the support granule in eggshell catalysts [181]. The poly-dispersed spherical metal particles were observed for all of the catalysts [138]. In some cases, the large cobalt particles were recognized in the SEM images.

Composition maps of CAT-Q-15 and CAT-Q-22 obtained from SEM-EDS analysis illustrate the homogeneous dispersion of cobalt over the entire analysed spot area. CAT Q-15 showed less dense and better homogeneous morphology than that of CAT-Q-22. Totally, it could be concluded that better active site distributions were achieved in these two catalysts compared to those of high cobalt content samples (CAT-Q-29 and CAT-Q-36). The cobalt particles over the surface of these two catalysts were agglomerated and exhibited non-uniform distribution. While it is the case that due to the application of high surface area support (SUP-Q-10 surface area:  $277.4 \text{ m}^2/\text{g}$ ), greatly dispersed catalysts were expected in this investigation [139]. Some reasons could be ascribed as the inconsistent mass distribution of cobalt metals over the support surface in CAT-Q-29 and CAT-Q-36, as well as the agglomeration of cobalt oxides. During the preparation steps, a thermal gradient occurred by evaporation of moisture from the outside. As a result of the thermal gradient, an outward flow from inside to the outside of the pores of support occurred and subsequently the metal oxides were concentrated on the support surface, particularly when the metal content was increased; which leads to more accumulation of metal oxide and inhomogeneous formation of lumps [182, 183].

## 7.6 Catalyst activity and selectivity in the FTS process

The F-T performance of the different catalysts were considered at 510 K, 20 bar and 3.0 NI/h.gcat. The hydrogenation activities of differently loaded catalysts were examined in a same reactor set-up and reaction conditions, as well as gaseous environment, to achieve a strict control on the synthesis system to ensure the comparison was done properly. The catalyst activities in terms of CO conversion as well as hydrocarbon/by-product selectivity were observed while the catalysts were on stream for 4 h from time to time and the results are listed in Table 7.6. It should be mentioned that the reaction temperature was adjusted to relatively lower than the F-T reaction temperature to prevent the maximum carbon monoxide adsorption rate of the Co catalyst. The results of characterization experiments provided evidence that the amount of cobalt loading had a significant influence on the size of the cobalt clusters formed over the support surface, as well as the cobalt-silica interactions. The results represented in Table 7.6 illustrate that as the cobalt content in the catalysts increased from 15 to 36 wt%, the hydrogenation activity of the catalyst in terms of carbon monoxide conversion was increased by 68.4 % (from 27.67 to 87.65 mol%).

**Table 7.6:** Catalytic performances of the different catalysts in F-T synthesis: CO conversion ( $X_{CO}$ ), products selectivity ( $S_{CO_2}$ ,  $S_{CH_4}$ ,  $S_{C_2-C_4}$ ,  $S_{C_5+}$ ), reaction conditions: 510 K, 20 bar and 3.0 NI/min.g<sub>cat</sub>

Catalyst	$X_{(CO)}$ (Mol %)	Selectivity of gas phase products (mol %)					
		$S_{(CO_2)}$	$S_{(CH_4)}$	$S_{(C_2)}$	$S_{(C_3)}$	$S_{(C_4)}$	$S_{(C_5+)}$
<b>CAT-Q-15</b>	27.67	1.96	41.85	4.07	8.10	7.16	38.82
<b>CAT-Q-22</b>	44.95	2.09	28.003	2.68	5.19	4.52	59.60
<b>CAT-Q-29</b>	61.74	2.88	24.09	0.21	0.39	0.34	74.95
<b>CAT-Q-36</b>	87.65	5.32	13.44	1.10	1.90	1.75	81.78

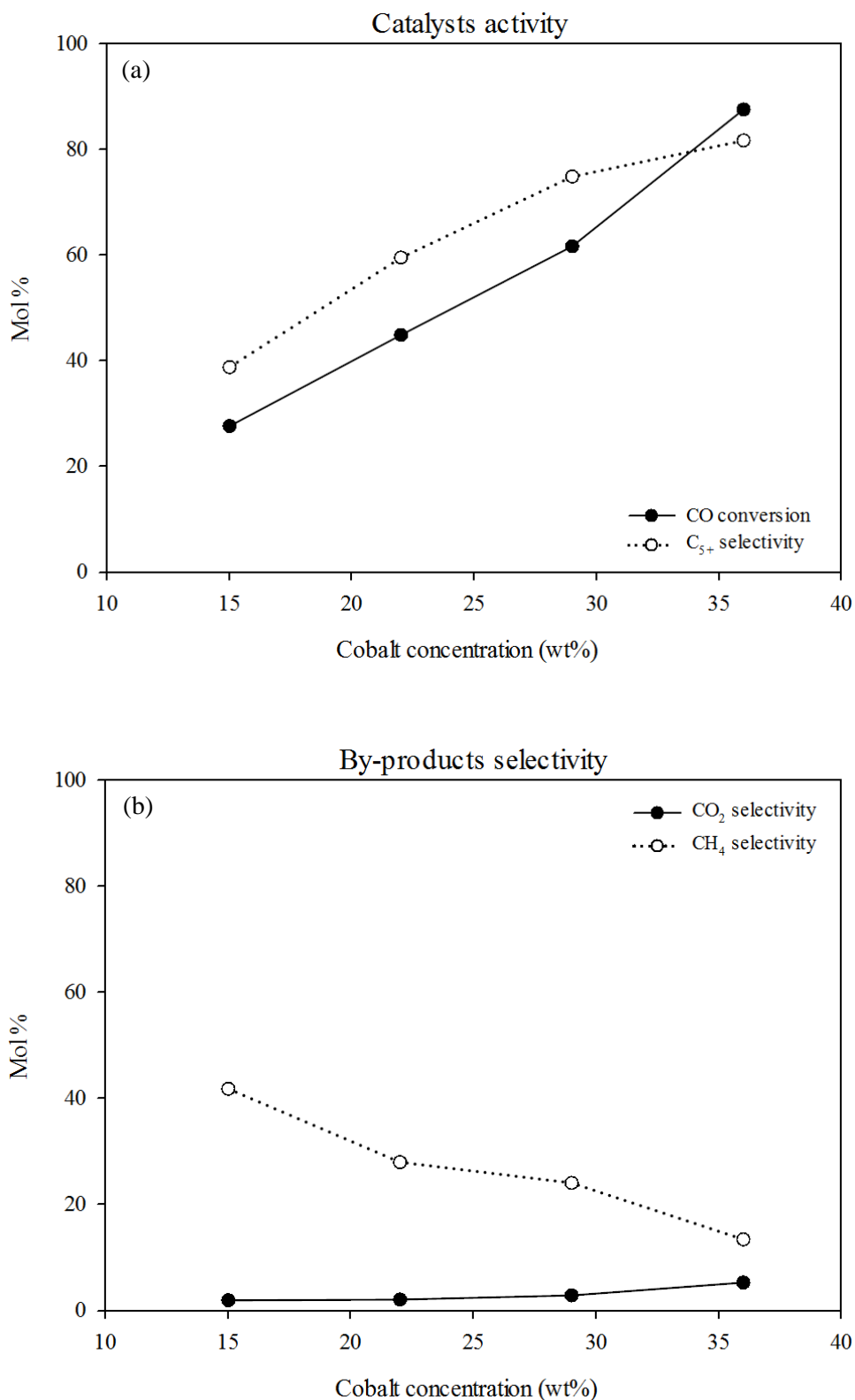


**Figure 7.14:** Effect of active metal concentration over support material surface on the catalytic performance of Co/SiO<sub>2</sub> catalyst in F-T synthesis of heavy hydrocarbons, reaction conditions: P=20 bar, T=510 K and WHSV=3.0 NI/h.g<sub>cat</sub>

The activities of different catalysts as well as by-products selectivity are shown in Figure 7.14 (a)-(b) as a function of the metal concentration. Figure 7.14 (a) clearly demonstrates that carbon monoxide conversion was increased linearly with increasing the concentration of the active sites from 15 to 29 wt% over the amorphous silica support surface. The results are in good agreement with those reported by Sun et al [71]. The increase in hydrogenation activity was slightly higher when the cobalt loading was increased to 36 wt% in CAT-Q-36. The increase in CO conversion was a consequence of the increase in the amount of well-dispersed cobalt species in CAT-Q-36. The formation of a larger cobalt crystalline size than in sample CAT-Q-29 was observed for this catalyst in the XRD analysis. Since the activity of the cobalt catalyst is proportional to the concentration of accessible surface metallic cobalt ( $\text{Co}^0$ ), the higher hydrogenation activity of CAT-Q-36 (CO conversion = 87.65 mol%) compared to that of the low-cobalt-content catalysts confirms that the cobalt particles have not been aggregated, due to the increase in cobalt loading and subsequently in cobalt crystalline size in this catalyst. In contrast to the investigation of Medina et al [184], who observed a decrease in CO conversion of a cobalt supported silica catalyst with the increasing of the metal content to above 20 wt%; the hydrogenation activity was increased in our case by increasing the metal loading. The temperature of the F-T synthesis regime was kept considerably constant in order to obtain the accurate results during the experiments.

The product distributions of the catalysts were largely affected by the amount of metal loading. All of the catalysts showed high selectivity in methane formation. The increases in the concentration of active sites resulted in a decrease in production of methane. The maximum  $\text{CH}_4$  selectivity was reported for the CAT-Q-15 ( $S_{\text{CH}_4} = 41.85 \text{ mol } \%$ ) and the minimum selectivity of methane was for CAT-Q-36 ( $S_{\text{CH}_4} = 13.44 \text{ mol } \%$ ). Figure 7.14 (b) supports this explanation by showing the methane selectivity as well as carbon dioxide

selectivity corresponding to the metal content in the catalysts. In contrast to the methane formation, Water-Gas-Shift (WGS) reaction showed a different trend. CAT-Q-15 showed the lowest carbon dioxide production; whereas the  $\text{CO}_2$  selectivity was increased by an increase in the metal content. CAT-Q-36 revealed the highest selectivity in  $\text{C}_{5+}$  hydrocarbon compared to the others ( $S_{\text{C}_{5+}} = 81.78 \text{ mol } \%$ ); while as it was expected, CAT-Q-15 was allocated the lowest selectivity in heavy hydrocarbons production ( $S_{\text{C}_{5+}} = 38.82 \text{ mol } \%$ ). Since the metal dispersion greatly influences the selectivity of the long-chain hydrocarbons, due to well-dispersed F-T active sites in all of the catalysts, the  $\text{C}_{5+}$  selectivity was relatively high in four of the catalysts ranging from 38.82 to 81.78 mol %.

It should be taken into account that the reactants' conversion, by-products' selectivity as well as long-chain hydrocarbons' selectivity, are all influenced by enhancement in the space velocity; which are in accordance with the kinetics and thermodynamics of the F-T synthesis. Since the space velocity was constant during all of the experiments, the decrease in the active site content resulted in an increase in the concentration of the reactants in the F-T regime and consequently a decrease in reactants' residence time. Generally high space velocity is associated with low residence time [24]. A part of the decrease in the reactant conversion could be ascribed to the fact that an increase in space velocity led to a decrease in reactant consumption due to low residence time (Figure 7.14a). The direct hydrogenation of carbon monoxide to produce methane could be associated with the increase in the production of methane by decreasing the active metal content from 36 to 15 wt% due to the low residence time of the reactants (Figure 7.14 (b)). The investigation confirms that the conversion per pass of reactants could be maximized by increasing the concentration of the active sites over the support surface without any dramatic reduction in accessibility of the  $\text{Co}^0$  particles due to formation of small hardly reducible particles as well as their agglomeration.

## 7.7 Conclusion

The study was carried out to examine the effect of metal precursor loading on the catalytic behaviour of the cobalt supported silica powder. The catalytic performance of an eggshell Co/SiO<sub>2</sub> catalyst was investigated by utilizing fixed-bed reactor technology in a Low-Temperature Fischer-Tropsch Synthesis (LTFT) process operating at 510 K bed temperature, 20 bar reaction pressure and 3.0 NI/h.gcat WHSV. The increase in the concentration of active metal sites resulted in a highly active supported cobalt catalyst. The highly-loaded catalysts with approximately 36 wt% cobalt content had weaker interaction with SiO<sub>2</sub> support than that of the less-loaded cobalt catalysts (cobalt loading: 22-29 wt%); which caused the catalyst to be reduced at a lower temperature than at which it was activated. The cobalt crystalline size and subsequently the cobalt particle size were greatly influenced by the metal loading. A small CoO and Co<sub>3</sub>O<sub>4</sub> crystalline size was obtained due to strong interactions between the metal precursor and silica support. It should be taken into account that the reduction of CoO<sub>x</sub> clusters would be suppressed if the cobalt-silica interaction became too strong. The reduction of CoO<sub>x</sub> clusters was promoted due to formation of relatively small cobalt crystalline in size (Co<sup>0</sup>=12.03 nm) and easily reducible particles (reduction temperature: 455°C), by increasing the concentration of active metal content to 36 wt%; which resulted in the synthesis of the highly dispersed cobalt supported silica catalyst. The conversion of the reactant was maximized (X<sub>CO</sub>=99 mol %) by enhancing the distribution of the active sites over the large surface area of the silica support.



---

# Chapter 8

---

## CONCLUSION

The aim of this thesis was to investigate the suitability of the Fischer-Tropsch synthesis process in the production of consumable liquid bio-fuels from nitrogen-rich syngas under moderate reaction conditions. For this purpose, a mini-scale bio-fuel generator was designed and developed to utilise the Low-Temperature Fischer-Tropsch synthesis (LTFT) technology to carry out the preliminary studies. The design and formulation of a supported highly-dispersed cobalt-based catalyst was the final aim of this thesis, in order to maximize the conversion per pass of reactants in the F-T regime. The investigations reported in this thesis consisted of : i) a comprehensive literature review on the Fischer-Tropsch synthesis process (Chapter 2); ii) the designing and developing of a F-T bio-diesel generator along with silica supported eggshell cobalt catalysts' formulation (Chapter 3); iii) an investigation on the effect of silica support's variables on the catalytic performance of the cobalt-based FTS process to produce heavy hydrocarbons (Chapter 4); iv) an optimization study of cobalt-based F-T synthesis at low/medium range pressure and low temperature reaction conditions to produce bio-diesel (Chapters 5 and 6); v) the effect of active site concentration on the hydrogenation activity of a supported cobalt-based catalyst in the Fischer-Tropsch synthesis process (Chapter 7). The main conclusions and suggestions for future works are summarized in the following paragraphs:

The designing of an effective and inexpensive catalyst for a low temperature / pressure FTS process is a complex task for researchers working in this area. During this work, an effort was made to design, develop and prepare a silica supported cobalt-based eggshell catalyst with consideration of the chemical and mechanical specifications of the prepared catalyst; as well as its cost as the main aspect in the design of the F-T catalyst. The proposed study advanced the research towards an integrated catalyzed liquid fuel production system utilizing a micro-sized catalyst's pellet distribution.

For this purpose, a series of four catalysts with dissimilar textures were prepared in order to consider the effect of support variables (surface area and pore size distribution) in the catalytic behaviour of a cobalt catalyst in the F-T synthesis process. The average pore diameter varied from 2.37 to 46.9 nm. The catalysts were characterized by using X-ray Fluorescence (XRF) analysis, nitrogen adsorption/desorption measurement, X-Ray Diffraction (XRD) analysis and Scanning Electron Microscopy (SEM) fixed with Energy-Dispersive Spectroscopy (EDS) analysis (Chapter 4, section 4.1 to 4.4), to examine the physicochemical properties of the cobalt catalysts. It was clear from BET/BJH measurements that the surface area significantly influenced the support's pore diameter. The highest pore size (46.9 nm) was reported for the catalyst with the lowest surface area ( $76.75 \text{ m}^2/\text{g}$ ). The catalyst preparation procedures also affected the supports' texture; thus after impregnation, a decrease in surface area and subsequently a change in pore size distribution of all of the catalysts were observed. The XRD patterns clearly confirmed that the support's pore size greatly influenced the metal cluster size. The presence of small cobalt crystalline (9.40 nm) was observed over the narrow pore size based catalyst. The larger cobalt crystalline (22.74 nm) and subsequently the  $\text{Co}^0$  particle diameter (17.05 nm) was formed with increasing the support pore diameter from 2.37 to 46.9 nm. The formation of poly-dispersed spherical cobalt

particles was confirmed by SEM analysis. The depositions of the active sites on the external surface of the supports were exhibited in SEM imaging. The catalyst with a large surface area showed better distribution in the active sites while the agglomerations of metal oxide were seen in the catalyst with a low surface area. It was concluded from EDS mapping that a highly-dispersed cobalt catalyst could be achieved by using high surface area supports. The hydrogenation studies of the prepared catalyst were performed by using a single-channel fixed-bed reactor. The results provided evidence that the catalyst pore size greatly influenced the catalytic activity in terms of carbon monoxide conversion as well as products' distribution in the F-T process. The reactant conversion was enhanced by the formation of more accessible active sites over the medium-pore size supports, ranging from 5.76 to 16.4 nm. The catalyst with 5.76 nm pore size revealed the highest activity of the F-T synthesis. The poorly dispersed catalyst with the lowest surface area (76.75) revealed the lowest conversion per pass of carbon monoxide in the F-T synthesis; which is as a function of metal dispersion. The chain growth probability was improved by increasing the pore size of the catalyst. It was concluded that the catalyst with the narrow pore size formed small cobalt of crystalline size which resulted in higher hydrogenation activity compared to chain growth power. The C<sub>5+</sub> hydrocarbon selectivity was maximized by increasing the catalyst's pore size due to the higher elementary polymerization rate affected by the larger cobalt particle size.

A systematic design and development of a laboratory-scale bio-diesel generator for hydrogenation of carbon monoxide has been principally presented in this thesis (Chapter 3). The aim was to design an in-expensive reactor system by using fixed-bed reactor technology to conduct the synthesis of liquid fuels at low pressure ( $2 \leq p \leq 10$  bar) and medium range pressure ( $10 \leq p \leq 25$  bar) reaction conditions, using a cylinder of simulated synthesis gas with the same gas ratio as generated from the biomass gasification process (hydrogen: 33 %,

carbon monoxide: 17 % and balanced with nitrogen (volume %)). The reaction conditions were optimized in order to maximize the activity of the cobalt-based eggshell catalyst in terms of reactant conversion to make the process cost-effective. The best combination of fixed-bed reactor, cobalt catalyst and synthesis reaction conditions with respect to reactant conversion, product selectivity and liquid fuel production were found to be at pressure = 10 bar, temperature = 518 K and WHSV = 2.4 NI/h.g<sub>cat</sub> for a set of low-pressure optimization investigations (Chapter 5). At this condition the CO conversion of 93.03 mol% was obtained and the long-chain hydrocarbons' selectivity was maximized to 68.56 mol%. A minimum reactor pressure of 6 bar was required to yield an acceptable productivity in the system. It was also proven that when the reactor operates at low pressure, the direct conversion of carbon monoxide to methane was increased; whereas the activity of WGS reaction was decreased. Evidence from the literature, shows that operating F-T synthesis at a low pressure reaction condition could accelerate the deactivation of a cobalt catalyst. In the current study it was found that such conditions led to a lower deactivation trend. In addition, it was concluded that the F-T synthesis process operated at low pressure reaction conditions and 2 and 6 bar were not efficient. A closed loop design for internal-external recycling of the tail gas (unreacted raw materials) in the product stream is thus required to remove unwanted products and convert un-reacted syngas to the desired product.

The optimization study of F-T synthesis at a medium-range pressure of the process (Chapter 6) demonstrated that medium-pressure reaction conditions ( $10 \leq p \leq 25$  bar) are required to achieve a highly-efficient fuel generating process in Low-Temperature F-T synthesis, with high productivity in the middle distillates production. During this study, due to the structure of the mini-scale F-T experimental rig, the hydrogenation activity of carbon monoxide was carried out in a pressurized system and therefore no pressure drop occurred during the

synthesis process. Nevertheless, operating the Fischer-Tropsch synthesis process at high pressure could decrease the pressure drop of continuous reactor systems at the same space velocity, in comparison to that of operating at low pressure reaction conditions in industrially relevant reaction conditions (temperature and space velocity). Furthermore, the investigation was successful in enhancing the consumption of carbon monoxide to the highest point (CO conversion = 99.9 mol %) through the stable activity of the catalyst in the F-T regime. The effect of reaction conditions at medium range reaction pressure were examined by planning a comprehensive set of experiments using the Taguchi method for the Design of Experiments (DOE). The adsorption rate on the catalyst, desorption rate of the products, as well as the reactants' concentration, were regulated by controlling the reaction parameters, especially the bed temperature. The F-T polymerization process operating at medium-range pressure was found to be an efficient method of producing long-chain paraffins and olefins. The product selectivity to linear alkanes and alkenes' products was studied in a cobalt-based fixed bed reactor over a vast range of industrially relevant process reactions on an impregnated eggshell catalyst. The fraction of diesel products ( $C_{12}-C_{22}$ ) in the produced liquid phase was maximized to 81.70 % with minimizing the cut of the gasoline products ( $C_7-C_{11}$ ) to 14.91%. The thermodynamic efficiency of the designed system as well as flow-reactor technology requires considerable improvement in order to enable the utilization of a highly active catalyst.

To increase the efficiency of a bio-fuel generator in single-pass F-T Synthesis process, the distribution of the metal active sites were enhanced in order to maximize the hydrogenation activity of the cobalt-based silica supported eggshell catalyst in the F-T catalytic process (Chapter 7). It was concluded that at medium-range pressure operation, the per-pass conversion of reactants over a Co-based catalyst could be maximized to 99.9 mol% without any concern in catalyst de-activity as well as without any suppression of  $CoO_x$  clusters, which

could have been caused by the strong interaction of Co-Si. The increase in the cobalt precursor loading up to 36 wt% resulted in the formation of moderate-sized cobalt crystalline clusters and subsequently easily reducible cobalt particles ( $\text{Co}^0 = 12.03 \text{ nm}$ ) with relatively weak interaction with the  $\text{SiO}_2$  support.

The significant aspects in the design and development of an F-T catalyst should be considered parallel to the development of the F-T catalytic process. Most of the recently performed research deals with the activity of the cobalt-based catalyst and selectivity of high molecular weight hydrocarbons as well as their resistance to attrition. Catalyst deactivation is an important aspect that should be investigated, to enhance the lifetime of this catalyst on stream, due to the relatively high cost of the cobalt precursor; which could result in favourable F-T process economy. Future study should investigate the effect of different cobalt precursor loading on catalytic behaviour of silica supported eggshell catalysts with a high concentration of active metals. It is suggested that the highly-loaded catalyst should be promoted with appropriate promoters.

An optimal bio-fuel generator using a fixed-bed reactor via the F-T synthesis process could be achieved by employing a highly active cobalt catalyst to produce bio-diesel. Heat transfer limitations as well as mass transfer limitations are two important drawbacks of a fixed-bed reactor which are considered as the main barrier in the exploitation of this system in F-T technology. The mass transfer limitation in fixed-bed reactors could be overcome by employing the eggshell catalyst. Supreme control in the reaction regime's temperature as a result of improved heat transfer will allow the usage of a highly-active cobalt catalyst. Considering the mentioned disadvantages along with the advantages of fixed-bed reactor technology, (e.g. ease of gas-liquid and catalyst-product separation, the ease of catalyst

loading as well as low cost of this reactor) could accelerate the application and commercialization of small scale bio-fuel generators in different industrial divisions including the agricultural sector.



## Appendix A

### X-ray Fluorescence (XRF) analysis of oxide particles

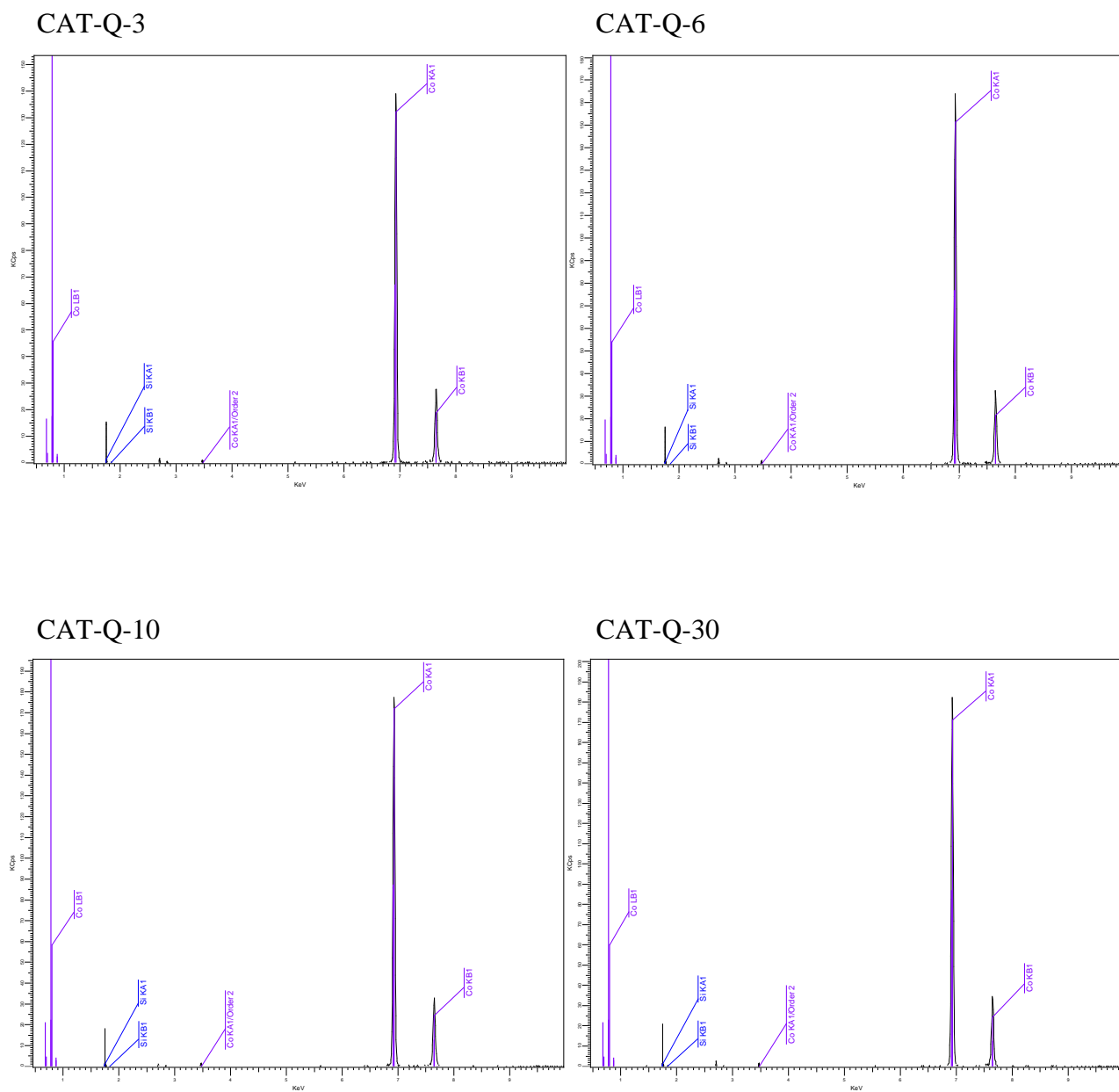


**Figure A.1:** X-ray Fluorescent (XRF) spectra of CAT-Q-3, CAT-Q-6, CAT-Q-10 and CAT-Q-30 in the vicinity of Co K $\alpha$ , Co K $\beta$ , Co L $\beta$ , Si K $\alpha$  and Si K $\beta$

A2

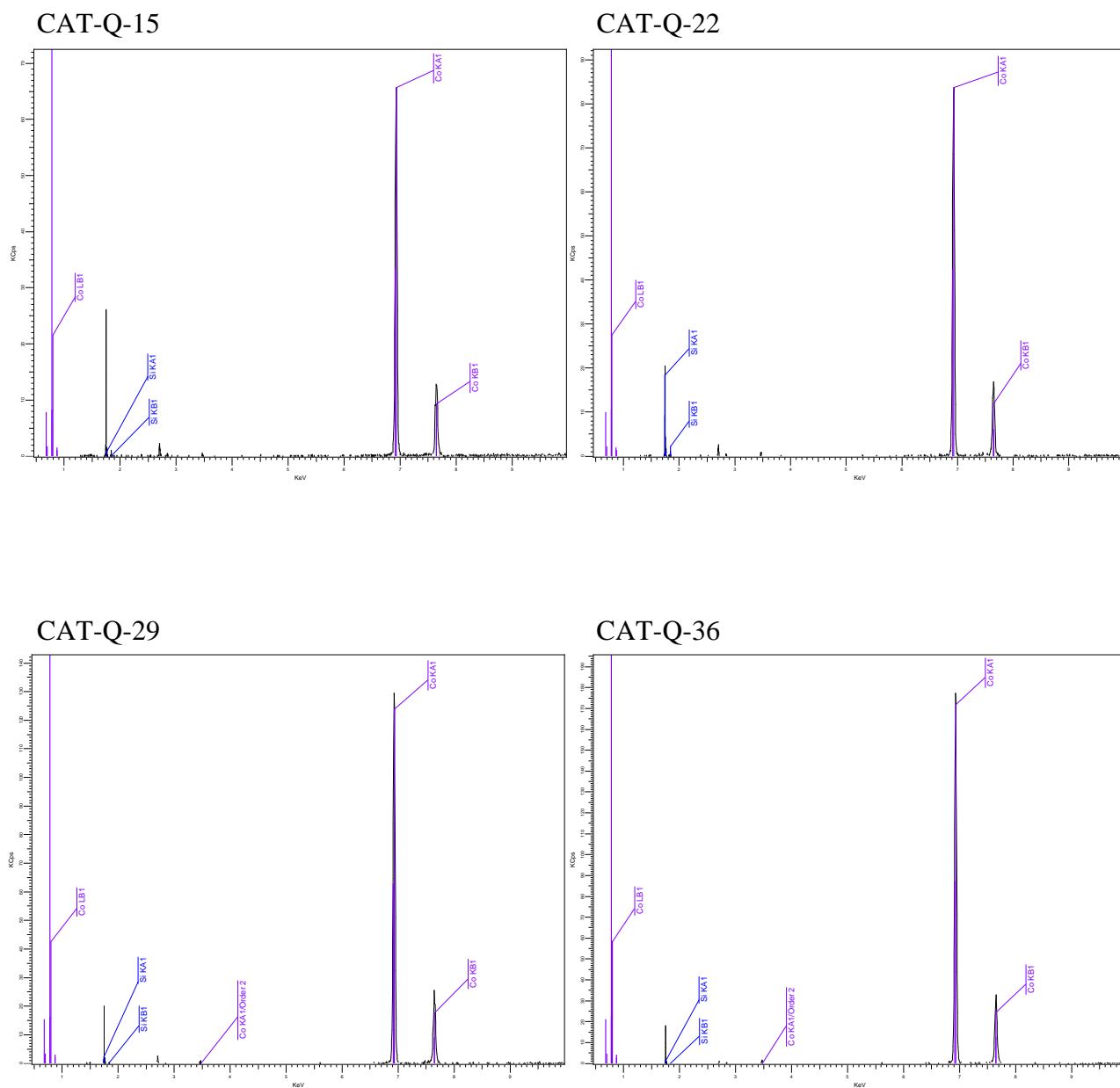


**Figure A.2:** X-ray Fluorescent (XRF) spectra of CAT-Q-15, CAT-Q-22, CAT-Q-29 and CAT-Q-36 in the vicinity of Co K $\alpha$ , Co K $\beta$ , Co L $\beta$ , Si K $\alpha$  and Si K $\beta$

## Appendix B

### Nitrogen adsorption/desorption analysis

**Table B.1:** Variables derived from nitrogen physisorption to measure the total surface area different support materials including SUP-Q-3, SUP-Q-6, SUP-Q-10, and SUP-Q-30,

SUP-Q-3			SUP-Q-6		
Slope (S g/cm <sup>3</sup> STP)	0.006205		Slope (S g/cm <sup>3</sup> STP)	0.007724	
Y-intercept (i g/cm <sup>3</sup> STP)	0.000034		Y-intercept (i g/cm <sup>3</sup> STP)	0.000093	
BET Constant (C <sub>BET</sub> )	181.433403		BET Constant (C <sub>BET</sub> )	84.394041	
V <sub>ml</sub> (cm <sup>3</sup> /g STP)	160.271505		V <sub>ml</sub> (cm <sup>3</sup> /g STP)	127.926281	
Adsorbate Cross-section (nm <sup>2</sup> )	0.1620		Adsorbate Cross-section (nm <sup>2</sup> )	0.1620	
$P/P_0$	$V_{ads}$ (cm <sup>3</sup> /g STP)	$\frac{P/P_0}{V_{ads}(1 - P/P_0)}$	$P/P_0$	$V_{ads}$ (cm <sup>3</sup> /g STP)	$\frac{P/P_0}{V_{ads}(1 - P/P_0)}$
0.057751340	154.9751	0.000395	0.057667747	114.2255	0.000536
0.076742180	162.4970	0.000512	0.076945093	121.0927	0.000688
0.119745850	175.8623	0.000774	0.116193491	132.4964	0.000992
0.156442723	185.3522	0.001001	0.157040086	142.7334	0.001305
0.199582435	195.1772	0.001278	0.199510924	152.6262	0.001633
SUP-Q-10			SUP-Q-30		
Slope (S g/cm <sup>3</sup> STP)	0.015549		Slope (S g/cm <sup>3</sup> STP)	0.038646	
Y-intercept (i g/cm <sup>3</sup> STP)	0.000144		Y-intercept (i g/cm <sup>3</sup> STP)	0.000309	
BET Constant (C <sub>BET</sub> )	109.323786		BET Constant (C <sub>BET</sub> )	126.014993	
V <sub>ml</sub> (cm <sup>3</sup> /g STP)	63.723157		V <sub>ml</sub> (cm <sup>3</sup> /g STP)	25.670440	
Adsorbate Cross-section (nm <sup>2</sup> )	0.1620		Adsorbate Cross-section (nm <sup>2</sup> )	0.1620	
$P/P_0$	$V_{ads}$ (cm <sup>3</sup> /g STP)	$\frac{P/P_0}{V_{ads}(1 - P/P_0)}$	$P/P_0$	$V_{ads}$ (cm <sup>3</sup> /g STP)	$\frac{P/P_0}{V_{ads}(1 - P/P_0)}$
0.057276470	58.6236	0.001036	0.059396437	24.1299	0.002617
0.080931774	62.7084	0.001404	0.083389108	25.7326	0.003535
0.114972484	67.3940	0.001928	0.119539749	27.6428	0.004912
0.160330899	72.6073	0.002630	0.160385425	29.4448	0.006487
0.201079484	76.8248	0.003276	0.199127270	30.9795	0.008026

## Appendix C

### Table of Analysis of Variance (ANOVA)

**Table C.1:** Tables of Analysis of Variance (ANOVA) for low/medium pressures optimisation studies

Source	Degree of Freedom ( <i>f</i> )	Sum of Square ( <i>SS</i> )	Variance (Mean Squares)	F ratio	P ratio
<b>Low-pressure optimization study</b>					
<b>Control factors:</b> Temperature, Pressure and Space velocity					
<b>Response variables:</b> Carbon monoxide conversion, Carbon dioxide selectivity, Methane selectivity, Heavy hydrocarbons selectivity, Liquid produced					
<b>One-way ANOVA: Carbon monoxide conversion versus Temperature</b>					
<b>Treat</b>	2	1633	817	1.96	0.221
<b>Error</b>	6	2497	416		
<b>Total</b>	8	4130			
S = 20.40		R-Sq = 39.55 %		R-Sq (adj) = 19.40 %	
<b>One-way ANOVA: Carbon monoxide conversion versus Pressure</b>					
<b>Treat</b>	2	1821	910	2.37	0.175
<b>Error</b>	6	2309	385		
<b>Total</b>	8	4130			
S = 19.62		R-Sq = 44.08 %		R-Sq (adj) = 25.44 %	
<b>One-way ANOVA: Carbon monoxide conversion versus Space velocity</b>					
<b>Treat</b>	2	637	318	0.55	0.605
<b>Error</b>	6	3493	582		
<b>Total</b>	8	4130			
S = 24.13		R-Sq = 15.41 %		R-Sq (adj) = 0.00 %	
<b>One-way ANOVA: Carbon dioxide selectivity versus Temperature</b>					
<b>Treat</b>	2	230.26	115.13	12.86	0.007
<b>Error</b>	6	53.71	8.95		
<b>Total</b>	8	283.97			
S = 2.992		R-Sq = 81.09 %		R-Sq (adj) = 74.78 %	

*Continued on the next page*

---

**One-way ANOVA: Carbon dioxide selectivity versus Pressure**

<b>Treat</b>	2	24.2	12.1	0.28	0.766
<b>Error</b>	6	259.8	43.3		
<b>Total</b>	8	284.0			

S = 6.580

R-Sq = 8.52 %

R-Sq (adj) = 0.00 %

**One-way ANOVA: Carbon dioxide selectivity versus Space velocity**

<b>Treat</b>	2	29.1	14.5	0.34	0.723
<b>Error</b>	6	254.9	42.5		
<b>Total</b>	8	284.0			

S = 6.518

R-Sq = 10.24 %

R-Sq (adj) = 0.00 %

**One-way ANOVA: Methane selectivity versus Temperature**

<b>Treat</b>	2	357	179	0.47	0.645
<b>Error</b>	6	2268	378		
<b>Total</b>	8	2626			

S = 19.44

R-Sq = 13.61 %

R-Sq (adj) = 0.00 %

**One-way ANOVA: Methane selectivity versus Pressure**

<b>Treat</b>	2	1507	754	4.04	0.077
<b>Error</b>	6	1119	186		
<b>Total</b>	8	2626			

S = 13.65

R-Sq = 57.40 %

R-Sq (adj) = 43.20 %

**One-way ANOVA: Methane selectivity versus Space velocity**

<b>Treat</b>	2	512	256	0.73	0.522
<b>Error</b>	6	2114	352		
<b>Total</b>	8	2626			

S = 18.77

R-Sq = 19.48 %

R-Sq (adj) = 0.00 %

**One-way ANOVA: Heavy hydrocarbons selectivity versus Temperature**

<b>Treat</b>	2	257	129	0.24	0.797
<b>Error</b>	6	3281	547		
<b>Total</b>	8	3539			

S = 23.39

R-Sq = 7.27 %

R-Sq (adj) = 0.00 %

---

*Continued on the next page*

---

---

**One-way ANOVA: Heavy hydrocarbons selectivity versus Pressure**

<b>Treat</b>	2	1348	674	1.85	0.237
<b>Error</b>	6	2191	365		
<b>Total</b>	8	3539			
S = 19.11		R-Sq = 38.09 %		R-Sq (adj) = 17.46 %	

**One-way ANOVA: Heavy hydrocarbons selectivity versus Space velocity**

<b>Treat</b>	2	708	354	0.75	0.512
<b>Error</b>	6	2831	472		
<b>Total</b>	8	3539			
S = 21.72		R-Sq = 20.01 %		R-Sq (adj) = 0.00 %	

**One-way ANOVA: Liquid produced versus Temperature**

<b>Treat</b>	2	1.944	0.972	1.43	0.310
<b>Error</b>	6	4.074	0.679		
<b>Total</b>	8	6.019			
S = 0.8241		R-Sq = 32.30 %		R-Sq (adj) = 9.74 %	

**One-way ANOVA: Liquid produced versus Pressure**

<b>Treat</b>	2	3.540	1.770	4.28	0.070
<b>Error</b>	6	2.479	0.413		
<b>Total</b>	8	6.019			
S = 0.6428		R-Sq = 58.81 %		R-Sq (adj) = 45.08 %	

**One-way ANOVA: Liquid produced versus Space velocity**

<b>Treat</b>	0.444	0.222	0.24	0.795	
<b>Error</b>	5.757	0.929			
<b>Total</b>	6.019				
S = 0.9639		R-Sq = 7.37 %		R-Sq (adj) = 0.00 %	

---

**Section II****Medium-pressure optimization study****Control factors:** Temperature, Pressure and Space velocity**Response variables:** Carbon monoxide conversion, Carbon dioxide selectivity, Methane selectivity, Heavy hydrocarbons selectivity, Gasoline product fraction, Diesel product fraction, Wax product fraction, Liquid produced

---

*Continued on the next page*

---

---

**One-way ANOVA: Carbon monoxide conversion versus Temperature**

<b>Treat</b>	3	2262.2	754.1	17.28	0.000
<b>Error</b>	12	523.8	43.6		
<b>Total</b>	15	2786			

S = 6.607

R-Sq = 81.20 %

R-Sq (adj) = 76.50 %

**One-way ANOVA: Carbon monoxide conversion versus Pressure**

<b>Treat</b>	3	77	26	0.11	0.951
<b>Error</b>	12	2709	226		
<b>Total</b>	15	2786			

S = 15.03

R-Sq = 2.75 %

R-Sq (adj) = 0.00 %

**One-way ANOVA: Carbon monoxide conversion versus Space velocity**

<b>Treat</b>	3	237	79	0.37	0.774
<b>Error</b>	12	2549	212		
<b>Total</b>	15	2786			

S = 14.57

R-Sq = 8.52 %

R-Sq (adj) = 0.00 %

**One-way ANOVA: Carbon dioxide selectivity versus Temperature**

<b>Treat</b>	3	927.28	309.09	87.71	0.00
<b>Error</b>	12	42.29	3.52		
<b>Total</b>	15	969.57			

S = 1.877

R-Sq = 95.64 %

R-Sq (adj) = 94.55 %

**One-way ANOVA: Carbon dioxide selectivity versus Pressure**

<b>Treat</b>	3	4.0	1.3	0.02	0.997
<b>Error</b>	12	965.6	80.5		
<b>Total</b>	15	969.6			

S = 8.970

R-Sq = 0.41 %

R-Sq (adj) = 0.00 %

**One-way ANOVA: Carbon dioxide selectivity versus Space velocity**

<b>Treat</b>	3	34.0	11.3	0.15	0.931
<b>Error</b>	12	935.5	78.0		
<b>Total</b>	15	969.6			

S = 8.830

R-Sq = 3.51 %

R-Sq (adj) = 0.00 %

---

*Continued on the next page*

---

---

**One-way ANOVA: Methane selectivity versus Temperature**

<b>Treat</b>	3	2329.7	776.6	13.66	0.00
<b>Error</b>	12	682.4	56.9		
<b>Total</b>	15	3012.1			

S = 7.541

R-Sq = 77.34 %

R-Sq (adj) = 71.68 %

**One-way ANOVA: Methane selectivity versus Pressure**

<b>Treat</b>	3	47	16	0.06	0.978
<b>Error</b>	12	2965	247		
<b>Total</b>	15	3012			

S = 15.72

R-Sq = 1.57 %

R-Sq (adj) = 0.00 %

**One-way ANOVA: Methane selectivity versus Space velocity**

<b>Treat</b>	3	169	56	0.24	0.868
<b>Error</b>	12	2843	237		
<b>Total</b>	15	3012			

S = 15.39

R-Sq = 5.61 %

R-Sq (adj) = 0.00 %

**One-way ANOVA: Heavy hydrocarbons selectivity versus Temperature**

<b>Treat</b>	3	3733	1244	11.00	0.001
<b>Error</b>	12	1357	113		
<b>Total</b>	15	5090			

S = 10.63

R-Sq = 73.34 %

R-Sq (adj) = 66.67 %

**One-way ANOVA: Heavy hydrocarbons selectivity versus Pressure**

<b>Treat</b>	3	112	37	0.09	0.964
<b>Error</b>	12	4979	415		
<b>Total</b>	15	5090			

S = 20.37

R-Sq = 2.20 %

R-Sq (adj) = 0.00 %

**One-way ANOVA: Heavy hydrocarbons selectivity versus Space velocity**

<b>Treat</b>	3	413	138	0.35	0.788
<b>Error</b>	12	4677	390		
<b>Total</b>	15	5090			

S = 19.74

R-Sq = 8.11 %

R-Sq (adj) = 0.00 %

---

*Continued on the next page*

---

---

**One-way ANOVA: Gasoline product fraction versus Temperature**

<b>Treat</b>	3	87.4	29.1	1.81	0.198
<b>Error</b>	12	192.9	16.1		
<b>Total</b>	15	280.3			

S = 4.009

R-Sq = 31.19 %

R-Sq (adj) = 13.99 %

**One-way ANOVA: Gasoline product fraction versus Pressure**

<b>Treat</b>	3	73.7	24.6	1.43	0.284
<b>Error</b>	12	206.7	17.2		
<b>Total</b>	15	280.3			

S = 4.150

R-Sq = 26.28 %

R-Sq (adj) = 7.85 %

**One-way ANOVA: Gasoline product fraction versus Space velocity**

<b>Treat</b>	3	4.6	1.5	0.07	0.976
<b>Error</b>	12	275.7	23.0		
<b>Total</b>	15	280.3			

S = 4.793

R-Sq = 1.64 %

R-Sq (adj) = 0.00 %

**One-way ANOVA: Diesel product fraction versus Temperature**

<b>Treat</b>	3	112.2	37.4	2.90	0.079
<b>Error</b>	12	154.7	12.9		
<b>Total</b>	15	266.9			

S = 3.591

R-Sq = 42.04 %

R-Sq (adj) = 27.54 %

**One-way ANOVA: Diesel product fraction versus Pressure**

<b>Treat</b>	3	64.7	21.6	1.28	0.326
<b>Error</b>	12	202.2	16.9		
<b>Total</b>	15	266.9			

S = 4.105

R-Sq = 24.24 %

R-Sq (adj) = 5.30 %

**One-way ANOVA: Diesel product fraction versus Space velocity**

<b>Treat</b>	3	13.2	4.4	0.21	0.889
<b>Error</b>	12	253.7	21.1		
<b>Total</b>	15	266.9			

S = 4.598

R-Sq = 4.95 %

R-Sq (adj) = 0.00 %

---

*Continued on the next page*

---

---

**One-way ANOVA: Wax product fraction versus Temperature**

<b>Treat</b>	3	1.86	0.62	0.49	0.699
<b>Error</b>	12	15.34	1.28		
<b>Total</b>	15	17.21			
S = 1.131		R-Sq = 10.82 %		R-Sq (adj) = 0.00 %	

**One-way ANOVA: Wax product fraction versus Pressure**

<b>Treat</b>	3	1.60	0.53	0.41	0.749
<b>Error</b>	12	15.61	1.30		
<b>Total</b>	15	17.21			
S = 1.140		R-Sq = 9.29 %		R-Sq (adj) = 0.00 %	

**One-way ANOVA: Wax product fraction versus Space velocity**

<b>Treat</b>	3	3.10	1.03	0.88	0.479
<b>Error</b>	12	14.11	1.18		
<b>Total</b>	15	17.21			
S = 1.084		R-Sq = 18.01 %		R-Sq (adj) = 0.00 %	

**One-way ANOVA: Liquid produced versus Temperature**

<b>Treat</b>	3	6.952	2.317	2.80	0.085
<b>Error</b>	12	9.915	0.826		
<b>Total</b>	15	16.867			
S = 0.9090		R-Sq = 41.22 %		R-Sq (adj) = 26.52 %	

**One-way ANOVA: Liquid produced versus Pressure**

<b>Treat</b>	3	1.45	0.48	0.38	0.772
<b>Error</b>	12	15.42	1.28		
<b>Total</b>	15	16.87			
S = 1.134		R-Sq = 8.59 %		R-Sq (adj) = 0.00 %	

**One-way ANOVA: Liquid produced versus Space velocity**

<b>Treat</b>	3	4.31	1.44	1.37	0.299
<b>Error</b>	12	12.56	1.05		
<b>Total</b>	15	16.87			
S = 1.023		R-Sq = 25.53 %		R-Sq (adj) = 6.91 %	

---

## Appendix D

### Energy-Dispersive Spectroscopy (EDS) analysis

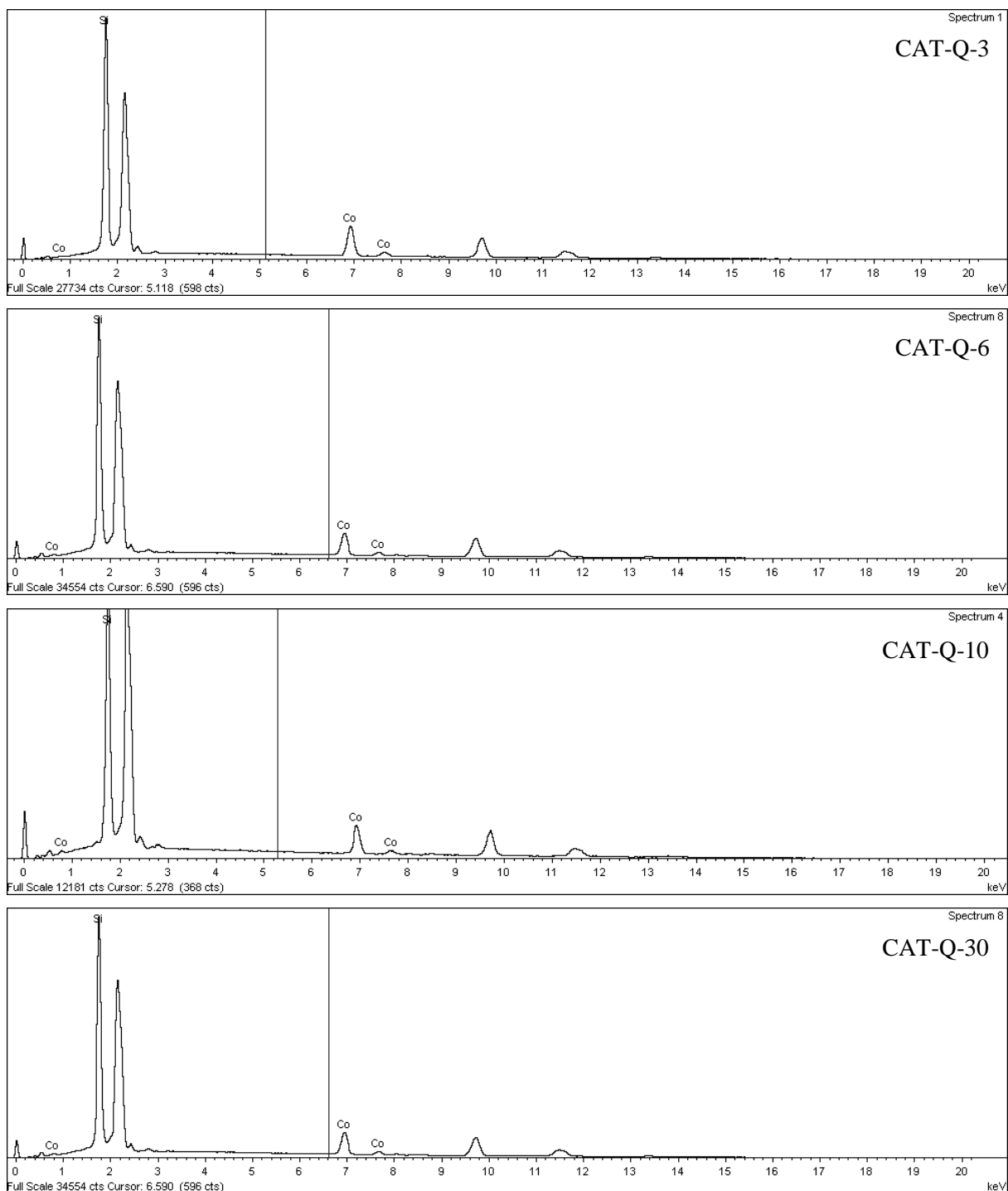


**Figure D.1:** Energy-Dispersive Spectroscopy (EDS) spectra of calcined and unreduced catalysts (CAT-Q-3, CAT-Q-6, CAT-Q-10 and CAT-Q-30) for elemental analysis of cobalt and silica

## D2

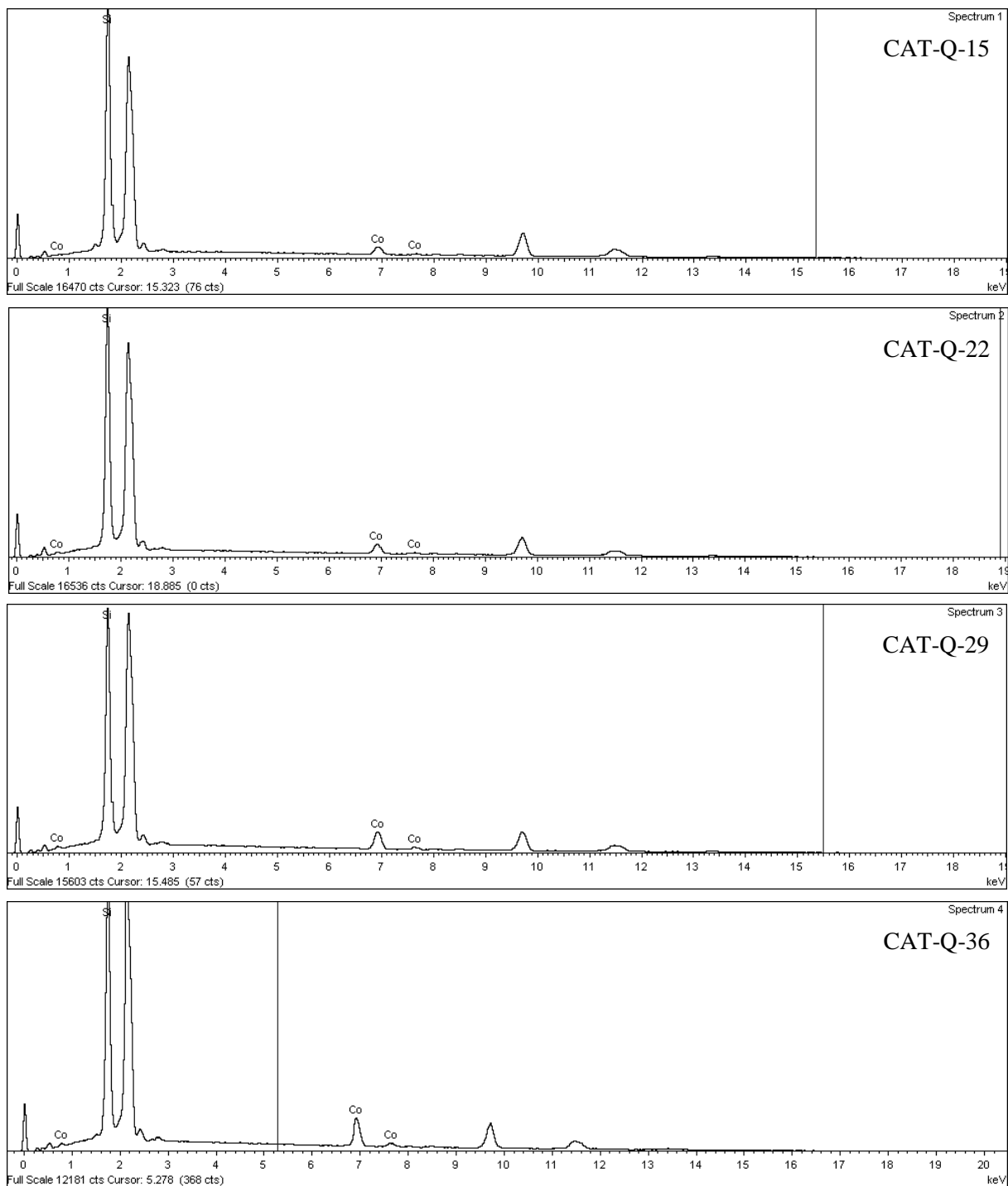


**Figure D.2:** Energy-Dispersive Spectroscopy (EDS) spectra of calcined and unreduced catalysts (CAT-Q-15, CAT-Q-22, CAT-Q-29 and CAT-Q-36) for elemental analysis of cobalt and silica

## Appendix E

### GC chromatogram

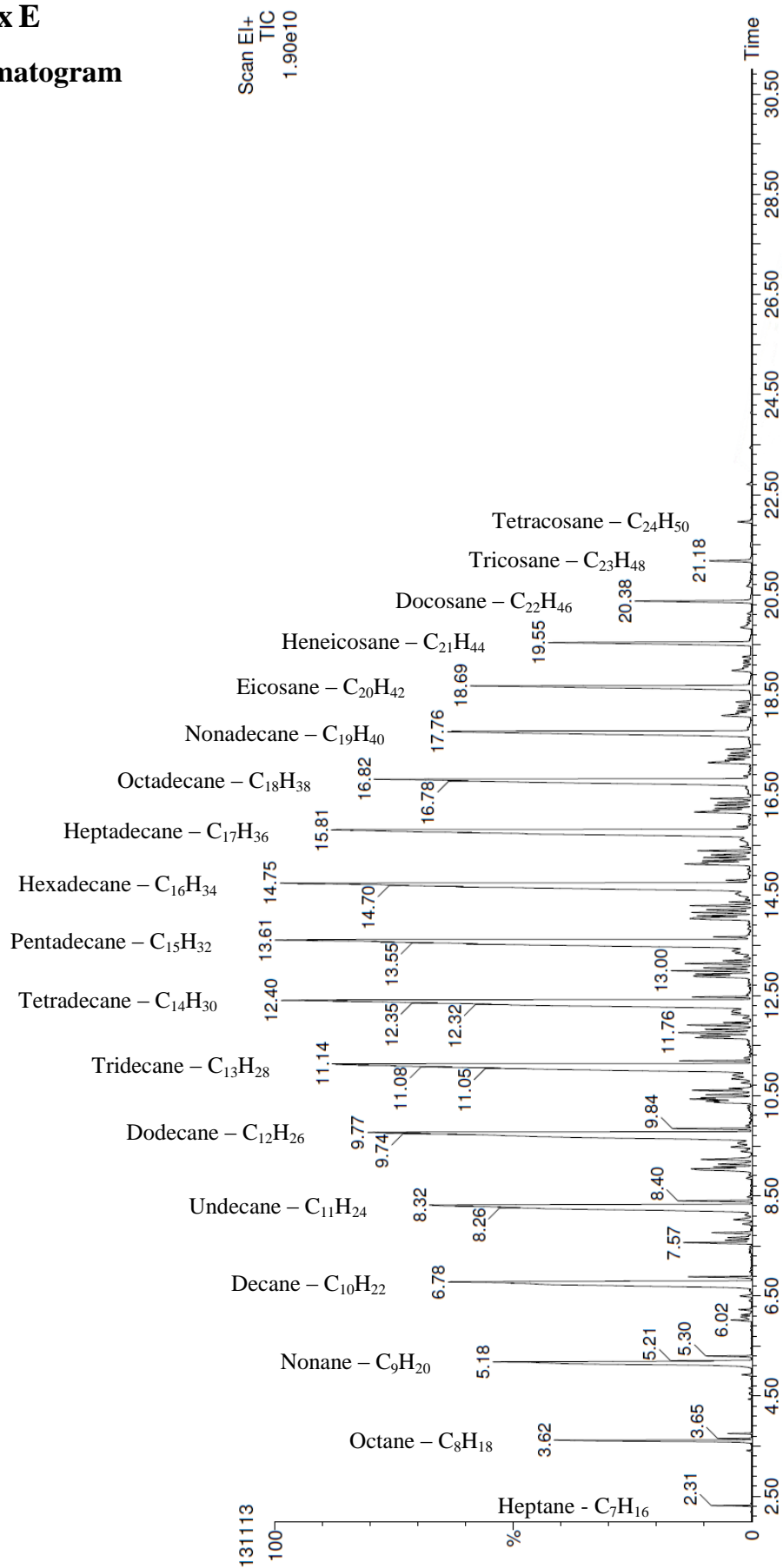
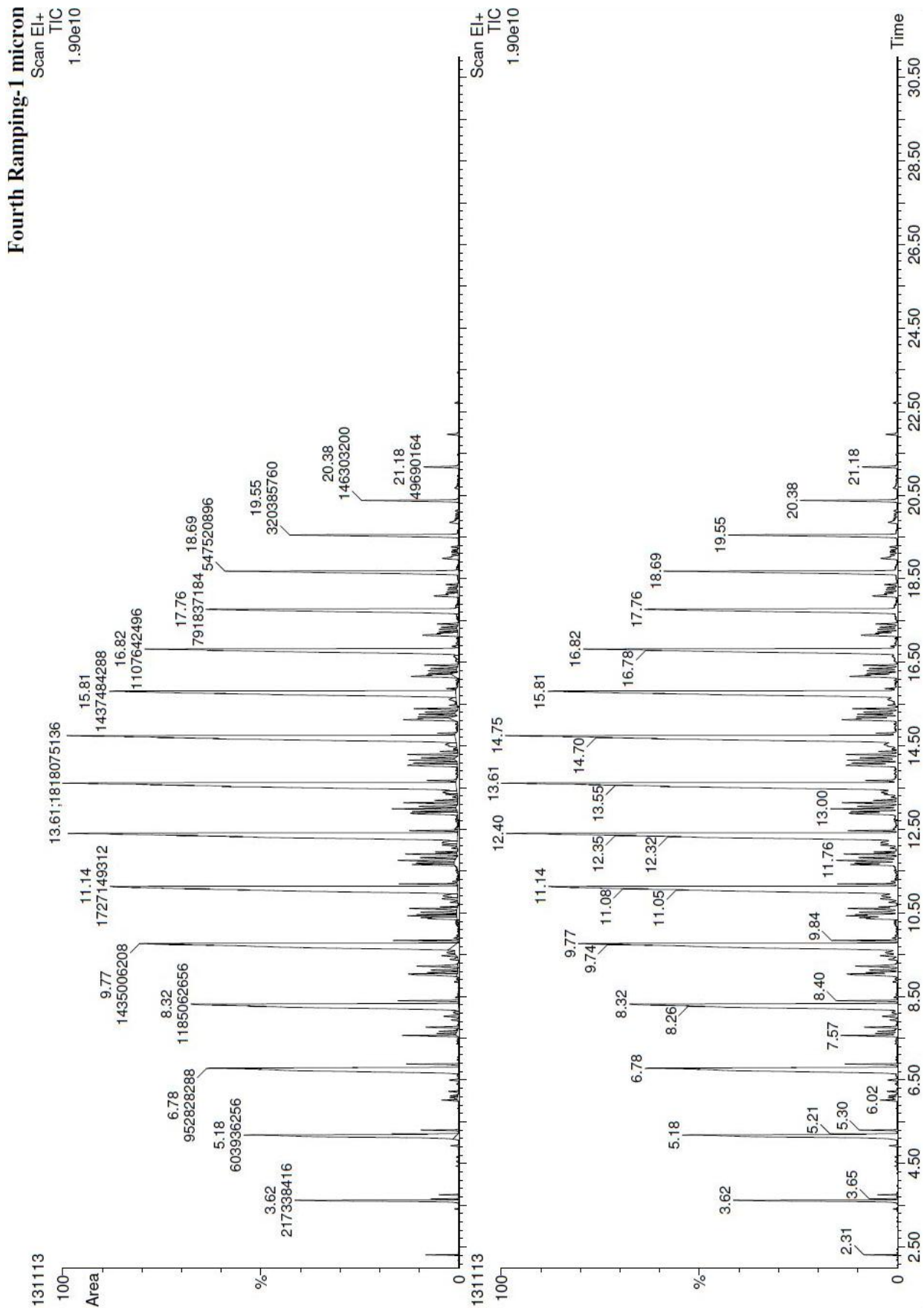


**Figure E.1:** Gas-Chromatography Mass-Spectrometry spectra of liquid sample (reaction operating conditions: P: 20 bar, T: 510 K, WHSV: 3.0 NI/h.g<sub>cat</sub>) (picture directly taken from PerkinElmer software)

Continuation of Figure E.1



# Appendix F

## GC-FID Chromatogram

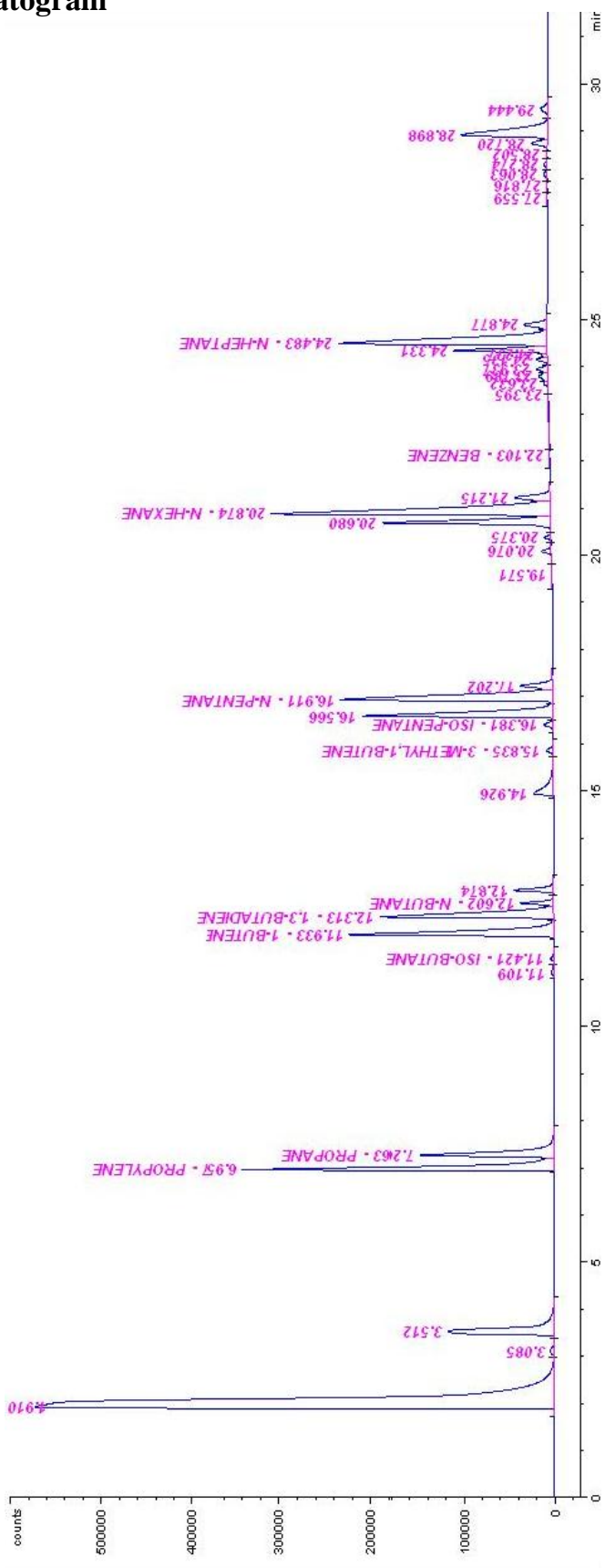


**Figure F.1:** Gas-Chromatography Flame-Ionization Detector (GC-FID) spectra of gaseous sample (reaction operating conditions: P: 20 bar, T: 510 K, WHSV: 3.0 NI/h.gcat (picture directly taken from HP ® 5890 software)



## References

- [1] A. N. Stranges, "A history of the fischer-tropsch synthesis in Germany 1926-45," *Studies in surface science and catalysis*, pp. 1-27, 2007.
- [2] E. N. Givens and B. H. Davis, "Synthetic lubricants: Advances in Japan up to 1945 based on Fischer-Tropsch derived liquids," *Fischer-Tropsch Synthesis, Catalysts and Catalysis*, vol. 163, p. 29, 2006.
- [3] A. de Klerk, "Chapter 12 - Transport Fuel: Biomass-, Coal-, Gas- and Waste-to-Liquids Processes," in *Future Energy (Second Edition)*, T. M. Letcher, Ed., ed Boston: Elsevier, 2014, pp. 245-270.
- [4] P. Basu, "Chapter 5 - Gasification Theory and Modeling of Gasifiers," in *Biomass Gasification and Pyrolysis*, P. Basu, Ed., ed Boston: Academic Press, 2010, pp. 117-165.
- [5] C. D. Chang, "Hydrocarbons from methanol," *Catalysis Reviews Science and Engineering*, vol. 25, pp. 1-118, 1983.
- [6] R. Y. Brogaard, R. Henry, Y. Schuurman, A. J. Medford, P. G. Moses, P. Beato, *et al.*, "Methanol-to-hydrocarbons conversion: The alkene methylation pathway," *Journal of Catalysis*, vol. 314, pp. 159-169, 2014.
- [7] Z. Liu and J. Liang, "Methanol to olefin conversion catalysts," *Current Opinion in Solid State and Materials Science*, vol. 4, pp. 80-84, 2// 1999.
- [8] K. P. Möller, W. Böhringer, A. E. Schnitzler, and C. T. O'Connor, "The conversion of methanol to hydrocarbons over ZSM5: Fixed bed vs. recycle reactor," in *Studies in Surface Science and Catalysis*. vol. Volume 130, F. V. M. S. M. Avelino Corma and G. F. José Luis, Eds., ed: Elsevier, 2000, pp. 2711-2716.
- [9] Z. Di, C. Yang, X. Jiao, J. Li, J. Wu, and D. Zhang, "A ZSM-5/MCM-48 based catalyst for methanol to gasoline conversion," *Fuel*, vol. 104, pp. 878-881, 2013.
- [10] IMechE, "Climate change adapting to the inevitable? ," *Institution of Mechanical Engineering*, p. 30, 2013.
- [11] E.I.A, "International Energy Outlook with projection to 2040," *United States Energy Information Administration*, p. 312, July 2013.
- [12] S. Czernik and A. Bridgwater, "Overview of applications of biomass fast pyrolysis oil," *Energy & Fuels*, vol. 18, pp. 590-598, 2004.
- [13] J. Perritano. *Top 10 Advantages of Biofuels*. Available: <http://www.howstuffworks.com/>
- [14] A. Murugesan, C. Umarani, R. Subramanian, and N. Nedunchezian, "Bio-diesel as an alternative fuel for diesel engines—A review," *Renewable and Sustainable Energy Reviews*, vol. 13, pp. 653-662, 2009.
- [15] S. Gill, A. Tsolakis, K. Dearn, and J. Rodríguez-Fernández, "Combustion characteristics and emissions of Fischer–Tropsch diesel fuels in IC engines," *Progress in Energy and Combustion Science*, vol. 37, pp. 503-523, 2011.
- [16] M. Lapuerta, O. Armas, J. J. Hernández, and A. Tsolakis, "Potential for reducing emissions in a diesel engine by fuelling with conventional biodiesel and Fischer–Tropsch diesel," *Fuel*, vol. 89, pp. 3106-3113, 2010.
- [17] Y. H. Kim, K.-W. Jun, H. Joo, C. Han, and I. K. Song, "A simulation study on gas-to-liquid (natural gas to Fischer–Tropsch synthetic fuel) process optimization," *Chemical Engineering Journal*, vol. 155, pp. 427-432, 2009.
- [18] X. Li, Z. Huang, J. Wang, and W. Zhang, "Particle size distribution from a GTL engine," *Science of the total environment*, vol. 382, pp. 295-303, 2007.

- [19] DECC. (2014, 20 May). *Reducing the UK's greenhouse gas emissions by 80% by 2050*. Available: [www.gov.uk](http://www.gov.uk)
- [20] JNCC, "The global biodiversity footprint of UK biofuel consumption," *Joint Nature Conservation Committee*, p. 40, September 2009.
- [21] J. Runyon. (2010, 20 May). *2011 Outlook for Clean Energy Jobs in the U.S. – Beating the Trend*. Available: [www.renewableenergyworld.com](http://www.renewableenergyworld.com)
- [22] P. Basu, *Biomass gasification and pyrolysis: practical design and theory*: Academic press, 2010.
- [23] DECC, "Use of UK biomass for electricity and CHP," *Department of Energy and Climate Change*, p. 9, September 2013.
- [24] M. H. Rafiq, H. A. Jakobsen, R. Schmid, and J. E. Hustad, "Experimental studies and modeling of a fixed bed reactor for Fischer–Tropsch synthesis using biosyngas," *Fuel processing technology*, vol. 92, pp. 893-907, 2011.
- [25] G. P. van der Laan, *Kinetics, selectivity and scale up of the Fischer-Tropsch synthesis*: [University Library Groningen][Host], 1999.
- [26] X. Wang and M. Economides, *Advanced Natural Gas Engineering*: Elsevier, 2013.
- [27] B. H. Davis, "Fischer–Tropsch synthesis: current mechanism and futuristic needs," *Fuel Processing Technology*, vol. 71, pp. 157-166, 2001.
- [28] H. Taylor, "Catalysis. Volume IV. Hydrocarbon Synthesis, Hydrogenation and Cyclization," *Journal of the American Chemical Society*, vol. 79, pp. 760-760, 1957.
- [29] A. de Klerk, *Fischer-Tropsch Refining*: John Wiley & Sons, 2012.
- [30] R. B. Anderson, H. Kölbl, and M. Ralek, *The Fischer-Tropsch Synthesis* vol. 16: Academic Press New York, 1984.
- [31] G. H. Olivé and S. Olive, "The chemistry of the catalyzed hydrogenation of carbon monoxide," *Springer, Berlin*, vol. 143, p. 176, 1984.
- [32] J. Yang, W. Ma, D. Chen, A. Holmen, and B. H. Davis, "Fischer–Tropsch synthesis: A review of the effect of CO conversion on methane selectivity," *Applied Catalysis A: General*, vol. 470, pp. 250-260, 2014.
- [33] A. Raje, J. R. Inga, and B. H. Davis, "Fischer-Tropsch synthesis: process considerations based on performance of iron-based catalysts," *Fuel*, vol. 76, pp. 273-280, 1997.
- [34] S. Storsæter, D. Chen, and A. Holmen, "Microkinetic modelling of the formation of C<sub>1</sub> and C<sub>2</sub> products in the Fischer–Tropsch synthesis over cobalt catalysts," *Surface science*, vol. 600, pp. 2051-2063, 2006.
- [35] M. Kollár, A. De Stefanis, H. E. Solt, M. R. Mihályi, J. Valyon, and A. A. Tomlinson, "The mechanism of the Fischer–Tropsch reaction over supported cobalt catalysts," *Journal of Molecular Catalysis A: Chemical*, vol. 333, pp. 37-45, 2010.
- [36] J. Yang, Y. Qi, J. Zhu, Y.-A. Zhu, D. Chen, and A. Holmen, "Reaction mechanism of CO activation and methane formation on Co Fischer–Tropsch catalyst: a combined DFT, transient, and steady-state kinetic modeling," *Journal of Catalysis*, vol. 308, pp. 37-49, 2013.
- [37] C. K. Rofer-DePoorter, "A comprehensive mechanism for the Fischer-Tropsch synthesis," *Chemical Reviews*, vol. 81, pp. 447-474, 1981.
- [38] E. F. Vansant, P. Van Der Voort, and K. C. Vrancken, *Characterization and chemical modification of the silica surface*: Elsevier, 1995.
- [39] L. Zhuravlev, "The surface chemistry of amorphous silica. Zhuravlev model," *Colloids and Surfaces A: Physicochemical and Engineering Aspects*, vol. 173, pp. 1-38, 2000.
- [40] D. Michel, V. Kazansky, and V. Andreev, "Study of the interaction between surface hydroxyls and adsorbed water molecules on porous glasses by means of infrared spectroscopy," *Surface Science*, vol. 72, pp. 342-356, 1978.
- [41] N. Sheppard, "Some studies of physical and chemical adsorption by means of infra-red spectroscopy," *Chimie Pure Et Appliquée*, vol. 4, p. 71, 1962.

- [42] V. Y. Davydov, A. Kiselev, and L. Zhuravlev, "Study of the surface and bulk hydroxyl groups of silica by infra-red spectra and D2O-exchange," *Transactions of the Faraday Society*, vol. 60, pp. 2254-2264, 1964.
- [43] H. E. Bergna, *The Colloid Chemistry of Silica* vol. 234. Washington, DC: American Chemical Society, 1994.
- [44] J. Peri and A. Hensley Jr, "The surface structure of silica gel," *The Journal of Physical Chemistry*, vol. 72, pp. 2926-2933, 1968.
- [45] B. Morrow and A. McFarlan, "Chemical reactions at silica surfaces," *Journal of non-crystalline solids*, vol. 120, pp. 61-71, 1990.
- [46] L. Zhuravlev, "Structurally bound water and surface characterization of amorphous silica," *Pure Appl Chem*, vol. 61, pp. 1969-1976, 1989.
- [47] J. Nawrocki, "The silanol group and its role in liquid chromatography," *Journal of Chromatography A*, vol. 779, pp. 29-71, 1997.
- [48] K. Unger, K. Lork, B. Pfleiderer, K. Albert, and E. Bayer, "Impact of acidic/hydrothermal treatment on pore structural and chromatographic properties of porous silicas: I. The conventional approach," *Journal of Chromatography A*, vol. 556, pp. 395-406, 1991.
- [49] V. M. Bermudez, "Proton nuclear magnetic resonance technique for determining the surface hydroxyl content of hydrated silica gel," *The Journal of Physical Chemistry*, vol. 74, pp. 4160-4161, 1970.
- [50] M. L. Hair, "Hydroxyl groups on silica surface," *Journal of Non-Crystalline Solids*, vol. 19, pp. 299-309, 1975.
- [51] P. Der Voort, "Modelling of the hydroxyl group population using an energetic analysis of the temperature-programmed desorption of pyridine from silica gel," *Journal of the Chemical Society, Faraday Transactions*, vol. 88, pp. 723-727, 1992.
- [52] I.-S. Chuang and G. E. Maciel, "A detailed model of local structure and silanol hydrogen bonding of silica gel surfaces," *The Journal of Physical Chemistry B*, vol. 101, pp. 3052-3064, 1997.
- [53] M. E. Dry, "Catalytic aspects of industrial Fischer-Tropsch synthesis," *Journal of Molecular Catalysis*, vol. 17, pp. 133-144, 11// 1982.
- [54] E. van Steen and M. Claeys, "Fischer - Tropsch Catalysts for the Biomass - to - Liquid (BTL) - Process," *Chemical engineering & technology*, vol. 31, pp. 655-666, 2008.
- [55] R. Guettel, U. Kunz, and T. Turek, "Reactors for Fischer - Tropsch Synthesis," *Chemical Engineering & Technology*, vol. 31, pp. 746-754, 2008.
- [56] C. Perego, R. Bortolo, and R. Zennaro, "Gas to liquids technologies for natural gas reserves valorization: The Eni experience," *Catalysis Today*, vol. 142, pp. 9-16, 2009.
- [57] W. C. Content, "Petroleum Technology, vol. 2," ed: Wiley & Sons, Hoboken, NJ, 2007.
- [58] A. Y. Khodakov, A. Griboval-Constant, R. Bechara, and V. L. Zholobenko, "Pore size effects in Fischer Tropsch synthesis over cobalt-supported mesoporous silicas," *Journal of Catalysis*, vol. 206, pp. 230-241, 2002.
- [59] Y.-N. Wang, Y.-Y. Xu, H.-W. Xiang, Y.-W. Li, and B.-J. Zhang, "Modeling of catalyst pellets for Fischer-Tropsch synthesis," *Industrial & engineering chemistry research*, vol. 40, pp. 4324-4335, 2001.
- [60] Z. Qu, W. Huang, S. Zhou, H. Zheng, X. Liu, M. Cheng, *et al.*, "Enhancement of the catalytic performance of supported-metal catalysts by pretreatment of the support," *Journal of Catalysis*, vol. 234, pp. 33-36, 8/15/ 2005.
- [61] A. Saib, M. Claeys, and E. Van Steen, "Silica supported cobalt Fischer-Tropsch catalysts: effect of pore diameter of support," *Catalysis today*, vol. 71, pp. 395-402, 2002.

- [62] B. C. Dunn, P. Cole, D. Covington, M. C. Webster, R. J. Pugmire, R. D. Ernst, *et al.*, "Silica aerogel supported catalysts for Fischer–Tropsch synthesis," *Applied Catalysis A: General*, vol. 278, pp. 233-238, 2005.
- [63] E. Peluso, C. Galarraga, and H. De Lasa, "Eggshell catalyst in Fischer–Tropsch synthesis: Intrinsic reaction kinetics," *Chemical engineering science*, vol. 56, pp. 1239-1245, 2001.
- [64] K. Triantafyllidis, A. Lappas, and M. Stöcker, *The Role of Catalysis for the Sustainable Production of Bio-fuels and Bio-chemicals*: Newnes, 2013.
- [65] S. A. Gardezi, J. T. Wolan, and B. Joseph, "Effect of catalyst preparation conditions on the performance of eggshell cobalt/SiO<sub>2</sub> catalysts for Fischer–Tropsch synthesis," *Applied Catalysis A: General*, vol. 447, pp. 151-163, 2012.
- [66] D. Song and J. Li, "Effect of catalyst pore size on the catalytic performance of silica supported cobalt Fischer–Tropsch catalysts," *Journal of Molecular Catalysis A: Chemical*, vol. 247, pp. 206-212, 2006.
- [67] J.-S. Girardon, A. S. Lermontov, L. Gengembre, P. A. Chernavskii, A. Griboval-Constant, and A. Y. Khodakov, "Effect of cobalt precursor and pretreatment conditions on the structure and catalytic performance of cobalt silica-supported Fischer–Tropsch catalysts," *Journal of Catalysis*, vol. 230, pp. 339-352, 2005.
- [68] Y. Zhang, Y. Liu, G. Yang, S. Sun, and N. Tsubaki, "Effects of impregnation solvent on Co/SiO<sub>2</sub> catalyst for Fischer–Tropsch synthesis: A highly active and stable catalyst with bimodal sized cobalt particles," *Applied Catalysis A: General*, vol. 321, pp. 79-85, 3/29/ 2007.
- [69] J.-S. Jung, S. W. Kim, and D. J. Moon, "Fischer–Tropsch Synthesis over cobalt based catalyst supported on different mesoporous silica," *Catalysis Today*, vol. 185, pp. 168-174, 2012.
- [70] A. M. Venezia, V. La Parola, L. F. Liotta, G. Pantaleo, M. Lualdi, M. Boutonnet, *et al.*, "Co/SiO<sub>2</sub> catalysts for Fischer–Tropsch synthesis; effect of Co loading and support modification by TiO<sub>2</sub>," *Catalysis Today*, vol. 197, pp. 18-23, 12/15/ 2012.
- [71] S. Sun, N. Tsubaki, and K. Fujimoto, "The reaction performances and characterization of Fischer–Tropsch synthesis Co/SiO<sub>2</sub> catalysts prepared from mixed cobalt salts," *Applied Catalysis A: General*, vol. 202, pp. 121-131, 7/31/ 2000.
- [72] Y. Zhang, Y. Liu, G. Yang, Y. Endo, and N. Tsubaki, "The solvent effects during preparation of Fischer–Tropsch synthesis catalysts: Improvement of reducibility, dispersion of supported cobalt and stability of catalyst," *Catalysis Today*, vol. 142, pp. 85-89, 2009.
- [73] H. Ming, B. G. Baker, and M. Jasieniak, "Characterization of cobalt Fischer–Tropsch catalysts: 2. Rare earth-promoted cobalt-silica gel catalysts prepared by wet impregnation," *Applied Catalysis A: General*, vol. 381, pp. 216-225, 2010.
- [74] A. Jess and C. Kern, "Modeling of Multi - Tubular Reactors for Fischer - Tropsch Synthesis," *Chemical engineering & technology*, vol. 32, pp. 1164-1175, 2009.
- [75] J. H. Yang, H.-J. Kim, D. H. Chun, H.-T. Lee, J.-C. Hong, H. Jung, *et al.*, "Mass transfer limitations on fixed-bed reactor for Fischer–Tropsch synthesis," *Fuel Processing Technology*, vol. 91, pp. 285-289, 2010.
- [76] S. Chambrey, P. Fongarland, H. Karaca, S. Piché, A. Griboval-Constant, D. Schweich, *et al.*, "Fischer–Tropsch synthesis in milli-fixed bed reactor: Comparison with centimetric fixed bed and slurry stirred tank reactors," *Catalysis Today*, vol. 171, pp. 201-206, 2011.
- [77] A. Jess, R. Popp, and K. Hedden, "Fischer–Tropsch-synthesis with nitrogen-rich syngas: fundamentals and reactor design aspects," *Applied Catalysis A: General*, vol. 186, pp. 321-342, 1999.
- [78] C. N. Satterfield, G. A. Huff Jr, H. G. Stenger, J. L. Carter, and R. J. Madon, "A comparison of Fischer-Tropsch synthesis in a fixed-bed reactor and in a slurry reactor," *Industrial & engineering chemistry fundamentals*, vol. 24, pp. 450-454, 1985.

- [79] O. González, H. Pérez, P. Navarro, L. C. Almeida, J. G. Pacheco, and M. Montes, "Use of different mesostructured materials based on silica as cobalt supports for the Fischer–Tropsch synthesis," *Catalysis Today*, vol. 148, pp. 140-147, 10/30/ 2009.
- [80] N. Osakoo, R. Henkel, S. Loiha, F. Roessner, and J. Wittayakun, "Palladium-promoted cobalt catalysts supported on silica prepared by impregnation and reverse micelle for Fischer–Tropsch synthesis," *Applied Catalysis A: General*, vol. 464–465, pp. 269-280, 8/15/ 2013.
- [81] H. Wu, Y. Yang, H. Suo, M. Qing, L. Yan, B. Wu, *et al.*, "Effect of TiO<sub>2</sub> promotion on the structure and performance of silica-supported cobalt-based catalysts for Fischer–Tropsch synthesis," *Journal of Molecular Catalysis A: Chemical*, vol. 390, pp. 52-62, 8// 2014.
- [82] A. Y. Khodakov, R. Bechara, and A. Griboval-Constant, "Fischer–Tropsch synthesis over silica supported cobalt catalysts: mesoporous structure versus cobalt surface density," *Applied Catalysis A: General*, vol. 254, pp. 273-288, 11/20/ 2003.
- [83] W. Ma, G. Jacobs, D. E. Sparks, M. K. Gnanamani, V. R. R. Pendyala, C. H. Yen, *et al.*, "Fischer–Tropsch synthesis: Support and cobalt cluster size effects on kinetics over Co/Al<sub>2</sub>O<sub>3</sub> and Co/SiO<sub>2</sub> catalysts," *Fuel*, vol. 90, pp. 756-765, 2// 2011.
- [84] J. Hong, E. Marceau, A. Y. Khodakov, A. Griboval-Constant, C. La Fontaine, F. Villain, *et al.*, "Impact of sorbitol addition on the structure and performance of silica-supported cobalt catalysts for Fischer–Tropsch synthesis," *Catalysis Today*, vol. 175, pp. 528-533, 10/25/ 2011.
- [85] M. K. Gnanamani, G. Jacobs, W. D. Shafer, and B. H. Davis, "Fischer–Tropsch synthesis: Activity of metallic phases of cobalt supported on silica," *Catalysis Today*, vol. 215, pp. 13-17, 10/15/ 2013.
- [86] J. van de Loosdrecht, B. Balzhinimaev, J. A. Dalmon, J. W. Niemantsverdriet, S. V. Tsybulya, A. M. Saib, *et al.*, "Cobalt Fischer-Tropsch synthesis: Deactivation by oxidation?," *Catalysis Today*, vol. 123, pp. 293-302, 5/30/ 2007.
- [87] S. Storsæter, B. Tøtdal, J. C. Walmsley, B. S. Tanem, and A. Holmen, "Characterization of alumina-, silica-, and titania-supported cobalt Fischer–Tropsch catalysts," *Journal of Catalysis*, vol. 236, pp. 139-152, 11/15/ 2005.
- [88] P. Hunpinyo, P. Narataruksa, S. Tungkamani, K. Pana-Supphamassadu, N. Chollacoop, H. Sukkathanyawat, *et al.*, "A comprehensive small and pilot fixed bed reactor approach for testing Fischer-Tropsch catalyst activity and performance on BTL route," *Arabian Journal of Chemistry*.
- [89] N. O. Elbashir, B. Bao, and M. M. El-Halwagi, "An Approach to the Design of Advanced Fischer-Tropsch Reactor for Operation in Near-Critical and Supercritical Phase Media," in *Proceedings of the 1st Annual Gas Processing Symposium*. vol. 1, H. E. Alfadala, G. V. R. Reklaitis, and M. M. El-Halwagi, Eds., ed Amsterdam: Elsevier, 2009, pp. 423-433.
- [90] R. Guettel and T. Turek, "Comparison of different reactor types for low temperature Fischer–Tropsch synthesis: A simulation study," *Chemical Engineering Science*, vol. 64, pp. 955-964, 3// 2009.
- [91] H. Schulz, "Short history and present trends of Fischer–Tropsch synthesis," *Applied Catalysis A: General*, vol. 186, pp. 3-12, 10/4/ 1999.
- [92] W. Chu, P. A. Chernavskii, L. Gengembre, G. A. Pankina, P. Fongarland, and A. Y. Khodakov, "Cobalt species in promoted cobalt alumina-supported Fischer–Tropsch catalysts," *Journal of Catalysis*, vol. 252, pp. 215-230, 12/10/ 2007.
- [93] Y. Zhang, H. Xiong, K. Liew, and J. Li, "Effect of magnesia on alumina-supported cobalt Fischer–Tropsch synthesis catalysts," *Journal of Molecular Catalysis A: Chemical*, vol. 237, pp. 172-181, 8/2/ 2005.
- [94] S. S. Itkulovaa, G. D. Zakumbaevaa, R. S. Arzumanovab, and V. A. Ovchinnikovb, "Production of hard hydrocarbons from synthesis-gas over co-containing supported catalysts," *Fischer-Tropsch Synthesis, Catalysts and Catalysis*, vol. 163, p. 75, 2006.

- [95] H. Schulz, "Comparing Fischer-Tropsch synthesis on iron-and cobalt catalysts: The dynamics of structure and function," *Studies in surface science and catalysis*, vol. 163, pp. 177-199, 2007.
- [96] G. Jacobs, T. K. Das, J. Li, M. Luo, P. M. Patterson, and B. H. Davis, "Fischer-Tropsch synthesis: influence of support on the impact of co-fed water for cobalt-based catalysts," *Fischer-Tropsch Synthesis, Catalysts and Catalysis*, vol. 163, p. 217, 2006.
- [97] C. Perego and P. Villa, "Catalyst preparation methods," *Catalysis Today*, vol. 34, pp. 281-305, 1997.
- [98] K. Acres, A. Bird, J. Jenkins, and F. King, "The design and preparation of supported catalysts," *Spec. Period. Rep. Catal*, vol. 4, pp. 1-30, 1981.
- [99] J. A. Anderson and M. F. Garcia, *Supported metals in catalysis* vol. 5: Imperial College Press London, 2005.
- [100] Carbolite. *ELF - Laboratory Chamber Furnaces*. Available: <http://www.carbolite.com/home/>
- [101] Bruker. (2008). *Bruker S8 Tiger Spectrometry Solutions*. Available: [www.bruker-axs.com](http://www.bruker-axs.com)
- [102] Y. Hirokawa, Y. Shibata, T. Konya, Y. Koike, and T. Nakamura, "X - ray fluorescence analysis of Co, Ni, Pd, Ag, and Au in the scrapped printed - circuit - board ash," *X - Ray Spectrometry*, vol. 42, pp. 134-140, 2013.
- [103] Bruker. (2014). *Technological innovation for wavelength dispersive X-ray fluorescence (WDXRF) spectrometry*. Available: <http://www.bruker.com/products/x-ray-diffraction-and-elemental-analysis/x-ray-fluorescence/s8-tiger/overview.html>
- [104] K. D. Hammond and W. C. Conner Jr, "Chapter One - Analysis of Catalyst Surface Structure by Physical Sorption," in *Advances in Catalysis*. vol. Volume 56, C. G. Bruce and C. J. Friederike, Eds., ed: Academic Press, 2013, pp. 1-101.
- [105] K. S. W. Sing, "Adsorption methods for the characterization of porous materials," *Advances in Colloid and Interface Science*, vol. 76-77, pp. 3-11, 7/1/ 1998.
- [106] S. Brunauer, P. H. Emmett, and E. Teller, "Adsorption of gases in multimolecular layers," *Journal of the American Chemical Society*, vol. 60, pp. 309-319, 1938.
- [107] C. Scherdel, G. Reichenauer, and M. Wiener, "Relationship between pore volumes and surface areas derived from the evaluation of N<sub>2</sub>-sorption data by DR-, BET- and t-plot," *Microporous and Mesoporous Materials*, vol. 132, pp. 572-575, 8// 2010.
- [108] G. Wang, K. Wang, and T. Ren, "Improved analytic methods for coal surface area and pore size distribution determination using 77&#xa0;K nitrogen adsorption experiment," *International Journal of Mining Science and Technology*, vol. 24, pp. 329-334, 5// 2014.
- [109] E. P. Barrett, L. G. Joyner, and P. P. Halenda, "The determination of pore volume and area distributions in porous substances. I. Computations from nitrogen isotherms," *Journal of the American Chemical society*, vol. 73, pp. 373-380, 1951.
- [110] Micromeritics. (October 2011, 28 June). *ASAP 2020 Accelerated Surface Area and Porosimetry System*. Available: [www.cif.iastate.edu](http://www.cif.iastate.edu)
- [111] W. Makowski, L. Chmielarz, and P. Kuśtrowski, "Determination of the pore size distribution of mesoporous silicas by means of quasi-equilibrated thermodesorption of n-nonane," *Microporous and Mesoporous Materials*, vol. 120, pp. 257-262, 4/15/ 2009.
- [112] B. Huang, C. H. Bartholomew, and B. F. Woodfield, "Improved calculations of pore size distribution for relatively large, irregular slit-shaped mesopore structure," *Microporous and Mesoporous Materials*, vol. 184, pp. 112-121, 1/15/ 2014.
- [113] Scintag. (1999). *Chapter 7: Basics of X-ray Diffraction* Available: [http://www.scribd.com/ugcc\\_sr0112](http://www.scribd.com/ugcc_sr0112)
- [114] B. D. Cullity, "Elements of X-ray Diffraction," *American Journal of Physics*, vol. 25, pp. 394-395, 1957.

- [115] B. Lavina, P. Dera, and R. T. Downs, "Modern X-ray diffraction methods in mineralogy and geosciences," *Reviews in Mineralogy and Geochemistry*, vol. 78, pp. 1-31, 2014.
- [116] H. Stanjek and W. Häusler, "Basics of X-ray Diffraction," *Hyperfine interactions*, vol. 154, pp. 107-119, 2004.
- [117] I. Inc., "Brochure, Inel - EQUINOX3000," Inel, Ed., ed. France.
- [118] ICDD. (29 January). *XRD Powder Diffraction File (PDF) combined by the Joint Committee on Powder Diffraction Standards (JCPDS)*. Available: <http://www.icdd.com>
- [119] Inel. (2009). *X-ray diffraction for the 21st century*. Available: <http://www.inel.fr/>
- [120] Olin. (30 June). *JEOL JSM-6060LV Scanning Electron Microscope (SEM)*. Available: <http://www.olin.edu/>
- [121] G. Höflinger. (2013, 30 June). *Brief Introduction to Coating Technology for Electron Microscopy*. Available: <http://www.leica-microsystems.com/science-lab/>
- [122] Mlcomeritics. *AutoChem II 2920, Automated Catalyst Characterization System*. Available: <http://www.micromeritics.com/product-showcase/AutoChem-II-2920.aspx>
- [123] C. M. Van Den Bleek, K. Van Der Wiele, and P. J. Van Den Berg, "The effect of dilution on the degree of conversion in fixed bed catalytic reactors," *Chemical Engineering Science*, vol. 24, pp. 681-694, 4// 1969.
- [124] D. van Herk, P. Castaño, M. Quaglia, M. T. Kreutzer, M. Makkee, and J. A. Moulijn, "Avoiding segregation during the loading of a catalyst–inert powder mixture in a packed micro-bed," *Applied Catalysis A: General*, vol. 365, pp. 110-121, 8/15/ 2009.
- [125] U. Mann, *Principles of chemical reactor analysis and design: new tools for industrial chemical reactor operations*: John Wiley & Sons, 2009.
- [126] G. Taguchi, S. Chowdhury, and Y. Wu, *Taguchi's quality engineering handbook*: Wiley, 2005.
- [127] M. O. Stephanie Fraley, Ben Terrien, John Zalewski. (2006). *Design of experiments via taguchi methods: orthogonal arrays (12 May 2006 ed.)*. Available: <https://controls.engin.umich.edu/>
- [128] R. K. Roy, *A primer on the Taguchi method*: Society of Manufacturing Engineers, 2010.
- [129] B. M. Gopalsamy, B. Mondal, and S. Ghosh, "Taguchi method and ANOVA: An approach for process parameters optimization of hard machining while machining hardened steel," *Journal of scientific & Industrial research*, vol. 68, pp. 686-695, 2009.
- [130] E. G. K. J. R.D. Deslattes, P. Indelicato, L. de Billy, E. Lindroth, J. Anton, J.S. Coursey, D.J. Schwab, J. Chang, R. Sukumar, K. Olsen, and R.A. Dragoset. (2003). *X-Ray Transition Energies*. Available: <http://www.nist.gov/>
- [131] K. Jalama, N. J. Coville, H. Xiong, D. Hildebrandt, D. Glasser, S. Taylor, *et al.*, "A comparison of Au/Co/Al<sub>2</sub>O<sub>3</sub> and Au/Co/SiO<sub>2</sub> catalysts in the Fischer–Tropsch reaction," *Applied Catalysis A: General*, vol. 395, pp. 1-9, 3/15/ 2011.
- [132] I. T. Ghampson, C. Newman, L. Kong, E. Pier, K. D. Hurley, R. A. Pollock, *et al.*, "Effects of pore diameter on particle size, phase, and turnover frequency in mesoporous silica supported cobalt Fischer–Tropsch catalysts," *Applied Catalysis A: General*, vol. 388, pp. 57-67, 11/20/ 2010.
- [133] E. Lira, C. M. López, F. Oropeza, M. Bartolini, J. Alvarez, M. Goldwasser, *et al.*, "HMS mesoporous silica as cobalt support for the Fischer–Tropsch Synthesis: Pretreatment, cobalt loading and particle size effects," *Journal of Molecular Catalysis A: Chemical*, vol. 281, pp. 146-153, 2/18/ 2008.
- [134] Y. Zhang, K. Hanayama, and N. Tsubaki, "The surface modification effects of silica support by organic solvents for Fischer–Tropsch synthesis catalysts," *Catalysis Communications*, vol. 7, pp. 251-254, 5// 2006.
- [135] C. Chen, H. Yuuda, and X. Li, "Fischer–Tropsch synthesis over one eggshell-type Co/SiO<sub>2</sub> catalyst in a slurry phase reactor," *Applied Catalysis A: General*, vol. 396, pp. 116-122, 4/15/ 2011.

- [136] D. Schanke, S. Vada, E. A. Blekkan, A. M. Hilmen, A. Hoff, and A. Holmen, "Study of Pt-Promoted Cobalt CO Hydrogenation Catalysts," *Journal of Catalysis*, vol. 156, pp. 85-95, 9// 1995.
- [137] T. Witoon, M. Chareonpanich, and J. Limtrakul, "Effect of hierarchical meso-macroporous silica supports on Fischer-Tropsch synthesis using cobalt catalyst," *Fuel Processing Technology*, vol. 92, pp. 1498-1505, 2011.
- [138] H. Karaca, P. Fongarland, A. Griboval-Constant, A. Y. Khodakov, K. Hortmann, and S. Van Donk, "Intergranular and intragranular cobalt repartitions in alumina supported Fischer-Tropsch catalysts promoted with platinum," *Comptes Rendus Chimie*, vol. 12, pp. 668-676, 6// 2009.
- [139] S. Bessell, "Support effects in cobalt-based fischer-tropsch catalysis," *Applied Catalysis A: General*, vol. 96, pp. 253-268, 3/26/ 1993.
- [140] Ø. Borg, N. Hammer, S. Eri, O. A. Lindvåg, R. Myrstad, E. A. Blekkan, *et al.*, "Fischer-Tropsch synthesis over un-promoted and Re-promoted  $\gamma$ -Al<sub>2</sub>O<sub>3</sub> supported cobalt catalysts with different pore sizes," *Catalysis Today*, vol. 142, pp. 70-77, 4/15/ 2009.
- [141] J. A. Lapszewicz, H. J. Loeh, and J. R. Chipperfield, "The effect of catalyst porosity on methane selectivity in the Fischer-Tropsch reaction," *J. Chem. Soc., Chem. Commun.*, pp. 913-914, 1993.
- [142] E. W. Kuipers, I. H. Vinkenburg, and H. Oosterbeek, "Chain Length Dependence of  $\alpha$ -Olefin Readsorption in Fischer-Tropsch Synthesis," *Journal of Catalysis*, vol. 152, pp. 137-146, 3// 1995.
- [143] E. Iglesia, S. L. Soled, R. A. Fiato, and G. H. Via, "Bimetallic Synergy in Cobalt Ruthenium Fischer-Tropsch Synthesis Catalysts," *Journal of Catalysis*, vol. 143, pp. 345-368, 10// 1993.
- [144] Ø. Borg, S. Eri, E. A. Blekkan, S. Storsæter, H. Wigum, E. Rytter, *et al.*, "Fischer-Tropsch synthesis over  $\gamma$ -alumina-supported cobalt catalysts: Effect of support variables," *Journal of Catalysis*, vol. 248, pp. 89-100, 5/15/ 2007.
- [145] S. Storsæter, Ø. Borg, E. A. Blekkan, and A. Holmen, "Study of the effect of water on Fischer-Tropsch synthesis over supported cobalt catalysts," *Journal of Catalysis*, vol. 231, pp. 405-419, 2005.
- [146] C. H. Bartholomew, "Mechanisms of catalyst deactivation," *Applied Catalysis A: General*, vol. 212, pp. 17-60, 2001.
- [147] N. E. Tsakoumis, M. Rønning, Ø. Borg, E. Rytter, and A. Holmen, "Deactivation of cobalt based Fischer-Tropsch catalysts: a review," *Catalysis Today*, vol. 154, pp. 162-182, 2010.
- [148] C. G. Visconti, L. Lietti, P. Forzatti, and R. Zennaro, "Fischer-Tropsch synthesis on sulphur poisoned Co/Al<sub>2</sub>O<sub>3</sub> catalyst," *Applied Catalysis A: General*, vol. 330, pp. 49-56, 10/10/ 2007.
- [149] D. J. Moodley, J. van de Loosdrecht, A. M. Saib, M. J. Overett, A. K. Datye, and J. W. Niemantsverdriet, "Carbon deposition as a deactivation mechanism of cobalt-based Fischer-Tropsch synthesis catalysts under realistic conditions," *Applied Catalysis A: General*, vol. 354, pp. 102-110, 2/15/ 2009.
- [150] A. M. Saib, A. Borgna, J. van de Loosdrecht, P. J. van Berge, and J. W. Niemantsverdriet, "XANES study of the susceptibility of nano-sized cobalt crystallites to oxidation during realistic Fischer-Tropsch synthesis," *Applied Catalysis A: General*, vol. 312, pp. 12-19, 9/8/ 2006.
- [151] Z. Yan, Z. Wang, D. B. Bukur, and D. W. Goodman, "Fischer-Tropsch synthesis on a model Co/SiO<sub>2</sub> catalyst," *Journal of Catalysis*, vol. 268, pp. 196-200, 12/10/ 2009.
- [152] G. W. Huber, C. G. Guymon, T. L. Conrad, B. C. Stephenson, and C. H. Bartholomew, "Hydrothermal stability of Co/SiO<sub>2</sub> fischer-tropsch synthesis catalysts," in *Studies in Surface Science and Catalysis*. vol. Volume 139, G. W. R. J.J. Spivey and B. H. Davis, Eds., ed: Elsevier, 2001, pp. 423-430.

- [153] B. H. Davis and M. L. Occelli, *Advances in Fischer-Tropsch synthesis, catalysts, and catalysis*: CRC Press, 2010.
- [154] J. A. Moulijn, A. E. van Diepen, and F. Kapteijn, "Catalyst deactivation: is it predictable?: What to do?," *Applied Catalysis A: General*, vol. 212, pp. 3-16, 4/30/ 2001.
- [155] A. M. Saib, D. J. Moodley, I. M. Ciobîcă, M. M. Hauman, B. H. Sigwebela, C. J. Weststrate, *et al.*, "Fundamental understanding of deactivation and regeneration of cobalt Fischer-Tropsch synthesis catalysts," *Catalysis Today*, vol. 154, pp. 271-282, 9/15/ 2010.
- [156] A. Tavasoli, A. N. Pour, and M. G. Ahangari, "Kinetics and product distribution studies on ruthenium-promoted cobalt/alumina Fischer-Tropsch synthesis catalyst," *Journal of Natural Gas Chemistry*, vol. 19, pp. 653-659, 11// 2010.
- [157] T. Riedel, M. Claeys, H. Schulz, G. Schaub, S.-S. Nam, K.-W. Jun, *et al.*, "Comparative study of Fischer-Tropsch synthesis with H<sub>2</sub>/CO and H<sub>2</sub>/CO<sub>2</sub> syngas using Fe- and Co-based catalysts," *Applied Catalysis A: General*, vol. 186, pp. 201-213, 10/4/ 1999.
- [158] A. Sari, Y. Zamani, and S. A. Taheri, "Intrinsic kinetics of Fischer-Tropsch reactions over an industrial Co-Ru/ $\gamma$ -Al<sub>2</sub>O<sub>3</sub> catalyst in slurry phase reactor," *Fuel Processing Technology*, vol. 90, pp. 1305-1313, 10// 2009.
- [159] M. J. Keyser, R. C. Everson, and R. L. Espinoza, "Fischer-Tropsch kinetic studies with cobalt-manganese oxide catalysts," *Industrial & engineering chemistry research*, vol. 39, pp. 48-54, 2000.
- [160] A. Irankhah, A. Haghtalab, E. V. Farahani, and K. Sadaghianizadeh, "Fischer-Tropsch Reaction Kinetics of Cobalt Catalyst in Supercritical Phase," *Journal of Natural Gas Chemistry*, vol. 16, pp. 115-120, 6// 2007.
- [161] H. Atashi, F. Siami, A. A. Mirzaei, and M. Sarkari, "Kinetic study of Fischer-Tropsch process on titania-supported cobalt-manganese catalyst," *Journal of Industrial and Engineering Chemistry*, vol. 16, pp. 952-961, 11/25/ 2010.
- [162] I. C. Yates and C. N. Satterfield, "Intrinsic kinetics of the Fischer-Tropsch synthesis on a cobalt catalyst," *Energy & Fuels*, vol. 5, pp. 168-173, 1991.
- [163] M.-S. Shin, N. Park, M.-J. Park, J.-Y. Cheon, J. K. Kang, K.-W. Jun, *et al.*, "Modeling a channel-type reactor with a plate heat exchanger for cobalt-based Fischer-Tropsch synthesis," *Fuel Processing Technology*, vol. 118, pp. 235-243, 2// 2014.
- [164] A. Lapidus, A. Krylova, J. Rathousky', A. Zukal, and M. Janc'a'lkova', "Hydrocarbon synthesis from carbon monoxide and hydrogen on impregnated cobalt catalysts II: Activity of 10% Co/Al<sub>2</sub>O<sub>3</sub> and 10% Co/SiO<sub>2</sub> catalysts in Fischer-Tropsch synthesis," *Applied Catalysis A: General*, vol. 80, pp. 1-11, 1/2/ 1992.
- [165] V. Frøseth and A. Holmen, "CO hydrogenation on Co/ $\gamma$ -Al<sub>2</sub>O<sub>3</sub> and CoRe/ $\gamma$ -Al<sub>2</sub>O<sub>3</sub> studied by SSITKA," *Topics in Catalysis*, vol. 45, pp. 45-50, 2007.
- [166] H. H. Storch, R. A. Anderson, and N. Golumbic, *The Fischer-Tropsch and related syntheses* vol. 6: Wiley New York, 1951.
- [167] E. Marguá, I. Queralt, and M. Hidalgo, "Application of X-ray fluorescence spectrometry to determination and quantitation of metals in vegetal material," *TrAC Trends in Analytical Chemistry*, vol. 28, pp. 362-372, 3// 2009.
- [168] M. Trépanier, A. Tavasoli, A. K. Dalai, and N. Abatzoglou, "Co, Ru and K loadings effects on the activity and selectivity of carbon nanotubes supported cobalt catalyst in Fischer-Tropsch synthesis," *Applied Catalysis A: General*, vol. 353, pp. 193-202, 2/1/ 2009.
- [169] A. Y. Khodakov, W. Chu, and P. Fongarland, "Advances in the development of novel cobalt Fischer-Tropsch catalysts for synthesis of long-chain hydrocarbons and clean fuels," *Chemical Reviews*, vol. 107, pp. 1692-1744, 2007.
- [170] A. Y. Khodakov, J. Lynch, D. Bazin, B. Rebours, N. Zanier, B. Moisson, *et al.*, "Reducibility of Cobalt Species in Silica-Supported Fischer-Tropsch Catalysts," *Journal of Catalysis*, vol. 168, pp. 16-25, 5// 1997.

- [171] A. Y. Khodakov, A. Griboval-Constant, R. Bechara, and F. Villain, "Pore-size control of cobalt dispersion and reducibility in mesoporous silicas," *The Journal of Physical Chemistry B*, vol. 105, pp. 9805-9811, 2001.
- [172] H. Ming and B. G. Baker, "Characterization of cobalt Fischer-Tropsch catalysts I. Unpromoted cobalt-silica gel catalysts," *Applied Catalysis A: General*, vol. 123, pp. 23-36, 3/2/ 1995.
- [173] G. Jacobs, T. K. Das, Y. Zhang, J. Li, G. Racoillet, and B. H. Davis, "Fischer-Tropsch synthesis: support, loading, and promoter effects on the reducibility of cobalt catalysts," *Applied Catalysis A: General*, vol. 233, pp. 263-281, 7/10/ 2002.
- [174] W. S. Yang, H. W. Xiang, Y. Y. Xu, and Y. W. Li, "Characteristics and reactivities of cobalt based mesoporous silica catalysts for fischer-tropsch synthesis," in *Studies in Surface Science and Catalysis*. vol. Volume 146, R. R. W.-S. A. C. W. L. Sang-Eon Park and C. Jong-San, Eds., ed: Elsevier, 2003, pp. 693-696.
- [175] Y. Wang, B. Hou, J. Chen, L. Jia, D. Li, and Y. Sun, "Ethylenediamine modified Co/SiO<sub>2</sub> sol-gel catalysts for non-ASF FT synthesis of middle distillates," *Catalysis Communications*, vol. 10, pp. 747-752, 2/15/ 2009.
- [176] F. Morales and B. M. Weckhuysen, "Promotion effects in Co-based Fischer-Tropsch catalysis," *Catalysis*, vol. 19, pp. 1-40, 2006.
- [177] H. P. Klug and L. E. Alexander, "X-ray diffraction procedures: for polycrystalline and amorphous materials," *X-Ray Diffraction Procedures: For Polycrystalline and Amorphous Materials, 2nd Edition*, by Harold P. Klug, Leroy E. Alexander, pp. 992. ISBN 0-471-49369-4. Wiley-VCH, May 1974., vol. 1, 1974.
- [178] B. Ernst, S. Libs, P. Chaumette, and A. Kiennemann, "Preparation and characterization of Fischer-Tropsch active Co/SiO<sub>2</sub> catalysts," *Applied Catalysis A: General*, vol. 186, pp. 145-168, 10/4/ 1999.
- [179] B. Ernst, L. Hilaire, and A. Kiennemann, "Effects of highly dispersed ceria addition on reducibility, activity and hydrocarbon chain growth of a Co/SiO<sub>2</sub> Fischer-Tropsch catalyst," *Catalysis Today*, vol. 50, pp. 413-427, 4/29/ 1999.
- [180] D. G. Castner, P. R. Watson, and I. Y. Chan, "X-ray absorption spectroscopy, x-ray photoelectron spectroscopy, and analytical electron microscopy studies of cobalt catalysts. 1. Characterization of calcined catalysts," *The Journal of Physical Chemistry*, vol. 93, pp. 3188-3194, 1989.
- [181] B. Jongsomjit, T. Wongsalee, and P. Praserthdam, "Catalytic behaviors of mixed TiO<sub>2</sub>-SiO<sub>2</sub>-supported cobalt Fischer-Tropsch catalysts for carbon monoxide hydrogenation," *Materials Chemistry and Physics*, vol. 97, pp. 343-350, 6/10/ 2006.
- [182] P. Reubroycharoen, T. Vitidsant, Y. Liu, G. Yang, and N. Tsubaki, "Highly active Fischer-Tropsch synthesis Co/SiO<sub>2</sub> catalysts prepared from microwave irradiation," *Catalysis Communications*, vol. 8, pp. 375-378, 3// 2007.
- [183] B. K. Sharma, M. P. Sharma, S. Kumar, S. K. Roy, S. K. Roy, S. Badrinarayanan, *et al.*, "Studies on cobalt-based Fischer-Tropsch catalyst and characterization using SEM and XPS techniques," *Applied Catalysis A: General*, vol. 211, pp. 203-211, 4/13/ 2001.
- [184] C. Medina, R. García, P. Reyes, J. L. G. Fierro, and N. Escalona, "Fischer Tropsch synthesis from a simulated biosyngas feed over Co(x)/SiO<sub>2</sub> catalysts: Effect of Co-loading," *Applied Catalysis A: General*, vol. 373, pp. 71-75, 1/31/ 2010.